CONTROL AND SUPPRESSION OF LAMINAR VORTEX SHEDDING OFF TWO-DIMENSIONAL BLUFF BODIES

A DISSERTATION
SUBMITTED TO THE DEPARTMENT OF
MECHANICAL ENGINEERING
AND THE COMMITTEE ON GRADUATE STUDIES
OF STANFORD UNIVERSITY
IN PARTIAL FULFILLMENT OF THE REQUIREMENTS
FOR THE DEGREE OF
DOCTOR OF PHILOSOPHY

Andre S. Chan
December 2012

I certify that I have read this dissertation and that, in my opinion, it is fully adequate in scope and quality as a dissertation for the degree of Doctor of Philosophy.

John Eaton, Co-Adviser

I certify that I have read this dissertation and that, in my opinion, it is fully adequate in scope and quality as a dissertation for the degree of Doctor of Philosophy.

Antony Jameson, Co-Adviser

I certify that I have read this dissertation and that, in my opinion, it is fully adequate in scope and quality as a dissertation for the degree of Doctor of Philosophy.

Robert MacCormack

Approved for the Stanford University Committee on Graduate Studies.

Patricia J. Gumport, Vice Provost Graduate Education

This signature page was generated electronically upon submission of this dissertation in electronic format. An original signed hard copy of the signature page is on file in University Archives.

Abstract

The focus of this research is on the control and suppression of vortex shedding of flow past bluff bodies. The motivation of this research stems from the aerodynamic problems encountered in the design and development of hard disk drives (HDD's). Two different computational fluid dynamic methods have been used in this research– the Semi-Implicit Method for Pressure Linked Equation (SIMPLE), that is widely employed in today's commercial incompressible flow solvers, and the high-order spectral difference (SD) method, recently developed for compressible flow solution. In addition to numerical simulation and verification, complementary experimental measurements have been performed to further validate the results. This research leads to two very different suppression techniques: 1) a passive control using a thin splitter plate positioned downstream of the bluff body; 2) an active control by way of counter rotating a cylinder pair.

The passive suppression technique places a thin splitter plate downstream of the bluff body in order to interfere with the vortex wakes and thereby suppress the vortex-induced forces on the bluff body itself. The present investigation examines the suppression of wake instabilities in the laminar shedding regime. Both bounded and unbounded flow conditions are examined. It is found that in the bounded flow condition, the channel walls have an additional stabilizing effect on the shedding control. With proper positioning of the splitter plate, vortex shedding is completely suppressed in a bounded flow with moderate blockage factor. Wind tunnel empirical experiments have also confirmed the effectiveness of a splitter plate in a bounded flow.

Active flow control by counter-rotating a pair of cylinders has been numerically investigated. It has also been investigated experimentally in partnership with the Gas

Dynamics Laboratory at Princeton University. It is demonstrated that it is possible to suppress unsteady vortex shedding for gap sizes from one to five cylinder diameters, at Reynolds numbers from 100 to 200. The degree of unsteady wake suppression is proportional to the speed and the direction of rotation, and there is a critical rotation rate where a complete suppression of flow unsteadiness can be achieved. In the doublet-like configuration at higher rotational speeds, a virtual elliptic body that resembles a potential doublet is formed, and the drag is reduced to zero. The shape of the elliptic body primarily depends on the gap between the two cylinders and the speed of rotation. Prior to the formation of the elliptic body, a second instability region is observed, similar to that seen in studies of rotating single cylinders. It is also shown that the unsteady wake suppression can be achieved by rotating each cylinder in the opposite direction, that is, in a reverse doublet-like configuration. This tends to minimize the wake interaction of the cylinder pair and the second instability did not make an appearance over the range of speeds investigated here.

Acknowledgments

This PhD experience has constantly reminded me that the whole process requires the enormous patience from many people whom I would like to sincerely acknowledge here. It certainly has been a fun and rewarding learning experience, especially when I have had the chance of working under the tutelage of arguably the world's best. First and foremost, I would like to express my heartfelt gratitude for my principal adviser, Professor Antony Jameson. Without his encouragement and advice throughout the years, the works in this PhD thesis would not have been realized. It is a great honor and privilege to make it to the list of his students. As said by many of his students before me, I share a deep respect for his knowledge in the field of mathematics, computational fluid dynamics and the science of flight. Without a doubt, he has the very best intention to see that his students succeed in life and be able to contribute to society beyond the classrooms. I am particularly thankful for his kindness, patience and support of my lifelong learning goal. He understands that I am not one of his typical graduate students and that I do have other important commitments in life outside the academic environment, like full time work and family. The thoughts of quitting have occurred in my mind more than once but the commitment and dedication he gives to his students have always convinced me otherwise. I cannot give up on myself when he has not given up on me. I truly appreciate his respect for my struggles in that regard. It is a very special relationship that I will cherish for the rest of my life.

The second most influential person in my graduate study is Professor Robert MacCormack. Before I came to Stanford, one of the first techniques I learned about the subject of CFD was the MacCormack method. It is probably by far one of the simplest and most elegant methods to use when one first learns about the subject. He was already the legend in the field and his work propelled me to go learn from him at Stanford. Not to be disappointed, it was enlightening to take AA214 B&C from him as those were two of my most favorite classes at Stanford. I am sincerely grateful for all the guidance and advice he has given me all these years. Professor MacCormack is probably one the most caring and nicest professors who can relate well with his students. Many will agree.

I would also like to thank Professor John Eaton for being the co-adviser. I consider him one of the pioneering researchers on the not-so-trivial subject of fluid dynamics of hard disk drives. Some of his works in the Eighties and Nineties have served me well as a basis for my current work of developing the latest generation of hard disk drives. I also would like to express my gratitude to Professor Juan Alonso who has been part of my journey during the first several years. His motivation and support have helped put my part-time graduate work in reasonably good academic order. Most importantly, I thank him for being a good friend I can always talk to. In addition, I would like to thank Professor Michael Saunders for being on my thesis defense committee.

I am grateful to my good friend, Professor Chunlei Liang of George Washington University. He was very supportive and helpful throughout much of the time when he was here at Stanford. He was instrumental in the development of the spectral difference code that has been used much throughout my research. I would also like to express my gratitude to Peter Dewey and Professor Alexander Smits of the Gas Dynamics Lab at Princeton University with whom I collaborated on the counter-rotating cylinder pair portion of this research. Their first-rate experimental results have provided me with enough evidence to feel confident about my numerical simulation results. I also would like to thank Professor Norberg of Lunds Universitet for providing me with some invaluable experimental data that I have used for benchmarking.

It also has been a great joy to be associated with the Aerospace Computing Laboratory. Since my PhD journey has been a long one, I have had the extended pleasure of meeting and making friends with many people who have come through the lab like Guido, John, Karthik, Kasidit, Ki-Hwan, Kui, Lala, Matt, Nawee, Patrice, Peter, Sachin and Yves. I can honestly say that they are all brilliant, gifted and most importantly fun to hang around with. Their influences have definitely helped this older lab mate learn and stay young.

Taking on the rarely accomplished part time PhD also requires tremendous commitments from my past and present employers (namely Quantum, IBM and Hitachi). In particular, I would like to sincerely acknowledge my managers, Andrew Hanlon, Stanley Wong, Bob Reinhart and Scott Abrahamson, for the time allowance and the financial support that helped facilitate this effort. I would also like to thank my colleagues, Chisin Chiang and Ferdi Hendriks, for their help along the way. Special thanks also go to AFSOR, NSF and KACST for providing partial funding for my research.

Above all, there are not enough words to show my sincere appreciation for my family. The most important figure is my wife, Lavinia, who has given me her unwavering support throughout these many years. Without her, it would be impossible for me to balance my career, family and graduate work. I also would like to thank my two children, Andrea and Simona, for making my academic journey fun, interesting and manageable. I hope I have instilled in them the value of lifelong learning. I thank my parents for their support of my education during the younger years. Their hard work, love, dedication and encouragement have shaped me to be who I am. I also thank my sister for being there for me and my parents. This thesis is dedicated to them.

Contents

List of Tables

List of Figures

Chapter 1

Introduction and motivation

1.1 Introduction

Vortex dominated flows have been a subject of great interest to scientists and engineers studying fluid flow phenomena. These types of flows involve complex wakes that can be two- or three-dimensional. Unstable vortex wakes are formed when there is a flow of fluid past a structure that is non-streamlined or typically referred to as a "bluff body". These unsteady wakes leads to vortex induced vibration of structures that can pose practical challenges across different engineering disciplines. Severe vortex induced vibration can lead to catastrophic structural failures. Vortex induced vibration problems are often encountered in the design of towers, buildings, oil rigs, offshore structures, bridges, pipelines, heat exchangers, etc. Any non-streamlined body is considered a bluff body when the pressure drag is dominant over viscous drag. Representative examples include the circular cylinder, sphere, square and rectangle. A streamlined airfoil can also be considered a bluff body if it is set a large angle of attack.

The majority of past research papers on bluff body flow have been devoted to the flow past a two-dimensional circular cylinder [1, 2, 3, 4, 5, 6, 7, 8, 9, 10, 11, 12, 13, 14, 15]. As noted by Roshko [11], the circular cylinder is, by far, the "quintessential" bluff body. The popularity of the circular cylinder comes from its simplicity and its practical importance in real engineering applications such as offshore pipelines, bridge towers, piers, etc. For experimental studies, it is convenient that circular-shaped tubings and rods are readily available. Yet, the flow past the circular cylinder can still be profoundly complex and provides a good general basis to understanding the flow past a bluff body across the various conditions. The research history of flow past a circular cylinder can be traced all the way back to d'Alembert with his famous "paradox" where he was perplexed by the zero drag outcome in his potential flow calculation, which contradicted the physical observation of a resisting force on a moving bluff body through a fluid. It was the absence of viscosity in d'Alembert's calculation that led his theory to this physical paradox. Through mostly empirical methods, much progress was made in the understanding of the role of viscosity in the production of drag in the flow past a bluff body. Real fluid is viscous and therefore will produce a resistance to shear stress when a body is moving relative to it.

The behavior of the vortex wakes depends on the balance of the inertial force and the viscous force and therefore is characterized into different regimes by a dimensionless Reynolds number,

$$Re = \frac{\rho U x}{\mu}, \tag{1.1}$$

where ρ is the gas density, U is the freestream velocity, x is the characteristic length, μ is the dynamic viscosity. At the limit of $Re = 0$, the flow can be considered somewhat artificial since it produces a flow pattern that is ideally symmetric about the bluff body centerline where the streamlines upstream look identical to those downstream. In reality, any flow of a very viscous fluid or of a small object such that $Re << 1$ produces a symmetric pattern. This is called "creeping" or "Stokes" flow where the inertial force is neglected. A smooth laminar flow is a result when the viscous force is dominant at a very low Reynolds number. The stagnation pressure that develops at the leading edge of the body is sufficient to drive the flow around the body. As the Reynolds number increases, the boundary layer thickens and the inertial force becomes more and more significant such that the leading edge stagnation pressure can no longer drive the flow around the body to the trailing edge. Eventually the fluid flow becomes detached from the body surface, resulting in flow separation. The characteristics of flow instabilities varies across a large range of Reynolds number from a coherent, repeating series of swirling vortices, known as the von Kármán vortex street, at the Reynolds number of less than a hundred to the regime of highly chaotic and stochastic turbulent eddies at very high Reynolds numbers in the range of several millions. For a circular cylinder, Roshko found that the formation of vortex wakes displays a level of sensitivity to the base pressure coefficient (C_{pb}), measured at 180° from the leading edge stagnation point, which he used in classifying the following vortex shedding regimes [11, 13].

a) $Re < 49$: Laminar steady regime

b) $49 \leqslant Re < 180$: Laminar vortex shedding regime

c) $180 < Re < 260$: 3-D wake transition regime

d) $260 < Re < 10^3$: Increasing disorder in the fine-scale three dimensionalities

e) $10^3 < Re < 10^5$: Shear-layer transition regime

f) $10^5 < Re < 4 \times 10^5$: Asymmetric reattachment regime (critical transition)

g) $4 \times 10^5 < Re < 8 \times 10^5$: Symmetric reattachment regime (supercritical regime)

h) $Re > 8 \times 10^5$: Boundary-layer transition regime (post-critical regime)

In addition to the research on flow past a circular cylinder, there have been a considerable number of numerical and experimental studies of the flow past rectangular and square bluff bodies. Some notable investigations have been carried out by Davis and Moore [16], Davis *et al.* [17], Okajima [18, 19], Okajima *et al.* [20], Kelkar *et al.* [21], Norberg [22], Sohankar *et al.* [23, 24, 25] and Sen and Mittal [26]. The interest in a rectangular shape stems largely from the design of buildings and road vehicles. For example, many large buildings including skyscrapers are essentially built with a square cross section. These buildings are subjected to wind-driven vibration, resulted from the vortex shedding characteristics of their respective shapes. A large road vehicle such as a moving truck can simplistically be viewed as a rectangular body. Such study can be useful in help guide the vehicle design for reducing drag and ultimately increasing fuel efficiency. Another example of flow past a square or rectangular cylinder is the read/write arm of a magnetic disk storage device, which serves as the motivating basis for this thesis research as discussed in the next section.

1.2 Motivation – the aerodynamics of hard disk drives

The motivation for this research stems from the author's line of work in designing hard disk drives (HDD's). The HDD industry has shown, for more than half a decade, remarkable advances in product development through technological innovations, astute design and efficient manufacturing processes. Over the time, there has been indisputable evidence of fierce competition in the HDD industry, as seen in the erosion of the price per gigabyte and the dwindling number of manufacturers. Yet, in order to survive in such a competitive environment, HDD makers have been able to offer more storage capacity year after year, even while sustaining chronically low profitability. The HDD industry marked its beginning in September 1956 when IBM introduced the first random-access storage unit of 5 million 7-bit characters (approximately 4.4 Megabytes) on 50 massive 24-inch aluminum disks in a system known as the RAMAC (Random-Access Method of Accounting and Control). The introduction of RAMAC put an end to the sequential storage on punched cards and magnetic tapes, although the use of magnetic tapes has continued until recently in a backup role. With the size bigger than a normal refrigerator and a ton of weight, the RAMAC was hardly ready for an average consumer but nonetheless became the standard storage device for business and scientific applications throughout large corporations and government agencies.

From the time of the RAMAC, the level of technical advancements has been astounding. The list below represents only some highlights of achievements that resulted from a whole array of technological innovations in magnetic physics, servo mechanics, electronics, software, and manufacturing processes combined from the RAMAC time to the present day:

a) Areal recording density has increased from 2,000 bits per square inch to nearly 10^{12} bits per square inch.

b) Track density has gone from 20 tracks per inch (TPI) to over 300,000 TPI.

c) Cost per Gigabyte has dropped from a staggering \$640,000 per month lease (extrapolated value based on \$3,200 monthly charge of a RAMAC in 1957 [27], excluding inflation) to less than \$0.10 for an outright ownership today.

In order to measure the success in technological innovations, areal recording density, which is a product of linear recording density and track density, is generally used throughout the HDD industry. The trend more or less follows the Moore's law of semiconductor development. The main driving mechanism to achieve higher areal density is in the magnetic recording technology of head and media. From the humble beginning of coating RAMAC's aluminum disk with a magnetic iron oxide, which was derived from a paint primer used for the Golden Gate Bridge, to the current usage of the state-of-the-art perpendicular magnetic recording heads and multi-layer anti-ferromagnetic coupled disks, the advancement in magnetic head and media technologies has provided the boost needed to achieve the ever growing level of areal density. In essence, these new technologies have produced a compound growth rate in areal density to almost 500 million times that of the RAMAC discussed here.

There are many challenging problems from a *fluid dynamic* perspective in the design and development of HDD's. The transducers that read and write data from and to the disk are carried by the ever-decreasing-sized slider that uses the pressure generated by the compressible lubrication flow to "fly" over a disk. To keep pace with areal density, one of the requirements is to reduce the flying height between the recording head and disk and that dimension has steadily decreased from 20 microns in the RAMAC days to currently less than the mean free path of air at 10 nanometers or below. To appreciate this fact, a diameter of a human hair is about 30 microns, larger than the flying height of the recording head used in the RAMAC. To cope with such a challenge, HDD companies need to commit a fair amount of valuable research and development spending on the mechanics of head disk interface, such as tribology, wear, filtration, and chemical deposition, to ensure the quality and reliability of HDD products for a long MTBF (Mean Time Between Failures) of over 2 million hours today.

Therefore, many new innovations are necessary to support the ever increasing areal density. Most innovations are out of pure technical necessities but some are driven by economics. For example, spindle motors needed to support high track density are required to have low mechanical runout (in the range of less than 1 microinch) and low acoustical noise while having a lasting reliability. Virtually every HDD in the market today uses a "fluid dynamic" bearing spindle motor (ball bearings were the norm only a few years ago) in order to achieve such a low runout and acoustic noise [28]. Customers continue to demand faster average access time. That means spindle motors have to spin at a faster rate, as high as 15,000 RPM (revolutions per minute) today. Actuator that carries the read/write heads has to seek faster, thus requiring the development of efficient mechanical design with the extreme geometrical precision. High performance magnets, such as neodymium, have been developed as dictated by the actuator and voice-coil motor design. Precise servo positioning algorithms and electronics are required to keep the recording head and actuator assembly on track, where the next track can be less than 10 microinches away. In addition, they must be able to randomly seek to any other tracks for data. Signals have to be processed in fast and efficient manners by the electronic board assembly, as this is where data are transferred between computer and the recording disk.

Aside from the aerodynamics of recording heads, of equal importance, especially in the high performance server drives, is the issue of internal HDD aerodynamics which primarily is the real motivation for this research. The internal flow inside an HDD is driven by aerodynamic friction of rotating disks. Accordingly the aerodynamic excitation depends on the diameter and the rotational speed of the disks, as well as the number of disks stacked in each HDD. Historically, disk diameters have been decreasing due to form factor reduction in computer packaging. This works in favor of lowering aerodynamic excitation. The rotational speed, on the other hand, has been steadily increasing to meet the performance demand. Today the fastest HDD's operate at Reynolds numbers and areal densities such that aerodynamic buffeting of the moving components including the arm, suspension, slider and disk, is once again an important issue. The flow inside the head disk assembly is complicated by the presence of bluff, non-aerodynamic components; notably the arm, suspension and slider. These are bodies which are highly susceptible to flow induced vibrations (FIV) and high aerodynamic pressure drag. With track densities surpassing 300,000 TPI and rotational speeds of up to 15,000 RPM, FIV poses problems for the servo control system to write and read data reliably within the track misregistration (TMR) budget. When bluff bodies are placed between spinning disks or between a spinning disk and the HDD enclosure, their blocking effect is stronger than the corresponding situation without disks or stationary nearby walls. This blocking effect also results in high aerodynamic power consumption, especially with the arm in the inner diameter position. The problem of FIV and TMR control can be addressed by bypassing high energy air ahead of the arm and suspension. This problem of combating aerodynamic buffeting in HDD's must always be seen in the context of minimizing FIV and running torque. Otherwise, the aerodynamic buffeting problem could simply be solved by replacing the air with a solid wherever possible. To a degree, inserting sector shaped plates (sometimes called damper plates or "anti-disks") between each pair of disks falls in this category of FIV countermeasures. In most HDD's the latter brute force solution is not a viable option in order to limit the total power dissipation of the HDD. Other issues driven by the overall behavior of HDD internal aerodynamics are the filtration system, acoustic emission, and heat transfer management. These must not be overlooked as they often determine the overall competitive performance of an HDD design.

1.3 Research objective

While the subject of vortex induced vibration and flow control is extremely broad, this research will focus primarily on laminar vortex shedding at a relatively low Reynolds number where the wakes are predominantly two-dimensional. Computational fluid dynamics (CFD) is used as the primary investigative tool in this research. Part of the objective is to compare the numerical results obtained from two entirely different codes: 1) a widely-used commercial incompressible code based on Semi-Implicit

Method for Pressure-Linked Equations (SIMPLE) and 2) the compressible high-order spectral difference code developed at Stanford's Aerospace Computing Laboratory (ACL). Both of these codes will be used to investigate the vortex shedding off bluff bodies and the effect of flow control techniques.

As the title of this thesis suggests, the main objective of this research is to investigate and find ways of controlling and suppressing the unsteady wakes past bluff bodies. The task is to apply both passive and active flow control techniques in order to gain a better understanding of the flow physics. The passive flow control typically refers to a technique that involves a geometrical modification that alters the vortex shedding characteristics, thereby reducing or suppressing body force fluctuations. In this particular research, this involves a placement of a detached thin splitter plate downstream of a bluff body in both unbounded flows and bounded channel flows. The active flow control, on the other hand, refers to a technique that involves a more dynamic alteration by means of adding or removing mass, momentum or energy to the flow. As there are almost unlimited ways of active flow modification, the research focuses on the basic spinning technique of a single circular cylinder and a pair of counter rotating cylinders, as inspired by Ludwig Prandtl's experiment and hypothesis.

Some experimental results have been obtained and used to verify the computational results. The passive flow control experiment will be conducted using laser Doppler vibrometer (LDV) in a very low speed wind tunnel used for HDD development. The active flow control experiment will be collaboratively investigated by a research team from the Gas Dynamics Lab at Princeton University using digital particle image velocimetry (DPIV) technique. The detailed of these experimental techniques are to be discussed in Appendix A.

Chapter 2

Overview of numerical methods

Computational fluid dynamics (CFD) has its root in the aerospace industry that largely began in the mid 1960's. Significant progress has been made in the following decades in both numerical methods and computing hardware. Today CFD has now become a well-established and valuable analysis tool suitable for industrial use in the development of aerodynamic design with accuracy and acceptable cost. Continual improvements in both numerical algorithms and hardware performance allow for the emergence of more complex CFD models.

A commercial incompressible CFD code and the Aerospace Computing Laboratory compressible code based on the high-order spectral difference (SD) method have both been used as the investigative tools for this research. Each code has its advantages and disadvantages. However, the primary reason for using both codes is so that comparison, as a means of validation, can be made amongst the obtained results. The commercial CFD code offers benefits in terms of ease of use in geometrical and mesh modification and good post processing capability. The numerical algorithm used in today's many commercial incompressible CFD codes is based on the nearly-four-decade-old Semi-Implicit Method for Pressure-Linked Equation (SIMPLE). Although many improvements have been made to the original SIMPLE algorithm, the solution accuracy is still at most second order and the efficiency often lacks that of the more recent codes developed in universities and government research agencies. The high-order SD scheme, on the other hand, has recently been developed and proven to be very robust and efficient in the simulation of a broad range of compressible flows, including flows with shock wave at high Mach numbers. Its usefulness in the low Mach region is verified in this research.

2.1 SIMPLE algorithm

Most commercial CFD codes solve the incompressible Navier-Stokes equations based on the SIMPLE algorithm, first developed by Patankar and Spalding in 1972 [29]. A few variants such as SIMPLE-Revised (SIMPLE-R), SIMPLE-Consistent (SIMPLE-C) and Pressure Implicit with Splitting Operators (PISO) were subsequently developed. The usual practice is to solve the partial differential equations as an instance of the generic conservation equation. The details of the SIMPLE algorithm is well documented in the original paper by Patankar and Spalding [29] and subsequent papers by Patankar [30] and Van Doormal and Raithby [31] as well as many textbooks, such as Patankar [32] and Ferziger and Perić [33].

In summary, the generalized transport equation can be expressed in the following manner:

$$\frac{\partial \rho\phi}{\partial t} + \nabla \cdot \left(\rho \overrightarrow{V} \phi\right) = \nabla \cdot (\Gamma \nabla \phi) + S_\phi \tag{2.1}$$

The two terms on the left hand side of the above equation 2.1 are the transient term and convection terms of any scalar quantity ϕ, respectively. These terms are balanced by the diffusive transport term and any sources or sinks, S_ϕ, on the right hand side, respectively. To solve the equation numerically, the generalized transport equation is discretized by integration over a finite set of control volumes:

$$\int_{\mathcal{V}} \frac{\partial \rho\phi}{\partial t} d\mathcal{V} + \int_{\mathcal{V}} \nabla \cdot \left(\rho \overrightarrow{V} \phi\right) d\mathcal{V} = \int_{\mathcal{V}} \nabla \cdot (\Gamma \nabla \phi)\, d\mathcal{V} + \int_{\mathcal{V}} S_\phi d\mathcal{V} \tag{2.2}$$

By applying the divergence theorem to convection and diffusion terms, the transport equation can be written as:

$$\int_{\mathcal{V}} \frac{\partial \rho\phi}{\partial t} d\mathcal{V} + \oint_{\mathcal{S}} \rho\phi \overrightarrow{V} \cdot \overrightarrow{n}\, d\mathcal{S} = \oint_{\mathcal{S}} \Gamma \nabla \phi \cdot \overrightarrow{n}\, d\mathcal{S} + \int_{\mathcal{V}} S_\phi d\mathcal{V} \tag{2.3}$$

The transient term can be discretized simply by the first order explicit Euler method. However, more commonly used in many commercial codes are the implicit Euler and Crank-Nicolson methods.

The convective flux is discretized and evaluated using the midpoint rule and various interpolation schemes such as first order upwinding and central differencing schemes.

$$\oint_{\mathcal{S}} \rho\phi\overrightarrow{V}\cdot\overrightarrow{n}d\mathcal{S} = \sum_f \left(\rho\overrightarrow{V}\cdot\overrightarrow{n}\mathcal{S}\right)_f \phi_f = \sum_f \dot{m}_f\phi_f \tag{2.4}$$

where $\dot{m}_f$ is the mass flux through each face f of the control volume. Figure 2.1 shows the notation of a typical control volume for a two-dimensional structured mesh. Here, the fluxes are evaluated through the faces n, e, w and s with respect to the central cell, P, and the adjacent cells N, E, W and S.

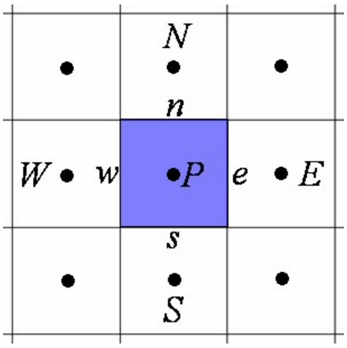

Figure 2.1: Control volume for a two-dimensional structured mesh.

The diffusive flux can also be discretized and evaluated using the midpoint rule as follows:

$$\oint_{\mathcal{S}} \Gamma\nabla\phi\cdot\overrightarrow{n}d\mathcal{S} = \sum_f \Gamma_f\left(\frac{\partial\phi}{\partial n}\right)_f \mathcal{S}_f \tag{2.5}$$

For closure, since the source term is a function of ϕ, it can be discretized by

$$\int_{\mathcal{V}} S_\phi d\mathcal{V} = (S_\phi)_P\Delta\mathcal{V} \tag{2.6}$$

In two dimensions, for example, combining all the discretized spatial terms results in the following linear algebraic equation.

$$a_P\phi_P + a_N\phi_N + a_E\phi_E + a_W\phi_W + a_S\phi_S = b_P \tag{2.7}$$

In a more general form, this equation is often written in literature as

$$a_P\phi_P + \sum_{nb} a_{nb}\phi_{nb} = b_P \tag{2.8}$$

where nb represents the neighboring cells. The a_{nb} terms are called the link coefficients and b_P contains all the source terms [30, 32].

Now consider the following conservation equations for fluid flow.

Conservation of Mass:

$$\frac{\partial \rho}{\partial t} + \nabla \cdot \left(\rho \overrightarrow{V}\right) = 0 \tag{2.9}$$

Conservation of Momentum:

$$\frac{\partial\left(\rho \overrightarrow{V}\right)}{\partial t} + \nabla \cdot \left(\rho \overrightarrow{V}\overrightarrow{V}\right) = \nabla \cdot \left(\overrightarrow{\overrightarrow{\tau}}\right) - \nabla p \tag{2.10}$$

where ρ is the density, $\overrightarrow{V}$ is the velocity vector, p is the pressure and $\overrightarrow{\overrightarrow{\tau}}$ is the viscous stress tensor.

As outlined by the method of solving the generalized transport equation, the flow variables can be solved similarly by applying the integration and divergence theorem to the flow equations.

$$\frac{d}{dt}\int_{\mathcal{V}} \rho d\mathcal{V} + \int_{\mathcal{S}} \rho \left(\overrightarrow{V} \cdot \overrightarrow{n}_{\mathcal{S}}\right) d\mathcal{S} = 0 \tag{2.11}$$

$$\frac{d}{dt}\int_{\mathcal{V}} \left(\rho \overrightarrow{V}\right) d\mathcal{V} + \oint_{\mathcal{S}} \left(\rho \overrightarrow{V}\right)\left(\overrightarrow{V} \cdot \overrightarrow{n}_{\mathcal{S}}\right) d\mathcal{S} = \oint_{\mathcal{S}} \left(\overrightarrow{\overrightarrow{\tau}} \cdot \overrightarrow{n}_{\mathcal{S}}\right) d\mathcal{S} - \oint_{\mathcal{S}} \left(p \overrightarrow{n}_{\mathcal{S}}\right) d\mathcal{S} \tag{2.12}$$

The calculation of pressure generally poses a problem in obtaining a solution to the Navier-Stokes equations at a constant density. This is due to the lack of an independent equation for pressure. The Navier-Stokes equations are non-linear with unknown velocity components. Therefore, solving the flow field requires a known pressure field. In compressible flow, both density and pressure are directly coupled through the equation of state and are solved simultaneously through the continuity, momentum and energy equations. It is obvious from the conservation equations that there are five unknowns (ρ, $\overrightarrow{V}$ and p) in four equations (continuity and three momentum equations). In an incompressible flow or flow at a low Mach number when the fluid density is treated as constant, there is no direct relationship that ties the continuity equation with the pressure term, which only appears as a source term in the momentum equations. Only the velocity components are coupled in the continuity and momentum equations. Essentially, this means velocity components cannot be solved until the pressure field is known, and vice versa. The idea behind the SIMPLE algorithm is to establish a discrete equation for pressure and solve the discrete continuity equation in a segregated manner. It couples the pressure and velocity terms after solving the discretized equations separately by an iterative approach. The original SIMPLE algorithm follows the use of the finite volume approach on a staggered mesh known as the *marker and cell* (MAC) scheme which was proposed by Harlow and Welch [34]. The calculation of the pressure term is interpolated based on its value at the cell centroids while the velocity terms are computed from the staggered control volumes. The reason for using a “staggered grid” approach is to avoid what is known as the *checkerboard* instability. When the values pressure and velocity are stored at the same cell centered location (i.e. co-located), they are linked at alternate nodes during the calculation of mass fluxes. This is also known as the *odd-even decoupling* effect that often leads to indeterminate oscillation of the pressure field. Figure 2.2 illustrates an example of this staggered mesh approach of the SIMPLE scheme on a two-dimensional Cartesian mesh.

For constant density, the momentum equation (2.10) can be written in semi-discrete form:

$$\rho\frac{\partial u_i}{\partial t} = -\rho\frac{\delta(u_i u_j)}{\delta x_j} - \frac{\delta p}{\delta x_i} + \mu\frac{\delta^2 u_i}{\delta x_j^2}. \tag{2.13}$$

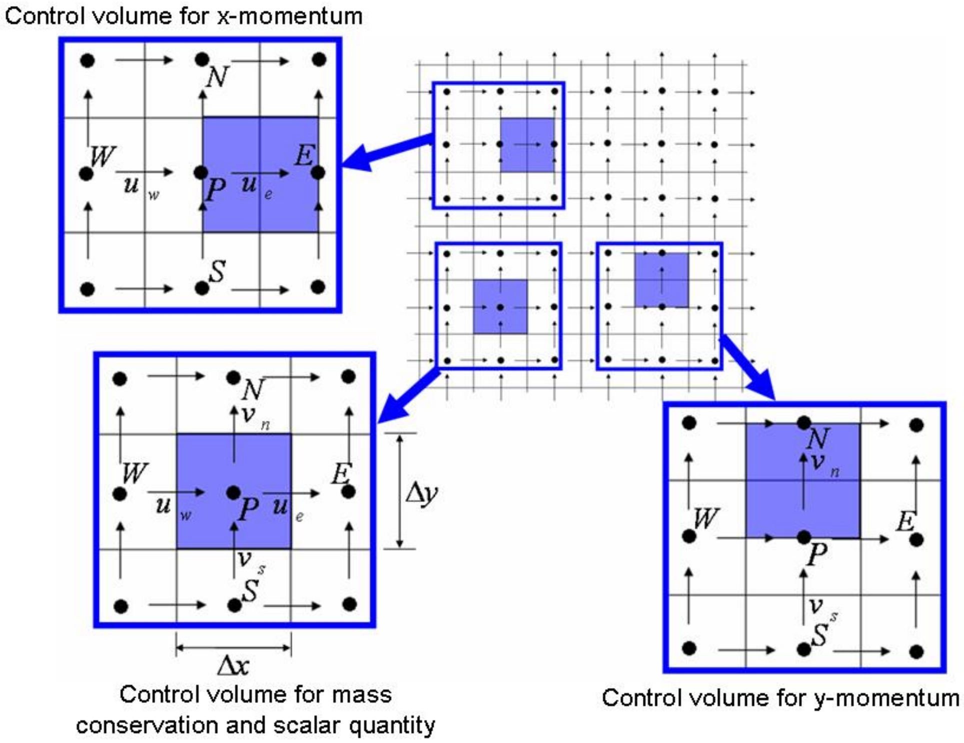

Figure 2.2: Staggered mesh pattern for SIMPLE family of algorithms.

Let H denote the convective and viscous terms such that

$$\rho \frac{\partial u_i}{\partial t} = H_i - \frac{\delta p}{\delta x_i}. \tag{2.14}$$

The most common method for time integration in many commercial codes is the implicit Euler method which leads to

$$\rho(u_i^{n+1} - u_i^n) = \Delta t \left(H_i^{n+1} - \frac{\delta p}{\delta x_i}^{n+1} \right). \tag{2.15}$$

The velocity field is divergence free at time n and is required from continuity relation to be so at the new time step $n+1$. This leads to solving what is known as the Poisson equation for pressure, i.e.

$$\frac{\delta}{\delta x_i} \left(\frac{\delta p}{\delta x_i}^{n+1} \right) = \frac{\delta}{\delta x_i} H_i^{n+1}. \tag{2.16}$$

However, the pressure and velocity field can only be determined if the Poisson equation is solved by some iterative procedure.

In two-dimensional form, the momentum equations at the new time step can be discretized as

$$a_P u_P - a_N u_n - a_E u_e - a_S u_s - a_W u_w = (p_P - p_W)\Delta y + b_P \tag{2.17}$$

$$a_P v_P - a_N v_n - a_E v_e - a_S v_s - a_W v_w = (p_P - p_S)\Delta x + b_P \tag{2.18}$$

where the a coefficients contain mass fluxes, viscosity, and diffusion terms. The coefficient b contains the source terms. Note that the pressure also appears only as a source term on the right hand side of the equation. The subscripts and notation correspond to those shown in figure 2.2.

These equations are often written in the following forms:

$$a_P u_P = \sum_{nb} a_{nb} u_{nb} + (p_P - p_W)\Delta y + b_P \tag{2.19}$$

$$a_P v_P = \sum_{nb} a_{nb} v_{nb} + (p_P - p_S)\Delta x + b_P. \tag{2.20}$$

The velocity components in these linear equations are therefore

$$u_P = \frac{\sum\limits_{nb} a_{nb} u_{nb} + b_e}{a_P} + \frac{1}{a_P}(p_P - p_W)\Delta y \tag{2.21}$$

$$v_P = \frac{\sum\limits_{nb} a_{nb} v_{nb} + b_n}{a_P} + \frac{1}{a_P}(p_P - p_S)\Delta x. \tag{2.22}$$

Since calculating the flow variables on staggered grid can be quite troublesome for geometrically complex problems such as in non-Cartesian or curvilinear coordinates, many commercial CFD codes use a popular procedure, proposed by Rhie and Chow [35], that prevents the *checkerboard* instability and allows for the use of the co-located cells. The Rhie-Chow approach calculates the mass fluxes by averaging the momentum equation to the cell faces using weighting factors based on link coefficient a_P from equations 2.19 and 2.20 instead of averaging them linearly. The cell face velocity is thus calculated from the local pressure gradient using this weighting procedure.

The core of the SIMPLE scheme is to establish the relationship between the velocity terms with the pressure corrections in order to enforce the mass conservation and solve for the pressure field. The pressure correction p' is established during time iteration steps by solving the discretized Poisson equation 2.16 for p'. In summary, the procedure for two-dimensional implementation can be outlined as shown below.

1. Guess the values of pressure p^* to start the iterative process.

2. Using the guessed value p^*, discretize and solve the momentum equations for the velocities u^* and v^* such that

$$u_P^* = \frac{\sum\limits_{nb} a_{nb} u_{nb}^* + b_e}{a_P} + \frac{1}{a_P}(p_P^* - p_W^*)\Delta y \tag{2.23}$$

$$v_P^* = \frac{\sum\limits_{nb} a_{nb} v_{nb}^* + b_n}{a_P} + \frac{1}{a_P}(p_P^* - p_S^*)\Delta x. \tag{2.24}$$

3. Calculate ρu^* and ρv^* for the internal grid points.

4. Discretize and solve the Poisson equation for the pressure correction p'
5. Calculate the velocity corrections by approximating

$$u'_P \approx \frac{1}{a_P}(p'_P - p'_W)\Delta y \tag{2.25}$$

$$v'_P \approx \frac{1}{a_P}(p'_P - p'_S)\Delta x \tag{2.26}$$

The corrected pressure and velocities are then obtained by $p^m = p^* + p'$, $u^m = u^* + u'$ and $v^m = v^* + v'$ to satisfy the continuity equation.

6. If the solution is converged, stop. Otherwise go to step 2.

2.1.1 SIMPLE-Revised

In 1980, Patankar proposed a new algorithm called SIMPLE-R which stands for SIMPLE-Revised to address the problem of divergence as a result of the omission of the velocity correction term

$$\frac{\sum\limits_{nb} a_{nb}u'_{nb}}{a_P}$$

when calculating the velocity correction from the discretized momentum equations [30]. The algorithm SIMPLE-R essentially requires an intermediate step of determining the pressure field from a Poisson equation based on pseudo-velocity components obtained from the velocity correction equation of the SIMPLE algorithm. This intermediate pressure p^m is used in the correction equations to again solve for velocity components and pressure, before moving on to the next iteration until convergence is achieved. In general, SIMPLE-R will result in fewer iteration steps but can be computationally more expensive than SIMPLE, as it will require more calculations in determining the intermediate pressure in each iteration.

2.1.2 SIMPLE-Consistent

Also commonly implemented in commercial solvers is SIMPLE-C, which stands for SIMPLE-Consistent. This variant also solves the conservation equations by coupling the pressure and velocity terms similar to the original SIMPLE. However, as pointed out by Patankar in the implementation of SIMPLE-R, the problem of ignoring the velocity correction term can lead to inconsistency when solving for the pressure correction term. In 1984, Van Doormaal and Raithby proposed that since $\sum\limits_{nb} a_{nb}u'_{nb}$ is of the same order as $\sum\limits_{nb} a_{nb}u'_{P}$, it imposes a less severe constraint on the pressure correction equation if one replaces a_P in SIMPLE with $a_P + \sum\limits_{nb} a_{nb}$ rather than ignoring $\sum\limits_{nb} a_{nb}u'_{nb}$ altogether [31]. This can be done with minimum change to the original SIMPLE algorithm, but does have a significant and positive impact on convergence. It can also be computationally less expensive than SIMPLE-R.

2.1.3 PISO

PISO, proposed by Issa in 1995, stands for Pressure-Implicit with Splitting of Operators [36]. This is yet another class of pressure correction approach based on the SIMPLE algorithm but requires slightly more computational effort. The algorithm calls for the second corrector steps for velocity and pressure after SIMPLE iteration is performed. The purpose of this additional step is to correct the momentum fluxes in order to satisfy the continuity more closely. Therefore, this allows for a faster convergence than the SIMPLE algorithm. PISO is proved to be useful in time dependent flow and models with irregular cells.

2.1.4 Commercial CFD codes

Many of the commercial CFD codes, including CFX, Fluent, and Star-CD, implement SIMPLE and/or any one of its variants [37]. The code chosen for this work is CFD-ACE+ by ESI Corporation. It uses the SIMPLE-C pressure-correction algorithm along with various spatial discretization schemes. Several optional schemes are available in CFD-ACE+ for spatial discretization of the convection term, namely 1st order upwind (1UDS), 2nd order upwind (2UDS) and central differencing (CDS). Typically, the solution from a 1st order upwind scheme tends to be more diffusive.

It is therefore avoided in this study as it can adversely affect the shedding characteristics of the wake vortices. In the Reynolds number range of the current study, a 2nd order scheme should be sufficient in yielding a reasonably accurate result. For time discretization, both the 1st order backward Euler and the 2nd order Crank-Nicholson (CN) schemes are available. The discretization scheme of the diffusion and source terms is fixed and no option can be set; however, it should produce 2nd order accuracy.

2.2 High-order spectral difference method

While second order methods for computational simulations of fluid flow are by now quite mature and reliable, they introduce levels of numerical diffusion that cause rapid attenuation of vortices. Consequently accurate simulation of vortex dominated flows can most readily be achieved by resorting to higher order methods. One of the most promising approaches is the discontinuous Galerkin (DG) method, for which the theoretical basis has been provided in a series of papers by Cockburn et al. [38, 39, 40, 41]. The rapid growth of the computational complexity of DG methods with increasing order has spurred the search for more efficient variants or alternatives. One approach is the nodal DG scheme in which the solution is represented by Lagrange interpolation at a set of collocation points in each element, and the quadratures required by the DG method are pre-integrated to produce local mass and stiffness matrices [42].

The spectral difference (SD) method has recently emerged as a promising alternative. The basic idea of the SD method was first put forward by Kopriva and Kolias [43] under the name staggered grid Chebyshev multidomain method. In order to discretize the conservation law

$$\frac{\partial u}{\partial t} + \frac{\partial}{\partial x} f(u) = 0, \tag{2.27}$$

they proposed to represent the solution by polynomials of degree N in each element and the flux by polynomials of degree $N + 1$ with interlocking collocation points for the solution and the flux. The flux collocation points include the element boundaries, where a single valued numerical flux is imposed which is common to each element and its neighbors on the left or right. Then the value of $\partial u/\partial t$ at each solution point is obtained directly as the derivative of the flux polynomial. Kopriva and Kolias used Chebyshev and Chebyshev-Lobatto points as the solution and flux collocation points, and it remains unclear whether the SD scheme is stable with this choice, although they did prove the scheme to be conservative. Some years later Liu, Vinokur and Wang presented a general formulation of SD methods on both quadrilateral and triangular elements [44]. Wang, Liu, May and Jameson extended it to 2D Euler equations on triangular grids [45]. Liang, Kannan and Wang improved the convergence of the method using implicit LU-SGS and p-multigrid schemes [46]. Some additional contributions are made by May and Jameson [47], Huang, Wang and Liu [48] and Sun, Wang and Liu [49]. The SD method combines elements from finite-volume and finite-difference techniques. Similar to the discontinuous Galerkin (DG) [50, 41] and spectral volume (SV) methods [51, 52], the SD scheme achieves high-order accuracy by locally approximating the solutions as a high degree polynomial inside each cell. However, being based on the differential form of the equations, its formulation is simpler than that of the DG and SV methods as no test function or surface integral is involved. Conservation properties are still maintained by a judicious placement of the nodes at quadrature points of the chosen simplex.

While the SD method has proved robust and productive in a variety of applications [53, 54, 55, 56, 57, 58], doubts have been raised about its stability. It has been shown by Huynh [59] that it can be weakly unstable in one dimension depending on the choice of flux collocation points, including the choice made by Kopriva and Kolias. It was recently proved by Jameson [60] that it is stable in an energy norm for all orders of accuracy if the interior flux collocation points are chosen as the zeros of the corresponding Legendre polynomials.

The implementation of the SD method on quadrilateral or hexahedral elements is simple as it allows one to use polynomial interpolation based on tensor product forms rather than the multivariate interpolation used with triangular or tetrahedral elements. In two dimensions, it involves only one-dimensional polynomials to construct flux values from solution points and to calculate derivatives on solution points from fluxes, etc. The formulation is summarized in the next section.

2.2.1 Spatial discretization

Consider the unsteady compressible two-dimensional Navier-Stokes equations in conservative form

$$\frac{\partial \boldsymbol{Q}}{\partial t} + \frac{\partial \boldsymbol{f}}{\partial x} + \frac{\partial \boldsymbol{g}}{\partial y} = 0, \tag{2.28}$$

where $\boldsymbol{Q}$ is the vector of conserved variables, and $\boldsymbol{f}$ and $\boldsymbol{g}$ are the total fluxes including both inviscid and viscous flux vectors. The inviscid and viscous fluxes of the Navier-Stokes equations can be written separately in the following form

$$\frac{\partial \boldsymbol{Q}}{\partial t} + \nabla \boldsymbol{F}_e(\boldsymbol{Q}) + \nabla \boldsymbol{F}_v(\boldsymbol{Q}, \nabla \boldsymbol{Q}) = 0, \tag{2.29}$$

where the conservative variables $\boldsymbol{Q}$ and Cartesian components $\boldsymbol{f}_e(\boldsymbol{Q})$ and $\boldsymbol{g}_e(\boldsymbol{Q})$ of the inviscid flux vector $\boldsymbol{F}_e(\boldsymbol{Q})$ are given by

$$\boldsymbol{Q} = \begin{bmatrix} \rho \\ \rho u \\ \rho v \\ E \end{bmatrix}, \quad \boldsymbol{f}_e(\boldsymbol{Q}) = \begin{bmatrix} \rho u \\ \rho u^2 \\ \rho u v \\ u(E+p) \end{bmatrix}, \quad \text{and} \quad \boldsymbol{g}_e(\boldsymbol{Q}) = \begin{bmatrix} \rho v \\ \rho u v \\ \rho v^2 + p \\ v(E+p) \end{bmatrix}. \tag{2.30}$$

Here ρ is the density, u and v are the velocity components in the x- and y-directions, p is the pressure and E is the total energy. The pressure is related to the total energy by

$$E = \frac{p}{\gamma - 1} + \tfrac{1}{2}\rho(u^2 + v^2), \tag{2.31}$$

where γ is a constant ratio of specific heat. For all numerical test cases in the present study, $\gamma = 1.4$ for air.

The Cartesian components $\boldsymbol{f}_v(\boldsymbol{Q}, \nabla \boldsymbol{Q})$ and $\boldsymbol{g}_v(\boldsymbol{Q}, \nabla \boldsymbol{Q})$ of the viscous flux vector

$\boldsymbol{F}_v(\boldsymbol{Q}, \nabla \boldsymbol{Q})$ are given by

$$\boldsymbol{f}_v(\boldsymbol{Q}, \nabla \boldsymbol{Q}) = \mu \begin{bmatrix} 0 \\ 2u_x + \lambda(u_x + v_y) \\ v_x + u_y \\ u\left[2u_x + \lambda(u_x + v_y)\right] + v(v_x + u_y) + \frac{C_p}{Pr} T_x \end{bmatrix}, \tag{2.32}$$

$$\boldsymbol{g}_v(\boldsymbol{Q}, \nabla \boldsymbol{Q}) = \mu \begin{bmatrix} 0 \\ v_x + u_y \\ 2v_y + \lambda(u_x + v_y) \\ v\left[2v_y + \lambda(u_x + v_y)\right] + u(v_x + u_y) + \frac{C_p}{Pr} T_y \end{bmatrix}, \tag{2.33}$$

where μ is the dynamic viscosity, C_p is the specific heat at constant pressure, Pr is the Prandtl number, and T is the temperature (λ is set to $-2/3$ according to the Stokes hypothesis).

To achieve an efficient implementation, all quadrilateral elements in the physical domain (x, y) determined by the one-level h-refinement are transformed into a standard square element $(0 \le \xi \le 1, 0 \le \eta \le 1)$. The transformation can be written as

$$\begin{pmatrix} x \\ y \end{pmatrix} = \sum_{i=1}^{K} M_i(\xi, \eta) \begin{pmatrix} x_i \\ y_i \end{pmatrix}, \tag{2.34}$$

where K is the number of points used to define the physical element, (x_i, y_i) are the Cartesian coordinates of those points, and $M_i(\xi, \eta)$ are the shape functions. For elements with straight edges, K is equal to 4. For elements lying on curved boundaries, 8 points (four mid-edge and four corner points) can define a quadratic representation and 12 points can define a third-order cubic representation. The metrics and the Jacobian of the transformation can be computed for each element. The governing equations in the physical domain are then transferred into the computational domain, and the transformed equations take the following form

$$\frac{\partial \tilde{\boldsymbol{Q}}}{\partial t} + \frac{\partial \tilde{\boldsymbol{f}}}{\partial \xi} + \frac{\partial \tilde{\boldsymbol{g}}}{\partial \eta} = 0, \tag{2.35}$$

where

$$\tilde{\boldsymbol{Q}} = |J| \cdot \boldsymbol{Q}, \;\; J = \begin{pmatrix} x_\xi & x_\eta \\ y_\xi & y_\eta \end{pmatrix} \;\; \text{and} \;\; \begin{pmatrix} \tilde{\boldsymbol{f}} \\ \tilde{\boldsymbol{g}} \end{pmatrix} = |J|\, J^{-1} \begin{pmatrix} \boldsymbol{f} \\ \boldsymbol{g} \end{pmatrix}. \tag{2.36}$$

In the standard element, two sets of points are defined, namely the solution points and the flux points. A fourth-order representation is illustrated as an example in figure 2.3

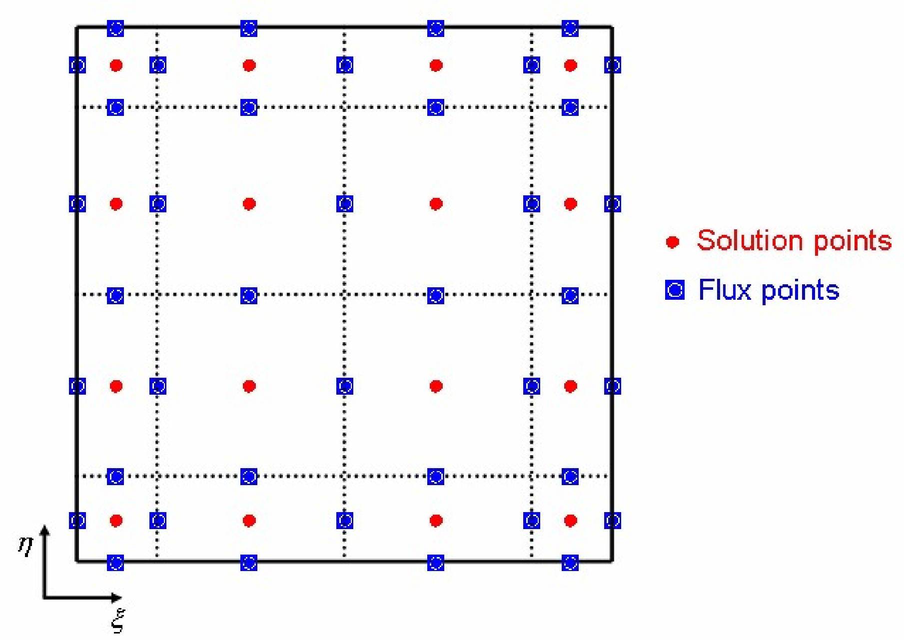

Figure 2.3: Distribution of flux and solution points for the 4th order SD scheme.

In order to construct a degree $(N-1)$ polynomial in each coordinate direction, solution values are required at N collocation points. The solution points in one dimension are chosen to be the Gauss quadrature points defined by:

$$X_s = \frac{1}{2}\left[1 - \cos\left(\frac{2s-1}{2N}\pi\right)\right], \quad s = 1, 2, \ldots, N. \tag{2.37}$$

The flux points are chosen to be the Gauss-Lobatto points [49, 61] given by:

$$X_{s+\frac{1}{2}} = \frac{1}{2}\left[1 - \cos\left(\frac{s}{N}\pi\right)\right], \quad s = 0, 1, \ldots, N. \tag{2.38}$$

Following the analysis of Huynh [59] and Jameson [60], the flux points are selected as the Legendre-Gauss quadrature points plus the two end points, 0 and 1. By setting $P_{-1}(\xi) = 0$ and $P_0(\xi) = 1$, the higher degree Legendre Polynomials can be calculated as:

$$P_n(\xi) = \frac{2n-1}{n}(2\xi - 1)P_{n-1}(\xi) - \frac{n-1}{n}P_{n-2}(\xi). \tag{2.39}$$

The locations of the interior Legendre-Gauss quadrature points are the roots of the equation $P_n(\xi) = 0$.

Using the solutions at N solution points, a degree $(N-1)$ polynomial can be built using the Lagrange basis defined as

$$h_i(X) = \prod_{\substack{s=1\\ s\neq i}}^{N} \left(\frac{X - X_s}{X_i - X_s} \right). \tag{2.40}$$

Similarly, using the fluxes at $(N+1)$ flux points, a degree N polynomial can be built for the flux using a similar Lagrange basis defined as

$$l_{i+\frac{1}{2}}(X) = \prod_{\substack{s=0\\ s\neq i}}^{N} \left(\frac{X - X_{s+\frac{1}{2}}}{X_{i+\frac{1}{2}} - X_{s+\frac{1}{2}}} \right). \tag{2.41}$$

The reconstructed solution for the conserved variables in the standard element is simply the tensor products of the two one-dimensional polynomials

$$\boldsymbol{Q}(\xi, \eta) = \sum_{j=1}^{N} \sum_{i=1}^{N} \frac{\tilde{\boldsymbol{Q}}_{i,j}}{|J_{i,j}|} h_i(\xi) \cdot h_j(\eta). \tag{2.42}$$

Similarly, the reconstructed flux polynomials take the following form:

$$\begin{aligned} \tilde{\boldsymbol{f}}\,(\xi, \eta) &= \sum_{j=1}^{N} \sum_{i=0}^{N} \tilde{\boldsymbol{f}}_{i+\frac{1}{2},j} l_{i+\frac{1}{2}}\,(\xi) \cdot h_j\,(\eta), \\ \tilde{\boldsymbol{g}}\,(\xi, \eta) &= \sum_{j=0}^{N} \sum_{i=1}^{N} \tilde{\boldsymbol{g}}_{i,j+\frac{1}{2}} h_i\,(\xi) \cdot l_{j+\frac{1}{2}}\,(\eta). \end{aligned} \tag{2.43}$$

The reconstructed fluxes are only element-wise continuous, but discontinuous across cell interfaces. Thus $\partial\tilde{\boldsymbol{f}}/\partial\xi$ and $\partial\tilde{\boldsymbol{g}}/\partial\eta$ reduce to polynomials of degree $N-1$ consistent with the solution.

For the inviscid flux, a Riemann solver using either Rusanov [62] or Roe [63] schemes is employed to compute a common flux at interfaces to ensure conservation and stability. In the present study, the flux vector at the element boundary interfaces is computed using the Roe solver with the entropy fix as suggested by Harten and Hyman[64].

The algorithm to compute the inviscid flux derivatives $\left(\partial\tilde{\boldsymbol{f}}_e/\partial\xi\right)_{i,j}$ and $(\partial\tilde{\boldsymbol{g}}_e/\partial\eta)_{i,j}$ can be summarized in the following steps.

a. Given the conservative variables, $\tilde{\boldsymbol{Q}}_{i,j}$, at the solution points, the conservative variables, $\boldsymbol{Q}_f$ (i.e. $\boldsymbol{Q}_{i+\frac{1}{2},j}$, $\boldsymbol{Q}_{i,j+\frac{1}{2}}$), at the flux points are evaluate using equation 2.42.

b. The inviscid fluxes at the interior flux points are computed using the solutions computed from the previous step.

c. The inviscid fluxes at the element interfaces, $\hat{\boldsymbol{f}}_e$ and $\hat{\boldsymbol{g}}_e$, are computed using the Rusanov or Roe solver.

- The Rusanov scheme takes the following form

$$\hat{\boldsymbol{f}}_e = \frac{1}{2}\left[(\tilde{\boldsymbol{f}}_{e,L} + \tilde{\boldsymbol{f}}_{e,R})\cdot\vec{\mathbf{n}} - \lambda(\boldsymbol{Q}_R - \boldsymbol{Q}_L)\right], \tag{2.44}$$

$$\hat{\boldsymbol{g}}_e = \frac{1}{2}\left[(\tilde{\boldsymbol{g}}_{e,L} + \tilde{\boldsymbol{g}}_{e,R})\cdot\vec{\mathbf{n}} - \lambda(\boldsymbol{Q}_R - \boldsymbol{Q}_L)\right], \tag{2.45}$$

  where $\vec{\mathbf{n}}$ is the normal direction of the interface, $\lambda = |V_n| + c$ is an upper bound for the absolute values of the characteristic speeds and V_n is the fluid velocity normal to edge interface and c is the sound speed. The subscripts L and R denote the flux points left and right of the element interface.

- The Roe scheme takes the following form

$$\hat{\boldsymbol{f}}_e = \frac{1}{2}\left[(\tilde{\boldsymbol{f}}_{e,L} + \tilde{\boldsymbol{f}}_{e,R})\cdot\vec{\mathbf{n}} - |\hat{A}|(\boldsymbol{Q}_R - \boldsymbol{Q}_L)\cdot\vec{\mathbf{n}}\right], \tag{2.46}$$

$$\hat{\boldsymbol{g}}_e = \frac{1}{2}\left[(\tilde{\boldsymbol{g}}_{e,L} + \tilde{\boldsymbol{g}}_{e,R}) \cdot \vec{\mathbf{n}} - |\hat{B}|(\boldsymbol{Q}_R - \boldsymbol{Q}_L) \cdot \vec{\mathbf{n}}\right], \tag{2.47}$$

where $\hat{A} = \left(\dfrac{\partial \tilde{\boldsymbol{f}}_e}{\partial \boldsymbol{Q}}\right)_f$ and $\hat{B} = \left(\dfrac{\partial \tilde{\boldsymbol{g}}_e}{\partial \boldsymbol{Q}}\right)_f$ are the Jacobians at the interface f.

d. The derivatives of the fluxes are computed at the solution points using the derivatives of the Lagrange operators l as follows:

$$\left(\frac{\partial \tilde{\boldsymbol{f}}_e}{\partial \xi}\right)_{i,j} = \sum_{k=0}^{N} \tilde{\boldsymbol{f}}_{k+\frac{1}{2},j} \cdot l'_{k+\frac{1}{2}}(\xi_i), \tag{2.48}$$

$$\left(\frac{\partial \tilde{\boldsymbol{g}}_e}{\partial \eta}\right)_{i,j} = \sum_{k=0}^{N} \tilde{\boldsymbol{g}}_{i,k+\frac{1}{2}} \cdot l'_{k+\frac{1}{2}}(\eta_j), \tag{2.49}$$

where

$$l'_{k+\frac{1}{2}}(X) = \sum_{\substack{m=0\\m\neq k}}^{N} \frac{1}{X_{k+\frac{1}{2}} - X_{m+\frac{1}{2}}} \prod_{\substack{s=0\\s\neq k\\s\neq m}}^{N} \left(\frac{X - X_{s+\frac{1}{2}}}{X_{k+\frac{1}{2}} - X_{s+\frac{1}{2}}}\right). \tag{2.50}$$

The solution procedures to get viscous fluxes can be described in the following steps.

a. Given the conservative variables, $\tilde{\boldsymbol{Q}}_{i,j}$, at the solution points, the conservative variables, $\boldsymbol{Q}_f$ (i.e. $\boldsymbol{Q}_{i+\frac{1}{2},j}$, $\boldsymbol{Q}_{i,j+\frac{1}{2}}$), are evaluated to the flux points.

b. Compute the average values at the element interface flux points, i.e. $\overline{\boldsymbol{Q}_f} = \frac{1}{2}[(\boldsymbol{Q}_f)_L + (\boldsymbol{Q}_f)_R]$. Apply appropriate conditions for u, v and T at specific boundary points.

c. Evaluate $\nabla \boldsymbol{Q}$ from $\overline{\boldsymbol{Q}_f}$ using equations 2.48 and 2.49 where $\nabla \boldsymbol{Q} = \left\{ \begin{array}{c} \boldsymbol{Q}_x \\ \boldsymbol{Q}_y \end{array} \right\}$ and $\boldsymbol{Q}_x = \dfrac{\partial \boldsymbol{Q}}{\partial \xi}\xi_x + \dfrac{\partial \boldsymbol{Q}}{\partial \eta}\eta_x$, etc.

d. Reconstruct the gradients, $\nabla \boldsymbol{Q}$, at the flux points from the solution points.

e. Compute the average of the flux-point gradient on the element interfaces $\overline{\nabla \boldsymbol{Q}_f} = \frac{1}{2}[((\nabla \boldsymbol{Q})_f)_L + ((\nabla \boldsymbol{Q})_f)_R]$.

f. Use $\overline{\boldsymbol{Q}_f}$ and $\overline{\nabla \boldsymbol{Q}_f}$ to compute viscous flux vectors described in equation 2.33 at the element interfaces.

g. Compute the viscous fluxes at the flux points and their derivatives at the solution points.

2.2.2 Temporal discretization

For time integration, equation 2.35 can be re-written as:

$$\frac{\partial \tilde{\boldsymbol{Q}}}{\partial t} = R(\tilde{\boldsymbol{Q}}), \tag{2.51}$$

where R is the spatial residual operator. The solution can then be obtained by simply using the forward Euler explicit scheme which can be written as:

$$\tilde{\boldsymbol{Q}}^{n+1} = \tilde{\boldsymbol{Q}}^{n} + dt \cdot R(\tilde{\boldsymbol{Q}}^{n}). \tag{2.52}$$

The solution can be advanced in time using a multi-stage Runge-Kutta scheme as follows:

$$\begin{aligned} \tilde{\boldsymbol{Q}}^{(0)} &= \tilde{\boldsymbol{Q}}^{n}; \\ \tilde{\boldsymbol{Q}}^{(i)} &= \sum_{k=0}^{i-1} \left[\alpha_{i,k} \tilde{\boldsymbol{Q}}^{k} + \Delta t \beta_{i,k} R(\tilde{\boldsymbol{Q}}^{k})\right], \quad i = 1, 2, ..., s; \\ \tilde{\boldsymbol{Q}}^{n+1} &= \tilde{\boldsymbol{Q}}^{s} \end{aligned} \tag{2.53}$$

where s is the number of stages and the coefficients α_{ik} and β_{ik} are chosen according to the stability and accuracy criteria such as those used in the widely known Jameson-Schmidt-Turkel (JST) scheme [65] and the strong-stability-preserving Runge-Kutta (SSPRK) schemes [66, 67]. In this research, all of the solutions are advanced in time using a fourth-order strong-stability-preserving five-stage Runge-Kutta scheme where

$s = 5$. The coefficients α_{ik} and β_{ik} are taken from the table of SSPRK(5,4) in Spiteri and Ruuth [68] and are listed in table 2.1.

Stages	5				
	1				
	0.44437049406734	0.555629505932661			
$\alpha_{i,k}$	0.62010185138540	0	0.37989814861460		
	0.17807995410773	0	0	0.82192004589227	
	0.00683325884039	0	0.51723167208978	0.12759831133288	0.34833675773694
	0.39175222700392				
	0	0.36841059262959			
$\beta_{i,k}$	0	0	0.25189177424738		
	0	0	0	0.54497475021237	
	0	0	0	0.08460416338212	0.22600748319395
CFL number	1.50818004975927				

Table 2.1: Coefficients for SSPRK(5,4) from Spiteri and Ruuth.

Chapter 3

Laminar vortex shedding off a bluff body

Some portions of this chapter were previously published by Chan & Jameson [69] [1] and Chan *et al.* [70] [2].

3.1 Introduction

As a preliminary to the study of laminar vortex suppression, it is vital to establish confidence in the results obtained from both commercial and SD codes by making comparisons with other known experimental and numerical results from past researchers. This chapter deals with numerical simulation and verification of the flow in the regime where the flow is predominantly laminar and two-dimensional. The condition covered in the study includes both unbounded flow and bounded flow in a confined channel. For an unbounded flow, the effects of the end conditions such as the inlet, outlet and wall boundaries are considered negligible or have very little influence on the vortex shedding characteristics. The nature of the bounded flow, on the other hand, depends

---

[1] Chan & Jameson, *Int. J. Num. Meth. Fluids.* Copyright 2010. Reproduced with permission from John Wiley and Sons. License Number 2671570769997.

[2] Chan *et al.* , *J. Fluid Mech.* Copyright 2011. Reproduced with permission from Cambridge University Press. License Number 2671560868712.

largely on the blockage ratio, β, which is typically defined as

$$\beta = \frac{d}{H}, \tag{3.1}$$

where d is the cylinder diameter or characteristic length and H is the height of the channel measured between two walls parallel to the direction of flow freestream. The geometrical definition of the computational domain used in this research is shown in figure 3.1.

3.2 Unbounded flow

It is well known that when a bluff body, such as a circular or a square cylinder, is placed in a uniform freestream an unsteady separation develops, leading to a von Kármán vortex street. Unbounded flow past a bluff body can be found in many engineering applications such as buildings, bridges, towers, wires and telescopes. The structural vibration caused by wake instabilities, known as vortex induced vibration, can have a catastrophic impact on the structure itself. One of the most notorious examples of vortex induced vibration is the Tacoma Narrows Bridge that was destroyed in 1940. Even in the laminar shedding regime, there can be a tremendous periodic loads on the structure when the vortex shedding is set in motion. The basic design of these structures oftentimes takes on the form of either circular or square cylinders.

3.2.1 Single stationary circular cylinder

In the low Reynolds number range of 50 to 194, the vortex wakes past a circular cylinder, for example, are purely two dimensional [13]. At higher Reynolds numbers, the wakes become increasingly complex and three dimensional. In this subsection, results from two-dimensional numerical simulations using both of the numerical schemes described in chapter 2 are presented and compared with some well known results. The comparisons are restricted to the laminar vortex shedding regime.

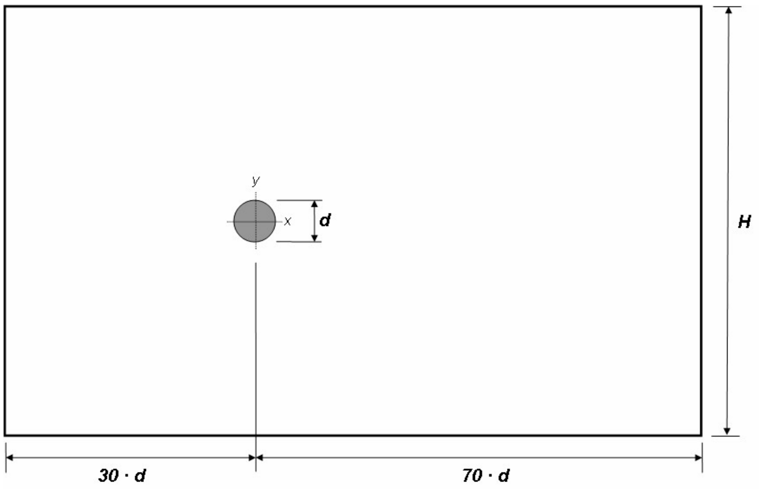

Figure 3.1: Geometrical definition of the computational domain.

ESI CFD-ACE+ results at $Re = 150$, $\beta = 0.015$

This simulation uses a 256 × 256 computational mesh with a uniform circumferential spacing around the circular cylinder. The normal spacing is increased geometrically with the grid layer next to cylinder surface being $0.0003{\cdot}d$. Figure 3.2 illustrates the mesh near the cylinder surface on an $x - y$ Cartesian coordinate system.

CFD-ACE+ offers options for time discretization by the first order Euler and the second order Crank-Nicolson (CN) schemes. For spatial discretization, the first-order backward Euler scheme, the second order central differencing scheme (CDS) and the second-order upwind schemes (2UDS) are available. In order to obtain sufficient accuracy, the first order schemes for both time and spatial discretization should be avoided since it is well known that these schemes lead to highly dissipative results. When using the CN scheme, it is found that spatial discretization with the 2nd order upwind difference scheme (2UDS) and CDS produce very similar results. Qualitatively, the instantaneous plot of the z-component of vorticity, shown on figure 3.3, reveals the typical von Kármán vortex street as one would expect from flow past a circular cylinder at $Re = 150$. It shows the formation of two rows of alternating

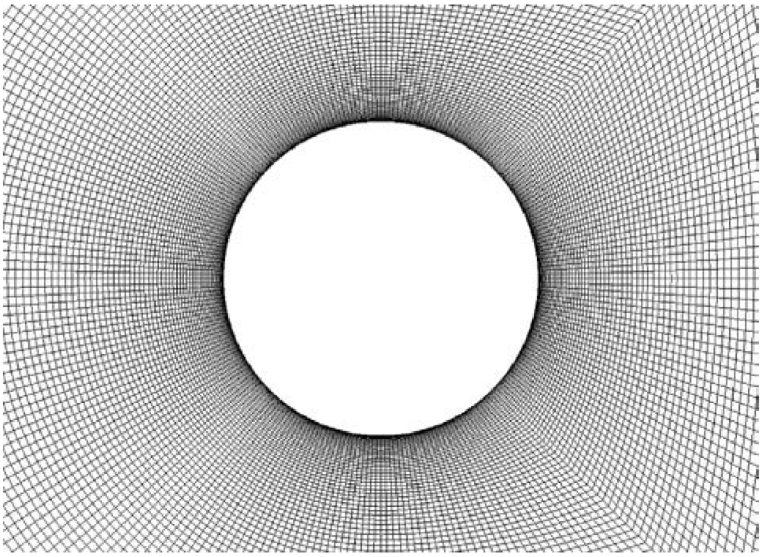

Figure 3.2: Mesh around the circular cylinder for simulation using ESI CFD-ACE+.

vortices in the wake of the cylinder. This asymmetrical flow pattern produces an oscillating pressure distribution (figure 3.4) on the cylinder, and leads to the fluctuation of coefficients of lift, C_L, and drag, C_D. Note that C_D oscillates twice as fast as C_L. The shedding pattern is regular but is subjected to viscous dissipation as each vortex moves further downstream away from the obstructing body. The rate of decay may be exaggerated in the simulations due to numerical dissipation. However, no spurious reflection is observed downstream confirming the correct pressure setting at the far right boundary.

When a first-order backward Euler scheme is used for time discretization, the Strouhal number, St, as well as the amplitudes of the drag and lift coefficients (figure 3.5) are significantly lower than the expected values from past publications such as those obtained by Belov *et al.* [71]. The shortcomings of the first-order time discretization become even more apparent in solutions on a coarser grid. A coarser grid is investigated in the interest of saving computational time to enable the study of numerous variations. Table 3.1 shows the comparison of the results for flow past a single circular cylinder at $Re = 150$ using these different schemes. It is obvious that the accuracy of St and $\overline{C_{pb}}$ suffers markedly when the backward Euler scheme is used.

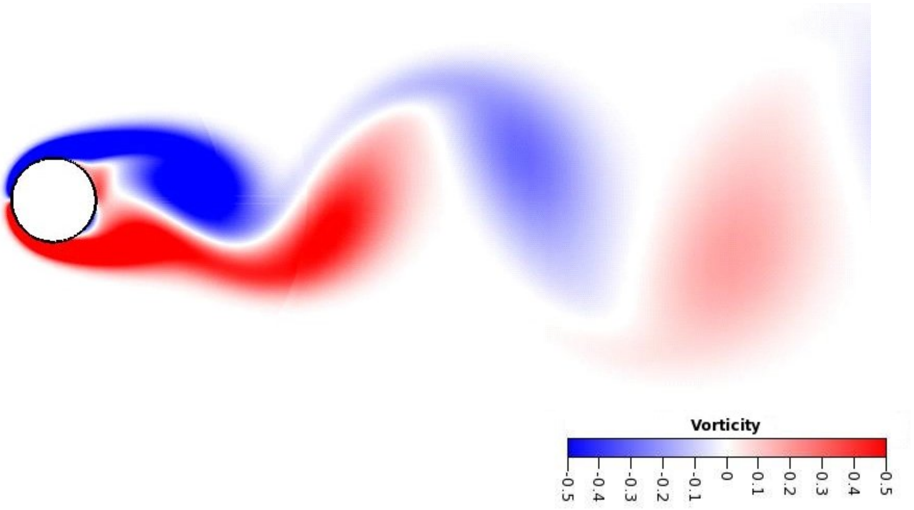

Figure 3.3: Instantaneous vorticity plot of flow past a circular cylinder, 2UDS, CN, $Re = 150$.

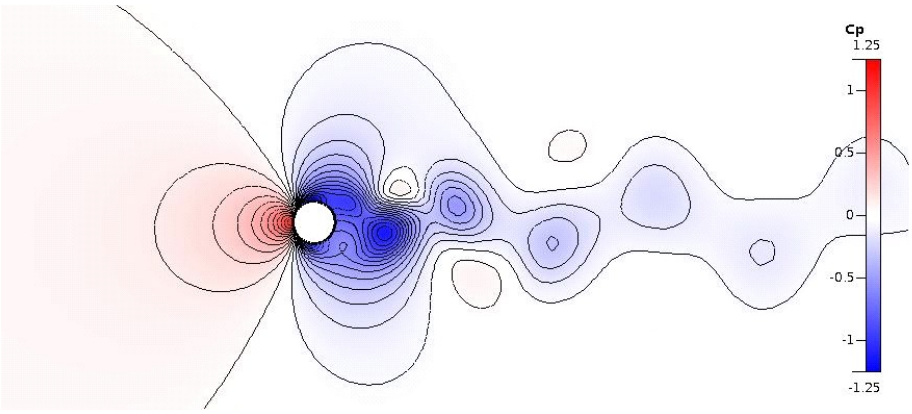

Figure 3.4: Instantaneous C_p plot showing isobar of flow past a circular cylinder, 2UDS, CN, $Re = 150$.

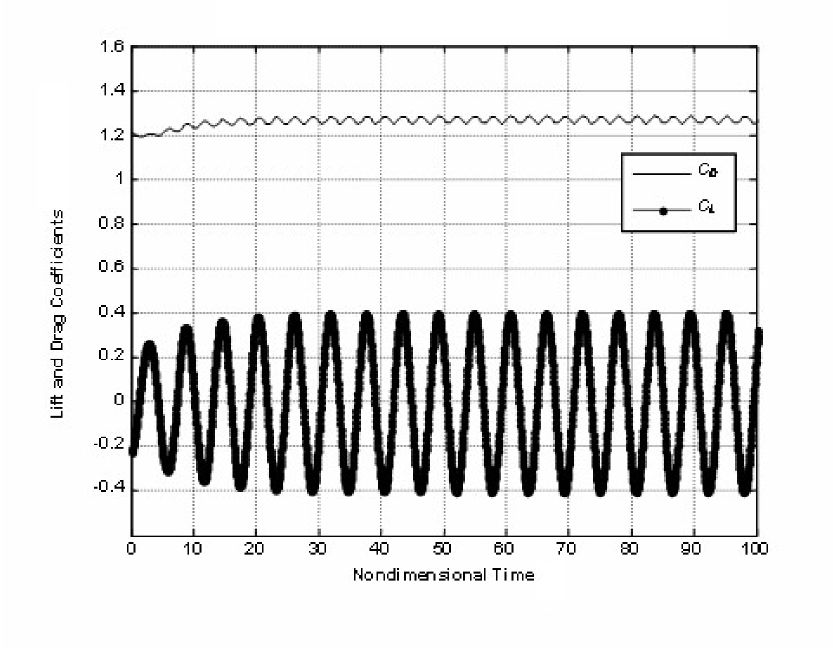

Figure 3.5: C_L and C_D of flow past a circular cylinder, unbounded, 2UDS, Euler, $Re = 150$.

Note that one of the techniques used to accelerate the onset of shedding is to perturb the initial condition by using very large time step, Δt, (e.g. 0.1) in the first few steps. Once the mean flow is established throughout the domain, Δt is then throttled back to the desired target (e.g. 0.0001 s). The plots shown in this section represent flow solutions in which the steady asymmetric shedding characteristics have already been established.

It is well known that the CN scheme can sometimes lead to non-physical, oscillatory solutions when Δt is set too large. In the interest of saving computational time, it is desirable to use the largest possible Δt that will not produce oscillations. CFD-ACE+ allows a biasing scheme where the two-level time discretization can be modified so that the code will solve the solution with more or less implicit information. For example, when the blending factor (also known as weighting or biasing factor) is set to 0.5, it produces the traditional CN scheme where the variables at time step n and $n + 1$ have equal weighting of first-order explicit and backward implicit Euler

	$Re = 150$				
Source	Cells	St	C_L	C_D	$\overline{C_{pb}}$
CFD-ACE+ (2UDS, Euler)	65,536	0.174	$\pm$ 0.401	1.268 $\pm$ 0.017	-0.73
CFD-ACE+ (CDS, CN)	65,536	0.181	$\pm$ 0.531	1.330 $\pm$ 0.028	-0.80
CFD-ACE+ (2UDS, CN)	65,536	0.180	$\pm$ 0.492	1.319 $\pm$ 0.023	-0.79
CFD-ACE+ (2UDS, Euler)	27,200	0.154	$\pm$ 0.146	1.132 $\pm$ 0.002	-0.57
CFD-ACE+ (CDS, CN)	27,200	0.175	$\pm$ 0.439	1.281 $\pm$ 0.019	-0.76
CFD-ACE+ (2UDS, CN)	27,200	0.174	$\pm$ 0.411	1.278 $\pm$ 0.017	-0.75
Belov *et al.* [71]	65,536	0.182	$\pm$ 0.486	1.168 $\pm$ 0.025	-0.82
Williamson [8, 13]	–	0.184	–	–	-0.85

Table 3.1: Flow past a circular cylinder at $Re = 150$: Comparison of St, C_L, C_D and $\overline{C_{pb}}$ for various numerical schemes and two different mesh densities.

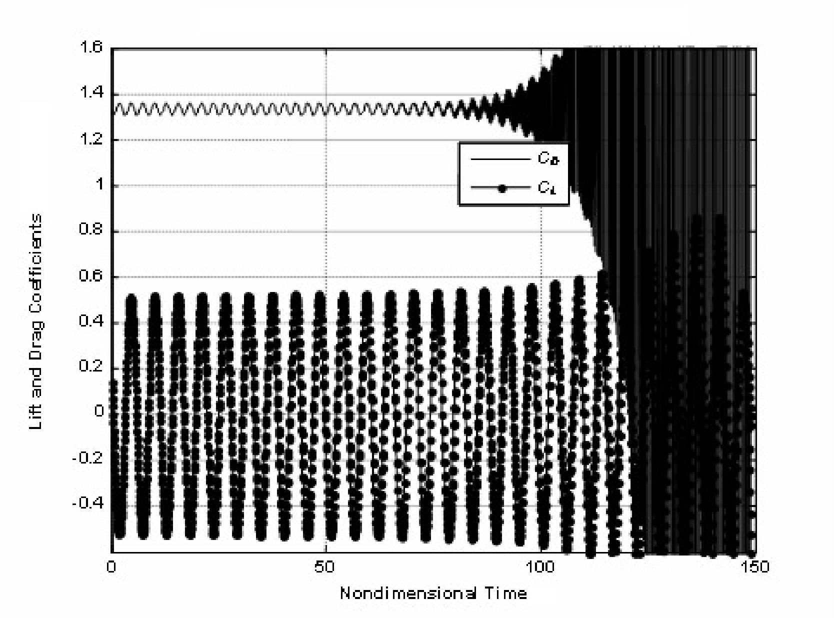

Figure 3.6: Numerical oscillation appears in flow solution using traditional Crank-Nicolson scheme ($B = 0.5$).

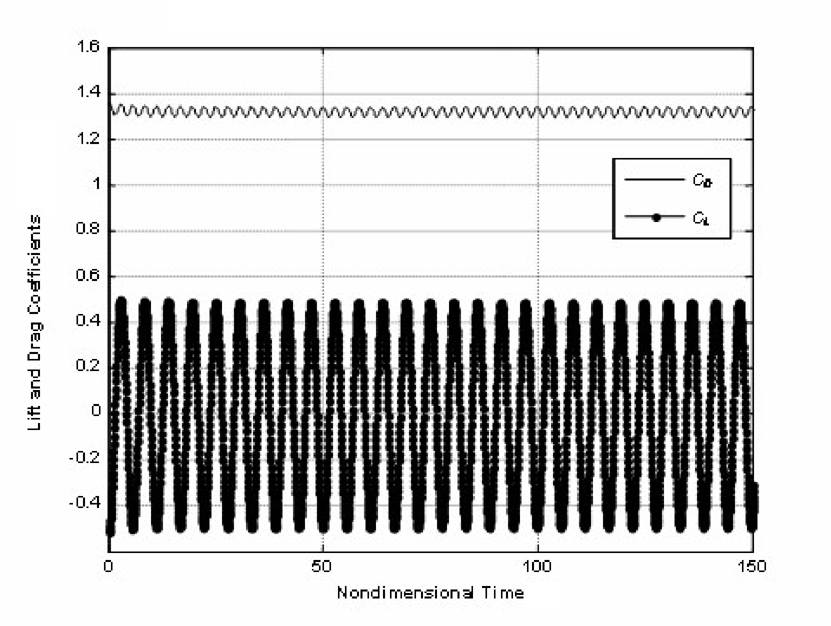

Figure 3.7: Flow solution using Crank-Nicolson scheme with $B = 0.6$.

schemes. When it is set to 1.0, it recovers the implicit Euler method. The blending scheme employed in the code essentially follows the theta method used for solving initial value problems of stiff systems of differential equations. When applied to the CN method in one-dimension, for example, the scheme takes the following form

$$\frac{\phi_i^{n+1} - \phi_i^n}{\Delta t} = k\left(B\frac{\phi_{i+1}^{n+1} - 2\phi_i^{n+1} + \phi_{i-1}^{n+1}}{\Delta x^2} + (1-B)\frac{\phi_{i+1}^n - 2\phi_i^n + \phi_{i-1}^n}{\Delta x^2}\right), \tag{3.2}$$

where B is the blending factor, k is the diffusion coefficient, ϕ is the solution variable, n is the time step and i is the cell being computed.

It has been found by Prothero and Robinson [72] and Berzins and Furzeland [73] that a factor of 0.55 produces accurate and stable results for large non-linear systems of stiff equations. In the present work, it is found that a default setting of 0.6 is sufficient to inhibit oscillation in the solutions. Figure 3.6 shows a diverged solution when the pure CN scheme ($B = 0.5$) is used with $\Delta t = 0.0001$, while figure 3.7 shows a stable solution with no significant deviation in C_D, C_L, or St from the references when the blending factor is set at 0.6. It is noted that a coarse mesh can produce reasonable results when the proper temporal and spatial differencing schemes are used. Note that setting B to 1.0 produces the backward implicit Euler scheme.

SD results at Re = 100, 150 and 200, $\beta = 0.015$

The intent of this section is to compare the SD numerical results for the flow past a single stationary circular cylinder at Re = 100, 150 and 200 with the results from a number of previous studies. The total number of cells used in this validation case is 6,384. The grid distribution is set in a similar and consistent manner that will be used throughout the present research. Figure 3.8 shows the grid distribution near the circular cylinder body surface.

Across the inlet, the Dirichlet boundary condition is specified with a uniform velocity of 0.1 m/s. The position of the inlet plane is far enough upstream for the flow to be considered unbounded and to have negligible influence on the vortex shedding behavior of the cylinder. It has been previously verified by Liang *et al.* [53, 55] that sufficient accuracy and efficient convergence can be achieved for calculations of flow past a bluff body when Mach number is set between 0.1 and 0.2. If the Mach number is set too low, such as $Ma = 0.05$, the computational efficiency can be severely affected. In the present work, the Mach number is set to $Ma = 0.1$ giving an effectively incompressible flow condition. This section provides additional verification of the SD results.

The upper and lower boundary conditions are set to a symmetrical slip condition. At the exit boundary, a fixed pressure equal to the free stream condition is specified while other flow variables are extrapolated so that the flow remains uniform at the inlet. An isothermal, no slip boundary condition is applied on the cylinder wall surface.

The SD results, as shown in table 3.2, figures 3.9 and 3.10, are computed using the 4th order SD scheme, with 102,144 degrees of freedom (DOF's). The Strouhal numbers at Re = 100 and 150 are identical to the experimental values reported by Williamson [8]. The computed mean base pressure coefficients, $\overline{C_{pb}}$, at these two Reynolds numbers are -0.70 and -0.84, respectively, and they also are in excellent

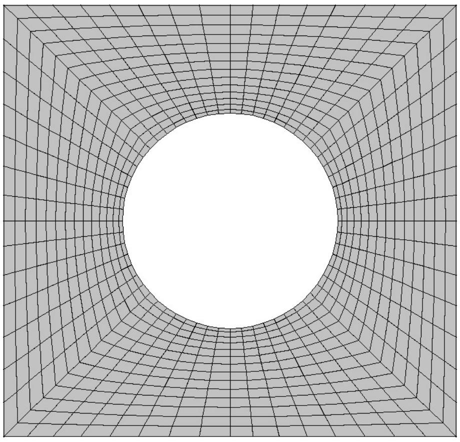

Figure 3.8: Grid distribution near the circular cylinder body surface.

agreement with the experimental values reported by Williamson and Roshko [10]. In addition, the computed lift and drag coefficients are well within the range of values reported in previous work. However, there appear to be some discrepancies at $Re = 200$, that may be due to the presence of flow three-dimensionality which the two-dimensional code cannot resolve. Nonetheless, the Strouhal number agrees well with the computational value by Henderson [74] and the upper transient value from the hysteretic transition regime reported by Miller and Williamson [12, 13]. Figure 3.11 shows the excellent agreement between the present SD calculation and the often-benchmarked Williamson's experimental result [8] of Strouhal number over the laminar shedding regime. Williamson's data is based on the parallel mode of vortex shedding which is believed to represent a truly two-dimensional shedding.

Critical Reynolds number

For an unbounded flow past a circular cylinder, Williamson [8, 13] found the onset of the wake instability to be at about $Re = 49$. Below this critical number, there is a steady region of closed recirculation where a separation bubble enclosing a symmetrical pair of vortices on each side of the wake. The length of this separation bubble increases with Re due to lower viscous stresses. In the present study using the 2nd

$Re = 100$

Source	St	C_L	C_D	$\overline{C_{pb}}$
Present SD [70]	0.164	± 0.325	1.338 ± 0.009	−0.70
Dewey & Smits (Exp.) [70]	0.163	–	–	–
Braza *et al.* [6]	0.160	± 0.25	1.364 ± 0.015	–
Ding *et al.* [75]	0.166	± 0.287	1.356 ± 0.010	–
Henderson [74]	0.165	–	–	−0.73
Kovásznay [2]	0.163	–	–	–
Liu *et al.* [76]	0.164	± 0.339	1.350 ± 0.012	–
Park *et al.* [77]	0.165	± 0.332	1.33 ± 0.009	−0.74
Sharman *et al.* [78]	0.164	± 0.325	1.33 ± 0.009	−0.72
Williamson [8, 13]	0.164	–	–	−0.71

$Re = 150$

Source	St	C_L	C_D	$\overline{C_{pb}}$
Present SD [70]	0.184	± 0.518	1.326 ± 0.026	−0.84
Dewey & Smits (Exp.) [70]	0.184	–	–	–
Belov *et al.* [71]	0.182	± 0.486	1.168 ± 0.025	−0.82
Chan & Jameson [69]	0.181	± 0.531	1.331 ± 0.028	−0.80
Henderson [74, 79]	0.186	–	–	−0.87
Kovásznay [2]	0.180	–	–	–
Park *et al.* [77]	0.184	± 0.516	1.32 ± 0.026	−0.85
Williamson [8, 13]	0.184	–	–	−0.85

$Re = 200$

Source	St	C_L	C_D	$\overline{C_{pb}}$
Present SD [70]	0.196	± 0.68	1.340 ± 0.045	−0.96
Dewey & Smits (Exp.) [70]	0.197	–	–	–
Belov *et al.* [71]	0.193	± 0.64	1.19 ± 0.042	−0.94
Braza *et al.* [6]	0.200	± 0.75	1.40 ± 0.05	–
Ding *et al.* [75]	0.196	± 0.659	1.348 ± 0.050	–
Henderson [74]	0.197	–	–	−1.01
Kovásznay [2]	0.193	–	–	–
Lecointe & Piquet [5]	0.194	± 0.5	1.58 ± 0.0035	–
Liu *et al.* [76]	0.192	± 0.69	1.31 ± 0.049	–
Miller & Williamson [12, 13]	0.197	–	–	−0.86
Mittal & Kumar [80]	0.193	± 0.66	1.316 ± 0.049	–

Table 3.2: Flow past a circular cylinder at $Re = 100$, 150 and 200: St, C_L, C_D and $\overline{C_{pb}}$

(a) $Re = 100$

(b) $Re = 150$

(c) $Re = 200$

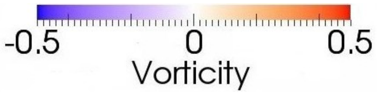

Figure 3.9: SD 4th order solution of unbounded flow past a single stationary circular cylinder: Instantaneous vorticity.

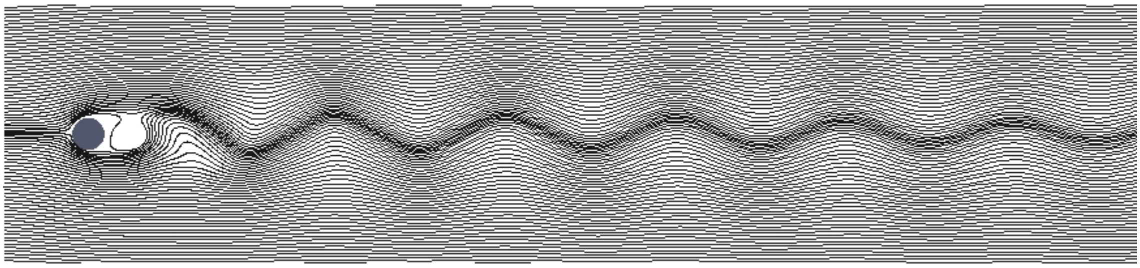

(a) $Re = 100$

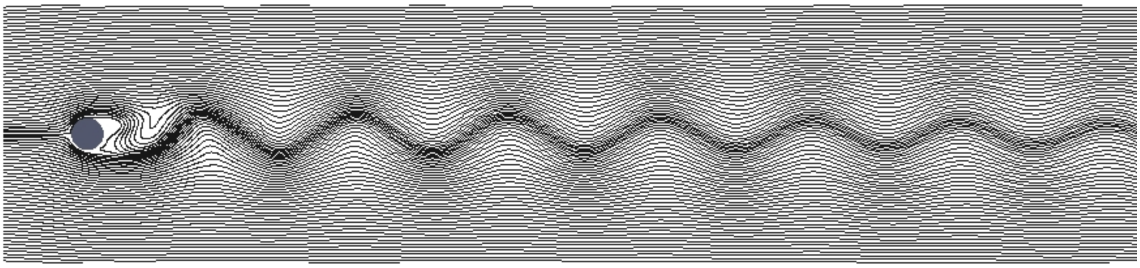

(b) $Re = 150$

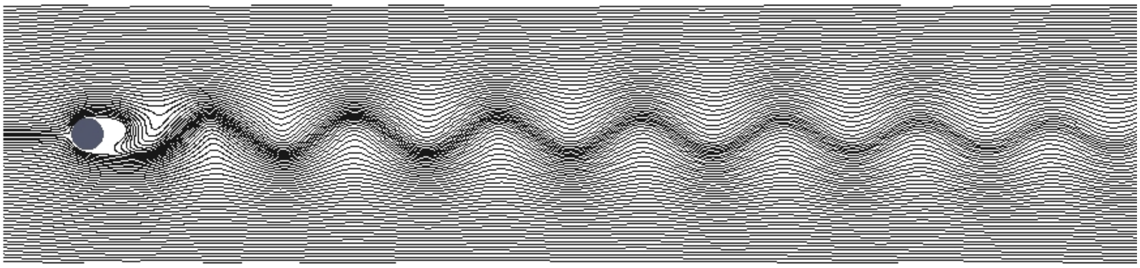

(c) $Re = 200$

Figure 3.10: SD 4th order solution of unbounded flow past a single stationary circular cylinder: Streamlines.

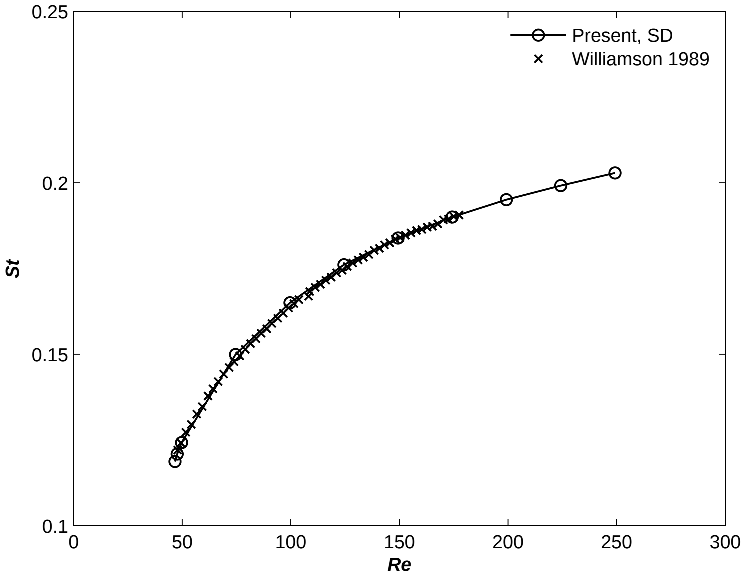

Figure 3.11: Strouhal number of unbounded flow past a circular cylinder. A comparison between SD numerical solution and Williamson experimental results.

order SD simulation, the critical *Re* is calculated from the non-zero value of the root-mean-square (RMS) of the lift component, $\sigma(C_L)$, and is found to be at about 46.8, which is in agreement with Norberg's finding[81]. It is, however, difficult to determine that the critical *Re* from figure 3.12 since the streamlines at $Re = 46.8$ look very much symmetrical and almost identical to those at $Re = 45.8$. The calculated value of $\sigma(C_L)$ for $Re = 46.8$ is very small at approximately 0.0001 but nonetheless is neither zero nor decaying towards it. The corresponding critical Strouhal number is calculated to be 0.1185, which is compared with prior studies as shown in table 3.3.

3.2.2 Single stationary square cylinder

Similar to the flow past a circular cylinder, the flow past a square cylinder at zero incident angle can also shed a periodic Kármán vortex street. Nonetheless, the key difference between the two cylinders is the location where the separation point occurs. For a circular cylinder, the location of the separation point depends on the Reynolds

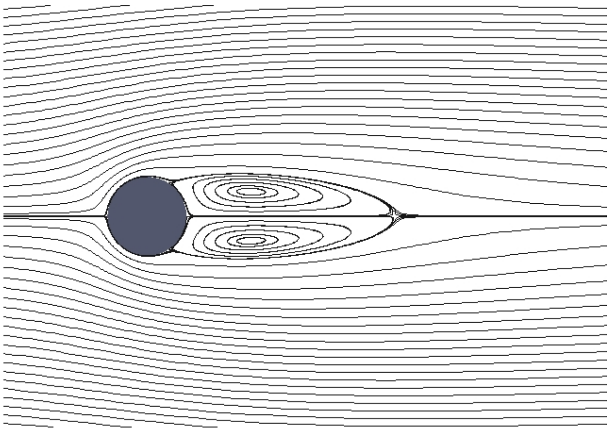

(a) $Re = 45.8$

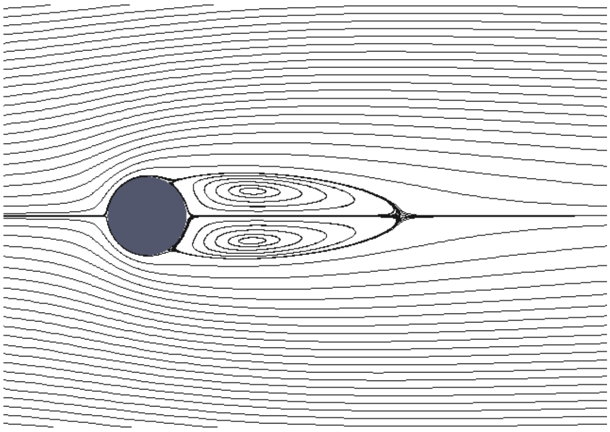

(b) $Re = 46.8$

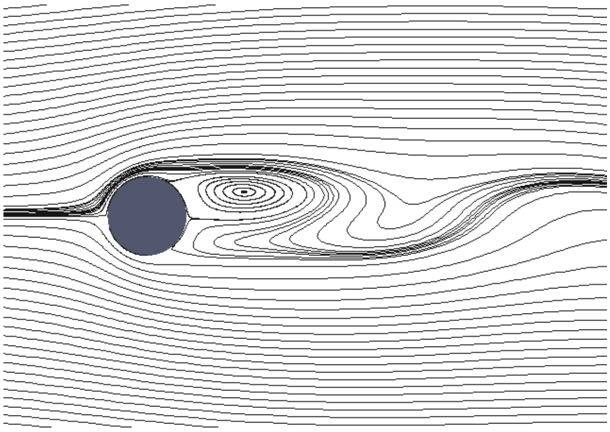

(c) $Re = 47.8$

Figure 3.12: Streamlines of flow near the critical Reynolds number, $\beta = 0.01$.

Source	Re_{crit}	St_{crit}
Present SD	46.8	0.1185
Sahin and Owens [82]	46.74	0.1167
Chen *et al.* [83]	47.9	0.138
Jackson [84]	46.184	0.13804
Ding and Kawahara [85]	46.389	0.126

Table 3.3: Unbounded flow past a circular cylinder: Comparison of critical Re and St.

number of the flow. For the flow at the very low Re, the separation point moves steeply from the rear stagnation or base point (i.e. $\theta = 180°$ from the front stagnation point as shown in figure 3.13) at $Re \approx 1$ towards the rear sharp corners of the square cylinder (i.e. $\theta = 135°$) [26] near $Re = 5$. In the range of $5 < Re \leqslant 40$, the separation point, shown by Sen *et al.* , is by and large at the rear sharp corners. A steady region of closed recirculation, similar to that of a circular cylinder is formed. The length of the recirculation bubble increases approximately linearly with Re. This is also found to be the case from an SD calculation using the mesh shown in figure 3.13 and boundary conditions similar to those imposed on the calculation of the unbounded flow past a circular cylinder. The streamlines in figure 3.14 for $Re = 39.8$ clearly shows the separation point to be at the rear sharp corners of the square cylinder.

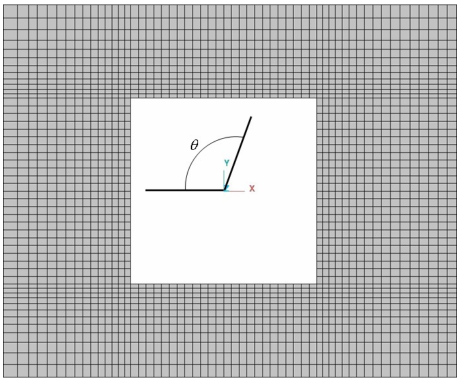

Figure 3.13: Grid distribution near the square cylinder body surface.

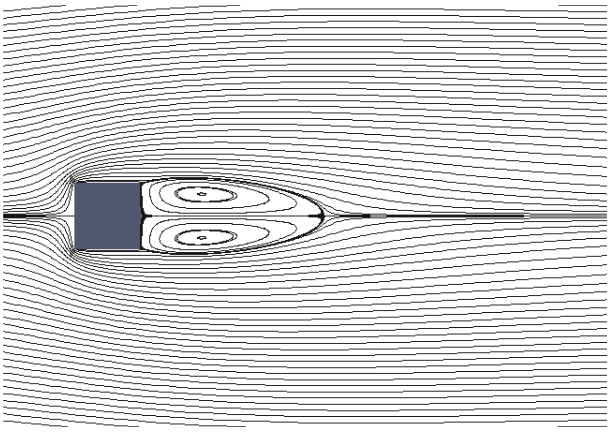

(a) $Re = 39.8$

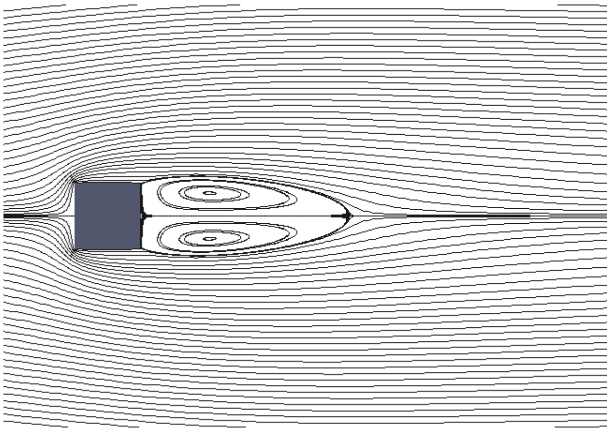

(b) $Re = 44.8$

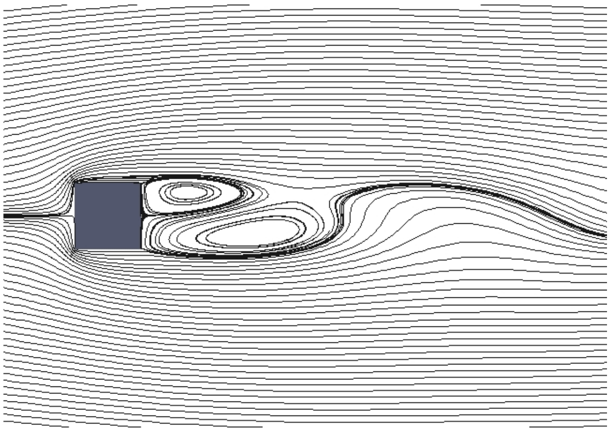

(c) $Re = 45.8$

Figure 3.14: Streamlines of flow near the critical Reynolds number, $\beta = 0.01$.

Laminar vortex shedding

Various researchers in the past seemed to agree from their numerical studies that the onset of vortex shedding of flow past a square cylinder occurs somewhere between $Re = 50$ and 60 [21, 25]. The deviation of this critical Reynolds number seems to be a result of the differences in numerical schemes, boundary conditions and blockages used in those studies. However, according to Norberg's earlier experimental investigation which is later cited by Sohankar *et al.* [24], the onset of vortex shedding for a very small blockage ($\beta = 0.0025$) occurs at $Re = 47$. From the present SD calculation using $\beta = 0.01$, it was found that the onset of vortex shedding occurs at $Re = 45.8$ (figure 3.14) which agrees well with Norberg's finding. Furthermore, it is shown in figure 3.15 that the Strouhal numbers over the range of laminar vortex shedding regime also agrees quite well with Norberg's 1996 experimental study (C. Norberg, personal communication, 2012).

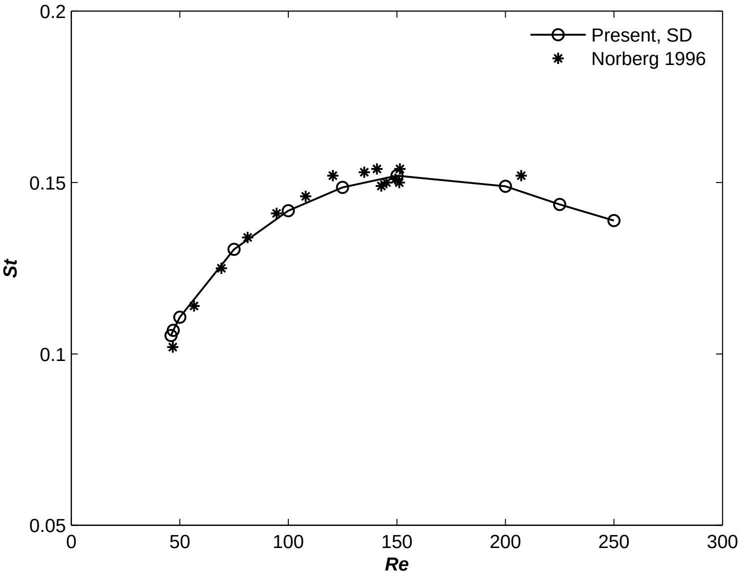

Figure 3.15: Strouhal number of unbounded flow past a square cylinder.

It was observed by Sohankar *et al.* [23, 24] that in the laminar vortex shedding regime the separation point of flow past a square cylinder occurs at the rear corners for $Re \leqslant 100$ (e.g. $Re = 75$ as shown in figure 3.16). The separation point occurs predominantly at the rear corners with an occasional jump to the front at $Re = 125$ and predominantly at the front corners at $Re = 150$. The present SD calculation also finds that at around $Re = 150$ the separation points occurs predominantly at the front corners. The separation point at the rear corners occur alternatively between the upper and lower corners. Figure 3.17 shows an instant when the flow separates on the upper corner surface. Note that the separation points are calculated based on the point in the flow field near to the square surface where the vorticity is zero. At $Re \geqslant 175$, the separation point is reported to be at the front corners of the square. Figure 3.18 obtained from the present SD calculation at $Re = 200$ shows the separation points to be at the front corners, thus supporting Sohankar's finding.

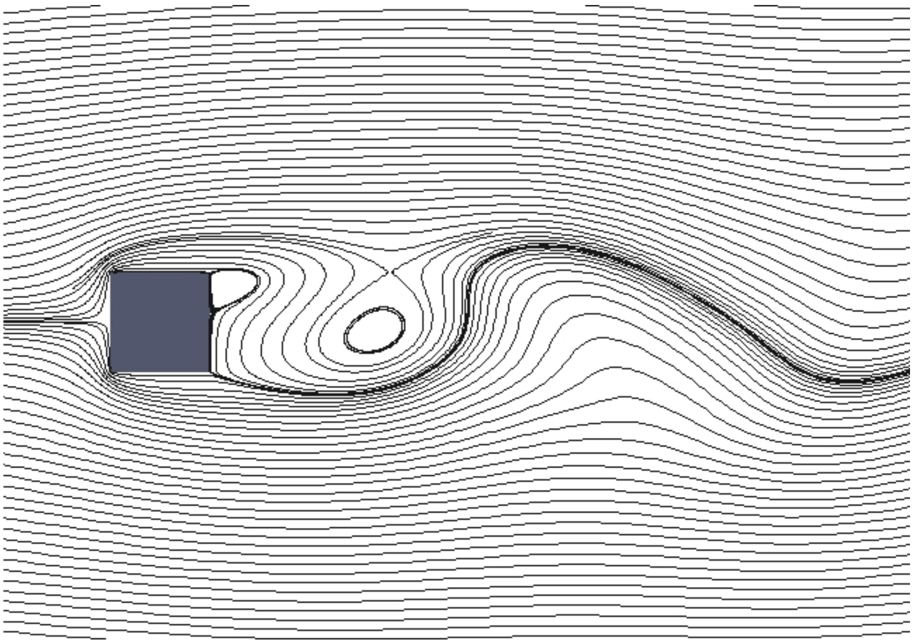

Figure 3.16: Streamlines at $Re = 75$, $\beta = 0.01$.

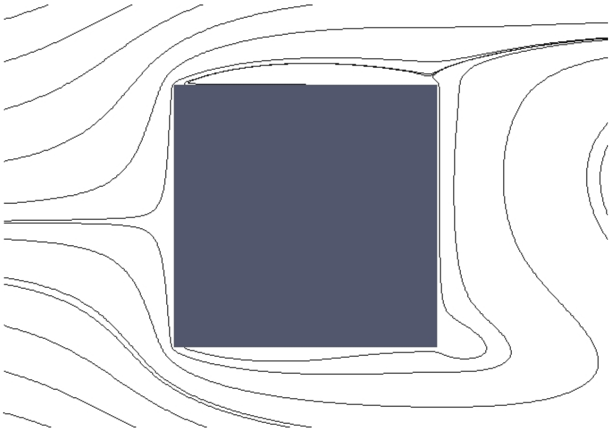

Figure 3.17: Instantaneous streamlines at $Re = 150$, $\beta = 0.01$, showing the separation points near the front corners as well as the rear top corner.

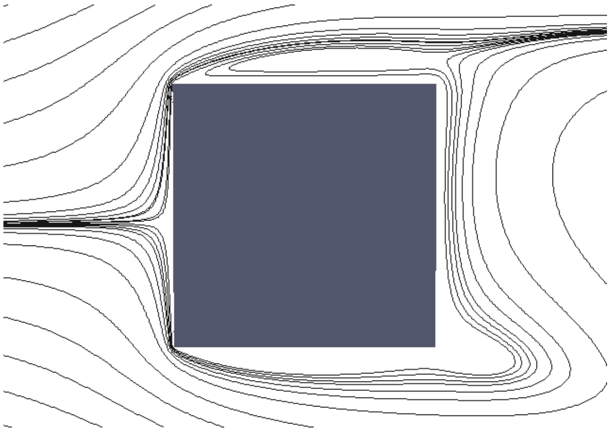

Figure 3.18: Instantaneous streamlines at $Re = 200$, $\beta = 0.01$, showing the separation points at the front corners.

3.3 Bounded flow: blockage effect

One of the objectives of the present study is to investigate the blockage effect on flow past a bluff body. Numerous practical examples of bounded flow can be found in many places such as a bridge pillar in a river, a moving truck in a tunnel and an electronic component in an enclosure. In the current research, the bluff body is assumed to be situated perfectly at the center. The upper and lower boundaries are brought equally closer as the blockage ratio, β increases. That is, at the limit, when $\beta = 0$, the flow is unbounded, and when $\beta = 1$, the flow is completely blocked.

The present study focuses on flow past a bluff body at $\beta \leqslant 0.5$. It has been shown by Chen *et al.* [83] and Sahin and Owens [82] that in this range of blockage, neutral stability of a symmetric solution is produced until it is lost through Hopf bifurcation at a given critical Reynolds number. At higher β, there are multiple solutions due to both Hopf and pitchfork bifurcations that can lead to symmetric or asymmetric solutions depending on the Reynolds number. The convergence of critical Reynolds number can be sensitive to mesh density in the higher blockage range above 0.5. The mesh densities used in Sahin and Owens ranges from 89,336 to 1,842,784 degrees of freedom (DOF).

When dealing with bounded flow with significant blockage factor, it is very important to make clear what kind of velocity profile is used in defining the flow parameters such as the Reynolds number, the Strouhal numbers, etc. Also the location of the bluff body in the flow field with respect to the inlet and outlet boundaries plays an important role in the behavior of the vortex wakes. Discrepancies amongst past researchers have often occurred as a result of not taking the definition of overall flow conditions into account.

With blockage effects, it is a common practice to define the flow parameters based on either the maximum and mean value of the developed velocity profile along the cross section upstream of the bluff body. At the inlet boundary, the streamwise flow velocity is set to be uniform. The flow is allowed to be fully developed over the distance of $30 \cdot d$ upstream of the bluff body. Figure 3.19 illustrates the inlet condition that are imposed throughout the current research.

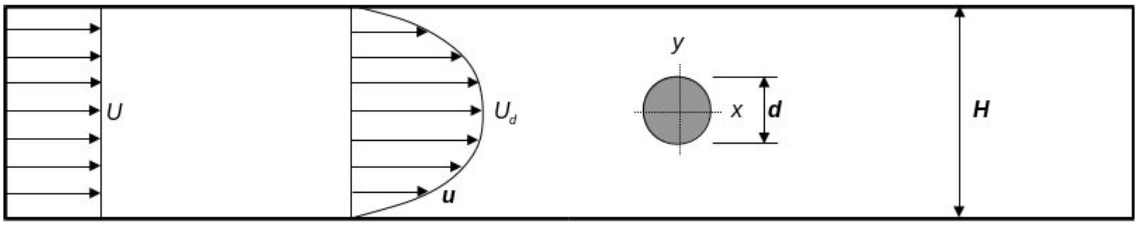

Figure 3.19: Inlet velocity profile.

The flow velocity is explicitly defined as follows

- U = Uniform inflow velocity,
- U_d = Maximum velocity of a fully developed inflow profile,
- U^* = Mean velocity of a fully developed inflow profile = $\int_{-H/2}^{H/2}(u/H)dy$.

The subscript "*d*" denotes a flow parameter calculated from the maximum velocity value upstream of the bluff body. The superscript "$*$" denotes it based on the mean velocity. For example, $Re_d = U_d\nu/d$, $Re^* = U^*\nu/d$, $St_d = fd/U_d$, $St^* = fd/U^*$, etc.

3.3.1 Bounded flow past a bluff body, $0 < \beta \leqslant 0.5$

Critical Reynolds numbers of flow past a circular cylinder

In the range of $0 < \beta \leqslant 0.5$, it has been demonstrated by Chen *et al.* and Sahin and Owen numerically that the blockage effect does not dramatically change the flow structures of the vortex wakes and the bifurcation properties as compared to the unbounded case. However, it was shown that the neutral stability curve of the critical Reynolds number based on maximum velocity increases monotonically as a function of β until it peaks at $\beta = 0.5$. The critical Reynolds number is determined at the point when the RMS value of the lift coefficient becomes non-zero. The corresponding critical Strouhal number also increases with the blockage ratio. Table 3.4 shows a reasonably good agreement of the results obtained from the current SD simulation with both Chen *et al.* and Sahin and Owen. Note that instead of using maximum streamwise velocity value, Chen *et al.* defined the Reynolds number based on an integral of the cross sectional velocity upstream of the circular bluff body as follows

$$U_m = \frac{1}{d}\int_{-d/2}^{d/2} u(y)dy.$$

Figure 3.20 illustrates the instantaneous streamlines at the critical Reynolds numbers for the corresponding blockage ratios. The upper and lower boundaries have a stabilizing effect on the flow perturbation as the shear layer from the boundaries puts a constraint on the separating shear layer from the cylinder wake thus increasing the Reynolds number at which the instability occurs. The size of the separation bubble at the critical Reynolds number decreases as the blockage ratio increases, due to a more increasing interaction of the shear layers between the confining walls and the cylinder.

	Present SD				Sahin & Owens [82]		Chen *et al.* [83]	
β	Re^*	St^*	Re_d	St_d	Re_d	St_d	Re_d	St_d
0.01	46.7	0.1187	46.8	0.1185	46.74	0.1167	47.9	0.138
0.05	43.5	0.1400	47.1	0.1295	–	–	–	–
0.1	39.9	0.1687	48.9	0.1378	50.75	0.1211	51.6	0.122
0.1667	43.1	0.2109	59.1	0.1536	–	–	–	–
0.2	48.2	0.2347	68.0	0.1661	69.34	0.1566	69.0	0.158
0.3	62.8	0.3134	92.5	0.2127	94.4	0.2093	92.0	0.215
0.4	76.1	0.4058	113.5	0.2719	–	–	110.1	0.286
0.5	78.8	0.5055	118.1	0.3374	123.75	0.3399	114.2	0.369

Table 3.4: Bounded flow past a circular cylinder: “Critical” Reynolds number and the corresponding Strouhal number, $0 < \beta \leqslant 0.5$. The superscript “$*$” denotes calculation based on mean velocity. The subscript “d” denotes calculation based on maximum velocity. Critical Re_d and St_d are given in comparison the values obtained by Sahin & Owens and Chen *et al.* .

Critical Reynolds numbers of flow past a square cylinder

In the current study, the SD mesh from the previous study of confined flow past circular cylinder is modified to suit a square body of length $1 \cdot d$. Aside from adjusting the

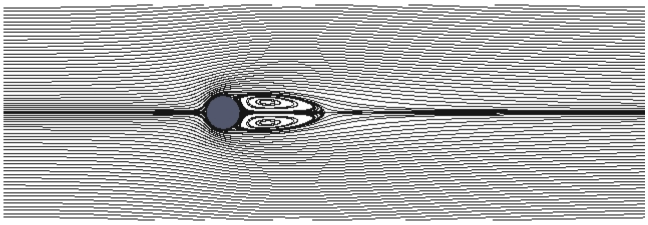

(a) $\beta = 0.1, (Re_d)_{crit} = 48.9$

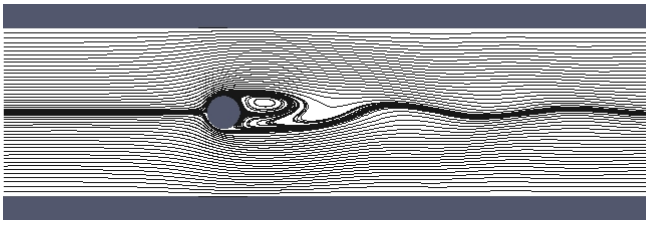

(b) $\beta = 0.2, (Re_d)_{crit} = 68.0$

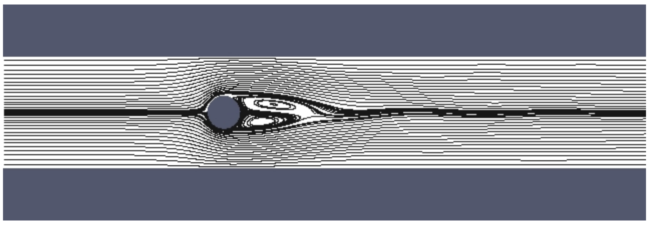

(c) $\beta = 0.3, (Re_d)_{crit} = 92.5$

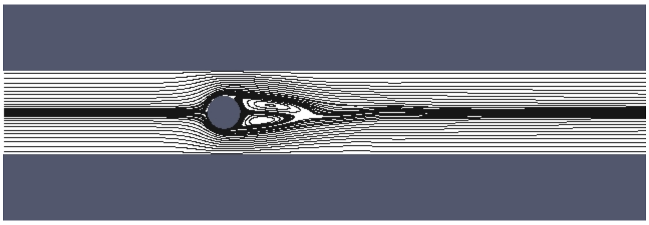

(d) $\beta = 0.4, (Re_d)_{crit} = 113.5$

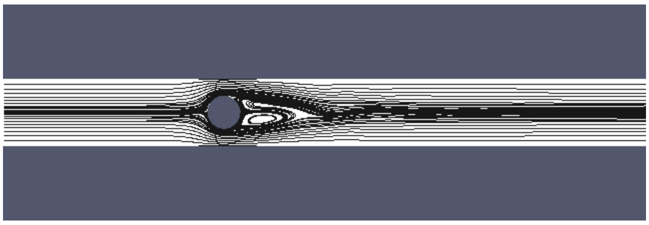

(e) $\beta = 0.5, (Re_d)_{crit} = 118.1$

Figure 3.20: SD solution of flow past a stationary circular cylinder at different blockages: instantaneous streamlines at the corresponding critical Reynolds number.

mesh around the body, all the computational domains including boundary conditions are kept substantially similar to those used for the circular cylinder. As discussed in the previous section, the SD result for the unbounded flow past a square cylinder compares quite well with known published data. Unlike the flow past a circular cylinder, there is very little published information on the critical Reynolds number of flow past a square cylinder in a confined channel. As in the case of a circular cylinder, the critical Reynolds numbers and the corresponding Strouhal number increases with increasing blockage ratio. However, the peak of the neutral stability curve occurs at a lower blockage ratio than that of the circular cylinder at somewhere between $\beta = 0.4$ to 0.5. Figure 3.21 shows the streamlines of flow past a square cylinder at various blockage ratios. The separation bubble also decreases in size with increasing blockage ratio. The separation point occurs at the rear corners for all blockage ratios in this study.

	Present SD			
β	Re^*	St^*	Re_d	St_d
0.01	45.7	0.1061	45.8	0.1058
0.05	42.5	0.1252	45.9	0.1159
0.1	40.9	0.1553	49.9	0.1273
0.1667	48.6	0.2012	65.8	0.1485
0.2	53.5	0.2265	74.8	0.1620
0.25	62.7	0.2701	90.2	0.1879
0.3	69.4	0.3169	101.7	0.2164
0.4	71.6	0.4181	107.0	0.2799
0.5	62.0	0.5229	93.0	0.3486

Table 3.5: Flow past a square cylinder in a confined channel: “Critical” Reynolds number and the corresponding Strouhal number, $0 < \beta \leqslant 0.5$. The superscript “$*$” denotes calculation based on mean velocity. The subscript “d” denotes calculation based on maximum velocity.

Unsteady laminar shedding regime

As in unbounded flow, increasing the Reynolds number beyond the critical value for the flow past bluff body in a confined channel also leads to a symmetry breaking

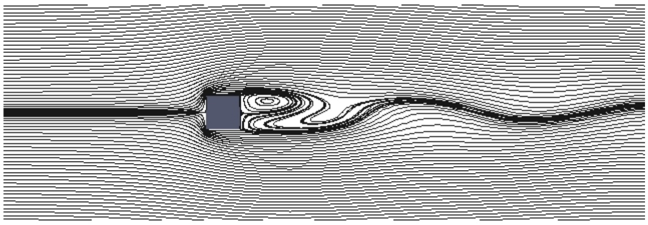

(a) $\beta = 0.1, (Re_d)_{crit} = 49.9$

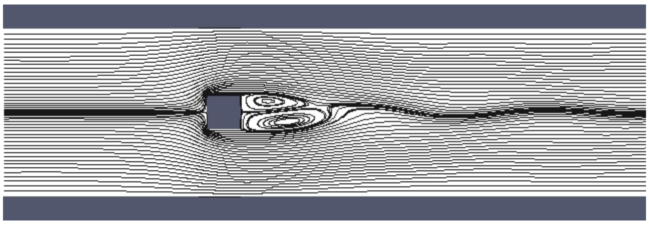

(b) $\beta = 0.2, (Re_d)_{crit} = 74.8$

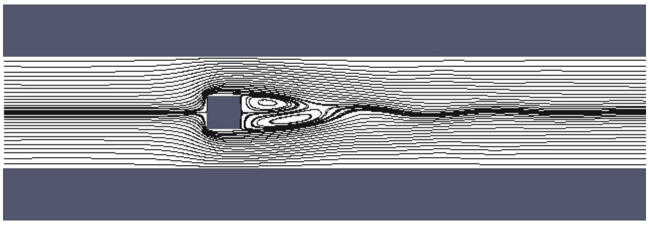

(c) $\beta = 0.3, (Re_d)_{crit} = 101.7$

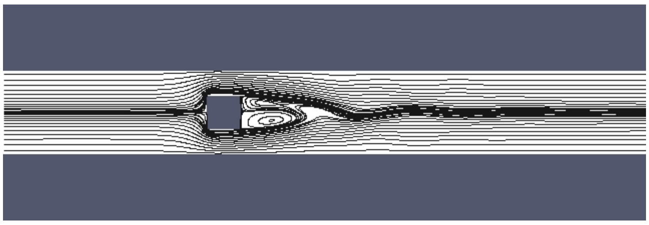

(d) $\beta = 0.4, (Re_d)_{crit} = 107.0$

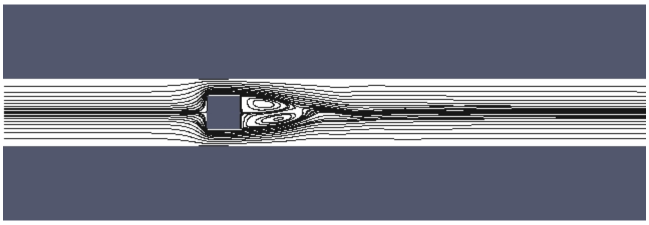

(e) $\beta = 0.5, (Re_d)_{crit} = 93.0$

Figure 3.21: SD solution of flow past a stationary square cylinder at different blockages: instantaneous streamlines at the corresponding critical Reynolds number.

Hopf bifurcation which causes the vortex wakes to detach from the cylinder body leading to an unsteady pattern of alternating vortices, i.e. von Kármán vortex street. Increasing flow confinement in the range of $0 < \beta \leq 0.5$ is found to have to an effect in increasing the Strouhal number and the mean drag coefficient. It is generally accepted from various publications that the unsteady vortex wakes for an unbounded flow past a circular cylinder are predominantly two-dimensional at $Re \lesssim 180$. These vortex wakes are periodic and sinusoidal in nature. The three dimensional wake transition regime falls in the range of $180 \leq Re \leq 260$ [14]. There has been no known study done for the onset of three-dimensionality in flow past a bluff body with blockages. From two-dimensional simulations, some indication of three-dimensionality can be detected when the fluctuation of the lift coefficient would cease to follow a purely sinusoidal pattern. However, it is not always a reliable measurement of three-dimensionality since various factors can influence the wake patterns such as mesh density and time step. In the end, it would be rather crude to rely on the two-dimensional results to predict flow beyond the transitional range. Therefore, the limit of the current investigation is set to $Re_d < 300$.

Since performing numerical flow simulation or empirical experiment requires a finite domain, the role of upper and lower boundaries can be an important factor in how the vortex wakes evolve no matter how small a blockage factor is. While it is possible to treat these boundaries with a symmetrical or periodic condition which essentially imposes a zero normal gradient, i.e. no flux through the boundaries, oftentimes one of the common practices is to impose a no-slip wall condition on them. In this study, both upper and lower boundaries are treated as non-slip walls. It is universally accepted that when the blockage factor is very small, say $\beta = 0.01$, the flow can safely be considered as unbounded. However, up to what value of β where one can consider the flow to be unbounded is not so clear. Figures 3.22 and 3.23 clearly show the effect of the blockage factor on the Strouhal number, St_d, the mean drag coefficient, $\overline{C_{D_d}}$, and the RMS value of the lift coefficient, $\sigma(C_{L_d})$, as function of Reynolds number for the flow past circular and square cylinders. From these plots, it can be concluded that increasing the blockage factor leads to an increase in St_d and $\overline{C_{D_d}}$ over the laminar shedding range. As noted in the previous section, the confinement has a stabilizing effect in which the critical Reynolds number is delayed to a higher value and the overall $\sigma(C_{L_d})$ curve decreases with increasing β.

It is often times more convenient and useful in the study of blockages to calculate the Strouhal number, lift and drag coefficients based on the mean velocity of incoming flow. Figures 3.24 and 3.25 are essentially replots of figures 3.22 and 3.23 calculated from the averaged velocity of the fully developed velocity profile upstream of the bluff body, denoted by the superscript "*". One particular reason for plotting this way is to be able to equivalently compare the flow characteristics using different velocity profiles.

It has been reported by Suzuki *et al.* [86] that there is a phenomenon called the "crisscross" motion of vortices. This occurs when a sufficient blockage effect forces the positive vortex that sheds off the upper portion of the bluff body to cross the negative vortex from the lower portion and move towards the lower wall, and vice versa. Suzuki *et al.* observed this pattern of motion from both numerical and experimental investigation. They reported that the crisscross motion appears whenever the von Kármán vortex street is formed at the blockage ratios of $\beta \geqslant 0.1$. At $\beta > 0.1$, the crisscross motion also occurs in the unsteady Reynolds number range prior to the formation of von Kármán vortex street. Figure 3.26 illustrates the crisscross motion of vortices as obtained from SD simulation. Once the vortices cross one another, they tend to dissipate and merge with the like-sign vortices coming off the respective walls.

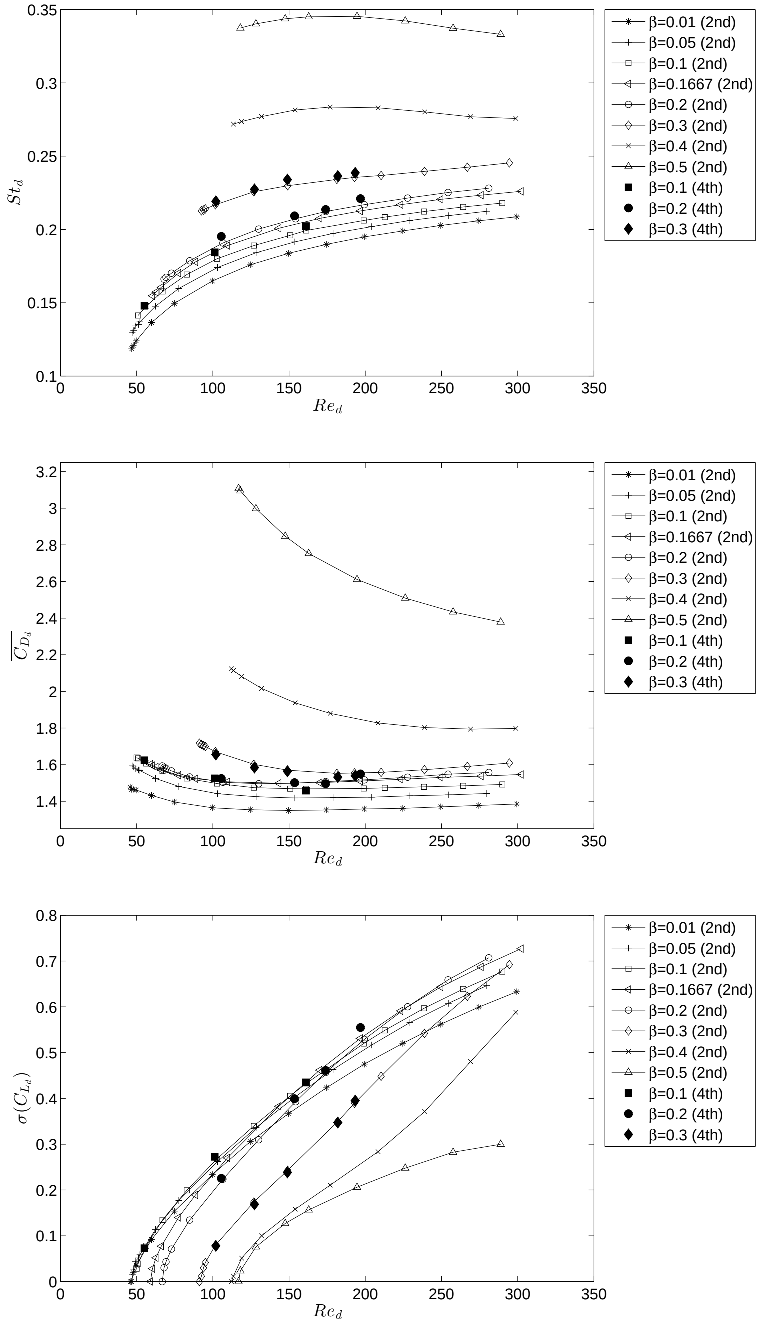

Figure 3.22: SD solutions of flow past a stationary circular cylinder at different blockages: St_d, $\overline{C_{D_d}}$, $\sigma(C_{L_d})$.

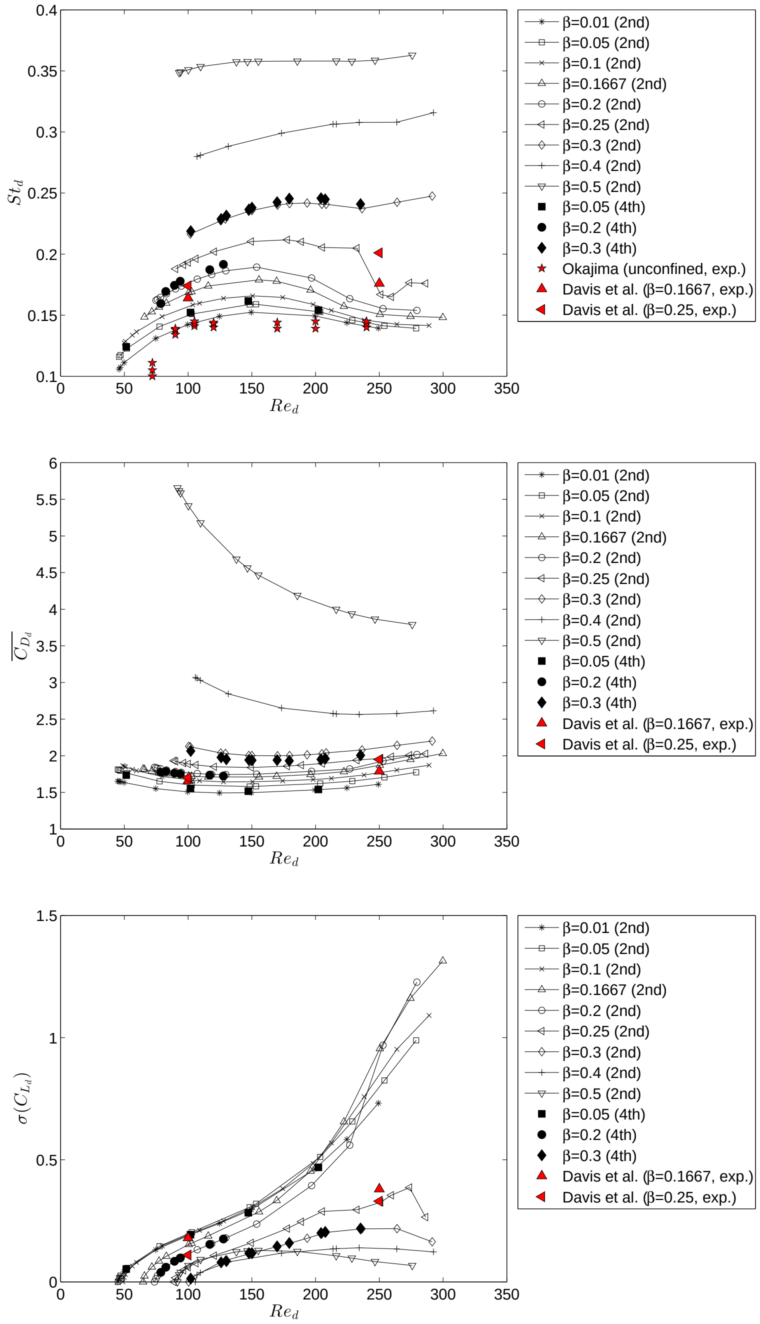

Figure 3.23: SD solutions of flow past a stationary square cylinder at different blockages: St_d, $\overline{C_{D_d}}$, $\sigma(C_{L_d})$.

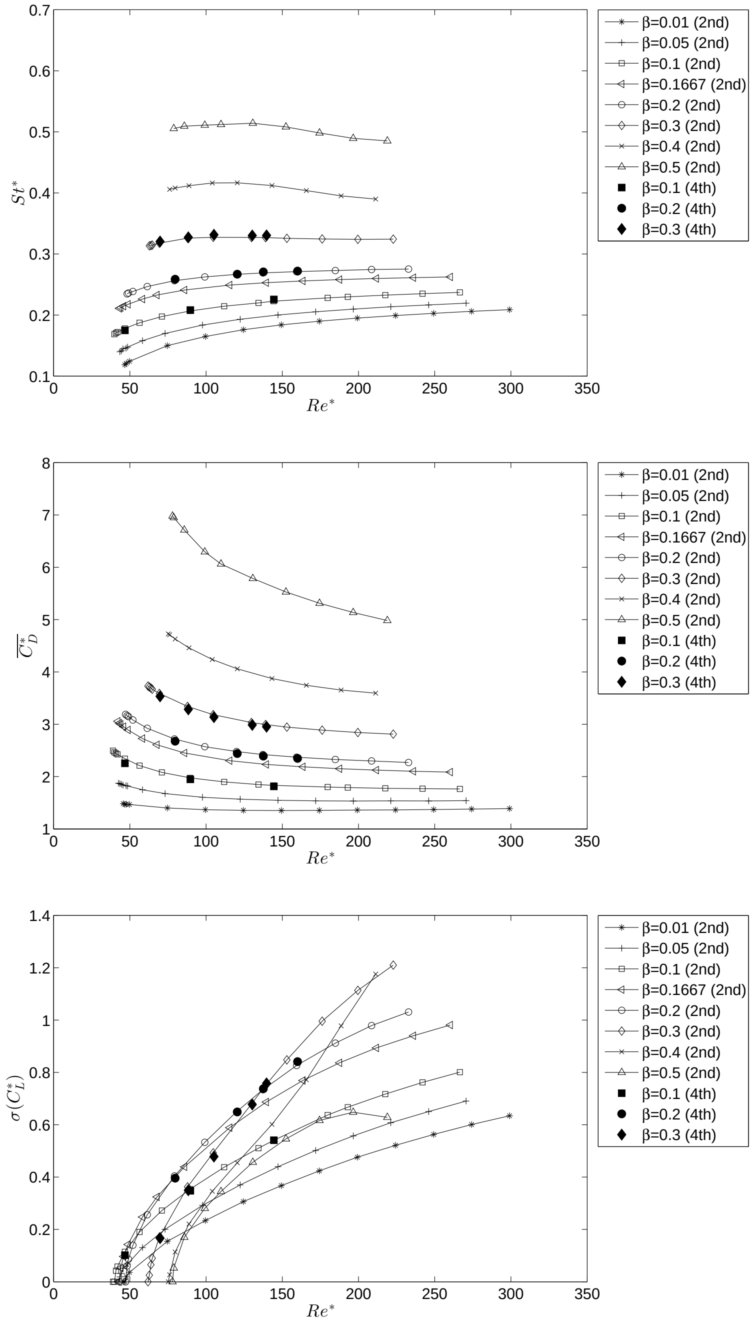

Figure 3.24: SD solutions of flow past a stationary circular cylinder at different blockages: St^*, $\overline{C_D^*}$, $\sigma(C_L^*)$.

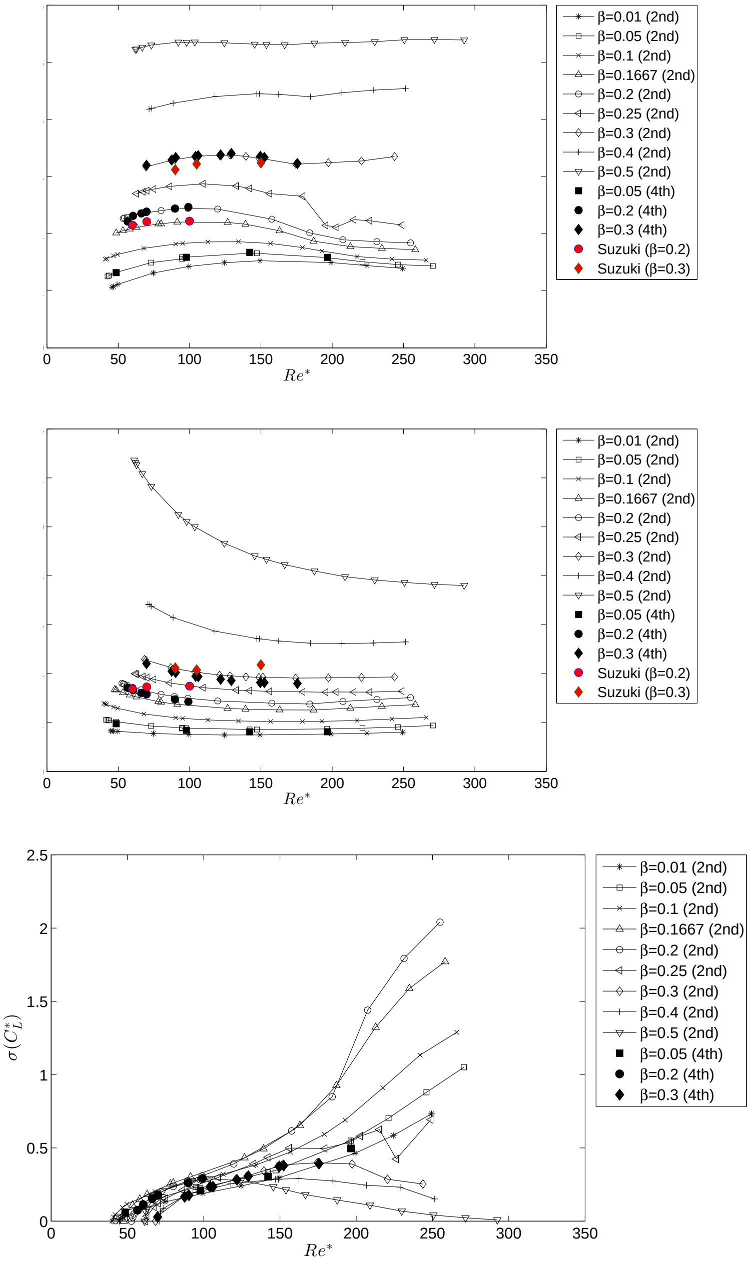

Figure 3.25: SD solutions of flow past a stationary square cylinder at different blockages: St^*, $\overline{C_D^*}$, $\sigma(C_L^*)$.

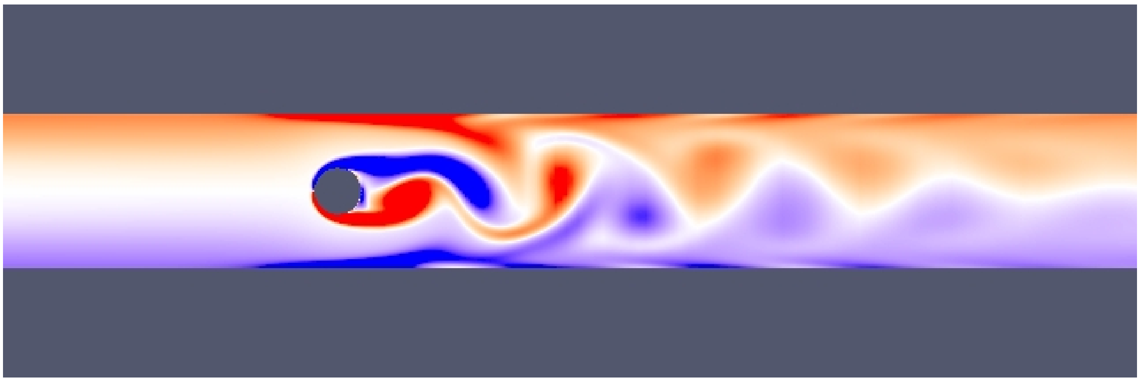

(a) $\beta = 0.3, Re_d = 181$, Circular cylinder

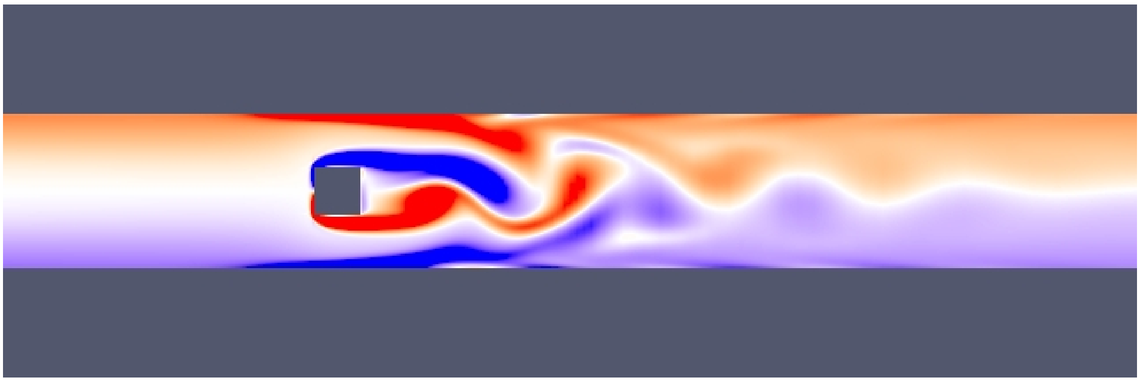

(b) $\beta = 0.3, Re_d = 180$, Square cylinder

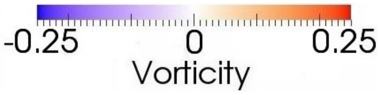

Figure 3.26: “Crisscross” motion of vortices: instantaneous vorticity.

Chapter 4

Splitter plate interference

4.1 Introduction

The use of splitter plates to control vortex formation in cylinder wakes is not a new concept. Roshko, in his 1954 NACA report [3], experimented with vortex suppression by placing a thin splitter plate at various separation distances along the mean zero streamline downstream of the circular cylinder base in order to interfere with its natural shedding at $Re = 14,500$. The wake interference caused the alteration of the suction base pressure coefficient, C_{pb}, and the Strouhal number, St, depending on the separation distance between the splitter plate and the circular body. Roshko reported less variation of the pressure distribution over the cylinder circumference in the presence of a splitter plate, which would mean attenuated flow induced vibrations (FIV). Roshko also noted that the mean drag coefficient, $\overline{C_D}$ was reduced from 1.15 to 0.72 in one of the splitter plate configurations. Thus, it can be further postulated from this report that splitter plate deployment, in addition to inhibiting vortex shedding instability, produces a streamlining effect on the flow past a bluff body.

Following the work of Roshko, Apelt *et al.* [87] investigated flows past circular cylinders with splitter plates attached to a circular cylinder in the Re range of 10^4 to 5×10^4. They found that at any ratio of the splitter plate length, l, to the cylinder diameter, d, or l/d, between 0 and 7, the flow characteristics past the cylinder can be altered, as evident from the variation seen on the Strouhal numbers, C_D and C_{pb}.

They concluded that the effectiveness of a splitter plate depends significantly on the length (l) of the plate. At $l/d > 5$, they observed that the drag component becomes constant and the unsteady vortex shedding is eliminated from the cylinder body even though they noted that the existence of a vortex street further downstream of the splitter plate.

Unal and Rockwell [7] experimented with the insertion of a long and thick plate with a sharp, wedge-like leading edge in the wake of a cylinder to control the development of wake instabilities in the Reynolds number range of $140 < Re < 3,600$. The plate is relatively thick (of the order of d) and its length is much greater than d, i.e. $l/d = 24$. Note that Unal and Rockwell used circular cylinders of various diameters to cover the range of Reynolds number in their study. Depending on the separation distance from the cylinder, l_s, a splitter plate can break the wake flow characteristics into two basic regimes: 1) pre-vortex formation and 2) post-vortex formation. Unal and Rockwell reported that at a relatively low Reynolds number, the unsteady von Kármán vortex street can be eliminated with a thick splitter plate at a separation distance of $l_{sc} = 2.8 \cdot d$ for $Re = 142$. Note that l_{sc} is the location of the splitter plate from the center of the circular cylinder as defined by Unal & Rockwell. As such, $l_{sc} = 2.8 \cdot d$, $3.2 \cdot d$, $5.2 \cdot d$ and $6.5 \cdot d$ would correspond to the current convention of $l_s = 2.3 \cdot d$, $2.7 \cdot d$, $4.7 \cdot d$ and $6.0 \cdot d$ respectively.

As an exercise for verification, it is found that the current numerical results are in good agreement with Unal and Rockwell's experimental results. It is assumed that the splitter plate thickness is $1 \cdot d$ and the leading edge length is $2 \cdot d$ for simulation purpose. Also, the cylinder body and the splitter plate are placed far enough from the top and bottom boundaries to be considered an unbounded flow condition. As shown on figure 4.1, the vortex shedding from a circular cylinder with the splitter plate at the separation distance of $l_{sc} = 2.8 \cdot d$ is found to be steady and symmetric along the mean center line and is thus classified as pre-vortex formation regime. At $l_{sc} \geqslant 3.2 \cdot d$, the vortex wakes become unsteady and the splitter plate is no longer effective in controlling the oscillation. Quantitatively, the Strouhal numbers obtained from the present numerical simulations (table 4.1) also compare well with the experimental results published by Unal and Rockwell. Numerical results for flow past a cylinder

l_{sc}	C_L	C_D	St	$\overline{C_{pb}}$
$2.8 \cdot d$	0.000 ± 0.000	0.946 ± 0.000	–	-0.31
$3.2 \cdot d$	0.000 ± 0.605	1.164 ± 0.036	0.150	-0.59
$5.2 \cdot d$	0.000 ± 0.436	1.200 ± 0.022	0.162	-0.62
$6.5 \cdot d$	0.000 ± 0.461	1.223 ± 0.020	0.167	-0.64
No splitter plate	0.000 ± 0.468	1.326 ± 0.021	0.180	-0.79

Table 4.1: Numerical results for flow past a circular cylinder with thick splitter plate used by Unal and Rockwell, $Re = 142$.

without a splitter plate are also provided for reference.

The simulations verify that if a thick and long splitter plate is properly placed, it is possible to disrupt the vortex formation. The splitter plate interference can either completely annihilate the instabilities of the vortex wakes (i.e. $2.8 \cdot d$) or, on the other hand, worsen the fluctuating lift and drag components (i.e. $3.2 \cdot d$), depending on the separation distance to the circular cylinder body.

In 2003, Mittal [88] suggested the use of a long detached splitter plate for control of vortex suppression. He found that in an unbounded flow at $Re = 100$, a splitter plate which has the length of $2 \cdot d$ or greater can completely suppress the fluctuating lift and drag components when placed at a separation distance of $l_{sc} = 2.68 \cdot d$. Some noticeable amount of fluctuating forces can also be achieved when the splitter plate length, l, is shorter than $2 \cdot d$. It was also found that when a splitter plate is placed at a separation distance of $l_{sc} > 2.68 \cdot d$, fluctuating forces can be worse than the case without splitter plate.

The question arises if it is possible to suppress the unsteadiness by a thin (i.e. $l_t < 0.1 \cdot d$) and short splitter plate (i.e. $l \leqslant 1 \cdot d$). In some real engineering applications, it can be impractical to have a controlling device such as a splitter plate several times longer than the cylinder body itself. Furthermore, how effective would a splitter plate be in a bounded flow? Several of the previous researches used a splitter plate that is attached to the bluff body. In order to minimize FIV on the bluff body itself, it is important that the splitter plate be physically separated from the bluff body. Attaching the splitter plate would directly connect its aerodynamic forces to the bluff

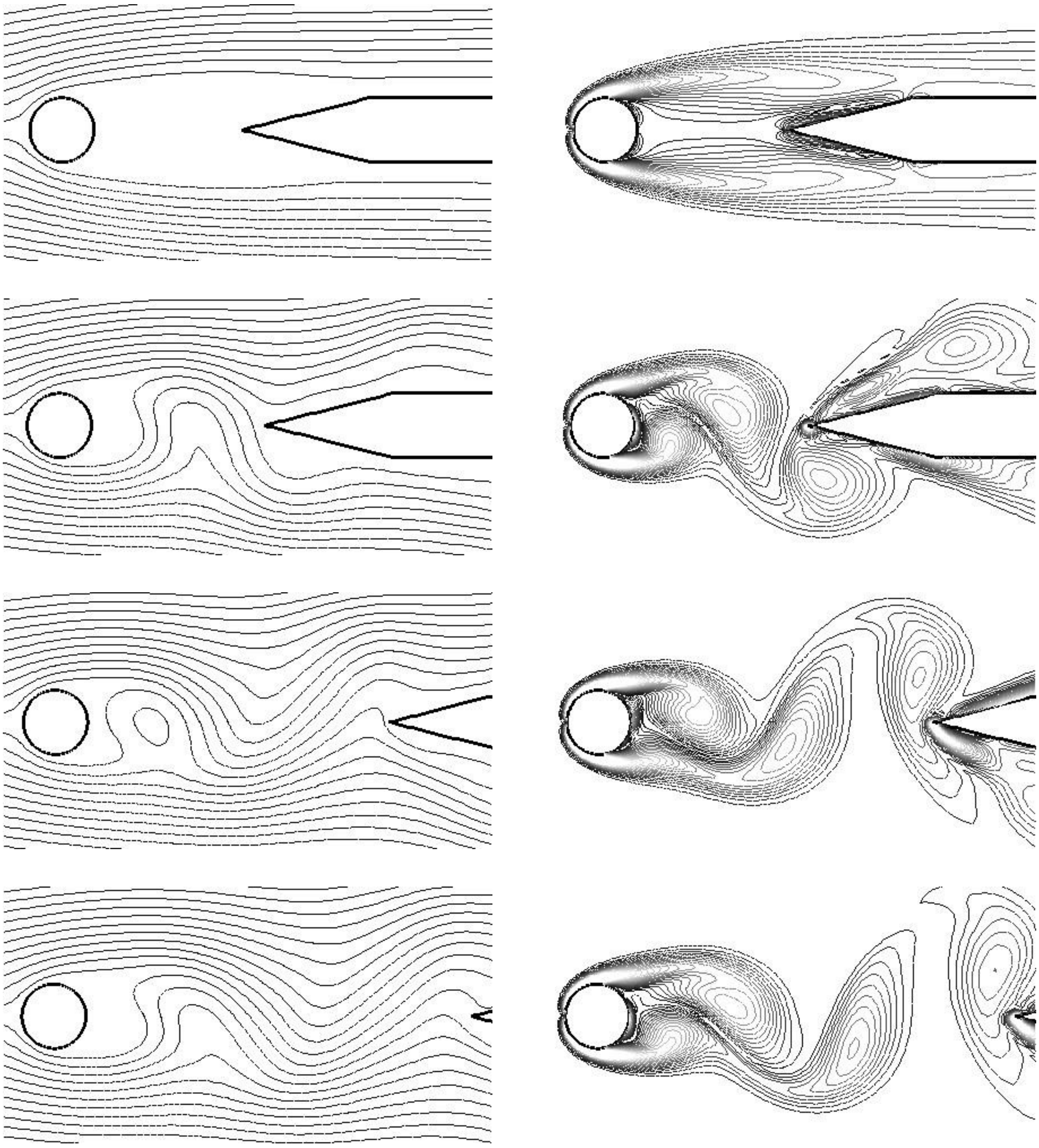

Figure 4.1: Numerical simulation of experimental results obtained by Unal and Rockwell. Left: instantaneous streamlines. Right: instantaneous iso-vorticity contour. First row, $l_{sc} = 2.8 \cdot d$; second row, $l_{sc} = 3.2 \cdot d$; third row, $l_{sc} = 5.2 \cdot d$; fourth row, $l_{sc} = 6.5 \cdot d$.

body. By detaching the splitter plate, any fluctuating forces acting on the splitter plate will not be directly coupled into the bluff body. This would allow the maximum attenuation of fluctuating forces on the bluff body. Hence, the present research work is focused on configurations with a detached splitter plate.

In this research, the following parameters used for splitter plate positioning is illustrated in figure 4.2, where

- $l \equiv$ the splitter plate length
- $l_t \equiv$ the splitter plate thickness
- $l_s \equiv$ the separation distance between bluff body and splitter plate

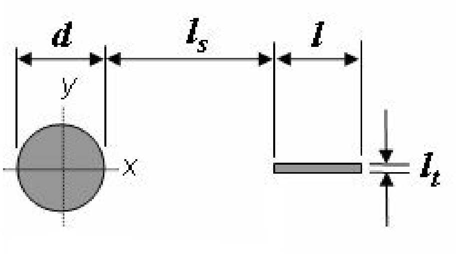

Figure 4.2: Configuration of a splitter plate downstream of a bluff body.

For convenience, a superscript “∗” is used to indicate the normalized values of these parameters with d:

- $l^* = \dfrac{l}{d}$
- $l_t^* = \dfrac{l_t}{d}$
- $l_s^* = \dfrac{l_s}{d}$

4.2 Splitter plate effect in an unbounded flow

4.2.1 Comparison between circular and square cylinders

This section compares the effect of a thin splitter plate ($l_t^* = 0.125$) downstream on cylinders of circular and square shape in an unbounded flow at $Re = 150$. The length of the splitter plate used in this comparison is $1 \cdot d$. From figure 4.3, it can be seen that the thin splitter plate does not completely suppress vortex shedding. However, it can be used to attenuate the force fluctuations on the bluff body by positioning it at a proper distance downstream of the bluff body. For the circular cylinder, the effective attenuation range is $0 < l_s^* \leqslant 2$. Due to the nature of the difference in shedding characteristics, the location where the first vortex lobe is formed in the wakes of the square cylinder is further downstream as compared to that of the circular cylinder. As a result, the attenuation range is extended to $0 < l_s^* \leqslant 2.5$ for the square cylinder. Figure 4.4 illustrates the flow patterns for circular and square cylinder for several locations of the splitter plate.

It can also be seen that if the separation distance is greater than the attenuation range, the splitter plate can amplify the force fluctuations beyond the value of the case without any splitter plate downstream as shown in table 4.2. For example, the standard deviation of lift for the flow past a circular cylinder without splitter plate is 0.3602. If the splitter plate is placed slightly downstream past the effective range, say at $l_s^* = 2.05$, the standard deviation of lift is increased to 0.4222 thereby defeating its purpose of force attenuation. The splitter plate would have to move much further downstream (i.e. $l_s^* \gtrsim 4$) before the wake interference that amplifies the force fluctuations would subside.

4.2.2 Effect of splitter plate length

This section examines the effect of varying the splitter plate length and the separation distance from the circular cylinder body in an unbounded flow condition at $Re = 125$. In studying the separation distance, the computational grids are re-meshed and adjusted so the physical representation is not lost. ESI CFD-ACE+ is used in this

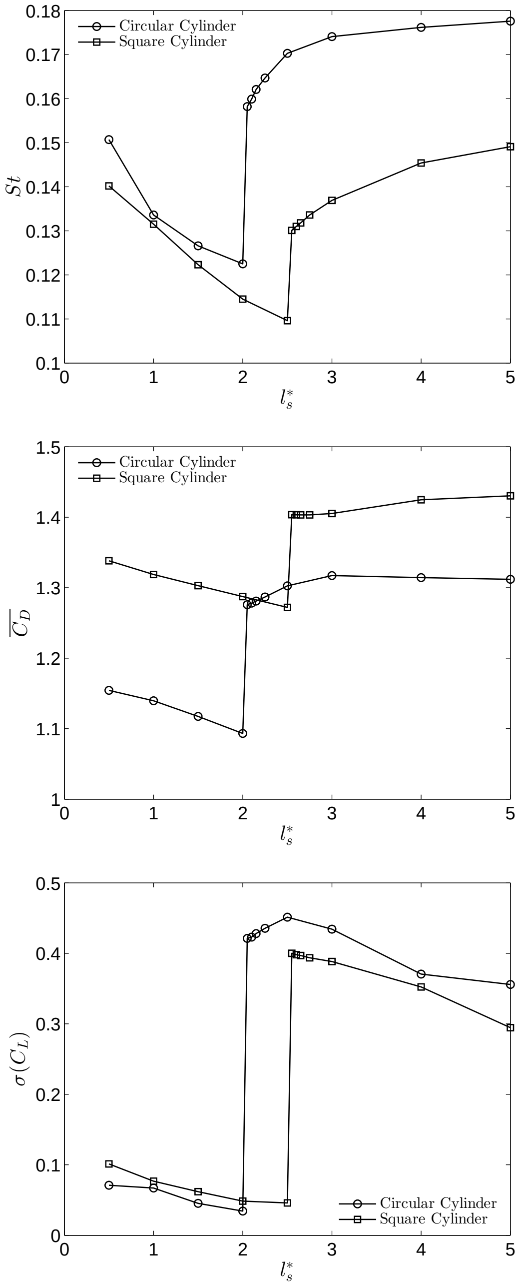

Figure 4.3: Unbounded flow past circular and square cylinders with splitter plate, $l^* = 1$, $l_t^* = 0.125$, $Re = 150$: Strouhal number (top), mean drag coefficient (middle), standard deviation of lift coefficient (bottom).

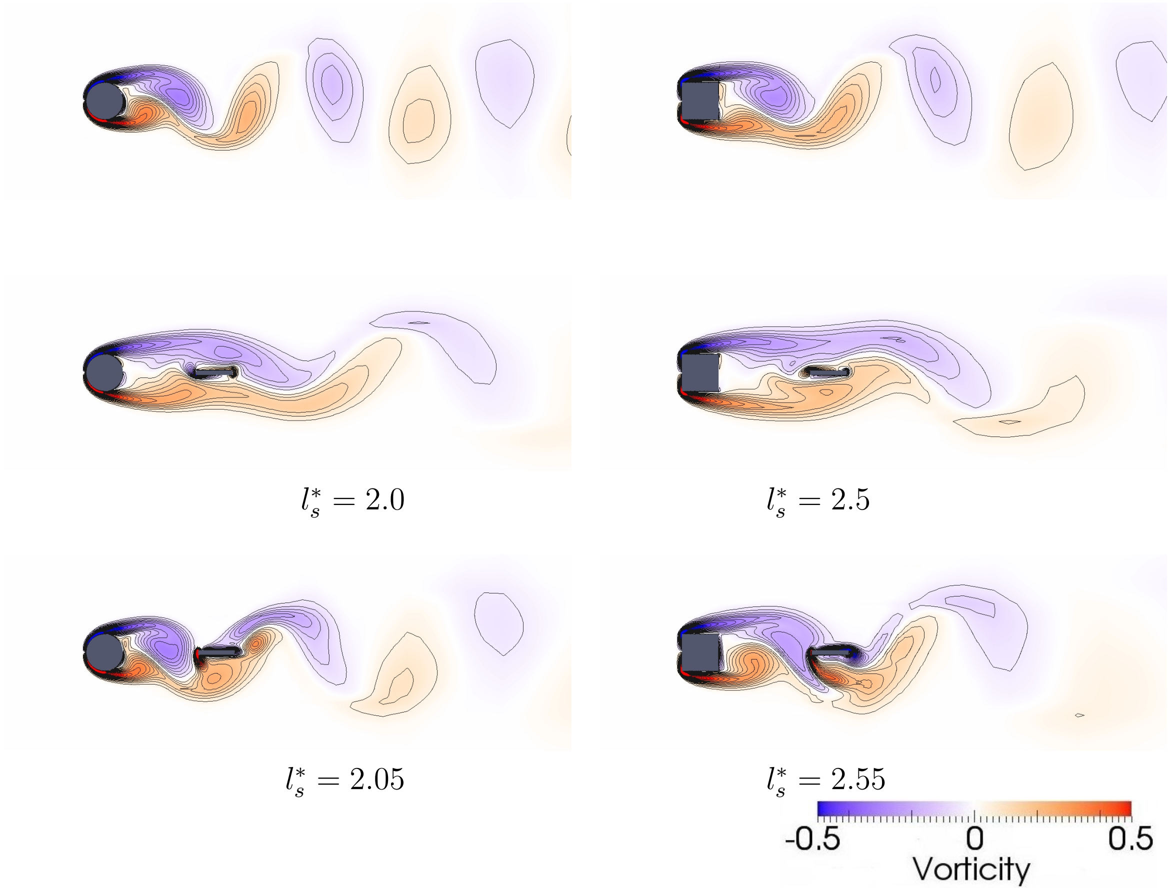

$l_s^* = 2.0$ $l_s^* = 2.5$

$l_s^* = 2.05$ $l_s^* = 2.55$

Figure 4.4: Instantaneous iso-vorticity contour showing the effectiveness of splitter plate ($l^* = 1$, $l_t^* = 0.125$) on flow past a circular cylinder (left column) and a square cylinder (right column), unbounded, $Re = 150$: no splitter plate (top); effective separation (middle); ineffective separation (bottom).

Circular cylinder

l_s^*	St	$\overline{C_D}$	$\sigma(C_L)$
No splitter plate	0.1816	1.3572	0.3602
2	0.1227	1.0975	0.0344
2.05	0.1583	1.2785	0.4222
5	0.1778	1.3145	0.3565

Square cylinder

l_s^*	St	$\overline{C_D}$	$\sigma(C_L)$
No splitter plate	0.1526	1.4988	0.2963
2.5	0.1097	1.2747	0.0460
2.55	0.1302	1.4065	0.4009
5	0.1494	1.4361	0.2957

Table 4.2: Tabulated numerical results: unbounded flow past circular and square cylinders with and without splitter plate ($l_t^* = 0.125$, $l^* = 1.0$) at $Re = 150$.

study because it offers the ease of adjusting the mesh to the separation distance. It is clear from the Strouhal plot on figure 4.5 that a splitter plate that is placed downstream of the cylinder body can interfere with the development of vortex wakes. The degree of effectiveness in vortex and FIV suppression depends largely on the splitter plate length and the separation distance. Sharp transition points at separation distances between 1.65 to 1.85 can be seen for all plate lengths ranging from 0.25 to 1. This also corresponds to the same point, where the sudden change in lift fluctuation and mean drag are observed. From these figures, it can be determined what the optimal separation distance is for a given splitter plate length. This is generally just before the transition to strong fluctuations. For example, the optimal separation distance for a splitter plate of length 1 is 1.8. The same effect on drag fluctuation can also seen. In contrast to the study by Unal and Rockwell [7], this type of thin splitter plate does not completely suppress the unsteadiness in the vortex wakes in unbounded flows. However, some reduction in vortex induced force fluctuations can still be realized when a splitter plate is placed at a proper distance downstream of the circular cylinder. In agreement with past researches, one of the most beneficial qualities of splitter plate interference in an unbounded flow, however, is the fact that there is a reduction in mean drag all across the various configurations. The benefit is greatly enhanced, again by the proper placement of the splitter plate. A thin splitter plate in an unbounded flow can therefore be a very effective streamlining device.

Thus, the relative placement between the circular cylinder body and the splitter plate is extremely critical. In a real world application, for example, there would be a drastic difference if the splitter plate were to be placed slightly behind the critical distance due to positioning tolerance.

Figure 4.6 illustrates the flow for the optimal separation distance of 1.8, which allows the $l^* = 1$ long splitter plate to break down incoming vortices, while a very similar vorticity contour is observed when the same splitter plate is moved slightly closer to a separation distance of 1.5. This is seen as an effective mechanism of decoupling the induction of force oscillations to the main body. On the other hand, by allowing a slight increase in separation distance, i.e. $l_s^* = 1.9$, an independent vortex lobe appears in the wakes. It is important to note also that when the splitter plate is placed further downstream of the optimal distance, it increases the amplitude of lift oscillation to a degree higher than the baseline without a splitter plate. The reason is partially due the upstream wake effects of the splitter plate that adversely interferes with the circular cylinder wakes. Such a placement of splitter plate allows the first independent vortex lobe to develop and in the meantime impedes its natural downstream motion. As the splitter plate is moved further away, the separation distance provides an area where vortex shedding can be locally intensified and the development of the first independent vortex lobe can even be enhanced by merging with the front vortex that rolls off from the leading edge of the splitter plate. As a result, it exacerbates the vortex-induced forces on the circular cylinder body. As the splitter plate gets shorter, the mechanism of breaking down an independent vortex lobe becomes less effective as the lobe itself is allowed to form by rolling around the splitter plate. While figure 4.6 shows an effective lobe break down using $l^* = 1$ long splitter plate at $l_s^* = 1.8$, figure 4.7 illustrates what happens to the vortex motion when the splitter plate length is shortened. This example shows the vorticity contour of the flow past

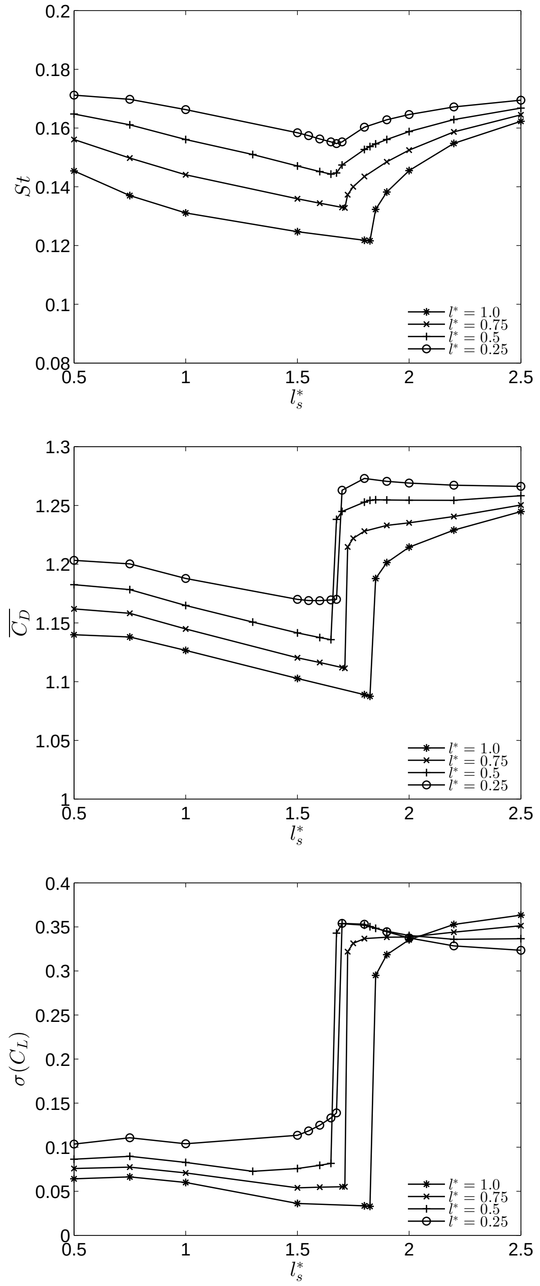

Figure 4.5: Flow past a circular cylinder with splitter plate, unbounded, $Re = 125$: Strouhal number (top), mean drag coefficient (middle), standard deviation of lift coefficient (bottom).

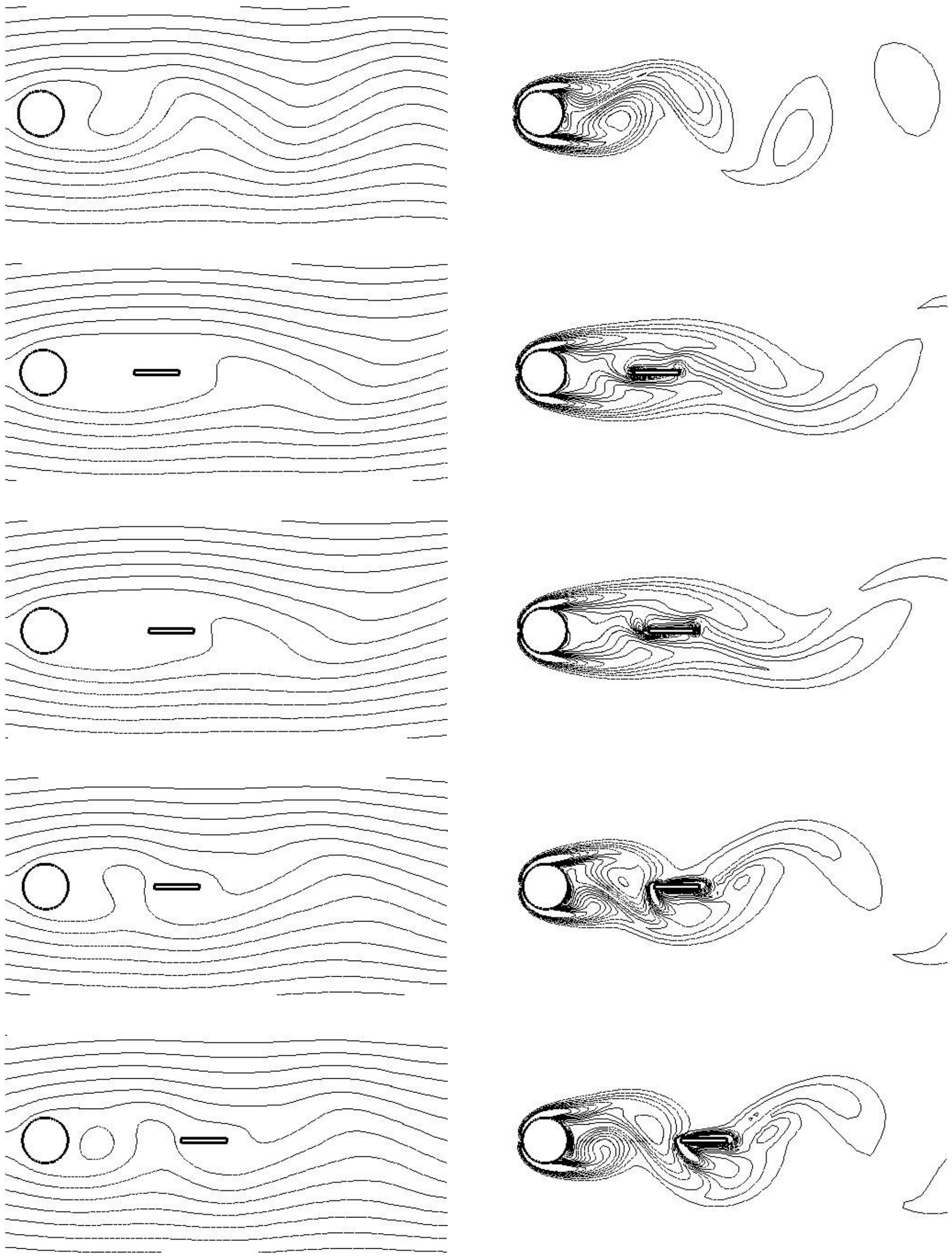

Figure 4.6: Numerical simulation of flow past a circular with a downstream splitter plate ($l^* = 1.0$) in an unbounded flow, $Re = 125$. Left: instantaneous streamlines. Right: instantaneous iso-vorticity contour. First row, no splitter plate; second row, $l_s^* = 1.5$; third row, $l_s^* = 1.8$; fourth row, $l_s^* = 1.9$; fifth row, $l_s^* = 2.5$.

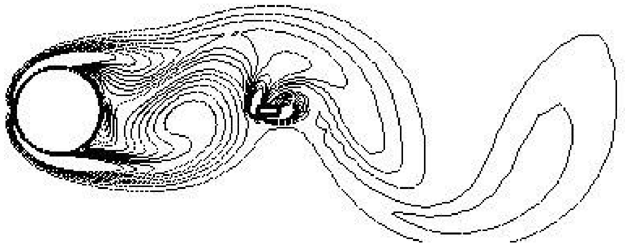

Figure 4.7: Instantaneous iso-vorticity contour of flow past a circular with a short ($l^* = 0.25$) splitter plate placed at $l_s^* = 1.8$ downstream in an unbounded flow, $Re = 125$.

circular cylinder with $l^* = 0.25$ long splitter plate, which is the shortest length used in the current study. The rolling motion allows an alternating vortex lobe to spread out in the cross plane direction, but each lobe has the chance of interacting with its counter-rotating pair effectively in a wider area. The phenomenon thus seems to further worsen the pressure instability surrounding the body and ultimately increase the lift oscillation amplitude. With the exception of the oscillation components of lift and drag, it can be seen that as the splitter plate length becomes very short, St and $\overline{C_D}$ also approach the value obtained from the baseline of flow without splitter plate.

The numerical experiments establish that the effectiveness in controlling force fluctuations depends largely on the proper combination of splitter plate length and separation distance. The optimal separation distance that was obtained is the distance which yields the lowest fluctuation amplitudes, e.g. $l_s^* = 1.8$ for $l^* = 1$ long splitter plate. The current set of data suggests that if a thin and short splitter plate is placed such that the separation distance is larger than 0 but less than the optimal distance, some noticeable amount of suppression can still be realized. On the other hand, having a splitter plate of an arbitrary length at a separation distance that is more than the optimal can exacerbate both lift and drag oscillations.

4.3 Splitter plate effect in a confined channel

4.3.1 Fully developed Poiseuille flow for $0 < \beta \leqslant 0.5$ at $Re^* = 150$

In this section, the effects of a splitter plate on the flow past circular and square cylinders in a confined channel are examined by SD simulation. Both upper and lower boundaries are stationary and the flow is allowed to fully develop upstream of the cylinder. It is shown that unsteady vortex shedding can be completely suppressed with a properly positioned splitter plate. The computational domain is constructed by modifying the mesh geometry used in the study of blockage effect in chapter 3. The splitter plate used in this study has a length of $l^* = 1$ and a thickness of $l_t^* = 0.125$. The simulation is performed at the same Reynolds number $Re^* = 150$ for $\beta = 0.01$, 0.1, 0.3 and 0.5. Note that the data set for $\beta = 0.01$ is taken from Section 4.2.1 on unbounded flow.

Figures 4.8 and 4.9 shows the effect of splitter plate in a flow with various blockages for circular cylinder and square cylinder respectively. Consistent with the data shown in chapter 3, increasing the blockage factor essentially produces higher values of St^* and $\overline{C_D^*}$. However, as the blockage factor increases, the standard deviation value of C_L^* increases up to a certain point and then decreases. The decrease in $\sigma(C_L^*)$ indicates that the upper and lower boundaries help stabilizing the flow by reducing wake instabilities.

It can be seen from figure 4.8 that for a thin splitter plate of length $l^* = 1$, the effective region of suppressing or attenuating vortex wakes off a circular cylinder is in the range of $0 < l_s^* \leqslant 2$. This fact is determined from the lower values of $\sigma(C_L^*)$ as compared to when the splitter plate is positioned outside of this zone. At a higher blockage, the splitter plate can produce complete vortex wake suppression when it is positioned at $1.3 \leqslant l_s^* \leqslant 2$ for $\beta = 0.3$ and $0 < l_s^* \leqslant 2$ for $\beta = 0.5$. A slight decrease in mean drag coefficient is also observed in the effective region. At $l_s^* > 2$, the splitter plate does not inhibit the vortex formation and thus loses its effectiveness. For $\beta = 0.3$, figure 4.10 illustrates the 3 effective regions: 1) partial wake attenuation,

2) complete vortex suppression and 3) ineffective region.

Similar characteristics are observed when this splitter plate is positioned downstream of a square cylinder as shown in figure 4.9. The effective region for a square cylinder is in the range of $0 < l_s^* \leqslant 2.5$. The complete suppression is observed at $1.25 \leqslant l_s^* \leqslant 2.5$ for $\beta = 0.3$ and $1 \leqslant l_s^* \leqslant 2.5$ for $\beta = 0.5$. At $l_s^* > 2.5$, the splitter plate becomes ineffective in attenuating unsteady wakes. Figure 4.11 illustrates the 3 effective regions for $\beta = 0.3$.

4.3.2 Plug flow versus Poiseuille flow

The present research work is particularly motivated by the need to find ways of reducing FIV of the read-write arm of a hard disk drive, which lies between the upper and lower surfaces of two disks in a multiple-platter configuration. Accordingly it is important to address the issue of how effective a detached splitter plate can be in suppressing unsteady vortex shedding behind a cylinder in a channel. One way to represent that flow condition is to set the upper and lower boundaries in the computational model to be moving at the same velocity as the inlet. These boundary condition settings effectively force the flow to have a uniform velocity profile as shown in figure 4.12. This is also known as a plug flow model which can simply be regarded as an idealized disk drive flow. On the other hand, if the upper and lower boundaries are set to be stationary and the bluff body is set far enough from the inlet, the flow velocity will fully develop into a parabolic profile as shown in figure 4.13.

Plug flow

The presence of moving walls on the upper and lower bounds at U_0 can have a significant effect on the vortex wakes of the cylinder. In this section, the effects of a splitter plate in both plug flow and Poiseuille flow at the same effective Reynolds number is examined for comparison. The same splitter plate ($l^* = 1$, $l_t^* = 0.1$) is positioned downstream of a circular cylinder at the same $Re^* = 125$ with $\beta = 0.5$. As shown in figure 4.14, the total vortex suppression region for $Re^* = 125$ is in the range of $1.125 \leqslant l_s^* \leqslant 1.714$. Figure 4.15 illustrates some examples of streamlines

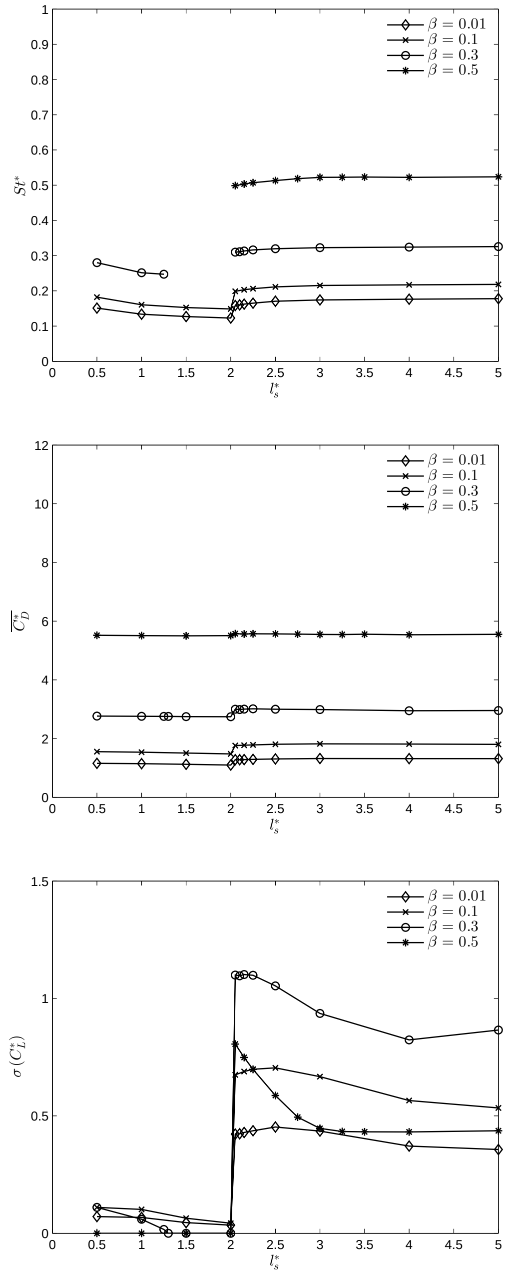

Figure 4.8: The effect of blockage on flow past a *circular* cylinder with splitter plate, $l^* = 1$, $l_t^* = 0.125$, $Re^* = 150$: St^* (top), mean C_D^* (middle), standard deviation of C_L^* (bottom).

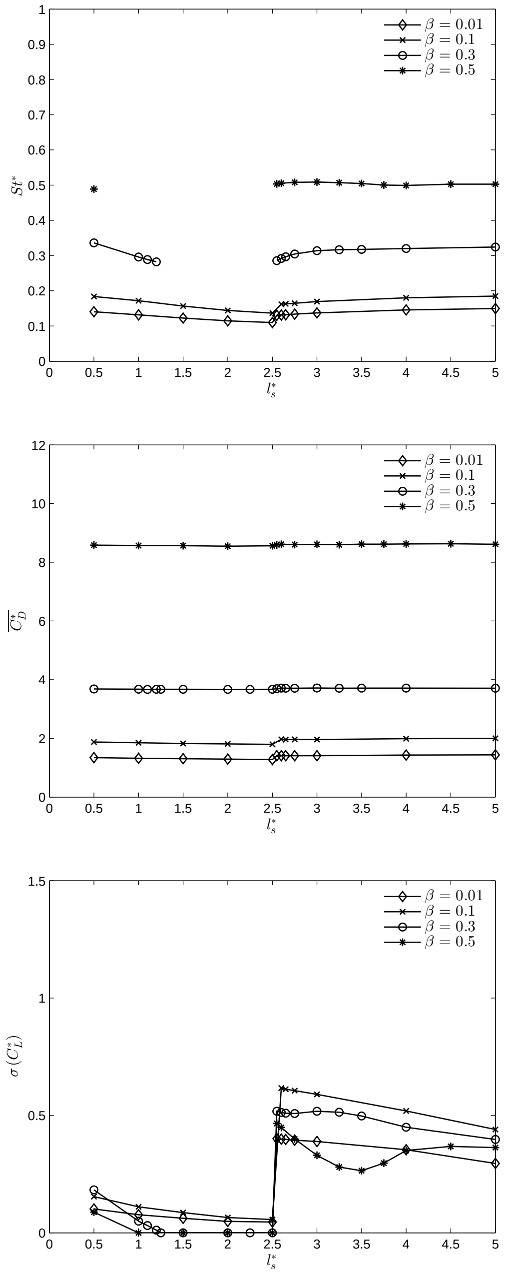

Figure 4.9: The effect of blockage on flow past a *square* cylinder with splitter plate, $l^* = 1$, $l_t^* = 0.125$, $Re^* = 150$: Strouhal number (top), mean drag coefficient (middle), standard deviation of lift coefficient (bottom).

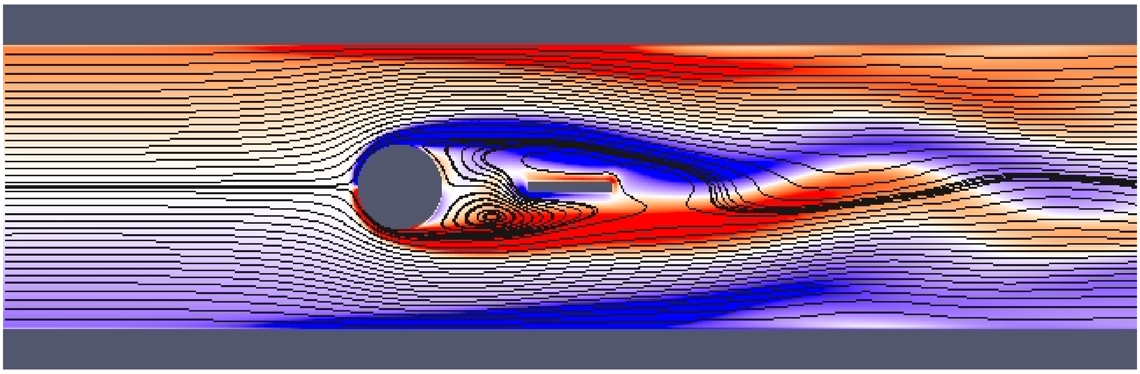

(a) Partial wake attenuation: $l_s^* = 1$; $\sigma(C_L^*) = 0.0597$

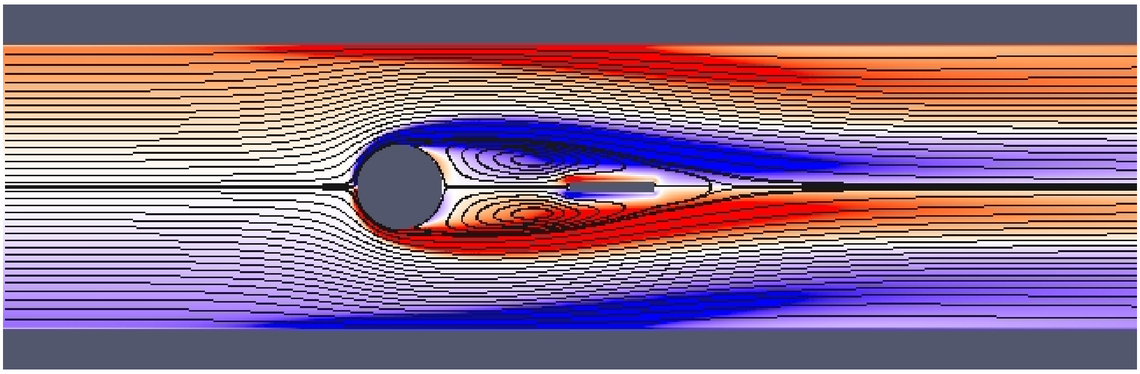

(b) Complete vortex suppresion: $l_s^* = 1.5$; $\sigma(C_L^*) = 0$

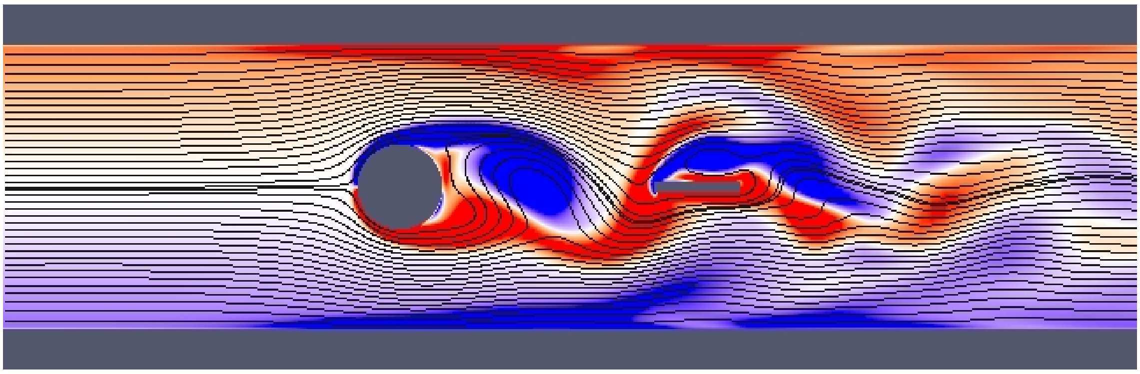

(c) Ineffective separation: $l_s^* = 2.5$; $\sigma(C_L^*) = 1.0534$

Figure 4.10: Overlay of instantaneous vorticity and streamlines: flow past a *circular* cylinder with splitter plate, $l^* = 1$, $l_t^* = 0.125$, $\beta = 0.3$, $Re^* = 150$.

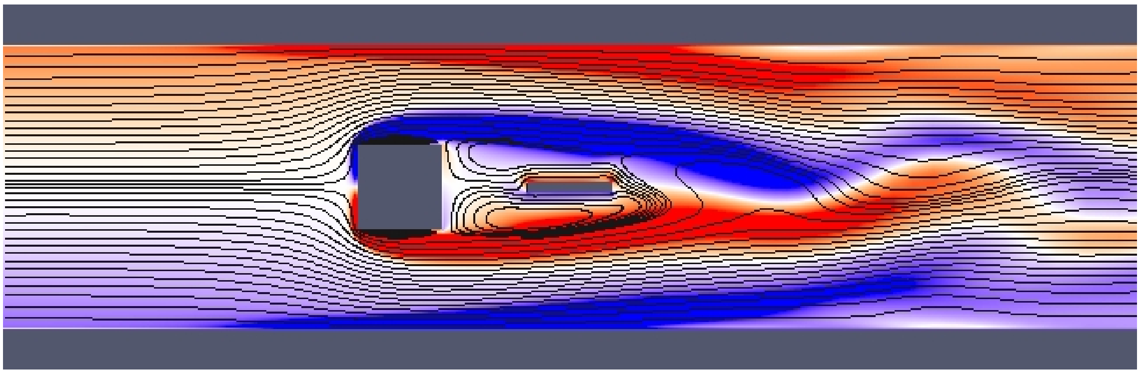

(a) Partial wake attenuation: $l_s^* = 1$; $\sigma(C_L^*) = 0.0493$

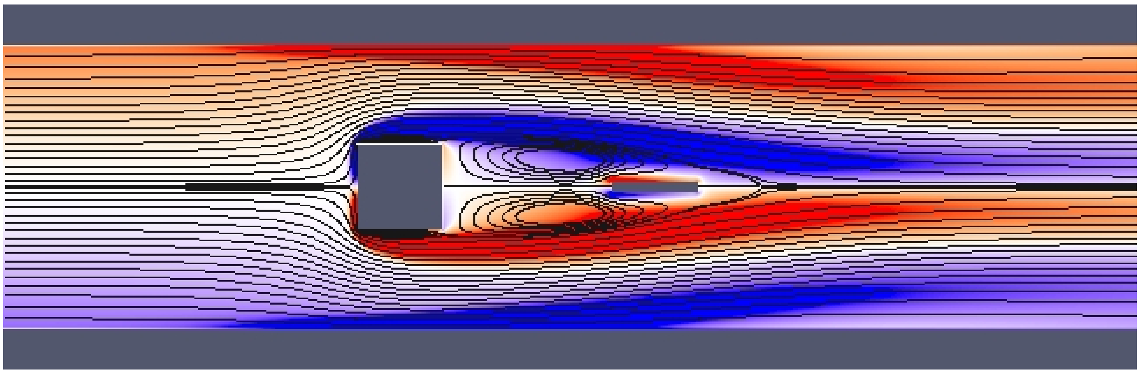

(b) Complete vortex suppresion: $l_s^* = 2$; $\sigma(C_L^*) = 0$

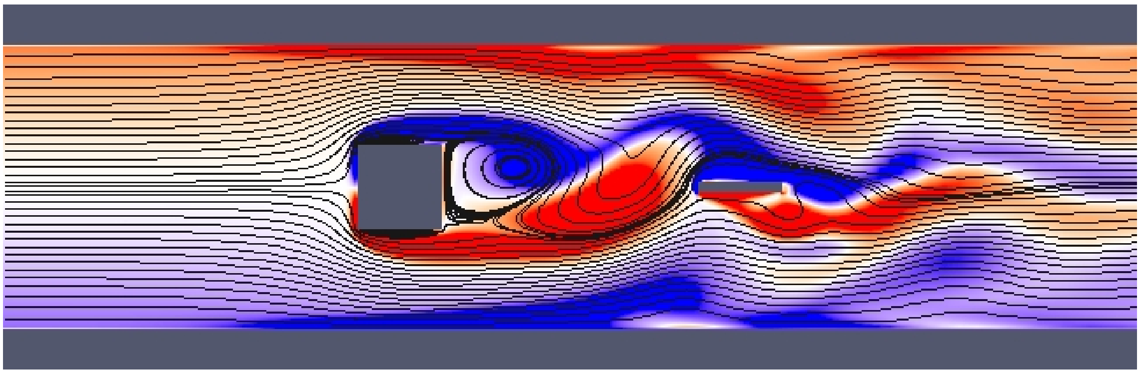

(c) Ineffective separation: $l_s^* = 3$; $\sigma(C_L^*) = 0.5179$

Figure 4.11: Overlay of instantaneous vorticity and streamlines: flow past a *square* cylinder with splitter plate, $l^* = 1$, $l_t^* = 0.125$, $\beta = 0.3$, $Re^* = 150$.

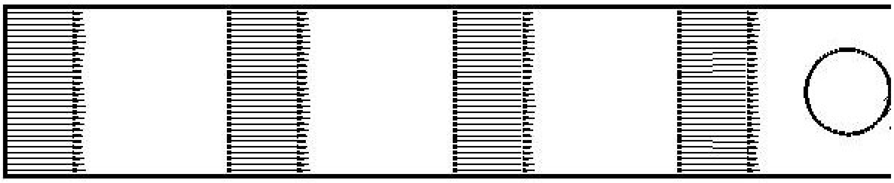

Figure 4.12: Incoming velocity profile of plug flow.

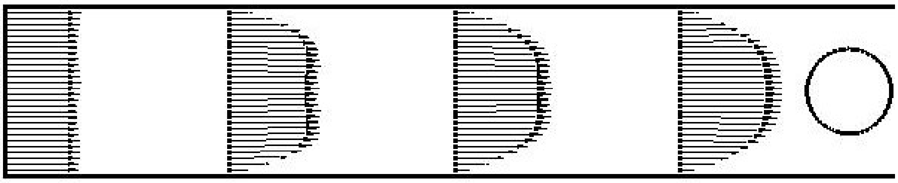

Figure 4.13: Incoming velocity profile of Poiseuille flow.

and vorticity contour of the three regions of effectiveness: 1) semi-effective (b), 2) effective (c & d) and 3) ineffective (e & f).

In the ineffective range of separation distance the vortex wakes can actually be intensified and all the fluctuating forces are correspondingly exacerbated. For example, in the effective region of the moving wall case, the peak-to-peak value of C_L^* of circular cylinder without splitter plate presence at $Re^* = 125$ is 0.74. If the splitter plate is improperly placed at say, $l_s^* = 2$, the peak-to-peak value of C_L^* increases to as much as 0.87. Similar behavior is observed in the ineffective region of the stationary wall case where a splitter plate is improperly placed at, $l_s^* = 2$, the peak-to-peak value of C_L^* is exacerbated to a value of 0.34 as compared to 0.21 when the splitter plate is absent.

While the splitter plate can completely suppress drag and lift oscillations in a bounded flow, the reduction of mean drag is less than that obtained in an unbounded flow. In fact, in the ineffective range of separation distance, the mean drag actually increases slightly. This can be attributed to the fact that the shear layers between the circular cylinder and the walls do not vary much in all of the simulated configurations.

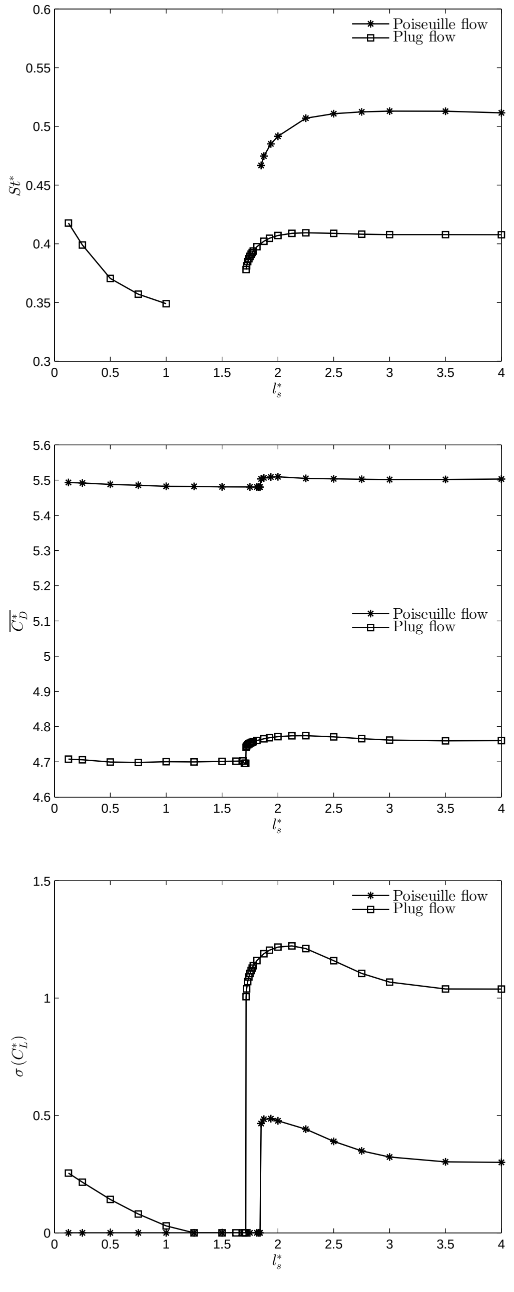

Figure 4.14: Comparison between plug flow and Poiseuille flow ($\beta = 0.5$) past a circular cylinder with splitter plate, $l^* = 1$, $l_t^* = 0.1$, $Re^* = 125$: Strouhal number (top), mean drag coefficient (middle), standard deviation of lift coefficient (bottom).

This can easily be seen in and that in the immediate area adjacent to the cylinder body for the most part, the vorticity contour reveals a remarkably similar profile in all of the configurations including the baseline and those with splitter plate of any length and separation.

Poiseuille flow

In the Poiseuille flow case (stationary upper and lower boundaries), the critical separation distance is approximately 1.845. In contrast to the plug flow condition, the effective suppression distance of the splitter plate in extends all the way inwards to the cylinder body. There appears to be only 2 categories of suppression (figure 4.14):

1. Effective: $0 < l_s^* \leqslant 1.845$
2. Ineffective: $l_s^* > 1.845$.

Figure 4.16 illustrates some examples of streamlines and vorticity contour of these two regions of effectiveness: 1) effective ($0 \leqslant l_s^* \leqslant 1.84$) and 2) ineffective ($l_s^* \geqslant 1.85$). Apart from the absence of a semi-effective range of separation distance, the stationary wall case shows similarities in the behavior and effectiveness of splitter plate to the flow and FIV, although the magnitudes of the both mean and fluctuating components are quite different. In the effective range, both cases exhibit the ability of a splitter plate to completely suppress the unsteadiness of the flow, while in the ineffective range the unsteady forces can actually be exacerbated.

4.3.3 Effects of splitter plate length in a plug flow

Using $\beta = 0.5$ as a test case, the effects of a splitter plate length in plug flow at $Re^* = 75$ are examined. The calculated Strouhal number for a cylinder without a splitter plate is approximately 0.421. As shown in figures 4.17 and 4.18, it appears that in the bounded flow case, the primary factor that is responsible for suppressing the force oscillations is the separation distance alone. The effect from the length of a splitter plate appears to be minimal. Obviously, there appears to be a critical separation distance of approximately 2.547 for all splitter plate lengths. Inside this

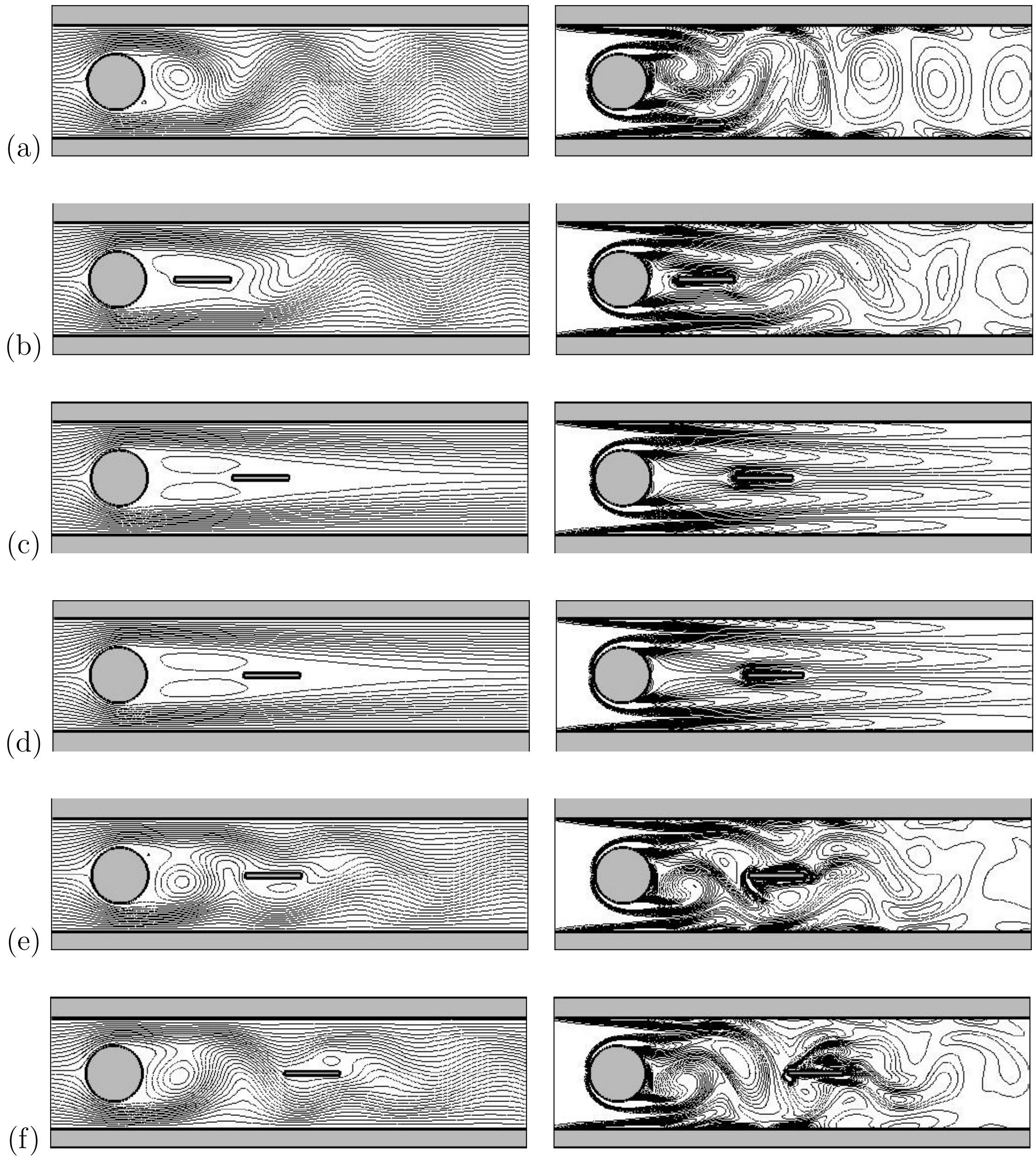

Figure 4.15: Numerical simulation of flow past a circular with a downstream splitter plate ($l^* = 1.0 \cdot d$) in a bounded ($\beta = 0.5$) plug flow (moving upper and lower boundaries), $Re^* = 125$. Left: instantaneous streamlines. Right: instantaneous iso-vorticity contour. (a) no splitter plate; (b) $l_s^* = 0.5$; (c) $l_s^* = 1.5$; (d) $l_s^* = 1.7125$; (e) $l_s^* = 1.715$; (f) $l_s^* = 2.5$.

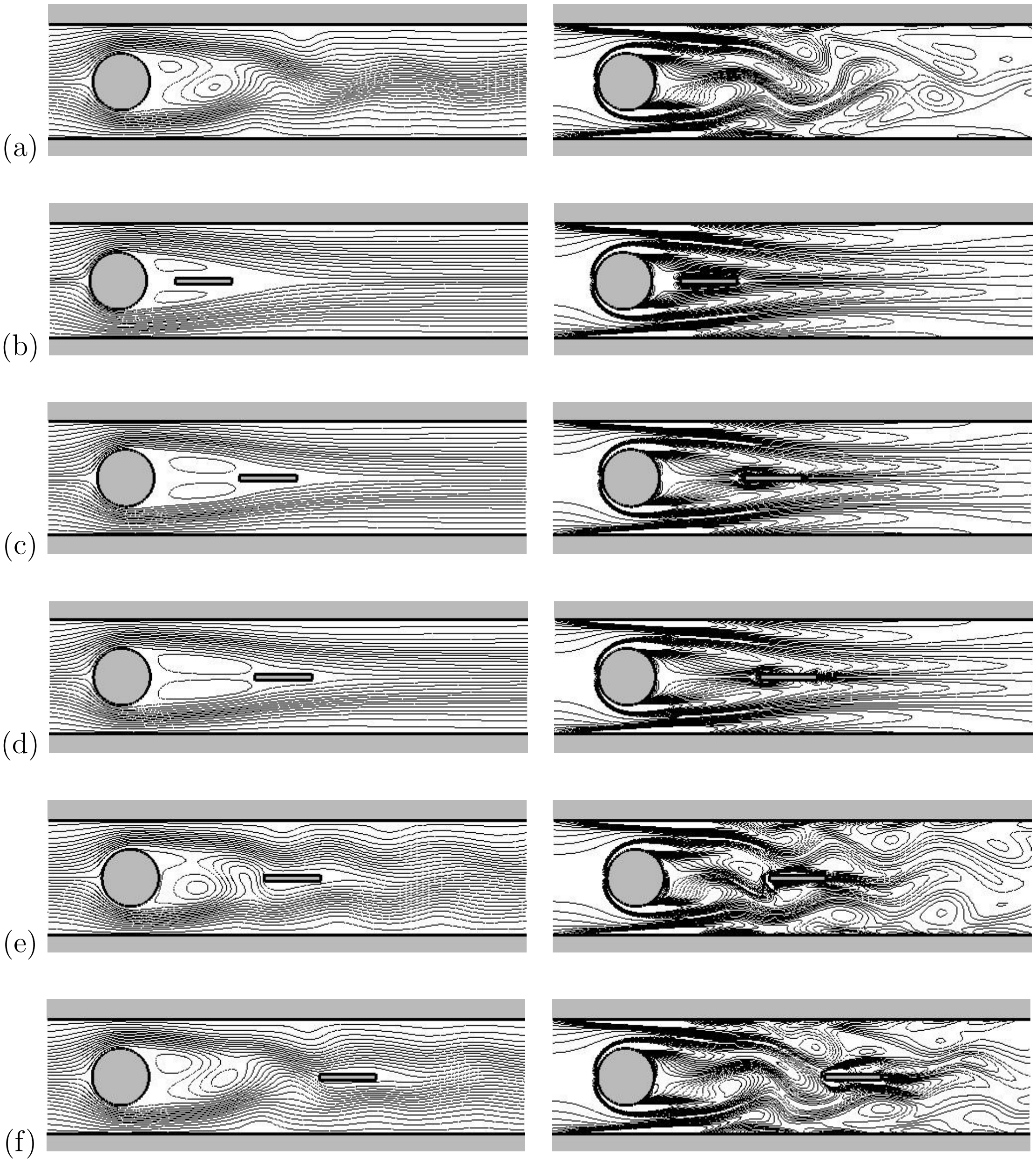

Figure 4.16: Numerical simulation of flow past a circular with a downstream splitter plate ($l^* = 1$) in a bounded ($\beta = 0.5$) Poiseuille flow (stationary upper and lower boundaries), $Re^* = 125$. Left: instantaneous streamlines. Right: instantaneous iso-vorticity contour. (a) no splitter plate; (b) $l_s^* = 0.5$; (c) $l_s^* = 1.5$; (d) $l_s^* = 1.84$; (e) $l_s^* = 1.85$; (f) $l_s^* = 3.0$.

critical separation distance, the splitter plate in the presence of moving upper and lower walls can either completely eliminate or partially reduce the unsteady vortex wakes and, as a result, lift and drag oscillations. Numerical experiments have been performed for plate lengths 0.25, 0.5, 0.75 and 1, at the separation distance between 0.25 and 5. The suppression of flow instability appears to be minimally dependent of the splitter plate length. However, if the splitter plate is too short, 0.25 for example, it is less effective and a complete suppression cannot be realized.

The primary factor is the separation distance. The suppression mechanism appears to depend on the full or partial physical presence of the splitter plate in the region of the first independent vortex lobe. The estimate of a critical separation distance of 2.547 is an approximate number based on the average distance between the largest effective l_s^* of 2.53125 and the smallest ineffective l_s^* of 2.5625 used in the simulation.

Complete suppression is no longer attained when the separation distance is too small, less than a second critical distance around 0.875. Similarly, this is an approximate number based on the average distance between the largest semi-effective l_s^* of 0.75 and the smallest effective l_s^* of 1.0 distance which decides whether there would be an attenuation of force oscillation. The splitter plate length, on the other hand, plays a role in the degree of effectiveness in attenuation, i.e. a complete or partial suppression of force oscillation. In bounded flow, the moving upper and lower walls also help stabilize the flow by damping out the vortex wakes. The critical separation for maximizing the suppression of FIV oscillation can vary according to the Reynolds number but can be found iteratively. In summary, the effectiveness of suppression can be classified into 3 categories:

1. Semi-effective: $0 < l_s^* < 0.875$
2. Effective: $0.875 \leqslant l_s^* \leqslant 2.547$
3. Ineffective: $ls^* > 2.547$.

In contrast to the unbounded flow, the position of the splitter plate of various lengths in the flow at this Re^* does not seem to alter the value of St^* significantly as

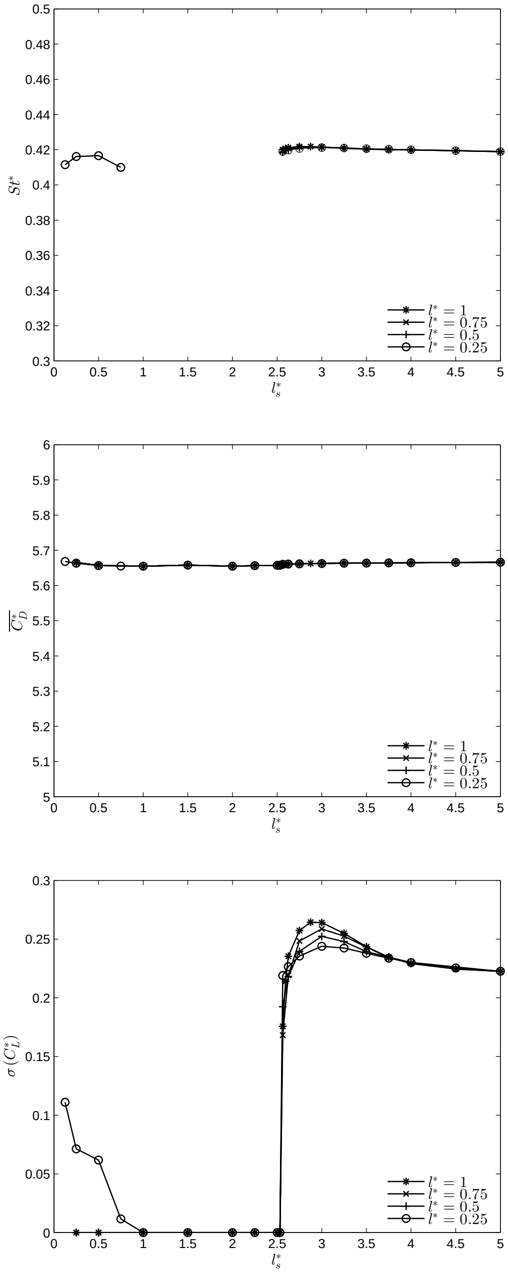

Figure 4.17: Circular cylinder with splitter plate in a plug flow, $l^* = 1$, $l_t^* = 0.1$, $\beta = 0.5$, $Re^* = 75$: St (top), mean C_D (middle), standard deviation of C_L (bottom).

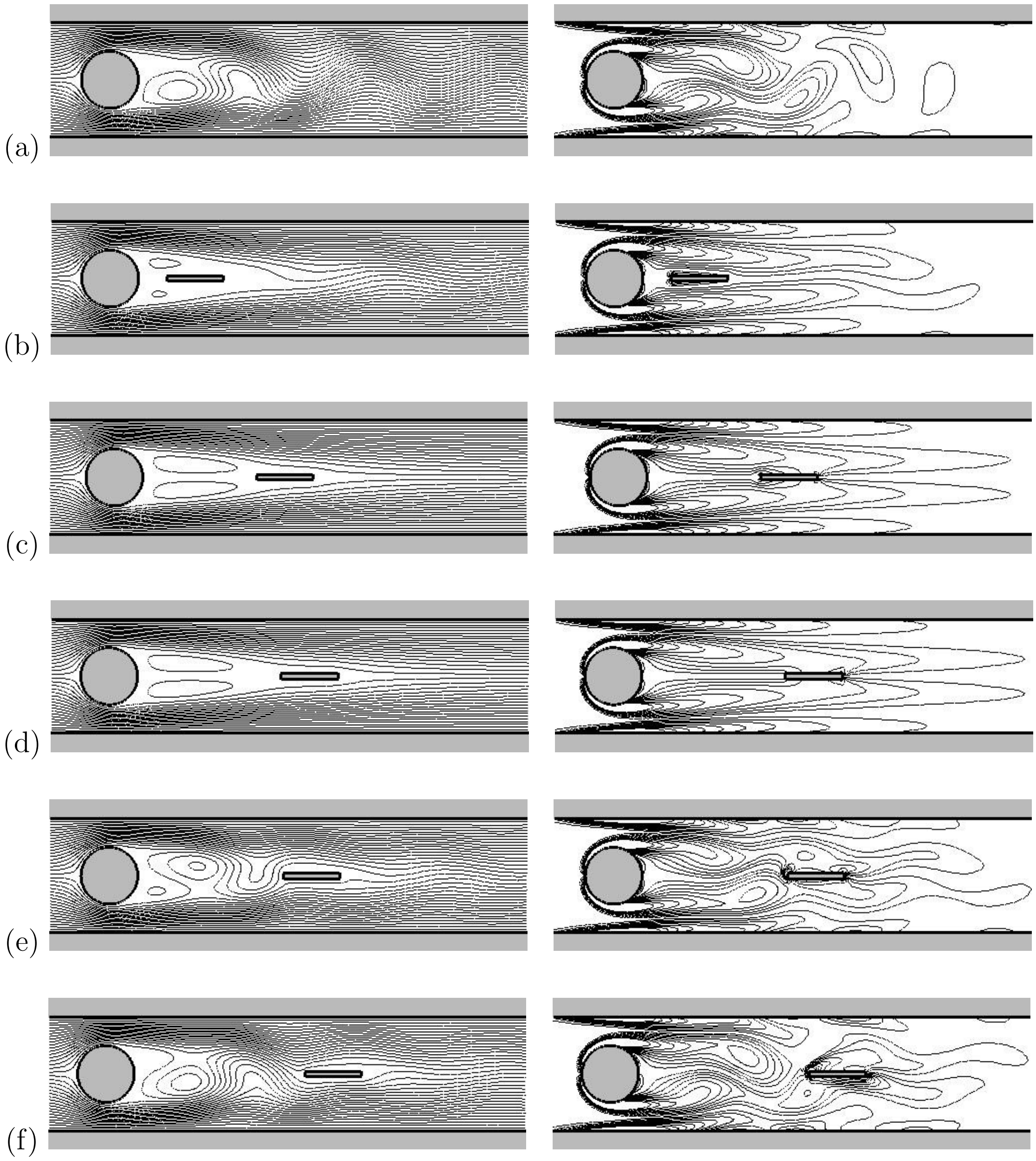

Figure 4.18: Numerical simulation of a circular cylinder with a downstream splitter plate ($l^* = 1.0$) in a plug flow, $\beta = 0.5$, $Re^* = 75$. Left: instantaneous streamlines. Right: instantaneous iso-vorticity contour. (a) no splitter plate; (b) $l_s^* = 0.5$; (c) $l_s^* = 2$; (d) $l_s^* = 2.53125$; (e) $l_s^* = 2.5625$; (f) $l_s^* = 3$.

shown in figure 4.17. Using a splitter plate of length $l^* = 1$, the splitter plate effect in the bounded flow configuration yields essentially two modes of vortex wakes – one that is steady and symmetrical at $2 \leqslant l_s^* \leqslant 2.53125$ and the other that is unsteady and asymmetrical with a constant shedding frequency at $1 \leqslant l_s^* \leqslant 2.5$. Note that the Strouhal number of the unsteady wake mode at this Reynolds number approximately coincides with the baseline value of $St^* = 0.21$ when splitter plate is absent.

4.4 Experimental verification

The experimental method used in this verification is described in section A.1 of appendix A. The whole test section of the wind tunnel is used for unbounded flow experiment. Since the diameter of the test specimen is 1/16 inch in diameter and the height of the test section is 1.5 inch, the approximate blockage factor is then 0.042 which is reasonably low enough to consider the flow in the test section unbounded. For bounded flow in a confined channel, a secondary enclosure provides the desired blockage factor for any given test specimen. With this technique, a comparison between the earlier numerical prediction and experimental result of flow induced vibration as measured by laser Doppler vibrometer (LDV) can be made for a circular cylinder in both unbounded flow and bounded flow.

4.4.1 Comparison between numerical and experimental results of circular cylinder with and without splitter plate

High blockage factor: $Re^* = 125$, $\beta = 0.5$

In this subsection, the flow at $Re^* = 125$ and $\beta = 0.5$ is investigated and considered as a model for Poiseuille flow. It is necessary to first establish a baseline where a circular cylinder is tested without the presence of a splitter plate. Once the baseline data is established, similar measurement can be made with the presence of a splitter plate.

Plotted in Figure 4.19 is the power spectrum showing the flow-induced vibration

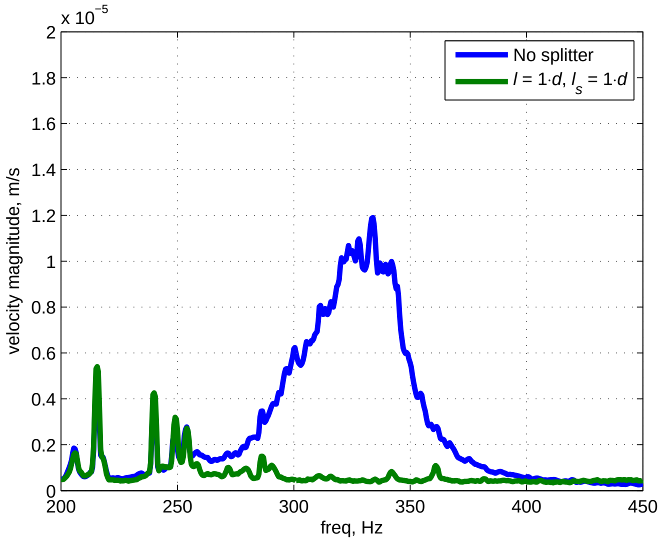

Figure 4.19: Circular cylinder motion without and with splitter plate at $l^* = 1$, $l_s^* = 1$, $Re^* = 125$, $\beta = 0.5$.

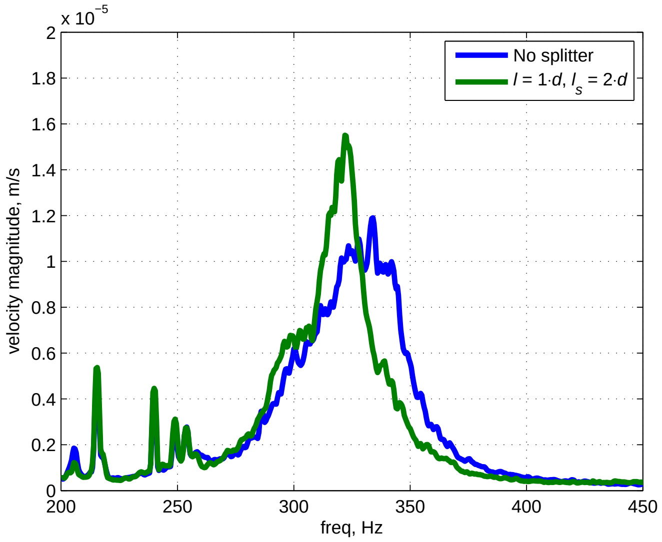

Figure 4.20: Circular cylinder motion without and with splitter plate at $l^* = 1$, $l_s^* = 2$, $Re^* = 125$, $\beta = 0.5$.

mode (blue line) of circular cylinder at 335 Hz due to vortex shedding and the complete suppression (red line) when a splitter plate of length $l^* = 1$ is placed downstream of the circular cylinder at $l_s^* = 1$ separation distance. This is in good agreement with the numerical results presented in the earlier section. Note that the spikes between 200 to 250 Hz can be attributed to both mechanical and electrical noise in the experimental system. It can also be shown that once the splitter plate is placed slightly beyond the critical distance, the oscillating motion can get worse than the case where the splitter plate is not present. Figure 4.20 illustrates a slight amplification of the magnitude of the cylinder oscillating motion as a result of placing the splitter plate at $l_s^* = 2$, which is in good agreement with the earlier numerical result that predicts the critical distance to be at 1.845.

By incrementally varying the position of a splitter plate downstream of the circular cylinder, the Strouhal numbers can be obtained as a function of separation distance similar to the numerical results shown earlier. Figure 4.21 shows a reasonably good correlation between experimental result and numerical prediction of the flow induced vibration on circular cylinder with the presence of a splitter plate. A slight discrepancy can be attributed to the differences in constraining the circular cylinder in the bounded flow between the numerical and experimental results. While the aerodynamic forces are obtained from the two-dimensional numerical analysis with the cylinder being rigidly fixed in space, the experimental setup allows the cylinder to move so that the LDV measurement can be made.

It is also possible to compare the forces on the circular cylinder as a function of separation distance of cylinder. The sinusoidal acceleration of the cylinder can be obtained directly by differentiating the velocity signal from LDV as follows

$$u = \dot{X} sin(\omega t),$$

$$a = \omega \dot{X} cos(\omega t).$$

The normalized quantity of the coefficient of lift, $|C_L^*|$, is then directly proportional to the normalized acceleration of the cylinder between the baseline and the measurement with splitter plate, i.e.

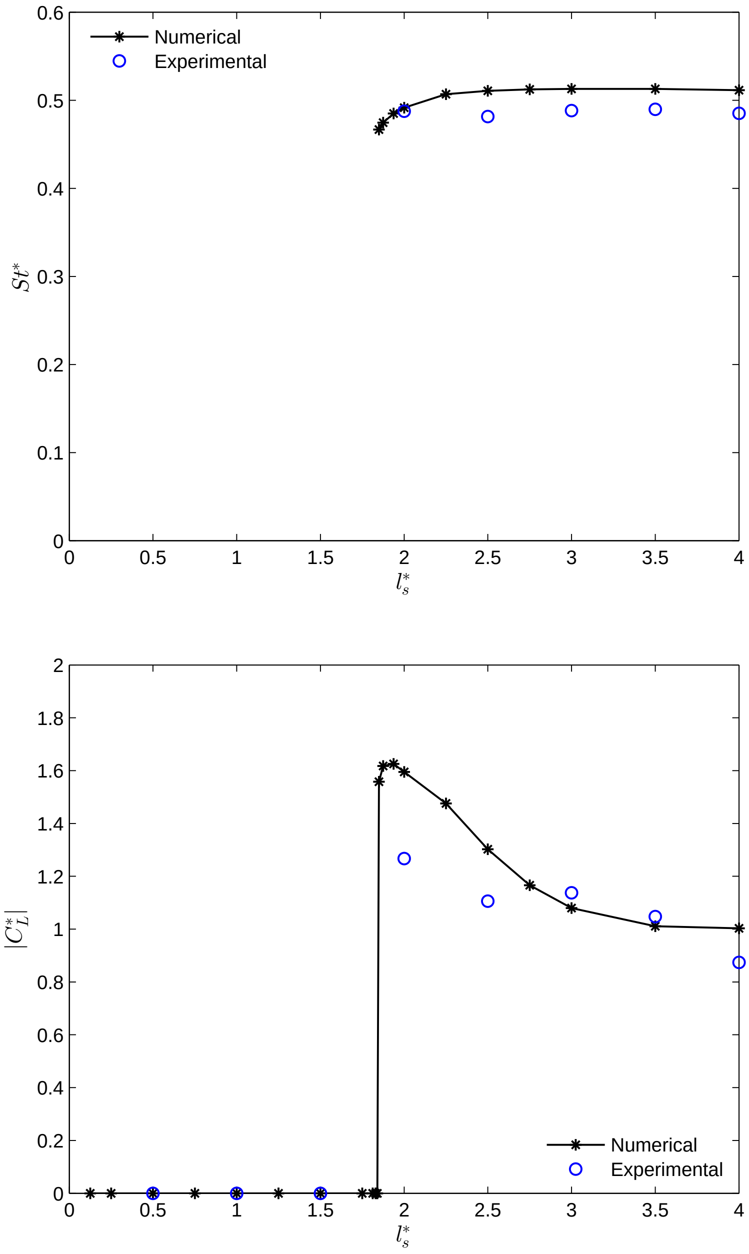

Figure 4.21: Numerical and experimental comparison of St^* and $|C_L^*|$ as a function of splitter plate separation distance, $Re^* = 125$, Poiseuille flow, $\beta = 0.5$.

$$|C_L^*| = \frac{(C_L^*)_{splitter}}{(C_L^*)_{no\ splitter}} \propto \frac{a_{splitter}}{a_{no\ splitter}} = \frac{(\omega \dot{X})_{splitter}}{(\omega \dot{X})_{no\ splitter}}.$$

Figure 4.21 also shows a comparable trend of $|C_L^*|$ between numerical and experimental results. In the separation range of less than 1.845, the splitter plate completely suppresses the vortex induced vibration mode at 335 Hz. On the other hand, a decreasing trend of amplification can be seen as the splitter plate is moved further away from the critical distance. The discrepancy between numerical and experimental C_L^* can again be attributed to the difference in the applied boundary conditions of the cylinder. While the circular cylinder is rigidly fixed in space in the numerical study, such is not the case in the current empirical experiment.

Low blockage factor: $Re = 125$, $\beta = 0.042$

In this subsection, the secondary enclosure is removed and the circular test specimen is placed midway between the upper and lower boundaries, thus yielding a low blockage factor for an unbounded flow consideration. The same measurement technique used in the previous subsection is applied. As shown in figure 4.22, there is a reasonably good agreement between the numerical and experimental results. However, near $l_s^* = 2$, the transition from the region where the splitter plate provides some attenuation to the region where it exacerbates the vibration is not clearly defined in the experimental data as compared to the numerical one. It can be postulated that the reason has to do with some lower frequency buffeting of the specimen and the splitter plate in this test condition. Note that the high blockage factor seems to have less buffeting problem which suggests that the close proximity of the upper and lower boundaries might have provided some additional stability to the test specimen.

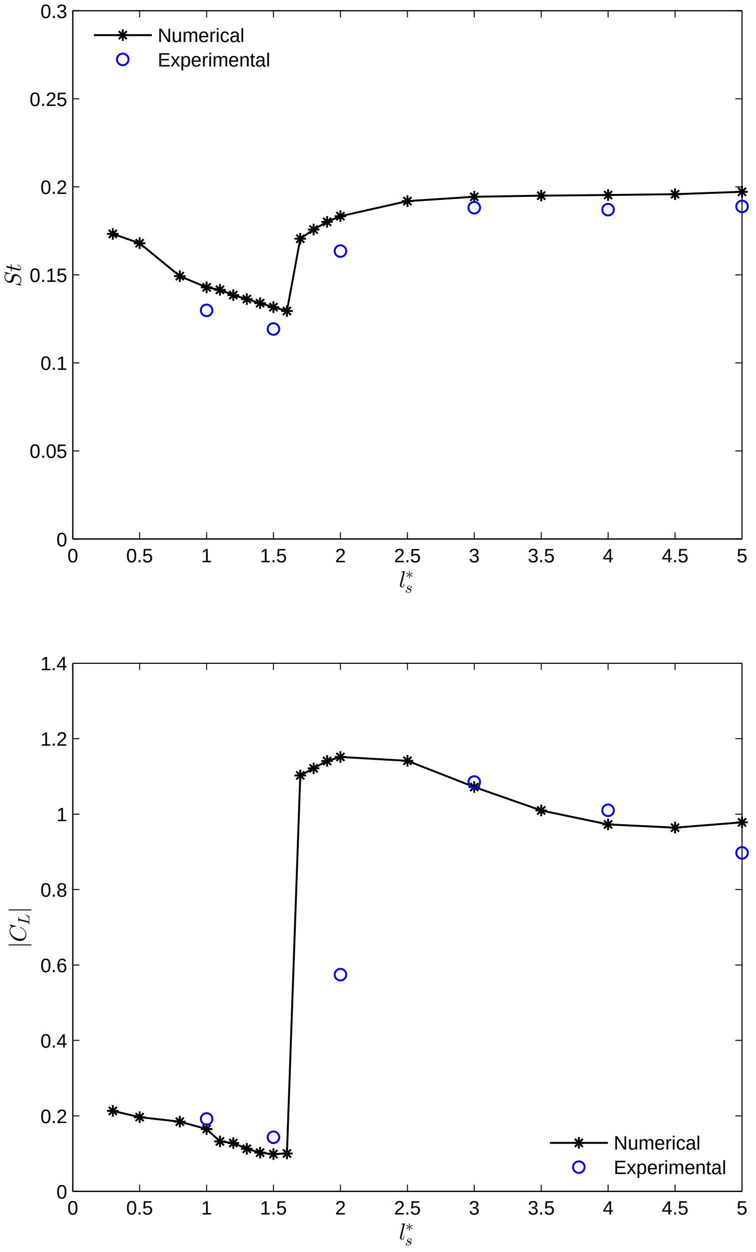

Figure 4.22: Numerical and experimental comparison of St and $|C_L|$ as a function of splitter plate separation distance, $Re = 125$, unbounded flow.

4.4.2 Splitter plate effect at $396 \leqslant Re^* \leqslant 632$, $\beta = 0.4$

Most of the presented results thus far involve relative low Reynolds number flows that are predominantly two-dimensional. For the most part, the results obtained from two-dimensional computation are well correlated with the experimental results. A slightly higher Reynolds number range is hereby considered where the flow becomes three-dimensional thus posing a certain amount of uncertainties and discrepancies with the two-dimensional simulation. In this section, a long, thin splitter plate ($l^* = 3.5$, $l_t^* = 0.1$) is used to investigate the effectiveness of vortex suppression in the Reynolds number range of $396 < Re^* < 632$. This range is chosen primarily within the capability limits of the hardware described in appendix A.1.

Figure 4.23 plots the numerical and experimental comparison of Strouhal number within this Reynolds number. The numerical data of St^* is calculated from the vortex shedding frequency obtained from two-dimensional CFD-ACE+ computation. The experimental data set is determined from the peak frequency detected from the circular cylinder motion using LDV measurement. It is clear from the figure that there are some discrepancies in the St^* value between numerical data and experimental data. The primary reason has to do with the obvious fact that the two-dimensional simulation cannot properly resolve flow three-dimensionalities. As suggested from the curve, the higher the Reynolds number the further apart the two curves are. Therefore, these margins of errors need to be taken into account.

From the numerical prediction shown in table 4.3, it was found that the rather long splitter plate is very effective in suppressing vortex shedding of a confined bluff body in this Reynolds number range. It completely eliminates the unsteadiness and also acts as a streamlining device by lowering the mean drag. The plots of instantaneous vorticity along with the frequency spectrum of the cylinder motion for some data points are illustrated in figures 4.24 to 4.30.

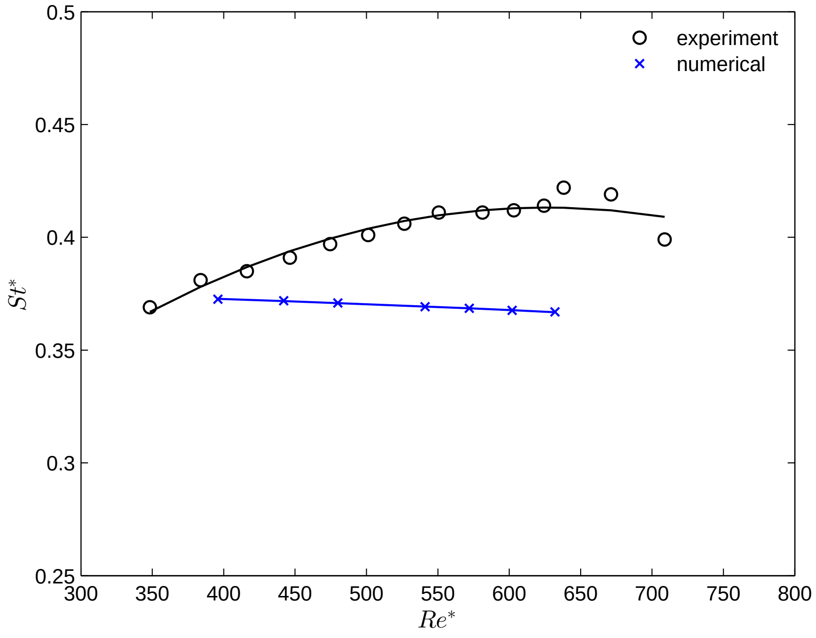

Figure 4.23: Numerical and experimental comparison of St^*, Poiseuille flow, $\beta = 0.4$.

	No splitter plate			$l^* = 3.5, l_s^* = 1$		
Re^*	St^*	$\sigma(C_L^*)$	$\overline{C_D^*}$	St^*	$\sigma(C_L^*)$	$\overline{C_D^*}$
396	0.3726	1.7016	3.0725	–	0.0000	2.6995
442	0.3719	1.7641	3.0709	–	0.0000	2.6470
480	0.3709	1.8089	3.0435	–	0.0000	2.6063
541	0.3692	1.8701	3.0197	–	0.0000	2.5540
572	0.3685	1.8999	3.0213	–	0.0000	2.5329
602	0.3676	1.9273	3.0167	–	0.0000	2.5126
632	0.3669	1.9531	3.0115	–	0.0000	2.7059

Table 4.3: Numerical results of St^*, $\sigma(C_L^*)$ and $\overline{C_D^*}$ for flow past a circular cylinder in Poiseuille flow, $\beta = 0.4$, at $Re^* = 396$, 442, 480, 541, 572, 602 & 632.

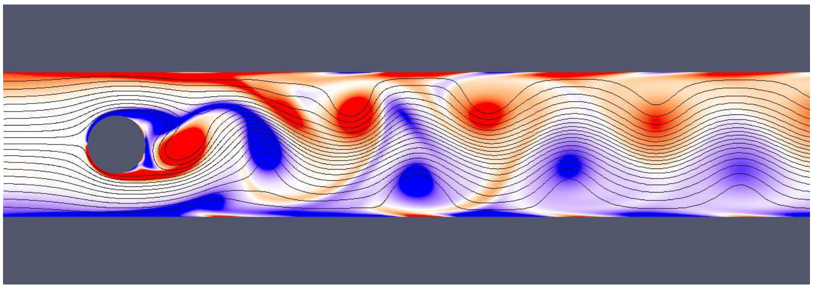

No splitter plate

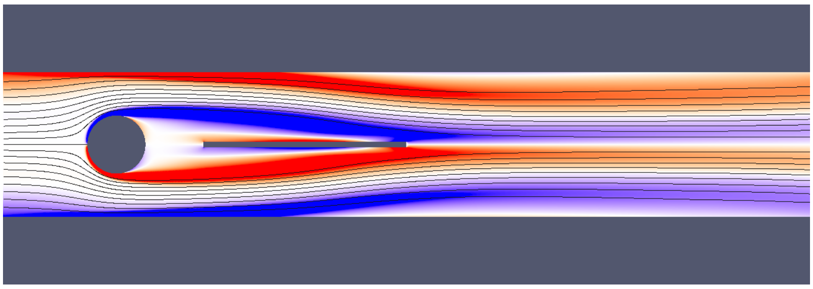

With splitter plate, $l^* = 3.5$, $l^*_s = 1$

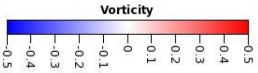

Instantaneous vorticity and streamlines (numerical).

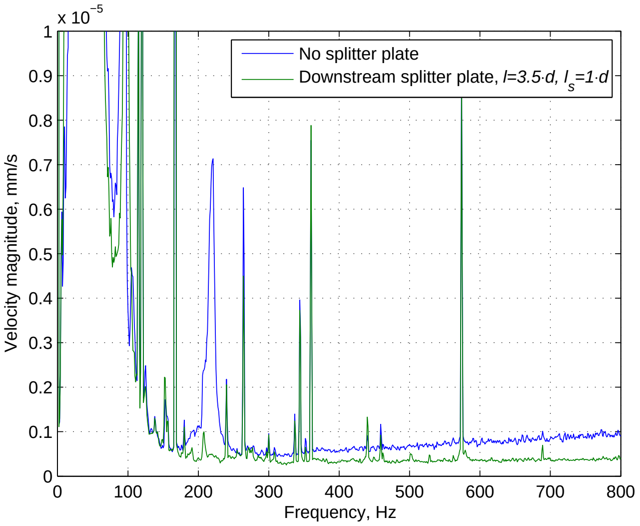

Frequency spectrum of cylinder motion (experimental)

Figure 4.24: Suppression of vortex induced mode at 221 Hertz using a splitter plate, Poiseuille flow, $Re^* = 396$, $\beta = 0.4$.

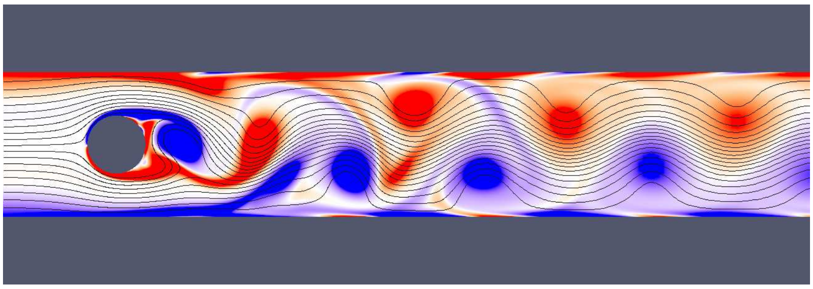

No splitter plate

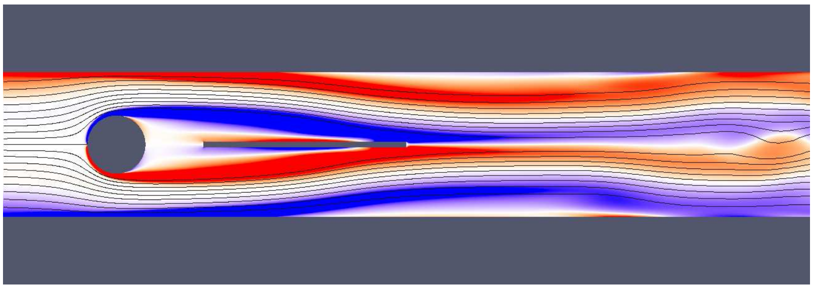

With splitter plate, $l^* = 3.5$, $l_s^* = 1$

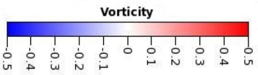

Instantaneous vorticity and streamlines (numerical).

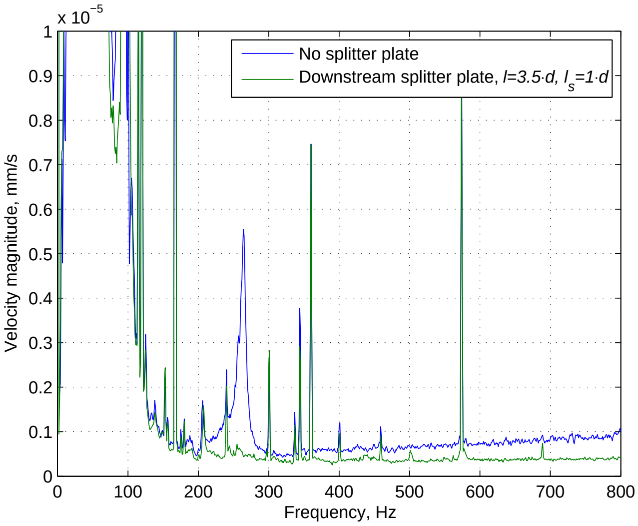

Frequency spectrum of cylinder motion (experimental)

Figure 4.25: Suppression of vortex induced mode at 264 Hertz using a splitter plate, Poiseuille flow, $Re^* = 442$, $\beta = 0.4$.

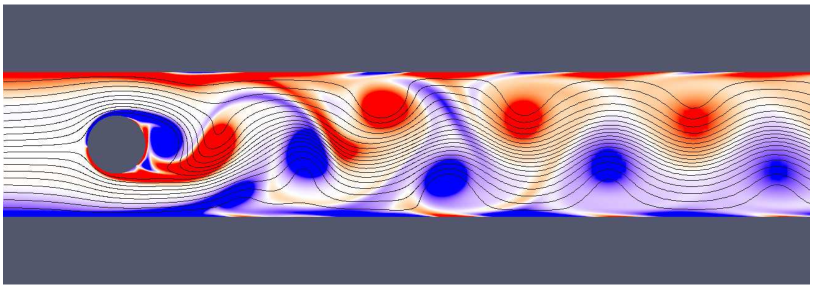

No splitter plate

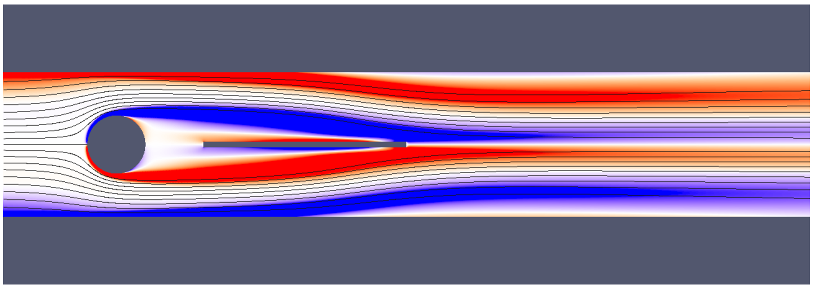

With splitter plate, $l^* = 3.5$, $l_s^* = 1$

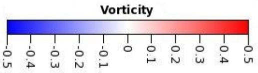

Instantaneous vorticity and streamlines (numerical).

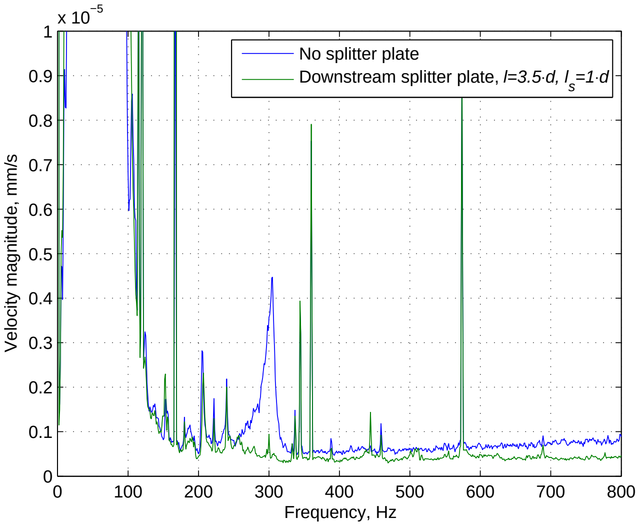

Frequency spectrum of cylinder motion (experimental)

Figure 4.26: Suppression of vortex induced mode at 305 Hertz using a splitter plate, Poiseuille flow, $Re^* = 480$, $\beta = 0.4$.

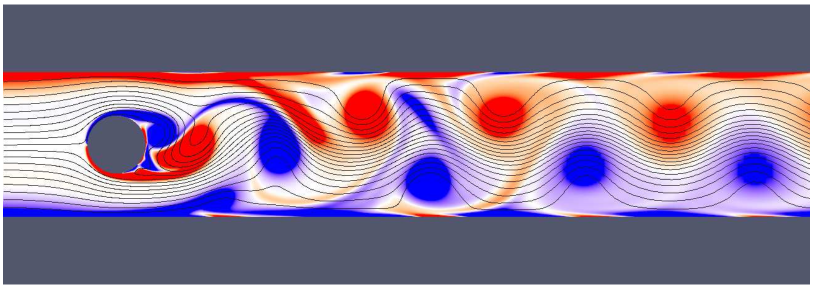

No splitter plate

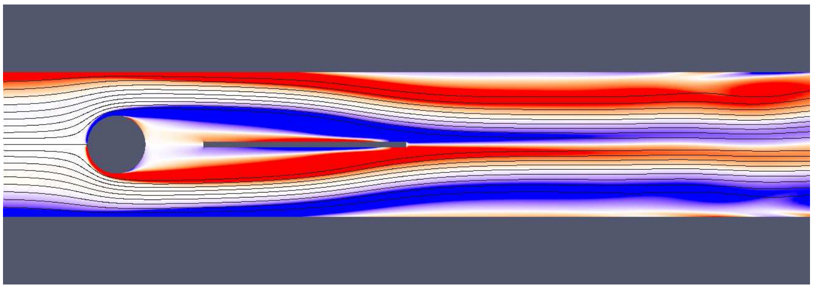

With splitter plate, $l^* = 3.5$, $l_s^* = 1$

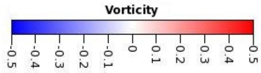

Instantaneous vorticity and streamlines (numerical).

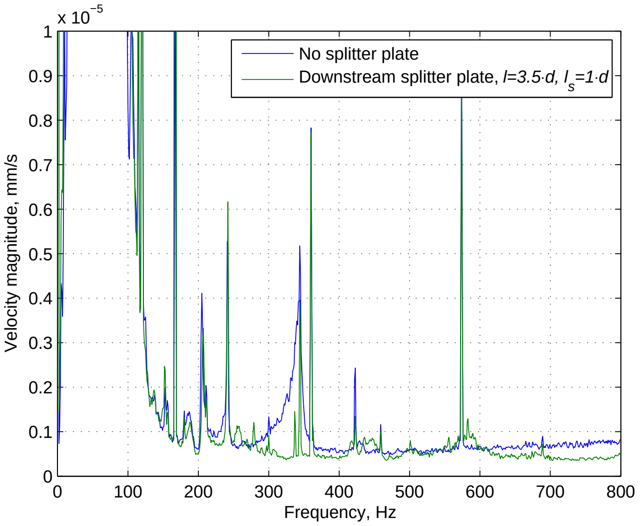

Frequency spectrum of cylinder motion (experimental)

Figure 4.27: Suppression of vortex induced mode at 344 Hertz using a splitter plate, Poiseuille flow, $Re^* = 541$, $\beta = 0.4$.

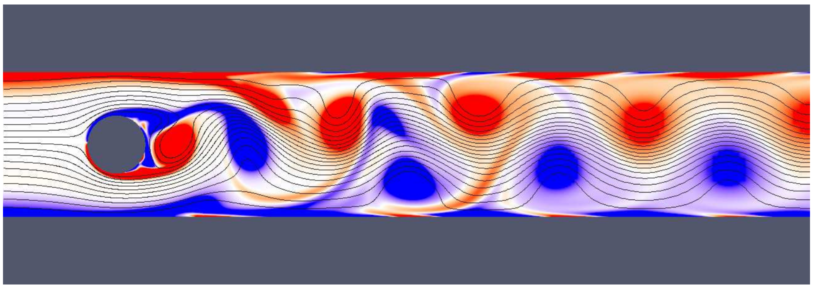

No splitter plate

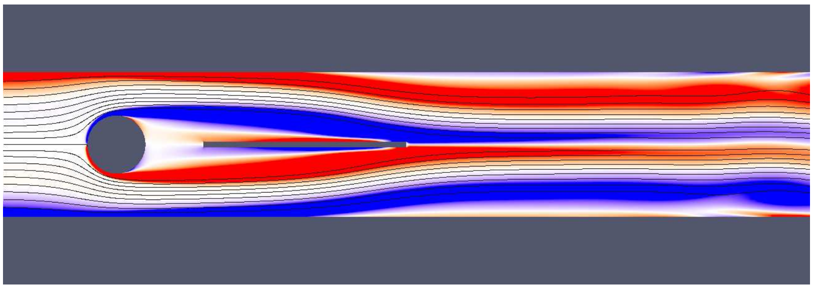

With splitter plate, $l^* = 3.5$, $l_s^* = 1$

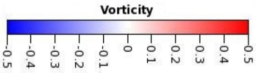

Instantaneous vorticity and streamlines (numerical).

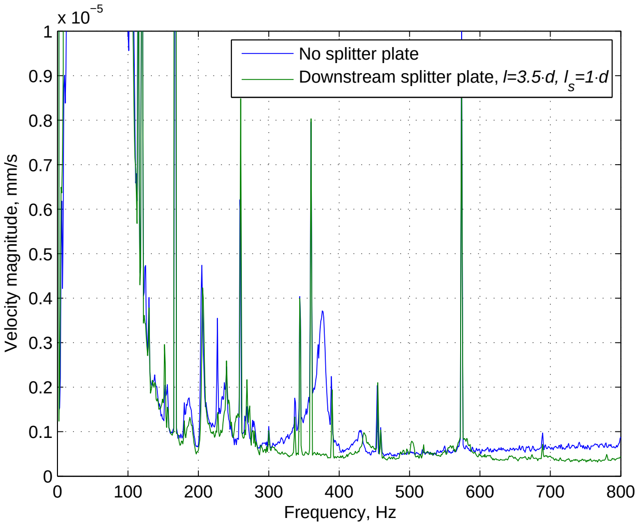

Frequency spectrum of cylinder motion (experimental)

Figure 4.28: Suppression of vortex induced mode at 376 Hertz using a splitter plate, Poiseuille flow, $Re^* = 572$, $\beta = 0.4$.

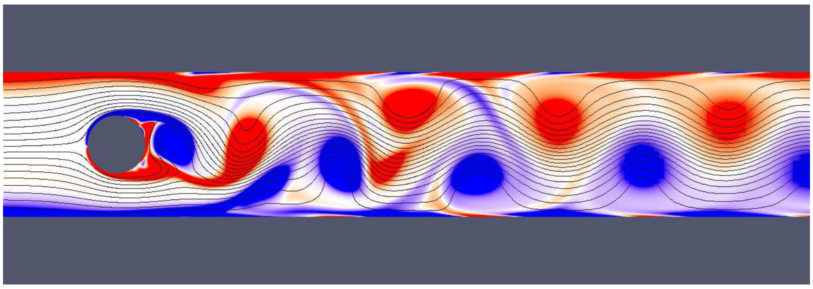

No splitter plate

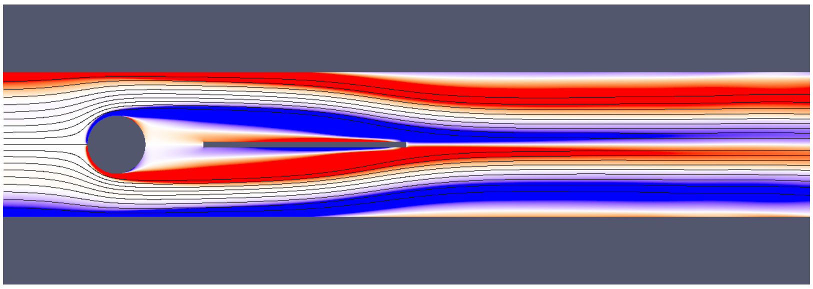

With splitter plate, $l^* = 3.5$, $l_s^* = 1$

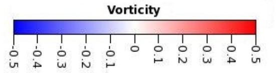

Instantaneous vorticity and streamlines (numerical).

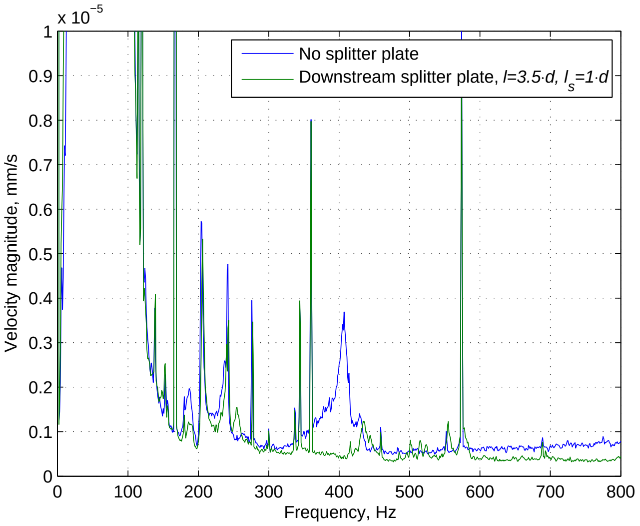

Frequency spectrum of cylinder motion (experimental)

Figure 4.29: Suppression of vortex induced mode at 407 Hertz using a splitter plate, Poiseuille flow, $Re^* = 602$, $\beta = 0.4$.

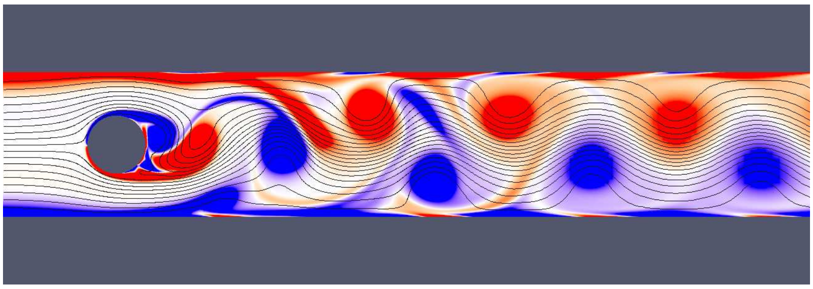

No splitter plate

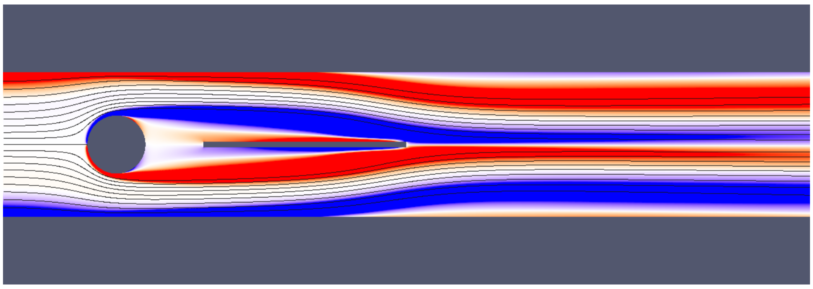

With splitter plate, $l^* = 3.5$, $l_s^* = 1$

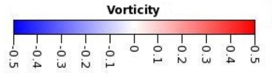

Instantaneous vorticity and streamlines (numerical).

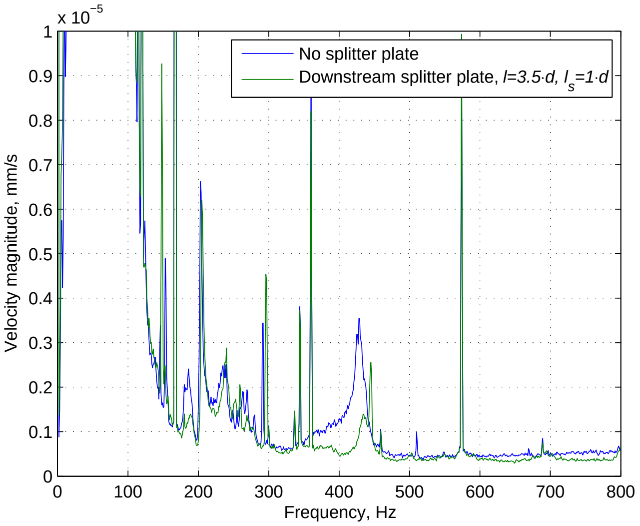

Frequency spectrum of cylinder motion (experimental)

Figure 4.30: Suppression of vortex induced mode at 429 Hertz using a splitter plate, Poiseuille flow, $Re^* = 632$, $\beta = 0.4$.

Chapter 5

Active vortex suppression by rotation

The contents of this chapter were previously published by Chan & Jameson [69] [1] and Chan *et al.* [70] [2] and reproduced here with minor modifications. The experimental portion of this chapter was carried out by Peter Dewey and Alexander Smits of the Gas Dynamics Laboratory at Princeton University.

5.1 Introduction

In the case of a circular cylinder, rotation is an effective technique for controlling unsteady vortex wakes. A nondimensional rotation speed relating the tangential velocity of the rotating cylinder surface to the free stream velocity can be defined as $\Omega = \omega d/2U$, where ω is the angular velocity of the cylinder. It has been studied by various researchers over the past century. Prandtl first studied the effect of rotating a cylinder situated in a uniform flow with the intent of demonstrating the lift generation by Magnus effect which serves as a basis for the "Flettner rotor" [89, 1]. The photographs from Prandtl's experiment clearly show that as Ω increases, the trailing

---

[1] Chan & Jameson, *Int. J. Num. Meth. Fluids.* Copyright 2010. Reproduced with permission from John Wiley and Sons. License Number 2671570769997.

[2] Chan *et al.* , *J. Fluid Mech.* Copyright 2011. Reproduced with permission from Cambridge University Press. License Number 2671560868712.

vortices weaken and the overall flow becomes more stable. At $\Omega = 4$, the flow clearly sheds no unstable eddies as the two stagnation points (front and aft) joined up on the high pressure bottom side. He also suggested that spinning a cylinder can be used as a way of preventing the eddy formation. It can thus be postulated from his works that spinning a cylinder changes the velocity gradient along the wall of the cylinder thereby modifying the boundary layer around the body as well as the shedding characteristics.

A number of researchers have studied both experimentally and numerically the effect of rotating a cylinder on vortex shedding. Some of the earlier works were performed numerically by Badr and Dennis [90] and experimentally by Coutanceau and Ménard [91]. Subsequently, a joint paper by these authors [92] were presented for a rotating cylinder at $10^3 \leqslant Re \leqslant 10^4$ for rotational speed of $0.5 \leqslant \Omega \leqslant 3$. They found that the vortex shedding can be suppressed at $\Omega = 3$ and the flow eventually approaches steady state.

In the laminar shedding regime, Badr *et al.* [93] numerically investigated steady and unsteady flow past a cylinder rotating at a relatively small rate (i.e. $\Omega \leqslant 1$) at $Re \leqslant 200$. They found from unsteady time-dependent results that if the cylinder is impulsively started from rest at $Re = 60$, 100 and 200, the flow does not tend to be a steady state as it still develops a periodic vortex shedding pattern. Tang and Ingham [94] provided the lift and drag coefficients and steady flow pattern of a rotating circular cylinder at $Re = 60$ and 100 for $\Omega \leqslant 1$ by solving the time independent Navier Stokes equations. Kang *et al.* [95] extended the numerical investigation further by solving the two-dimensional unsteady incompressible flow equations. They showed that a complete vortex suppression can be achieved by rotating a circular cylinder at a rate faster than the critical rotational speed. They found the critical speeds to be $\Omega = 1.4$, 1.8 and 1.9 for $Re = 60$, 100 and 200, respectively. In recent years, more efforts have been carried to extend the limit to a higher rotational rates to further understand the physics of flow past rotating circular cylinder in the laminar regime by Stojković *et al.* [96, 97] and Mittal & Kumar [80].

5.2 Single rotating circular cylinder at $Re = 100$, 150 and 200

Using the mesh from the unbounded stationary case, a non-slip, isothermal, moving boundary condition is applied at the circular cylinder wall such that it rotates at a constant speed ω as shown in figure 5.1. One of the advantages of the current numerical SD method is that a flow solution can be quickly obtained using the 2nd order calculation. If desired, a more accurate solution can then be obtained by using the 2nd order solution as an initial condition to start a higher order solution. Instead of using a higher order and letting the solution develop from an impulsive start, appreciable computation time can be saved with this restarting technique. Also, in studying the effect at different rotational speeds, a solution from $\Omega = 2$, say, can be used to start $\Omega = 2.5$ and thereby tremendously reducing the overall computational time.

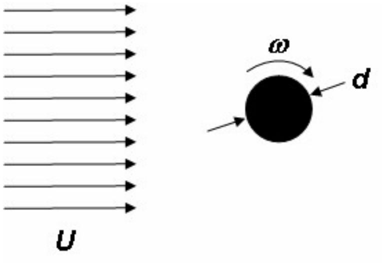

Figure 5.1: Configuration for unbounded flow past a rotating circular cylinder.

The mean and standard deviation values of lift and drag and the Strouhal number for $Re = 100$, 150 and 200 are plotted in figure 5.2 as a function of rotational speeds from the 4th order SD calculations. In general, there is very little difference in the mean lift and drag coefficients in the investigated range of Reynolds numbers. Figure 5.3 shows the instantaneous vorticity and streamlines as a function of rotational speeds. While there are substantial difference in the standard deviation values in the first unsteady range (below $\Omega = 2$), the speeds at which the complete vortex suppression occur are $\Omega = 1.9$, 2, and 1.95 for $Re = 100$, 150 and 200 respectively. In

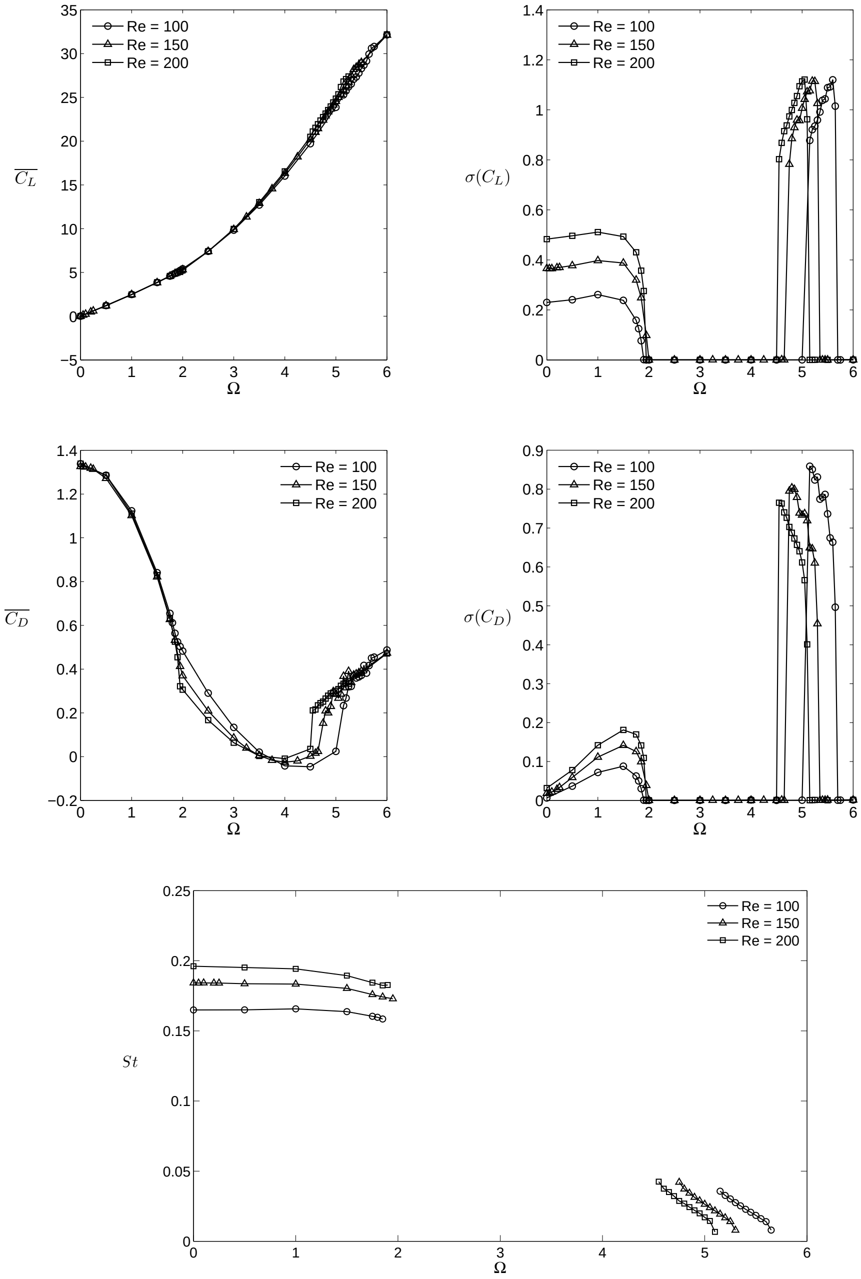

Figure 5.2: Unbounded flow past a rotating circular cylinder at $Re = 100$, 150, and 200: mean C_L (top, left), standard deviation of C_L (top, right), mean C_D (middle, left), standard deviation of C_D (middle, right) and St (bottom).

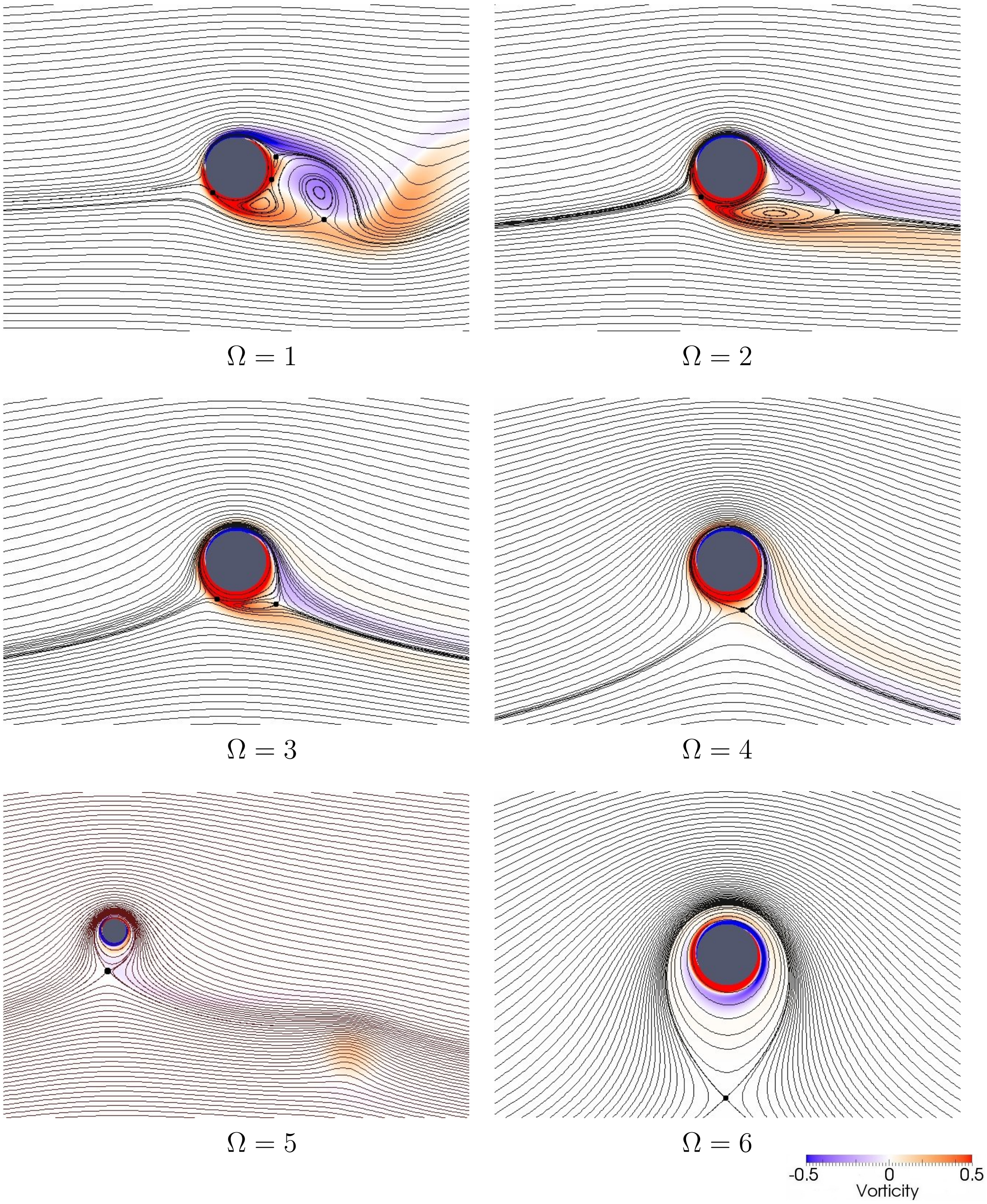

$\Omega = 1$ $\Omega = 2$

$\Omega = 3$ $\Omega = 4$

$\Omega = 5$ $\Omega = 6$

Figure 5.3: Flow past a rotating circular cylinder in unbounded flow at $Re = 150$: instantaneous streamlines and vorticity at various rotational speeds. Flow is unsteady at $\Omega = 1, 5$ and steady at $\Omega = 2, 3, 4, 6$. Stagnation points are represented by "$\bullet$".

the steady region of $2 \leqslant \Omega \leqslant 12$, Stojković *et al.* [96, 97] discovered an unexpected behavior where the flow becomes unsteady in the narrow range of $4.8 \leqslant \Omega \leqslant 5.15$ for $Re = 100$. Mittal & Kumar [80] later reported a similar phenomenon which they termed the "second instability" for $Re = 200$ in the range of $4.35 < \Omega < 4.75$. They postulated that it occurs because the balance between the advection and diffusion of vorticity is disturbed. They observed the build up of positive vorticity in the slow moving flow near the stagnation point in the near wake that, once it gathered enough strength, shed at a lower frequency than that seen in the regime of the first instability. The present SD calculation confirms the existence of secondary instability in the following range:

- $Re = 100$: $5.15 \leqslant \Omega \leqslant 5.65$
- $Re = 150$: $4.75 \leqslant \Omega \leqslant 5.3$
- $Re = 200$: $4.55 \leqslant \Omega \leqslant 5.1$

The second instability is illustrated in figure 5.3 for $\Omega = 5$ at $Re = 150$. A recent three-dimensional direct numerical simulation by El Akoury *et al.* concluded that the effect of rotation actually attenuates the secondary instability and increases the critical Reynolds number. For $\Omega = 0.5$, they extrapolated the critical Reynolds number to be 219.8, where the flow three-dimensionality starts to transition. This is much higher than the universally accepted value of $Re = 180$ for flow past a stationary circular cylinder (i.e. $\Omega = 0$).

A direct comparison can be made, as shown in figure 5.4 for a rotating cylinder at $Re = 200$ with the recent study performed by Mittal & Kumar [80] who calculated numerical incompressible flow solutions based on a finite element formulation. In the lower speed range, only slight variations in the flow solutions are seen amongst the 3rd and 4th order SD methods and Mittal & Kumar's method. The 2nd order SD method can effectively be used to provide a quick prediction of the stable range. Also plotted is the time-averaged power coefficient which is defined by

$$\overline{CP} = \overline{C_D} + \frac{|\overline{C_M}|\omega d}{2U}, \tag{5.1}$$

where $\overline{C_M}$ is the time-averaged moment coefficient calculated from the moment about the cylinder center. The power required to spin the cylinder is approximately constant in the first unsteady range and steadily increases with speed in the steady and second instability regimes.

5.2.1 Compressibility effect consideration

As the rotational speed increases, it is apparent that a larger discrepancy occurs between the solutions from the compressible SD code and those using Mittal & Kumar's incompressible flow solver. The SD solutions shows the occurrence of the secondary instability in the speed range of $4.5 < \Omega < 5.15$ as compared to Mittal & Kumar's solution of $4.4 < \Omega < 4.8$. One explanation for the difference is that the compressibility effect can no longer be neglected when the circular cylinder is rotated at a high enough speed.

Mach Number	C_D	C_{Dp}	C_{Dv}	C_L	C_{Lp}	C_{Lv}
0.05	0.0581	−0.3481	0.4061	10.2450	9.8253	0.4193
0.1	0.0637	−0.3353	0.3990	9.9640	9.5472	0.4168
0.2	0.0901	−0.2747	0.3648	8.8534	8.4456	0.4078

Table 5.1: Flow past a single rotating circular cylinder: C_L and C_D variations as a function of Mach number at $Re = 200$, $\omega = 3\Omega$ (steady flow). Subscripts: $p =$ pressure and $v =$ viscous.

Figure 5.5 and table 5.1 show the effect of compressibility on density and Mach contours and on the force coefficients at $Re = 200$, $\omega = 3\Omega$, calculated at freestream Mach numbers, Ma_∞, of 0.05, 0.10 and 0.20. For $Ma = 0.2$, the local Mach number around the cylinder spinning at a very high rotational speed, e.g. $\Omega = 5$, can become supersonic, thus yielding an entirely different flow problem. For very low Mach numbers, such as the case of $Ma = 0.05$, the current SD solver suffers the same inefficiency as most other density based compressible flow solvers. In this research, $Ma = 0.1$ is used since it is efficient, robust and yields results very close to those obtained using incompressible flow solvers, as shown in this section for the single rotating cylinder and in figure 5.24 for the counter-rotating cylinder pair.

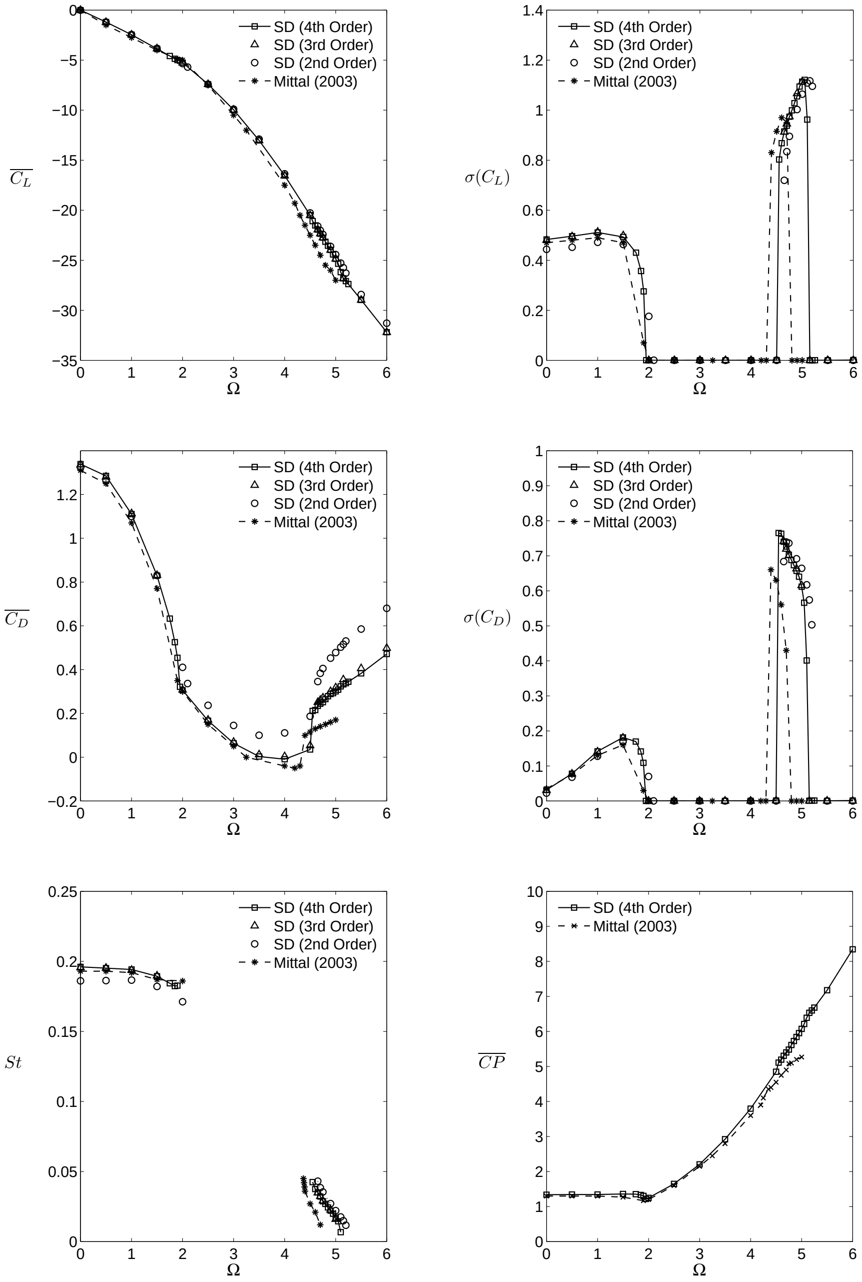

Figure 5.4: SD order comparison for flow past a rotating circular cylinder at $Re = 200$: mean C_L (top, left), standard deviation of C_L (top, right), mean C_D (middle, left), standard deviation of C_D (middle, right), St (bottom, left), mean CP (bottom, right).

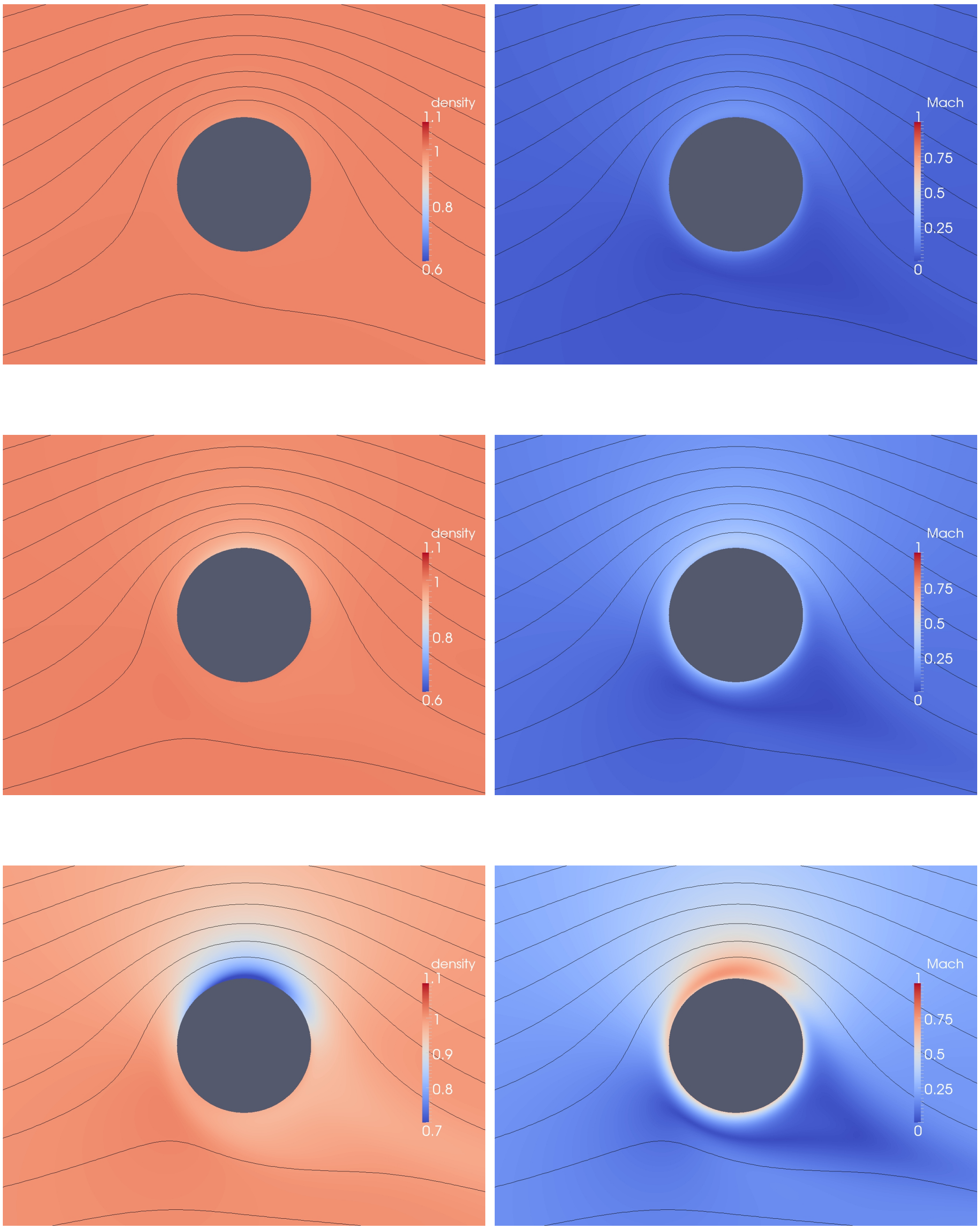

Figure 5.5: Flow past a single rotating circular cylinder, $Re = 200$, $\omega = 3\Omega$: normalized density (left) and Mach (right) contours at $Ma = 0.05$ (top), 0.10 (middle) and 0.20 (bottom).

5.3 Flow past a pair of identical, stationary circular cylinders

The flow past a pair of identical circular cylinders in a close proximity has been used as a model by past researchers who were interested in the interaction of vortex wakes of multiple bluff bodies in freestream. These past studies were mostly experimental. Notable works were initially done by Bearman and Wadcock [98], Zdravkovich [99] and Williamson [100]. The flow over a pair of non-rotating identical circular cylinders placed normal to the free stream is characterized by the mutual interaction between the cylinder wakes that lead to a number of particular flow states according to the Reynolds number, $Re = Ud/\nu$, and the gap spacing, $g^* = g/d$. Here, U is the free stream velocity, d is the cylinder diameter, ν is the kinematic viscosity and g is the distance between the two cylinder surfaces. In the Reynolds number range of 100 to 200, an unsteady two-dimensional vortex wake has been examined experimentally by Williamson [100], numerically by Kang [101] (see appendix B.1), and analytically by Peschard and Le Gal [102]. These studies found that for $g^* < 1$ vortices are shed asynchronously from the cylinder pair, and Kang classified the vortex shedding mode as being either flip-flopping ($0.4 < g^* < 1.5$) or following a von Kármán vortex street representative of a single bluff body ($g^* < 0.4$). These findings are supported by Kim [103] and Sumner *et al.* [104]. For $g^* \geq 1$, two synchronized vortex shedding modes from the cylinder pair are observed, either in-phase or anti-phase (figure 5.6). Williamson [100] noted that for $1 < g^* < 5$ the anti-phase mode is predominant and stable since each vortex generally keeps its form while being gradually dissipated further downstream of the bodies. Within this gap spacing regime, however, it was possible for the wake to "flip" to in-phase shedding synchronization and *vice versa*, particularly for smaller gaps such as $g^* = 1$. The in-phase mode is unstable as the opposite-signed vortices tend to coalesce into a larger vortex cell. This mode often leads to non-sinusoidal lift and drag variations, and it breaks down into alternative shedding modes when the gap is small. Numerically, the formation of the in-phase shedding mode can be induced by disturbing the flow using either a tripping technique at the beginning of a time marching routine, or by using an artificially large time step

Figure 5.6: Idealized synchronized vortex shedding modes in the wake of a non-rotating cylinder pair. Left: In-phase shedding. Right: Anti-phase shedding.

and/or introducing some non-streamwise flow component.

Figure 5.7 illustrates the numerical result for the anti-phase mode, at $Re = 150$ and $g^* = 1$, which Williamson experimentally observed as being stable. Figure 5.8 illustrates the in-phase vortex shedding mode, also at $Re = 150$ and $g^* = 1$, which Williamson found to be unstable. Each "binary" pair of like-sign vortices tends to coalesce into a larger single vortex cell before eventually being dissipated far downstream. To obtain a numerical result for the in-phase mode, one can use the technique of perturbing the flow velocity by artificially injecting a non-streamwise component into the computational domain for a few time steps. The purpose is to "trip" the flow so that the non-streamwise component will encourage the flow to develop into an in-phase pattern. Another method that proved successful is to artificially increase the time step Δt and/or limit the convergence criteria so that the residual error builds up for a few time steps. When Δt is throttled back down and a reasonable convergence criterion is re-established (typically a reduction of the residual errors by four orders of magnitude), the resulting initial disturbance tends to encourage the in-phase instability to form. Moreover simulations at the Reynolds number of 200 with $g^* = 2.4$, as shown in figures 5.9 and 5.10, predict wake patterns, which closely resemble the patterns observed by Williamson in his experiment, as can be seen in figures 6(a) and (b) of his report [100]. For these simulations, the boundary conditions are set up to replicate the channel width, length and blockage factor used in Williamson's experiment.

In order to gain a better understanding of the process of vortex shedding off a cylinder pair, it is useful to draw the instantaneous streamline patterns based on

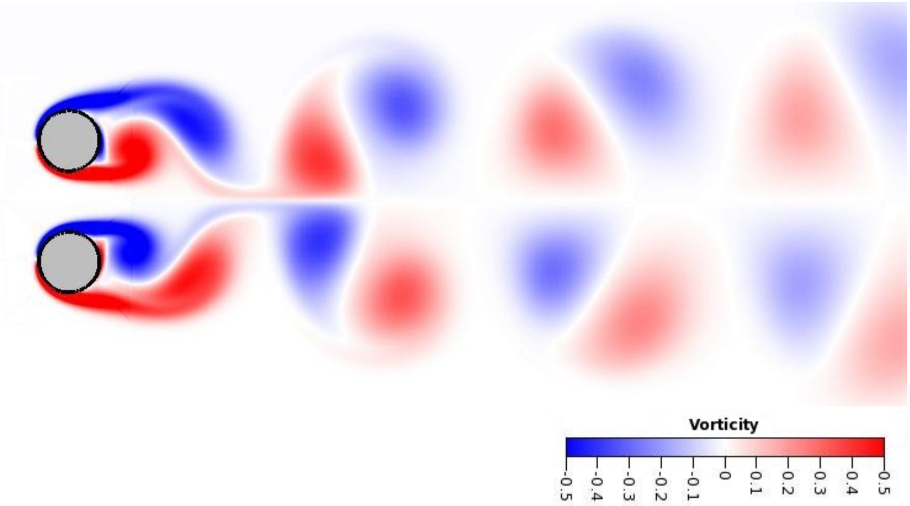

Figure 5.7: Anti-phase vortex shedding mode in the wake of a non-rotating cylinder pair: Instantaneous vorticity at $Re = 150$, $g^* = 1$.

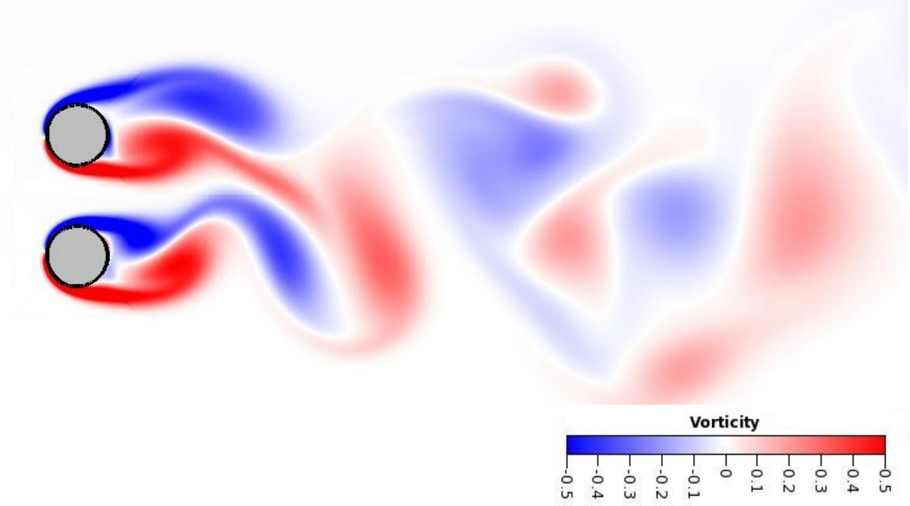

Figure 5.8: In-phase vortex shedding mode in the wake of a non-rotating cylinder pair: Instantaneous vorticity at $Re = 150$, $g^* = 1$.

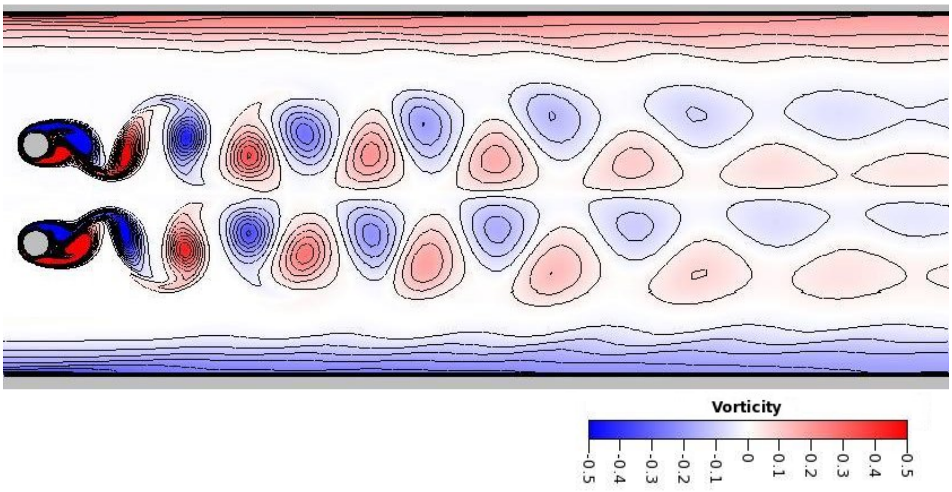

Figure 5.9: Anti-phase vortex shedding mode in the wake of a non-rotating cylinder pair: Instantaneous vorticity at $Re = 200$, $g^* = 2.4$.

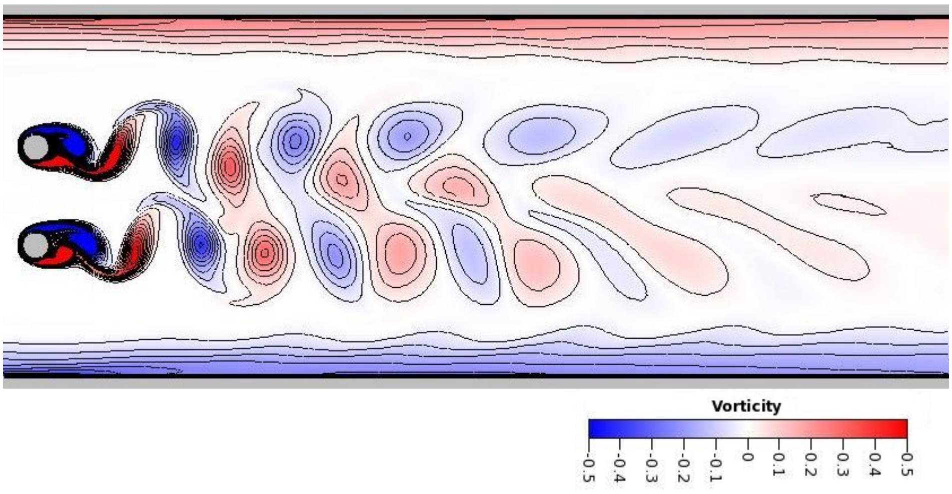

Figure 5.10: In-phase vortex shedding mode in the wake of a non-rotating cylinder pair: Instantaneous vorticity at $Re = 200$, $g^* = 2.4$.

the model that was proposed by Perry *et al.* [105]. Figure 5.11 illustrates the vortex shedding process of the anti-phase mode. One complete cycle is approximately represented from subfigures (a) to (h). The critical points are centers and saddles, denoted by '*C*' and '*S*' respectively. Each separatrix – a streamline which leaves or terminates at a saddle point – is represented by a darker line along with directional arrows.

Since the anti-phase mode is stable, there is a perfect balance in the wakes such that the vortex street of the upper cylinder is a mirror-image of the lower cylinder. The streamline at the half way between two cylinders is steady, making it a symmetry line throughout the whole shedding process. The formation of a synchronous pair of inner vortex lobes can be seen from subfigures (a) to (e) and the formation of a synchronous outer vortex pair from subfigures (e) to (h). As described in Perry's model for a single cylinder, a pair of instantaneous "alleyways", which are shown in figure 5.12 by the cross-hatched areas, are observed to open, widen and close during the generating process of each vortex lobe. The in-phase shedding mode of a cylinder pair, on the other hand, is observed to be asymmetrical and asynchronous as shown in figure 5.13. This is also observably clear from the unsynchronized behavior of each pair of instantaneous alleyways.

5.4 Counter-rotating circular cylinder pair

This study was inspired by the original work of Prandtl who hypothesized that steady, symmetric streamlines can be generated by two touching cylinders rotating in the opposite direction [1, 89]. It has been found in several recent studies that the unsteady, two-dimensional wake instabilities from a pair of circular cylinders separated by a normalized gap spacing, g^*, can be attenuated and even entirely suppressed when the cylinders are counter rotated [106, 69]. Counter rotation can be achieved in two different rotational configurations; the doublet-like and reverse doublet-like configuration as shown in figure 5.14. Yoon *et al* investigated the doublet-like configuration for a number of normalized gap distances at $Re = 100$ and showed that there exists a critical rotational speed, Ω_{crit}, that can completely suppress the unsteady vortex

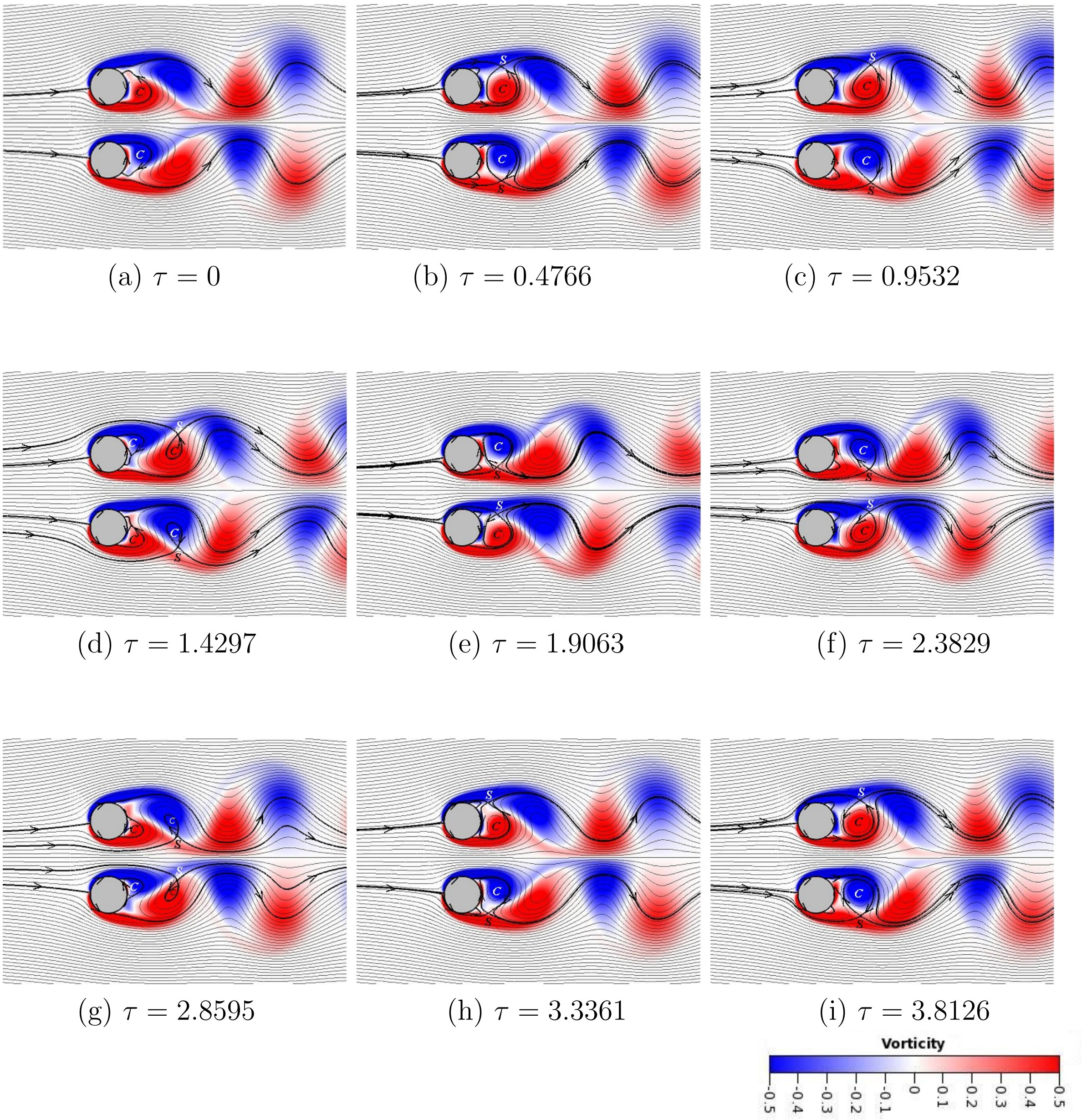

(a) $\tau = 0$ (b) $\tau = 0.4766$ (c) $\tau = 0.9532$

(d) $\tau = 1.4297$ (e) $\tau = 1.9063$ (f) $\tau = 2.3829$

(g) $\tau = 2.8595$ (h) $\tau = 3.3361$ (i) $\tau = 3.8126$

Figure 5.11: Flow in the near wake of a pair of cylinder during an anti-phase vortex shedding mode: instantaneous streamlines and vorticity contour. Slightly more than one complete shedding cycle is shown. Non-dimensional time increment between each frame: $\tau = (U\Delta t)/d$. Separatrices are represented by darker lines with arrows. 'S' is a saddle point. 'C' is a center point.

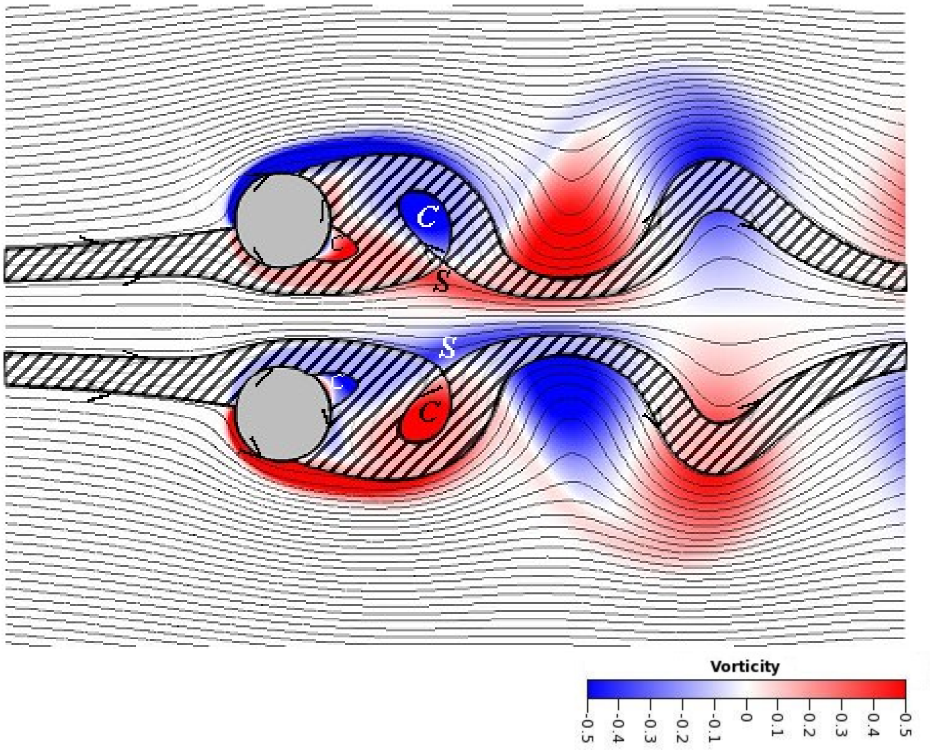

Figure 5.12: Flow in the near wake of a pair of cylinder during an anti-phase vortex shedding mode: instantaneous alleyways are shown by the cross-hatched areas.

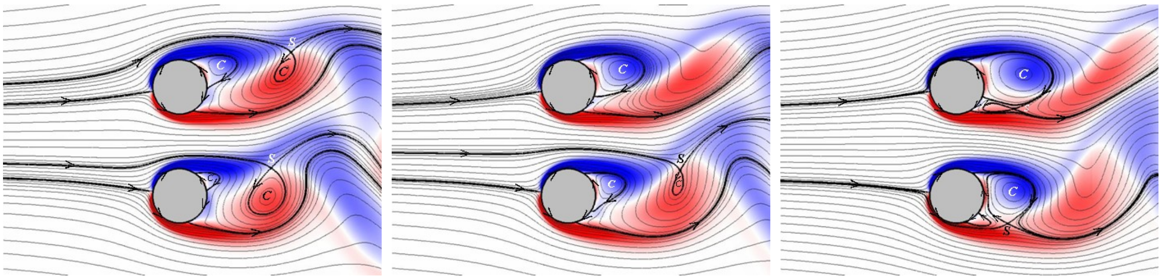

(a) $\tau = 0$ (b) $\tau = 0.7153$ (c) $\tau = 1.4305$

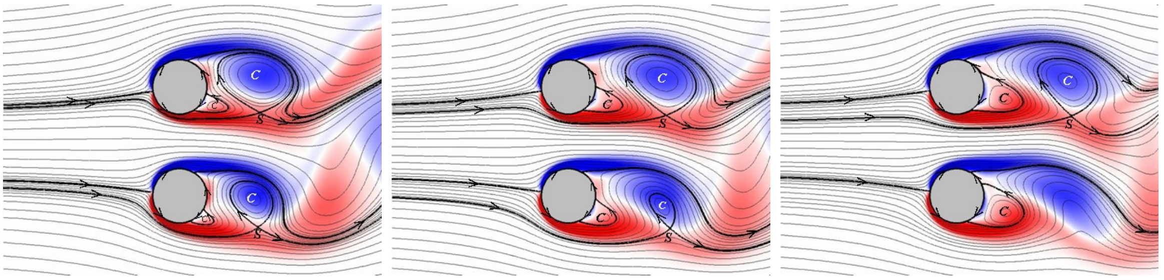

(d) $\tau = 2.1458$ (e) $\tau = 2.8610$ (f) $\tau = 3.5763$

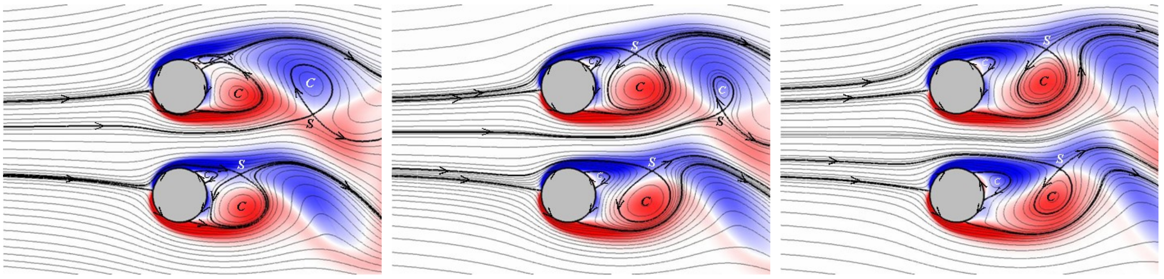

(g) $\tau = 4.2915$ (h) $\tau = 5.0068$ (i) $\tau = 5.7221$

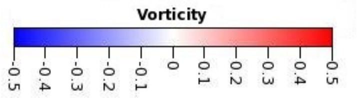

Figure 5.13: Flow in the near wake of a pair of cylinder during an in-phase vortex shedding mode: instantaneous streamlines and vorticity contour. Approximately one complete shedding cycle is shown. Non-dimensional time increment between each frame: $\tau = (U\Delta t)/d$. Separatrices are represented by darker lines with arrows. 'S' is a saddle point. 'C' is a center point.

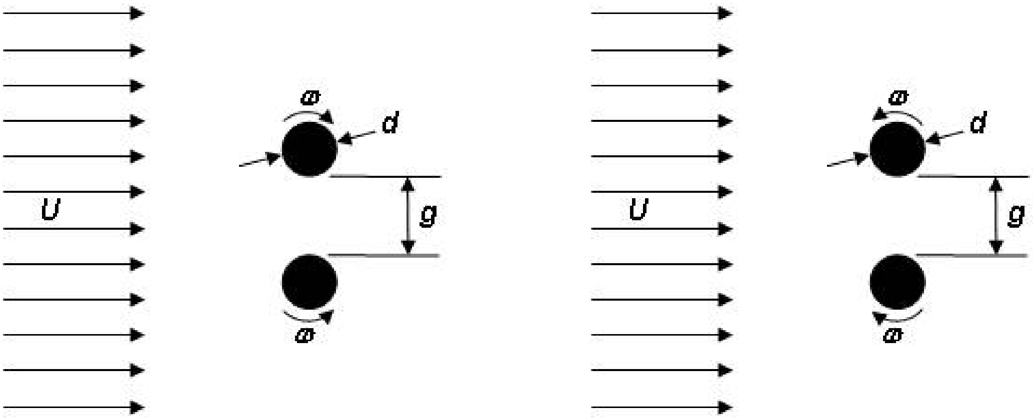

Figure 5.14: Counter-rotating circular cylinder pair. Left: Doublet-like configuration. Right: Reverse doublet-like configuration.

wakes [106]. It was also found that decreasing gap spacing correlates to a reduction in critical vortex suppression speed. The vortical wake structure present when the cylinders were rotated below the critical suppressing speed could be classified in a similar manner to non-rotating cylinders and it depends on both g^* and Ω. The unsteady regime for $g^* = 0.7$ leads to a single vortex street, while larger a gap spacing yields either in-phase or anti-phase synchronous vortex shedding. Chan and Jameson [69] extended this work by showing that the unsteady vortex wake could be suppressed in the reverse doublet-like configuration as well. For $Re = 150$ and $g^* = 1$, they obtained $\Omega_{crit} = 1.5$ for the doublet-like configuration and 3.5 for the reverse doublet-like configuration. Additionally, they found that for the doublet-like configuration an increase in rotational speed past the critical speed results in the creation of a symmetric flow pattern that resembles a doublet potential flow and is dubbed a “virtual elliptic body”.

In this work, these results are confirmed using a higher order simulation method as well as the results from the experiment [70]. Furthermore, the effect of gap spacing ($g^* = 1$, 3, and 5) and Reynolds number ($Re = 100$, 150, and 200) on the unsteady suppression for both the doublet-like and reverse doublet-like configurations as well as the formation of virtual elliptical bodies have been investigated. In the previous work of Chan and Jameson [69], the simulations were performed with the commercial code CFD-ACE+ for incompressible flow simulations. In the current work the high-order spectral difference (SD) method for compressible flow simulations described in chapter 2 is used. The focus is on relatively low Reynolds numbers so that it can be assumed that the flow past the counter-rotating circular cylinder is predominantly two-dimensional. This allows a large matrix of simulations using the two-dimensional SD code which is computationally much less expensive than the three-dimensional SD code. This two-dimensional assumption will be validated with experimental results in the later section.

The origin and size of the computational domain are shown in figure 5.15. The x-axis is in the streamwise direction, and the y-axis is normal to both the streamwise axis and the spanwise axis of the circular cylinder pair. Across the inlet, the Dirichlet boundary condition is specified with a uniform velocity of 0.1 m/s. The Reynolds numbers based on the cylinder diameter and upstream velocity are 100, 150 and 200. The size of the computational domain in the y-direction is $66.328d$, matching what is used in the experimental model. The dimension is far enough for the flow to be considered unbounded and to have negligible influence on the vortex shedding behavior of the cylinder pair. Both the upper and lower boundary conditions are set to a symmetrical slip condition. At the exit boundary, a fixed pressure is specified while other flow variables are extrapolated so that the flow remains uniform at the inlet. An isothermal, no slip boundary condition is applied on the cylinder wall surfaces.

In order to construct the SD computational model, a computational domain can be constructed using a commercial mesh generator. The domain for $g^* = 1$ uses a total of 7,000 cells (figure 5.16). A study of mesh density and SD order of accuracy is presented in appendix B.2. The mesh is constructed to be finer near the cylinder surface (figure 5.17), starting with the smallest radial spacing of 1.78% of diameter, and gets progressively coarser radially outward. The circumferential resolution is constant and there are 60 cells along the cylinder periphery. Figure 5.17 illustrates the solution collocation points (16 per cell) by the 4th order SD around a cylinder surface. The computational domains for other values of g^* are constructed in a similar manner. The study by Ou *et al.* [57] indicates that the 4th order SD approximation for a similar size model leads to a mesh-independent result with sufficient accuracy.

One of the main advantages of using the SD scheme is that the total computational time can be reduced by first producing a less accurate result using a lower order scheme (that is, 2nd order) to establish the general flow pattern and then switching to higher order (that is, 4th order) after the error residual norm has converged to a satisfactory level. In addition, any solution from a higher order scheme can be used to restart another solution of a lower scheme. This proved to be particularly useful when stepping through different rotational speeds.

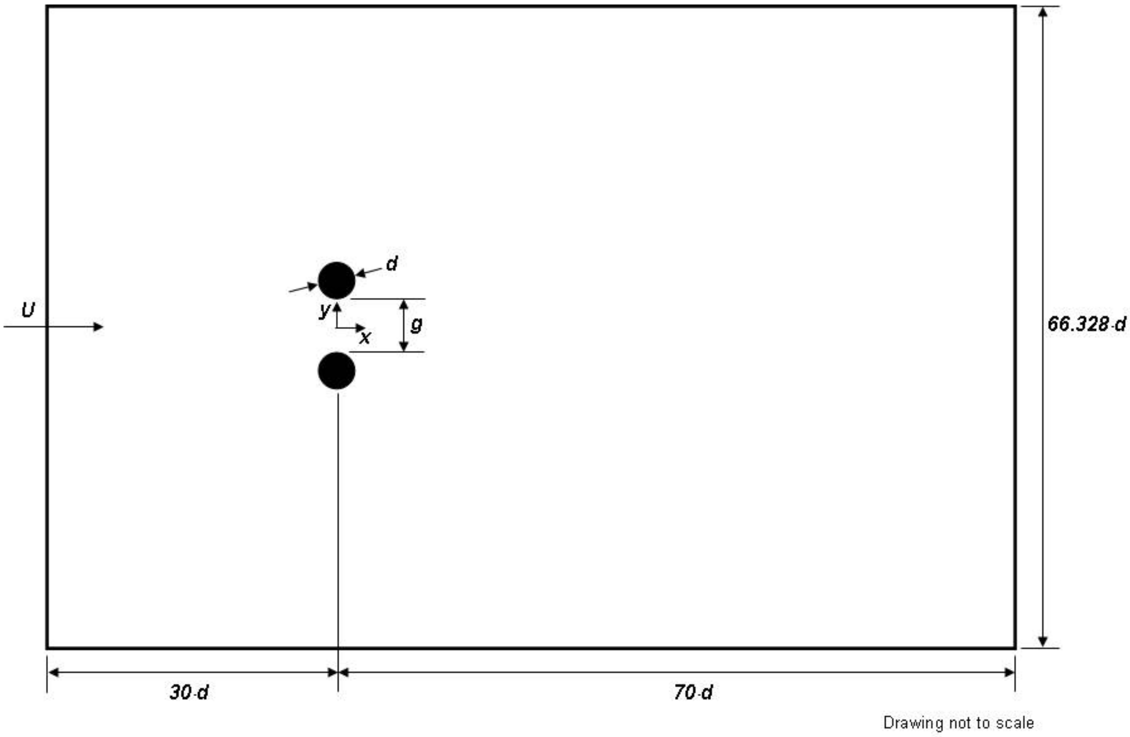

Figure 5.15: The geometry of the computational domain.

Both steady and unsteady flow solutions are considered. The results shown in the next section are determined when the computation reaches a statistically stable solution and which the solution from the impulsive start is excluded. Since the focus is primarily on the research of the suppression of the unsteady vortex shedding, it is

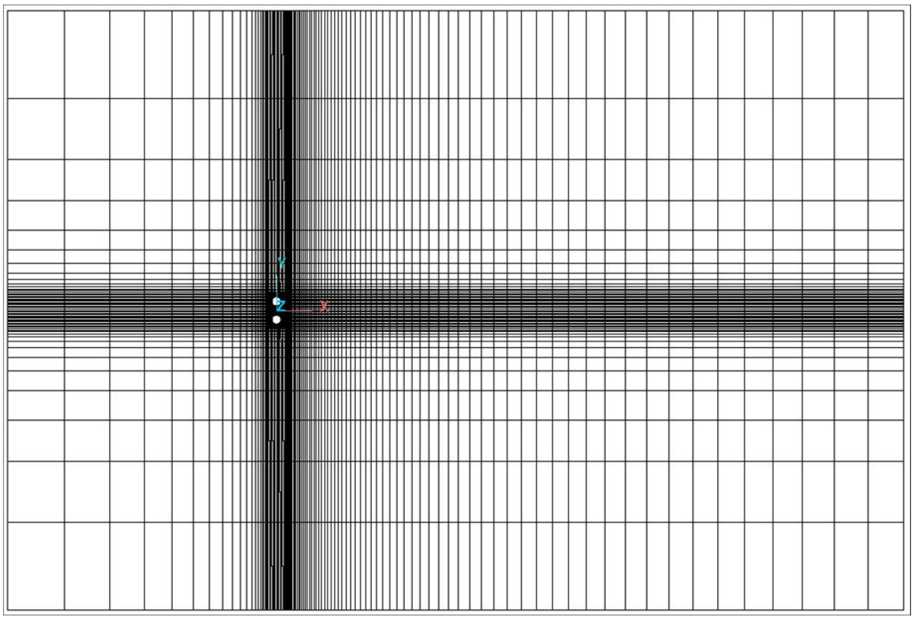

Figure 5.16: Mesh of the entire flow field ($g^* = 1$).

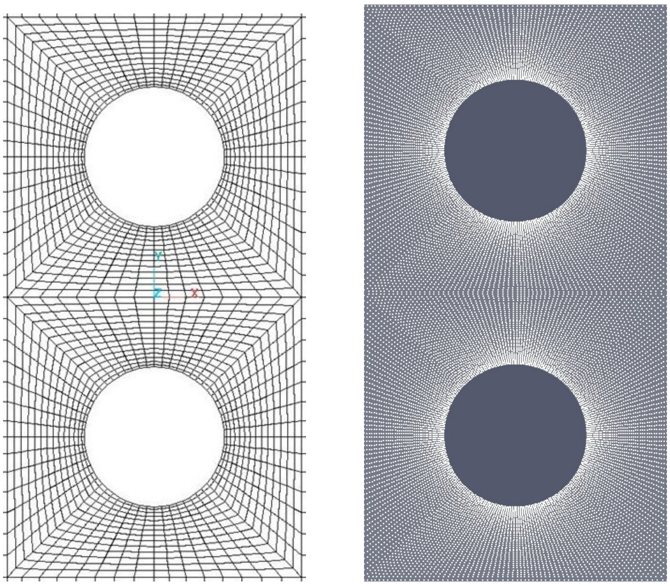

Figure 5.17: Left: Mesh around the cylinder pair surfaces ($g^* = 1$). Right: 4th order SD solution collocation points around the cylinder pair surfaces ($g^* = 1$).

of less interest as for how the final solution is established. Hence, in order to balance the solution accuracy and the computational time, the 4th order SD method is only implemented to obtain the final flow solution. This means, for $g^* = 1$ as an example, there are 112,000 degrees of freedom in the SD computational domain.

5.4.1 Doublet-like counter rotation

Here, the results for the doublet-like counter-rotating cylinder pair (see figure 5.14) with $g^* = 1$, 3 and 5, and $Re = 100$, 150 and 200 are presented. In this configuration, the cylinders rotate in a manner that enhances the interaction of the vortex streets in the wake of each individual cylinder, and there is a critical rotation rate at which the wake instabilities are suppressed completely. Increasing the gap spacing corresponds to attenuation in the interaction, corresponding to a higher critical rotational speed. Nonetheless, relatively low rotational speeds ($\Omega_{crit} < 2$) were required to suppress wake instabilities for all cases.

For $g^* = 3$ and 5, the stable anti-phase shedding mode was observed when the cylinders were rotated below Ω_{crit} for all Reynolds numbers. The case for $g^* = 3$ and $Re = 200$ is shown in figure 5.18. Note the excellent agreement between the SD computation and the independent experiment performed by Dewey and Smits at the Gas Dynamics Lab at Princeton University [70]. The experiments have been performed in a water tunnel using digital particle image velocimetry to visualize the flow. In this particular mode, the vortices shed by the cylinder pair remain stable and coherent throughout the entire domain. As the rotational speed increases, the vortex strength decreases until the unsteady vortex wake is entirely suppressed. At a rotational rate at or slightly above Ω_{crit}, vorticity lobes extend downstream from the surface of the cylinders, but with a further increase in rotational speed the vorticity remains concentrated in the immediate area of the cylinders.

For the cases with $g^* = 1$, the unstable in-phase vortex shedding mode was observed at $Re = 150$ and 200 for all rotational speeds below the critical value. At the lowest Reynolds number investigated, $Re = 100$, the vortices shed by the cylinder pair coalesced to form a single von Kármán vortex street, shown in figure 5.19. This

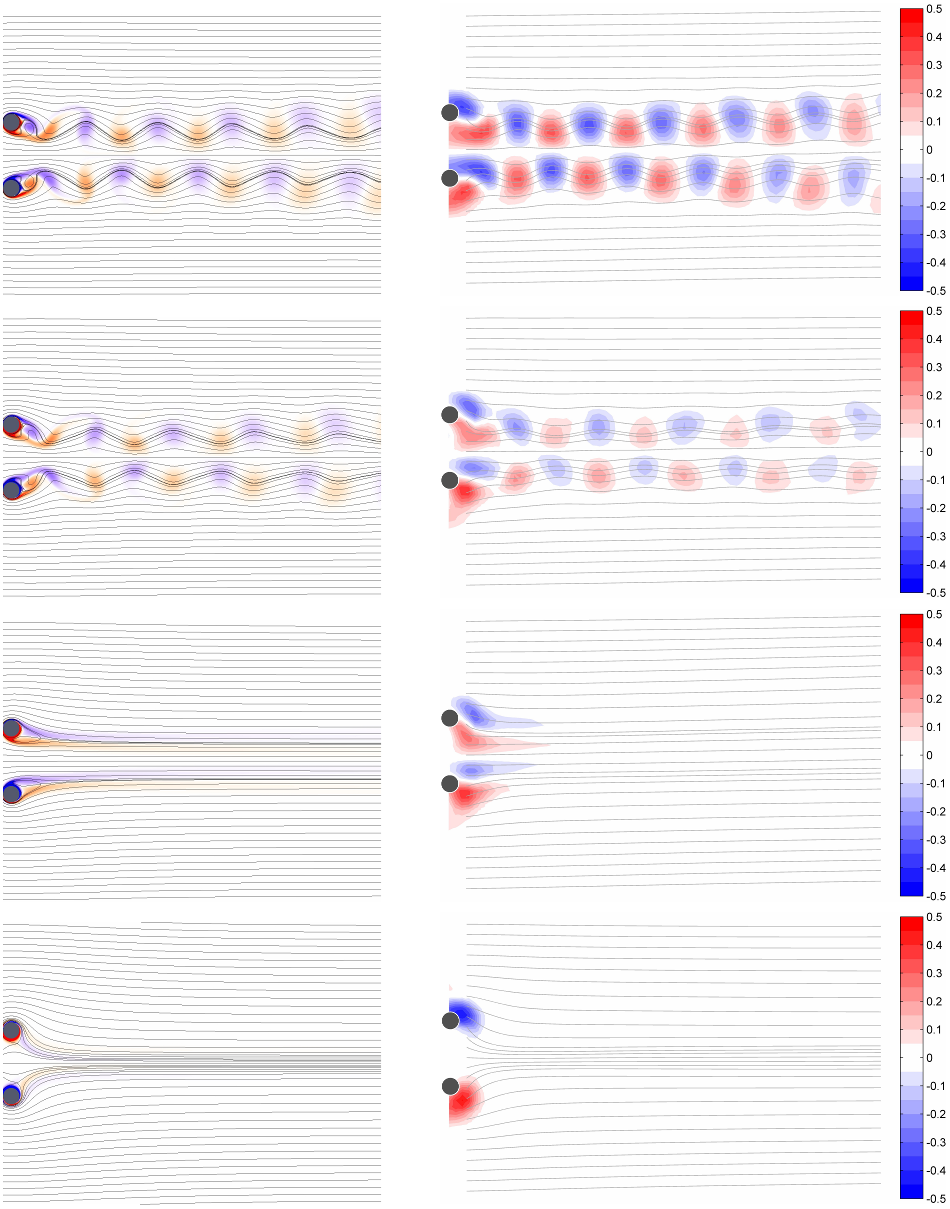

Figure 5.18: Doublet-like rotational configuration: streamlines and vorticity at various rotational speeds for $g^* = 3$, $Re = 200$. Left: computational results. Right: experimental results. First row, $\Omega = 1$; second row, $\Omega = 1.5$; third row, $\Omega = 1.85$ (computational) and 1.88 (experimental); fourth row, $\Omega = 3$. For this case, $\Omega_{crit} = 1.85$ (computational), and 1.88 (experimental). Vorticity contour levels for the computational and experimental results are the same.

phenomenon was also observed at the same Reynolds number by [106] for $g^* = 0.7$. In the case of a non-rotating cylinder pair, the single vortex street shedding mode is only observed at smaller gap spacings ($g^* = 0.4$), as found by Kang *et al.* [101], so that counter rotation of the cylinders decreases the gap spacing required to achieve this particular mode. A more detailed discussion of vortex suppression speeds is taken up in section 5.4.3.

Increasing the rotational speed above Ω_{crit} results in a closed vortex system taking the form of a virtual elliptical body, similar in appearance to that of a doublet in potential flow. The computational results clearly display the evolution of this flow pattern at $Re = 150$, as seen in figures 5.20, 5.21 and 5.22 for $g^* = 1$, 3 and 5 respectively. Note that prior to the formation of the virtual elliptical body, there exists a region of second instability which will be discussed later in section 5.4.4. The second instability is illustrated here for $\Omega = 3.25$ in figure 5.21 and $\Omega = 3.75$ in figure 5.22. The experimental DPIV data did not have sufficient spatial resolution to resolve the stagnation point created by the closed vortex system (P. Dewey and A. Smits, personal communication, 2010). Instead, streaklines in the immediate wake were visualized using 10 consecutive images obtained with a Sony HDR-SR10 HD camcorder recording at 30 frames per second. These streaklines, shown in figure 5.23, clearly illustrate the presence of the stagnation point in the wake of the cylinder pair, indicating the presence of the virtual elliptical body above a certain rotational speed. This also confirms the predictions of Chan and Jameson [69] using a lower-order numerical simulation.

The forces exerted on each cylinder are numerically evaluated in terms of lift and drag coefficients defined by:

$$C_L = \frac{2L}{\rho U^2 d}, \text{ and } C_D = \frac{2D}{\rho U^2 d}, \tag{5.2}$$

where L and D are the lift and drag force acting on the cylinder, computed by summing the normal and tangential forces from the pressure and viscous stress terms.

By rotating a cylinder, positive or negative lift can be generated depending on the direction of the spin. From potential flow theory, the lift force asymptotically

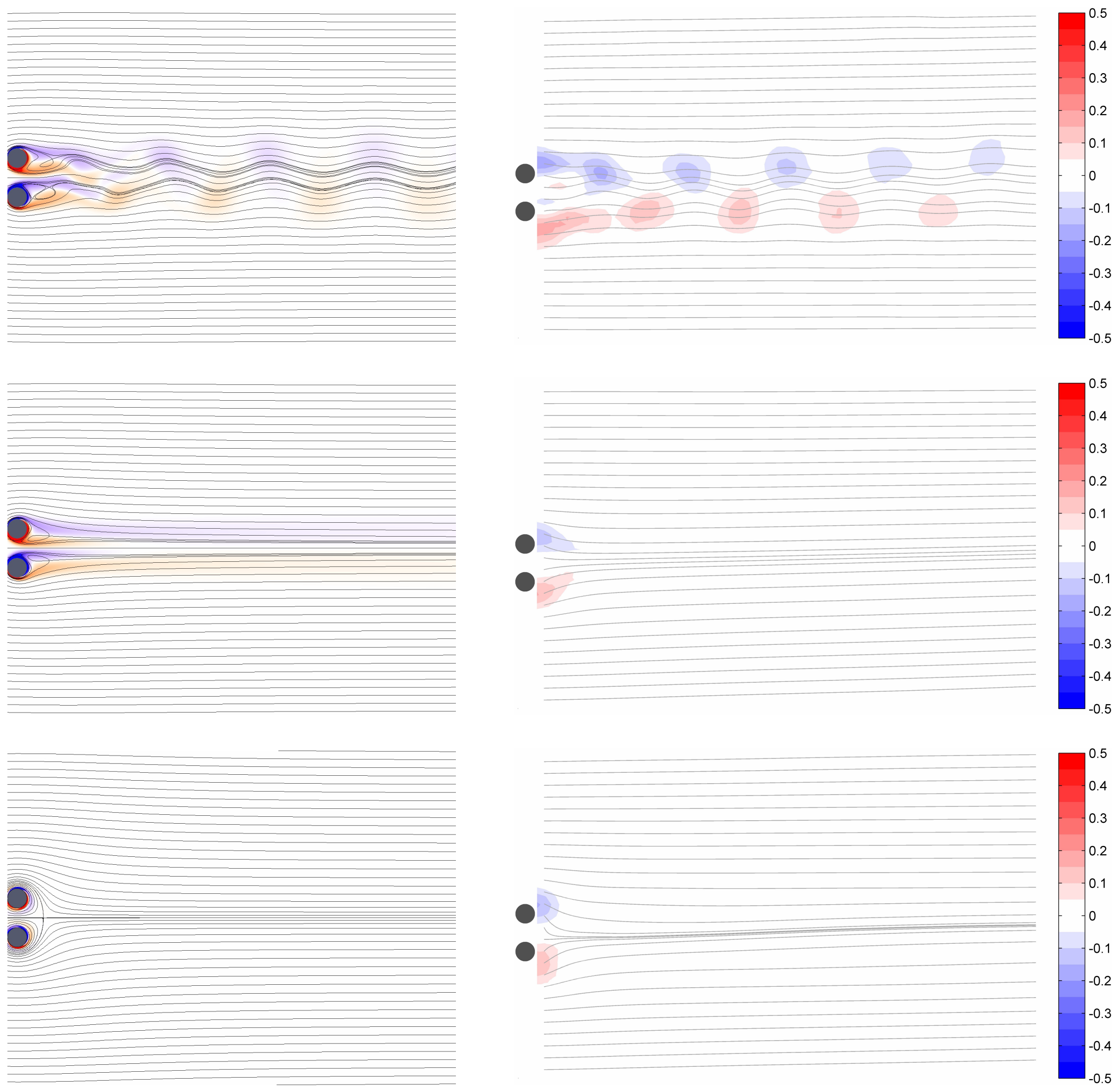

Figure 5.19: Doublet-like rotational configuration: streamlines and vorticity at various rotational speeds for $g^* = 1$, $Re = 100$. Left: computational results. Right: experimental results. First row, $\Omega = 1.2$; second row, $\Omega = 1.5$; third row $\Omega = 3$. For this case, $\Omega_{crit} = 1.35$ (computational), and 1.4 (experimental). Vorticity contour levels for the computational and experimental results are the same.

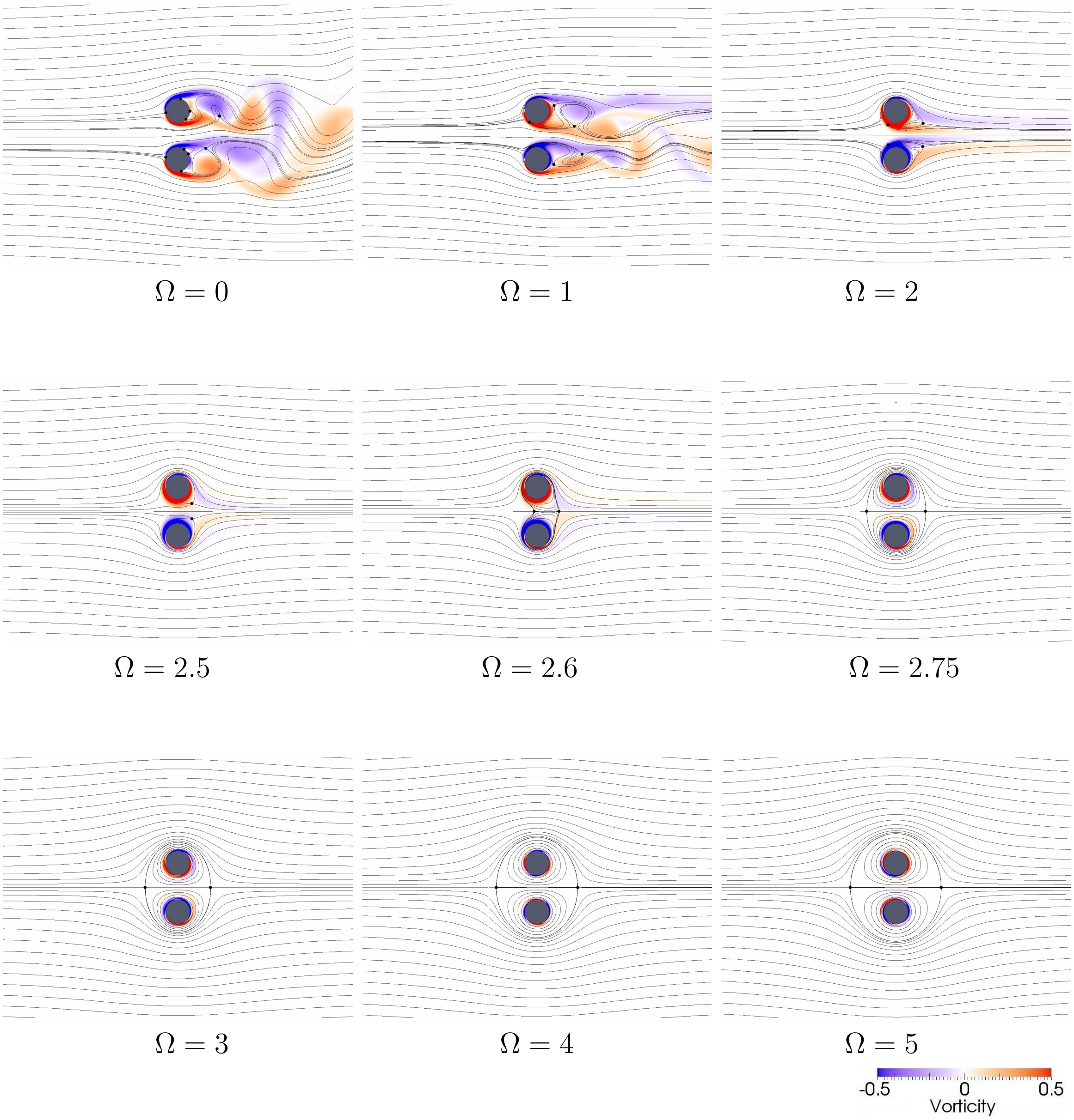

$\Omega = 0$ $\Omega = 1$ $\Omega = 2$

$\Omega = 2.5$ $\Omega = 2.6$ $\Omega = 2.75$

$\Omega = 3$ $\Omega = 4$ $\Omega = 5$

Figure 5.20: Evolution of virtual elliptical body for the doublet-like configuration (computational results): instantaneous streamlines and vorticity, $Re = 150$, $g^* = 1$. Stagnation points are represented by "•".

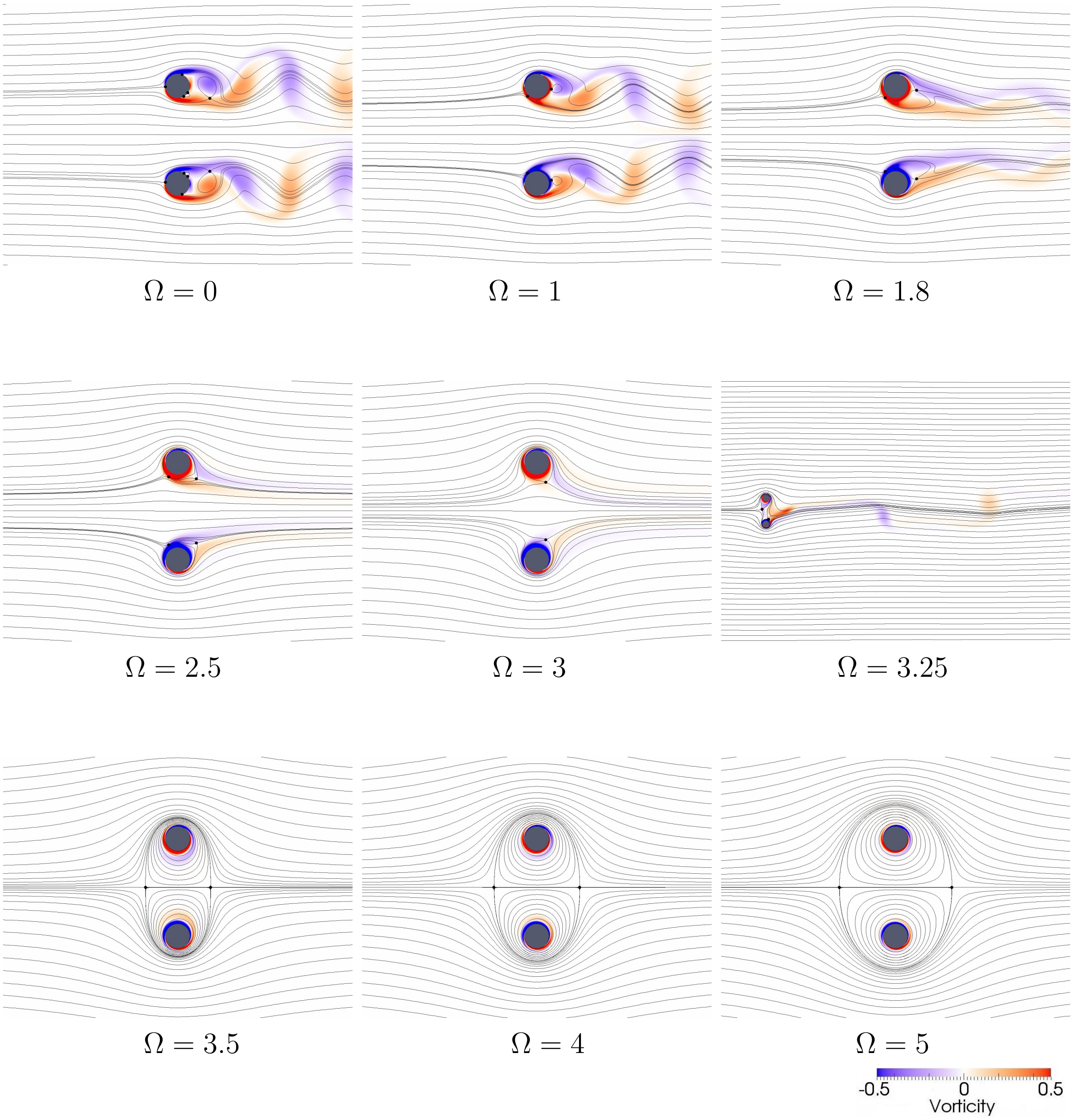

$\Omega = 0$ $\Omega = 1$ $\Omega = 1.8$

$\Omega = 2.5$ $\Omega = 3$ $\Omega = 3.25$

$\Omega = 3.5$ $\Omega = 4$ $\Omega = 5$

Figure 5.21: Evolution of virtual elliptical body for the doublet-like configuration (computational results): instantaneous streamlines and vorticity, $Re = 150$, $g^* = 3$. Stagnation points are represented by "●".

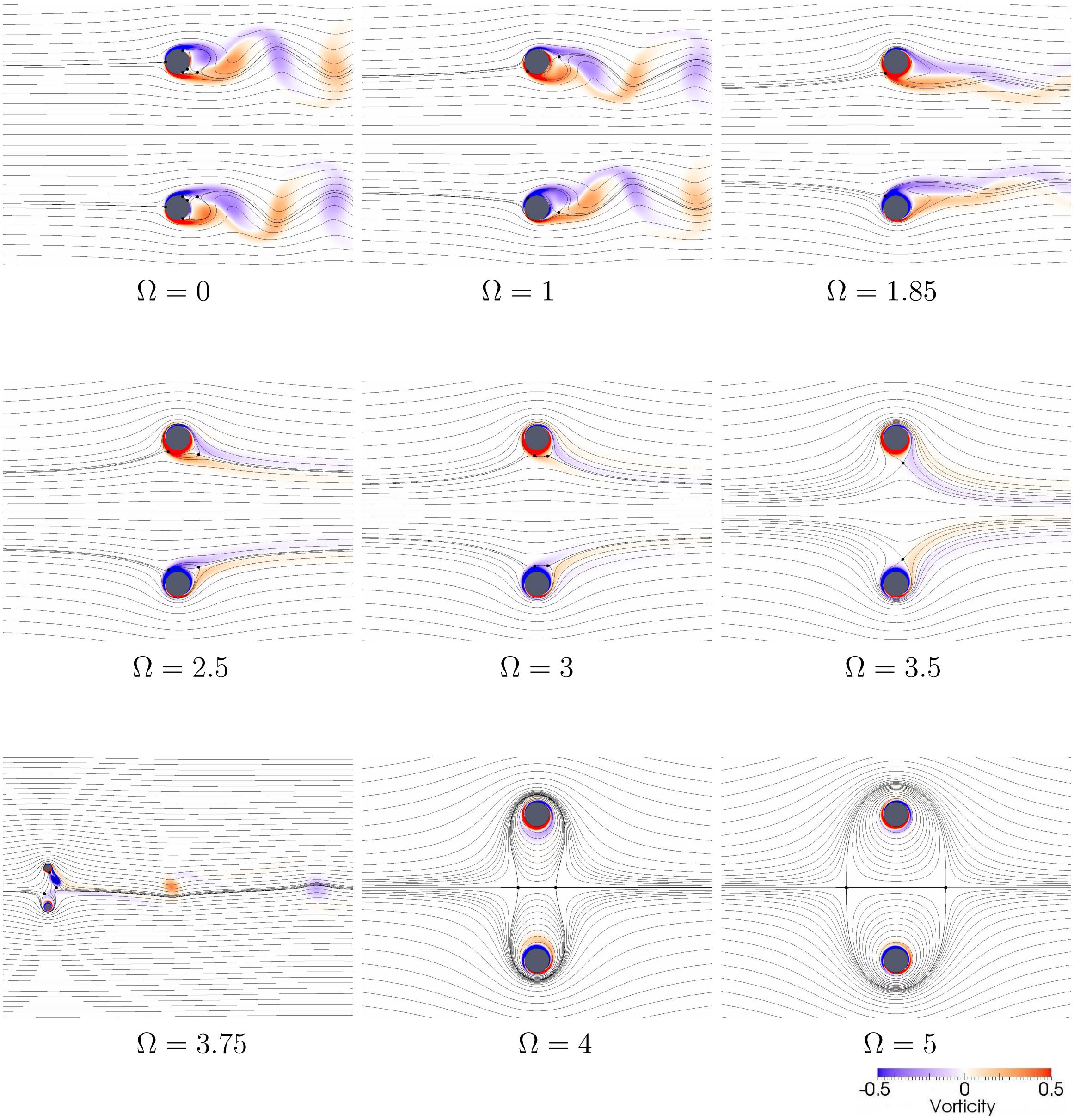

$\Omega = 0$ $\Omega = 1$ $\Omega = 1.85$

$\Omega = 2.5$ $\Omega = 3$ $\Omega = 3.5$

$\Omega = 3.75$ $\Omega = 4$ $\Omega = 5$

Figure 5.22: Evolution of virtual elliptical body for the doublet-like configuration (computational results): instantaneous streamlines and vorticity, $Re = 150$, $g^* = 5$. Stagnation points are represented by "●".

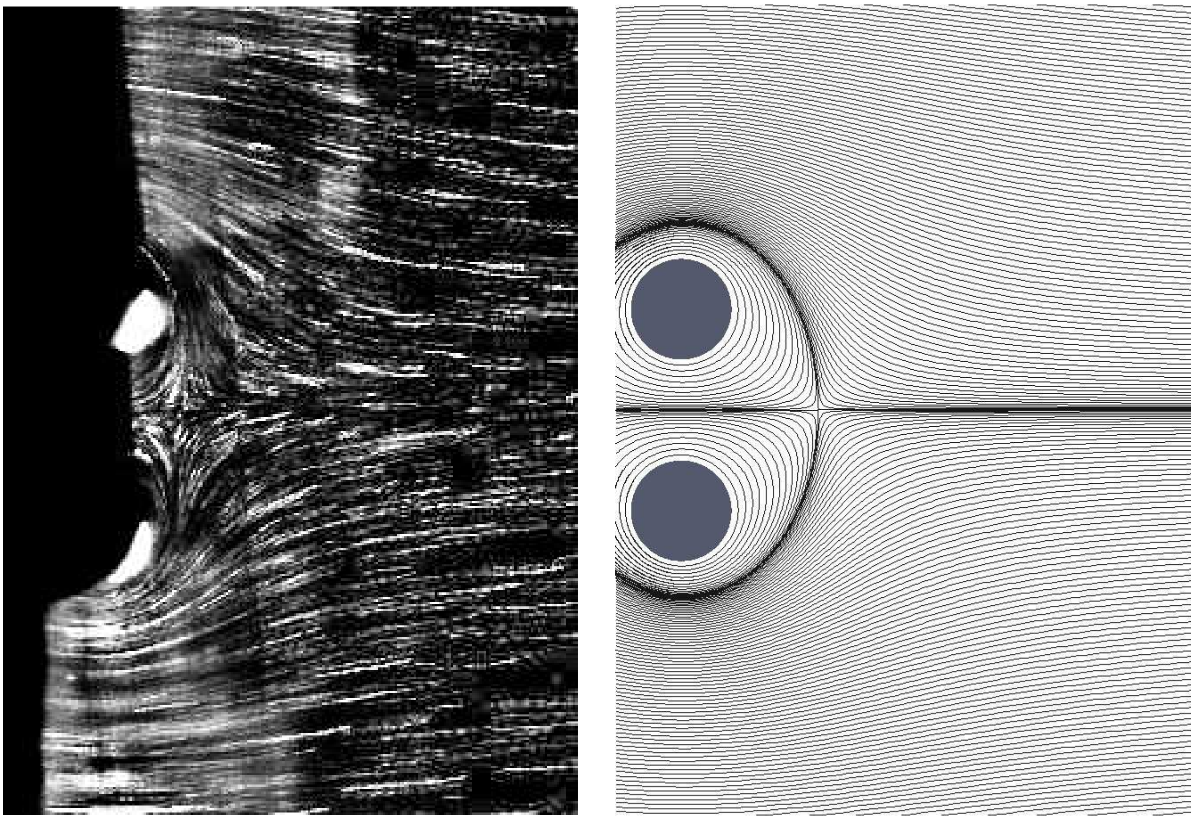

Figure 5.23: Experimental streaklines (left) and computational streamlines (right) showing the existence of the stagnation point and virtual elliptical body for the doublet-like rotational configuration: $g^* = 1$, $Re = 150$, $\Omega = 3.1$.

increases with spin rate. In a viscous fluid, however, Mittal and Kumar [80] showed that at $Re = 200$ potential flow theory over-predicts the lift curve of a single rotating cylinder in the range of $0 \leqslant \Omega \leqslant 5$. As in their calculation, the main contribution to the lift in the case of the rotating cylinder pair comes from the pressure term while the viscous stress contribution is relatively small. Figure 5.24 shows that the time-averaged values of the lift coefficient $\overline{C_L}$ for each cylinder in the doublet-like rotation have the same amplitude but opposite sign, thus yielding a net zero lift for the pair, as expected. The results are virtually independent of Reynolds number, and in the lower speed range ($0 \leqslant \Omega \leqslant 2.5$) they are also independent of gap spacing and the value of $\overline{C_L}$ for each cylinder is close to the value obtained by Mittal and Kumar [80] at $Re = 200$ for a single rotating cylinder. For most of the investigated values of the Reynolds number and g^*, the lift forces cause a repelling force on each cylinder. The only exception is for $g^* = 1$ and $\Omega > 4$ where the faster rotation produces an attracting force. The interaction between the two cylinders prevents the exponential increase of $\overline{C_L}$ with rotation rate seen in the case of the single cylinder. The maximum lift occurs at $\Omega \approx 2.65$ for $g^* = 1$, $\Omega \approx 4.5$ for $g^* = 3$, and $\Omega > 5$ for $g^* = 5$.

As to the behavior of the time-averaged drag coefficient, $\overline{C_D}$, figure 5.25 shows that it generally decreases with increasing rotational rate. The results are only shown for one cylinder because the problem is symmetrical in the mean. As found in the case of the mean lift coefficient, the degree of wake interaction and its effect on the mean drag coefficient depends primarily on g^* and that the effect of Reynolds number is small. For $0 < \Omega < 2.5$, most of the drag reduction comes from the pressure term. For $2.5 \leqslant \Omega < 3$, a small net thrust is observed in this "transitional" range. For $3 \leqslant \Omega \leqslant 5$, the pressure drag rises almost linearly with increasing speed while the viscous drag drops linearly at about the same rate, so that the total mean drag is approximately zero. It is in this speed range that the virtual elliptic body forms and grows larger with respect to the increasing speed. Note that for $g^* = 1$ and $\Omega \approx 4$, $\overline{C_L}$ is also zero thus yielding a neutrally stable and steady flow system.

Also plotted on figures 5.24 and 5.25 are the results obtained by Chan and Jameson [69] for the lift and drag coefficients at $Re = 150$ and $g^* = 1$ using a second order accurate commercial incompressible flow code. The results are generally in good agreement with the current study, and both investigations show the same trends in the lift and drag behavior. The current work finds the cross-over speed, where $\overline{C_L}$ of each cylinder is zero, at $\Omega \approx 4.1$, versus 4.3 from the previous study. This cross-over speed is where the lift force on each cylinder transitions from repelling to attracting. Both studies also find similar characteristics in the drag behavior in that there is a slight positive net thrust prior to the formation of the closed vortex system, that is, the virtual elliptic body. In the speed range where the elliptic body is formed, the form drag balances out the viscous drag yielding approximately zero net drag and the flow pattern resembles a potential doublet. Additionally, the unsteady vortex suppression speed is $\Omega = 1.6$ compared to the value of 1.5 found by Chan and Jameson [69]. Nonetheless, small discrepancies are observed in the lift coefficient where the virtual elliptic body is observed ($\Omega \geq 3$). Two primary contributing factors to the differences are the order of accuracy of the method and the effect of compressibility. The present results have been computed with the fourth order accurate version of the SD scheme at Mach 0.1. Based on the results reported by Ou *et al.* [57], the compressibility effect is believed to be very small, while fourth order accuracy is sufficient to produce negligible numerical errors with the mesh that has been used in this work. Accordingly, the current results are believed to be more reliable than those presented by Chan and Jameson [69].

For the low speed range where the pressure term accounts for most of the drag reduction, the mechanism for the mean drag reduction is similar for all gap spacings. The transitional range where a small net thrust is observed occurs at a faster speed with increasing gap size, that is, at $Re = 150$, $2.5 < \Omega < 3.2$ for $g^* = 3$ and $2.5 < \Omega < 3.6$ for $g^* = 5$. In general, the larger the gap size, the more the vortex wakes become like those shed from a single spinning cylinder. As noted in section 5.2, one very interesting result reported by Stojković *et al.* [96, 97] as well as Mittal and Kumar [80] for a single spinning cylinder is the appearance of a second instability in the form of a one-sided vortex shedding mode. In the present case of a pair of counter-rotating cylinders in the doublet configuration, a similar second instability is observed, due to the release of the one-sided vortex that is built up by slow moving vorticity near the stagnation point for each cylinder. As a result, the key difference for the larger gap sizes compared to the case with $g^* = 1$ is the existence of a second instability prior to the formation of the virtual elliptic body. There is a slight jump in the mean drag when the second instability occurs above $\Omega = 3$ for $g^* = 3$ and above $\Omega = 3.5$ for $g^* = 5$. At higher rotation rates, the virtual elliptic body appears and there is an exact balance between the pressure and viscous drags that produces zero mean drag.

The drag forces were not obtained in the experiment, but the time-averaged velocity profiles give some insight into the overall momentum balance. To get a sense for the momentum balance for the experimental and computational work, the streamwise velocity contours and the corresponding velocity profiles are shown in figures 5.27 and 5.28 for the case of $g^* = 1$ and $Re = 100$, where the single von Kármán vortex street is present. The velocity profiles are taken at a distance of 10 diameters downstream of the cylinder pair. At lower rotational speeds, a velocity deficit is observed to extend far downstream of the cylinder pair. As the rotational speed increases, the velocity deficit region moves closer to the cylinder pair, until at the highest rotational speeds investigated the deficit region is almost entirely contained in the region where the virtual elliptic body can be found. This results in a very small velocity deficit, indicating that the drag due to momentum flux is negligible in this instance. As observed from the experiments, the velocity deficit decreases to almost zero over the range of $\Omega = 2$ to 4, which is consistent with the computational findings.

The Strouhal numbers, $St = fd/U$, are shown in figure 5.26. Only cases resulting in an anti-phase shedding are shown since this mode produces a distinctly dominant shedding frequency f. There is excellent agreement between the results from the SD computation and those from the experiment. The Reynolds number dependence is most noticeable in going from $Re = 100$ to 150, but is relatively small in going from 150 to 200. The effect of gap spacing is not significant, except in the region of the second instability, that is for $3 < \Omega < 4$. For $g^* = 1$, the shedding mode is predominantly in-phase for $0 < \Omega < 1$ and therefore these data points were not included.

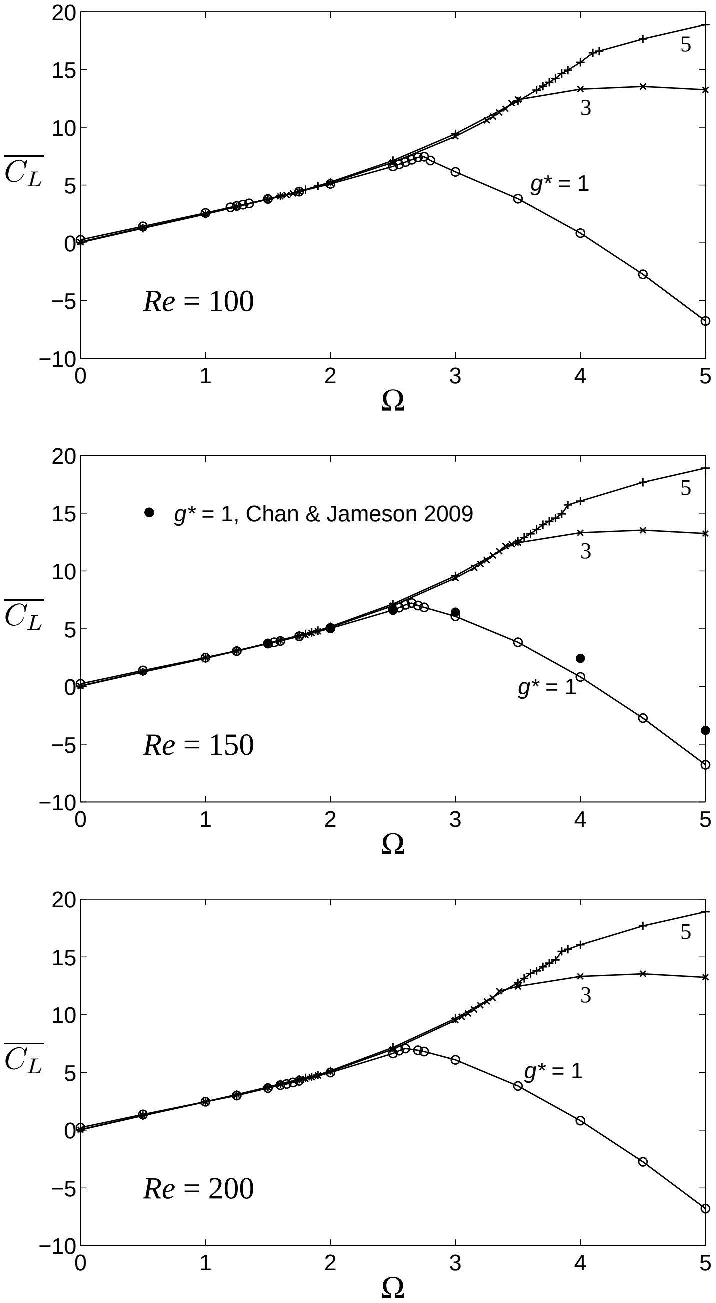

Figure 5.24: Flow past a doublet-like counter-rotating cylinder: numerically determined time-averaged values of the lift coefficient (upper cylinder).

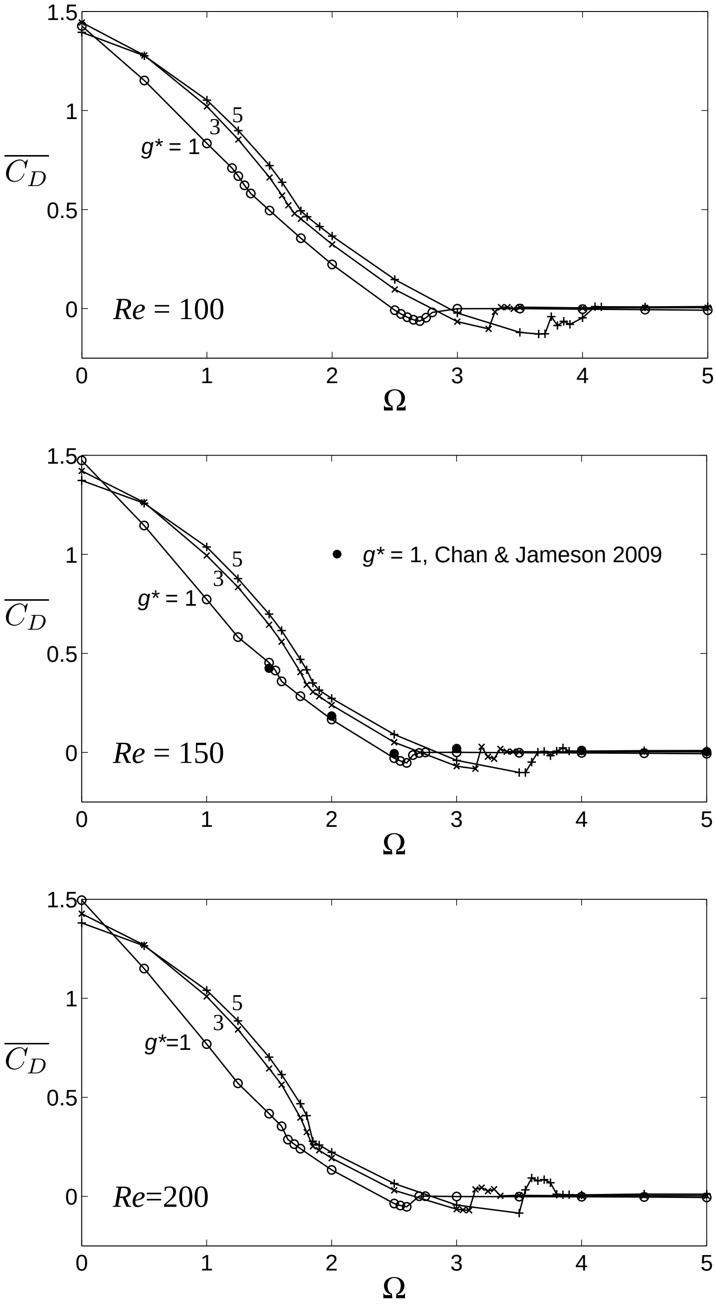

Figure 5.25: Flow past a doublet-like counter-rotating cylinder: numerically determined time-averaged values of the drag coefficient (upper cylinder).

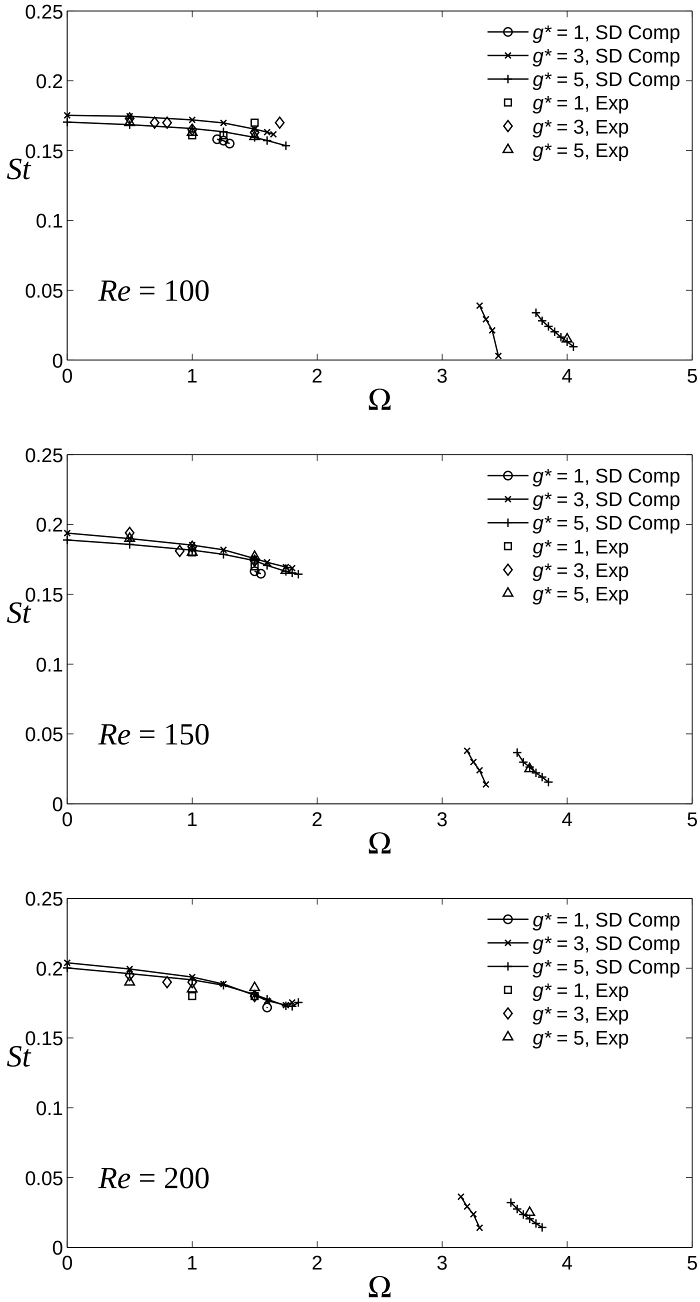

Figure 5.26: Flow past a doublet-like counter-rotating cylinder: numerically determined Strouhal number (anti-phase shedding only).

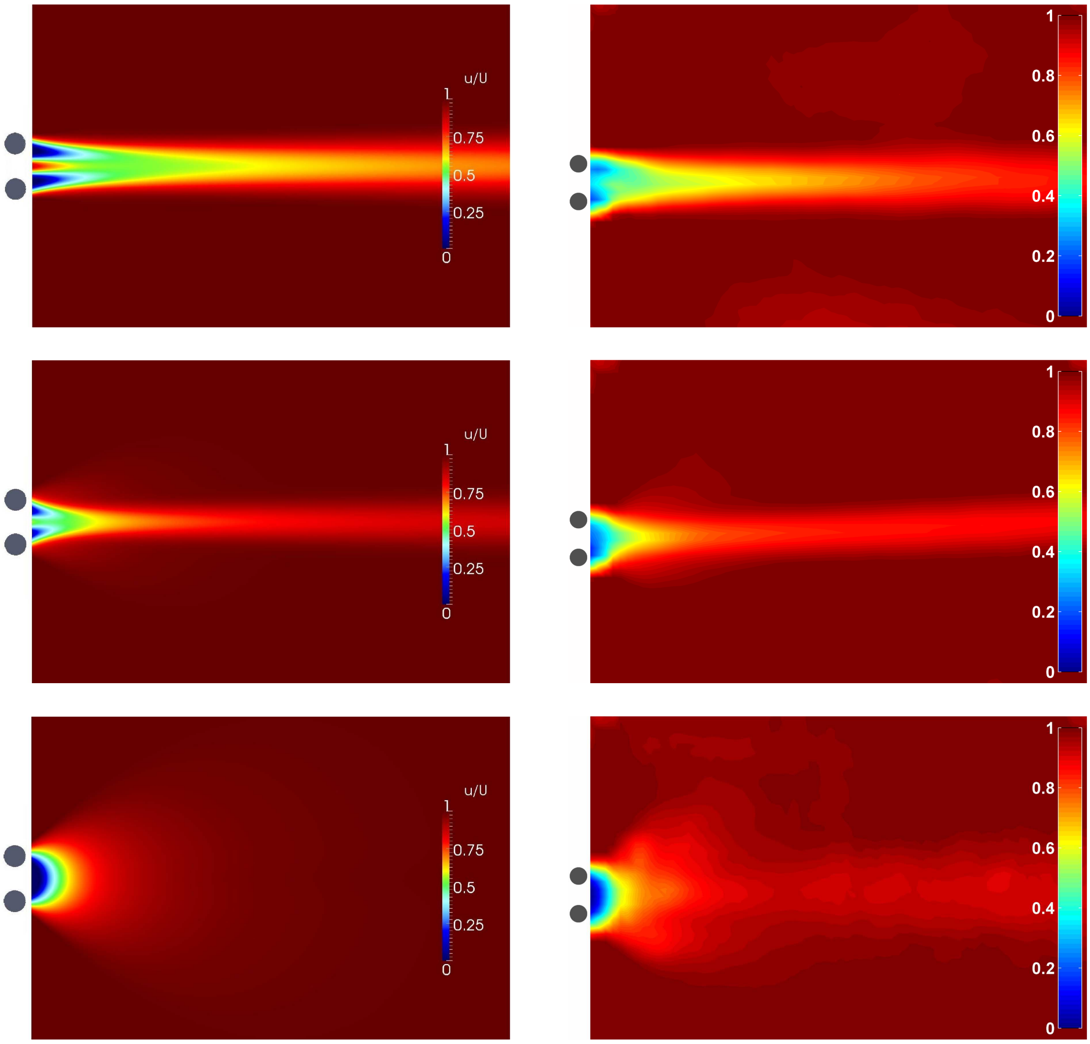

Figure 5.27: Doublet-like rotational configuration: normalized streamwise velocity contours at various rotational speeds for $g^* = 1$, $Re = 100$. Left: computational results. Right: experimental results. First row, $\Omega = 1.5$; second row, $\Omega = 2$; third row, $\Omega = 4$

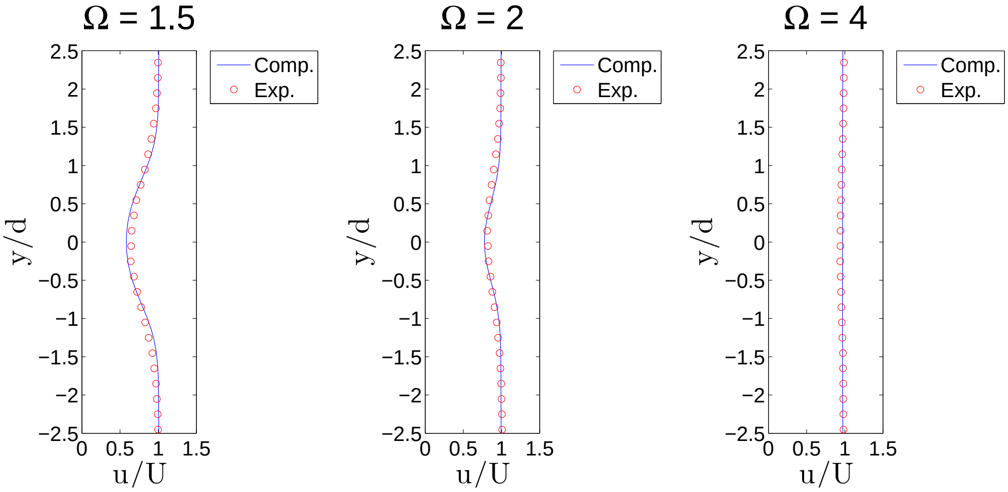

Figure 5.28: Velocity profiles at $10d$ downstream from cylinder center

Simple vortex shedding model of a doublet-like counter-rotating cylinder pair

Figure 5.29 shows the instantaneous separatrices, saddle points (S) and centers (C) as a function of various steady rotational rates following Perry's model of vortex shedding mechanism [105]. For a steady rotation, a circulating region is formed along the cylinder surface by a one-directional separatrix whose center coincides with the center of a cylinder. This circulation region enlarges as the rotational speed increases. The associated saddle point is formed slightly upstream of the cylinder center but moves further downstream with increasing rotational speeds.

In the immediate near-wake region of each cylinder, there is a saddle point and center whose behaviors depend on the rotational speed of the cylinder. At $\Omega = 1$, the flow is unsteady and the alleyways (3 per each cylinder as shown in (a) of figure 5.29) open, widen and close indicating a vortex shedding process. As the rotational speed increases, the widths of these alleyways become narrower, and the overall flow becomes more stable. When the flow is steady at $\Omega = 1.5$, the flow is symmetric along the centerline between the two cylinders. There is only one alleyway that exists for each cylinder. As the rotational speed increases further, the width of each alleyway narrows and while the circulating region around each cylinder enlarges, the circulating region in the near wake becomes smaller. The rear saddle point in the near wake appears to move much more rapidly toward the front saddle point. At $2.43 < \Omega < 2.44$, there appears to be a transition region where the upper and lower pair of separatrices merge and the front saddle points vanish. In this transition, the two pairs of separatrices merged causing the upper and lower alleyways to close. A new alleyway along the centerline is then formed by the two newly merged separatrices as shown in (e), (f), and (g). This alleyway continues to narrow as the rotational speed increases.

A second transition occurs at $2.56 < \Omega < 2.565$ where both saddle points associated with each cylinder are forced toward one another at the symmetric centerline as shown in (g). The alleyway is extremely narrow at this point. However, these two saddle points cannot merge at the centerline as there would be 3 incoming and 3 outgoing paths and would thus violate the notion of 2 stable manifolds (incoming paths) and 2 unstable manifolds (outgoing paths). Therefore, two new saddle points are then formed along the centerline and the alleyway no longer exists. As the rotational speed increases, the forward saddle point is pushed further upstream. At $\Omega = 2.755$, a symmetry line coincides the vertical line across the cylinders centers and the virtual elliptic body is formed.

5.4.2 Reverse doublet-like counter rotation

When the cylinder pair is rotated in a reverse doublet configuration (see figure 5.14), the interaction of the vortex wakes between the two rotating cylinders is substantially reduced when the gap spacing is increased because the rotation serves to push the wakes away from one another. Figure 5.30 compares the computational and experimental vorticity contours and streamlines at various rotation rates for $Re = 200$ and $g^* = 3$. It is apparent that the vortex shedding from one cylinder becomes increasingly independent from that of the other cylinder as the rotation rate increases. However, the effect of gap size on the wake interaction is important at the smallest gap ($g^* = 1$) where an in-phase shedding mode exists at all Reynolds numbers for $\Omega < 1$. As shown figure 5.31, the vortex shedding mode transitions to a stable,

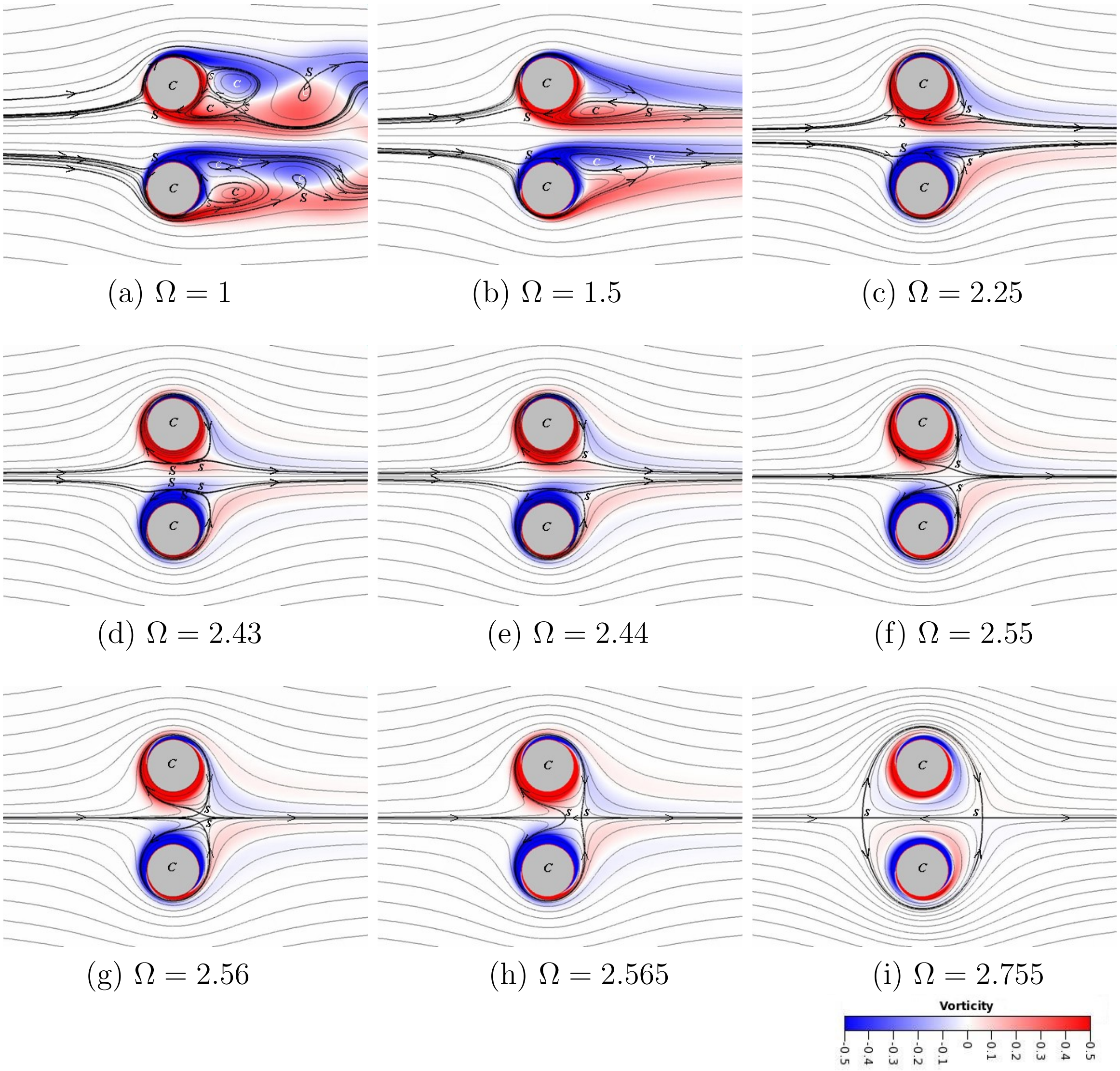

(a) $\Omega = 1$ (b) $\Omega = 1.5$ (c) $\Omega = 2.25$

(d) $\Omega = 2.43$ (e) $\Omega = 2.44$ (f) $\Omega = 2.55$

(g) $\Omega = 2.56$ (h) $\Omega = 2.565$ (i) $\Omega = 2.755$

Figure 5.29: Evolution of virtual elliptical body for the doublet-like configuration (computational results): instantaneous streamlines and vorticity, $Re = 150$, $g^* = 1$. Separatrices are represented by darker lines with arrows. 'S' is a saddle point. 'C' is a center point.

anti-phase pattern at $\Omega = 1$. This synchronization helps stabilize the vortex street pair and maintain its form further downstream. In this regime, a vortex shed from the upper cylinder is counter-balanced by a vortex of opposite sign shed from the lower cylinder. The upper vortex street perfectly mirrors the lower with the line of symmetry being half way between the cylinders, and the strength of each vortex is maintained for long distances downstream. As the gap increases, however, the wake interaction drastically reduces (see figure 5.32 for $g^* = 3$ and figure 5.33 for $g^* = 5$), thus effectively causing the vortex wakes from each cylinder to behave like that from a single rotating cylinder.

The mean lift coefficients, shown in figure 5.34, are almost independent of gap size and Reynolds number, but the effect of the gap is much more apparent in the drag curves shown in figure 5.35. It should be noted that as the gap increases, the value of $\overline{C_D}$ approaches the value of a single rotating cylinder as given by Mittal and Kumar [80]. This is also the case for $\overline{C_L}$. As observed by Chan and Jameson [69], the reverse doublet-like rotation produces an attracting force with a magnitude that increases with the rotation rate. The Strouhal numbers plotted in figure 5.36 show little dependence on the gap spacing and rotation rate, although there is a distinct Reynolds number dependence, especially at the lower rotation rates. Also, the results obtained from the SD computation generally agree very well with the experimental results.

5.4.3 Unsteady vortex suppression

The standard deviation of the lift and drag coefficients for the doublet-like rotation are shown in figure 5.37; the corresponding values for the reverse doublet-like are shown in figure 5.38. The standard deviation gives a reasonably good prediction of the critical rotation speed, Ω_{crit}, where the unsteady wakes are suppressed, in that steady flow is observed when the standard deviation value is zero.

The computationally determined values of Ω_{crit} are compared with the experimental values in figure 5.39, and they are summarized in table 5.2. There is excellent

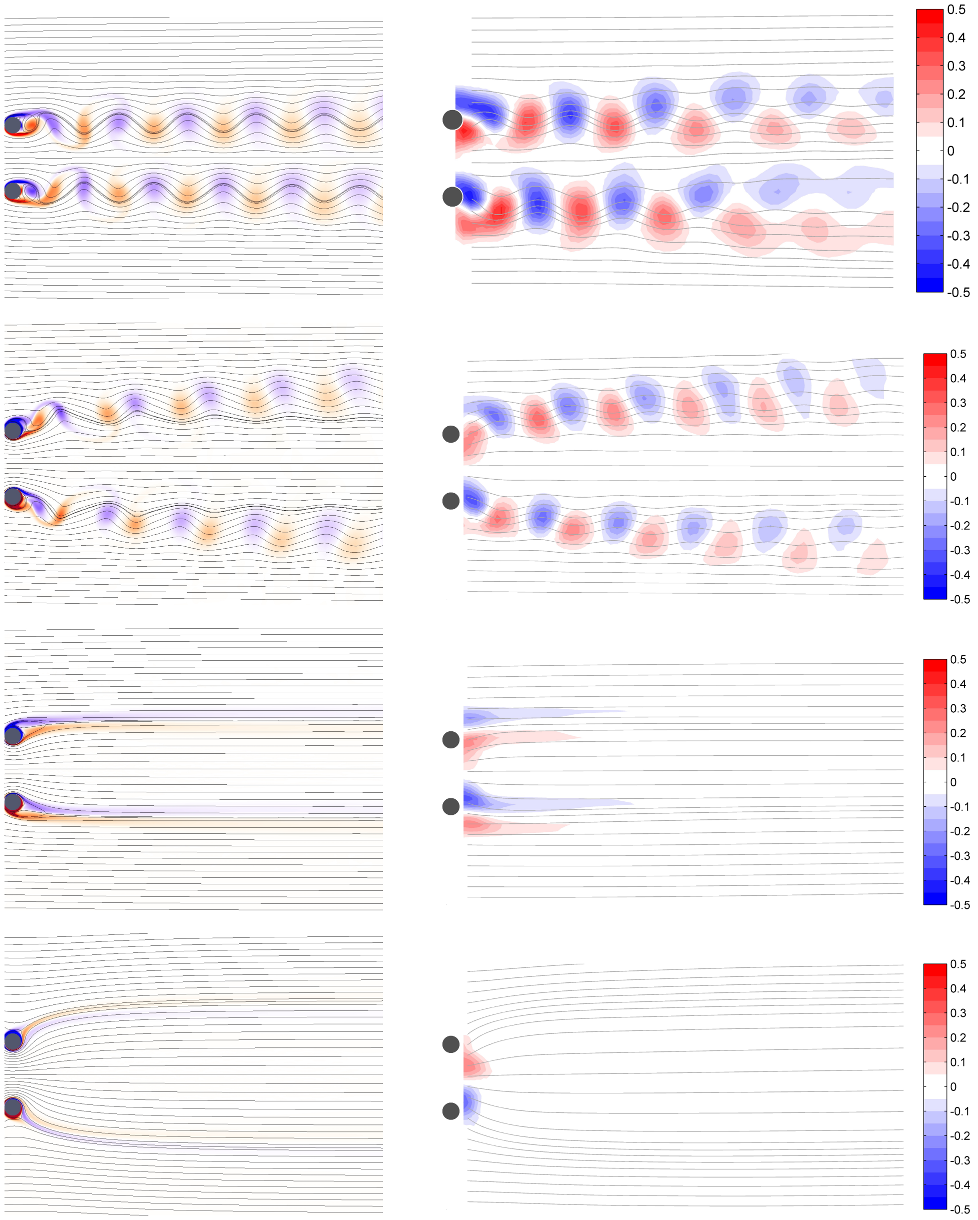

Figure 5.30: Reverse doublet-like rotational configuration: streamlines and vorticity at various rotational speeds for $g^* = 3$, $Re = 200$. Left: computational results. Right: experimental results. First row, $\Omega = 0$; second row, $\Omega = 2$; third row, $\Omega = 2.4$; fourth row, $\Omega = 5$. Vorticity contour levels for both computational and experimental results are the same.

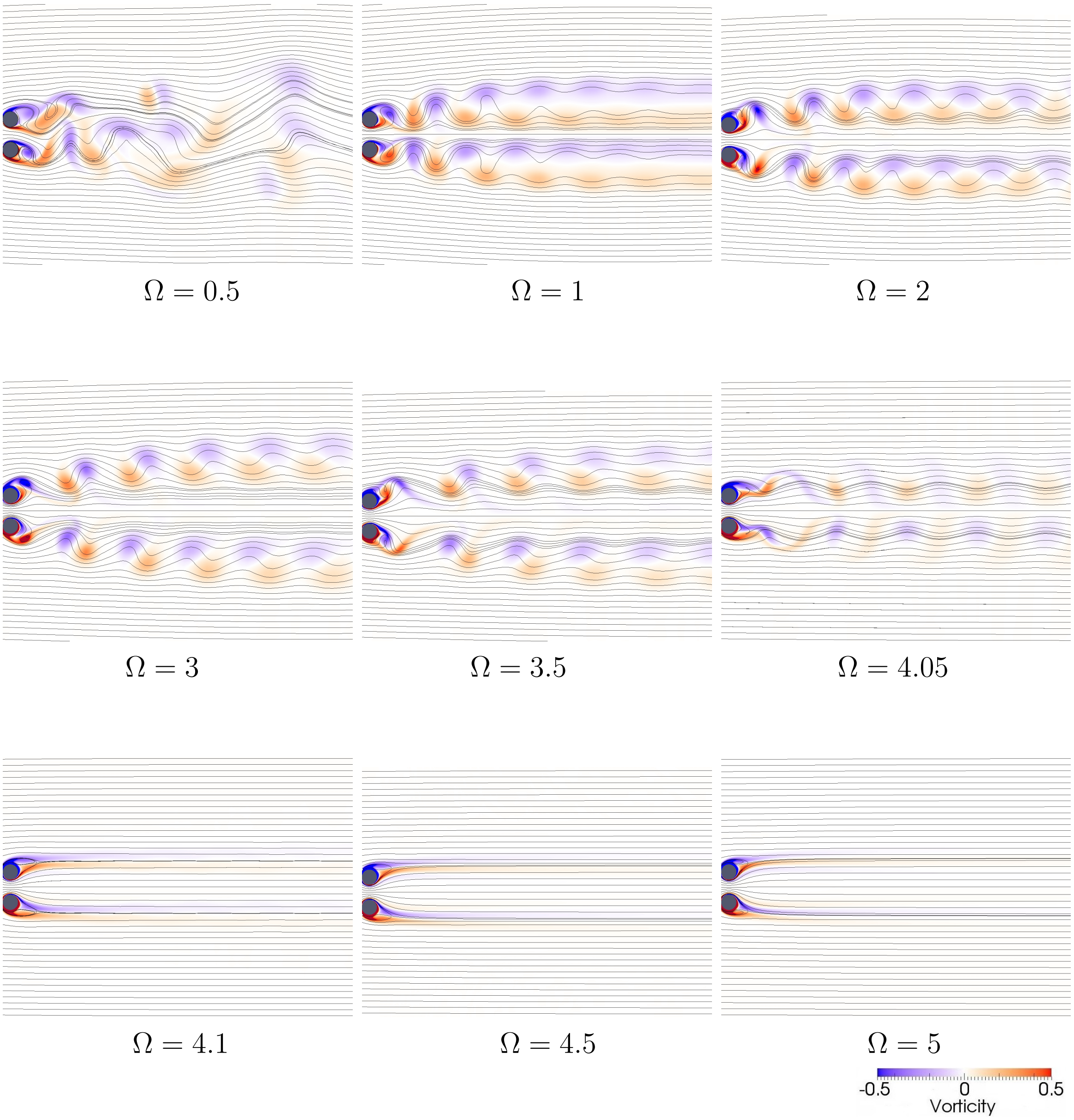

$\Omega = 0.5$ $\Omega = 1$ $\Omega = 2$

$\Omega = 3$ $\Omega = 3.5$ $\Omega = 4.05$

$\Omega = 4.1$ $\Omega = 4.5$ $\Omega = 5$

Figure 5.31: Instantaneous streamlines and vorticity for reverse doublet-like counter rotating cylinder (computational results): $Re = 150$, $g^* = 1$.

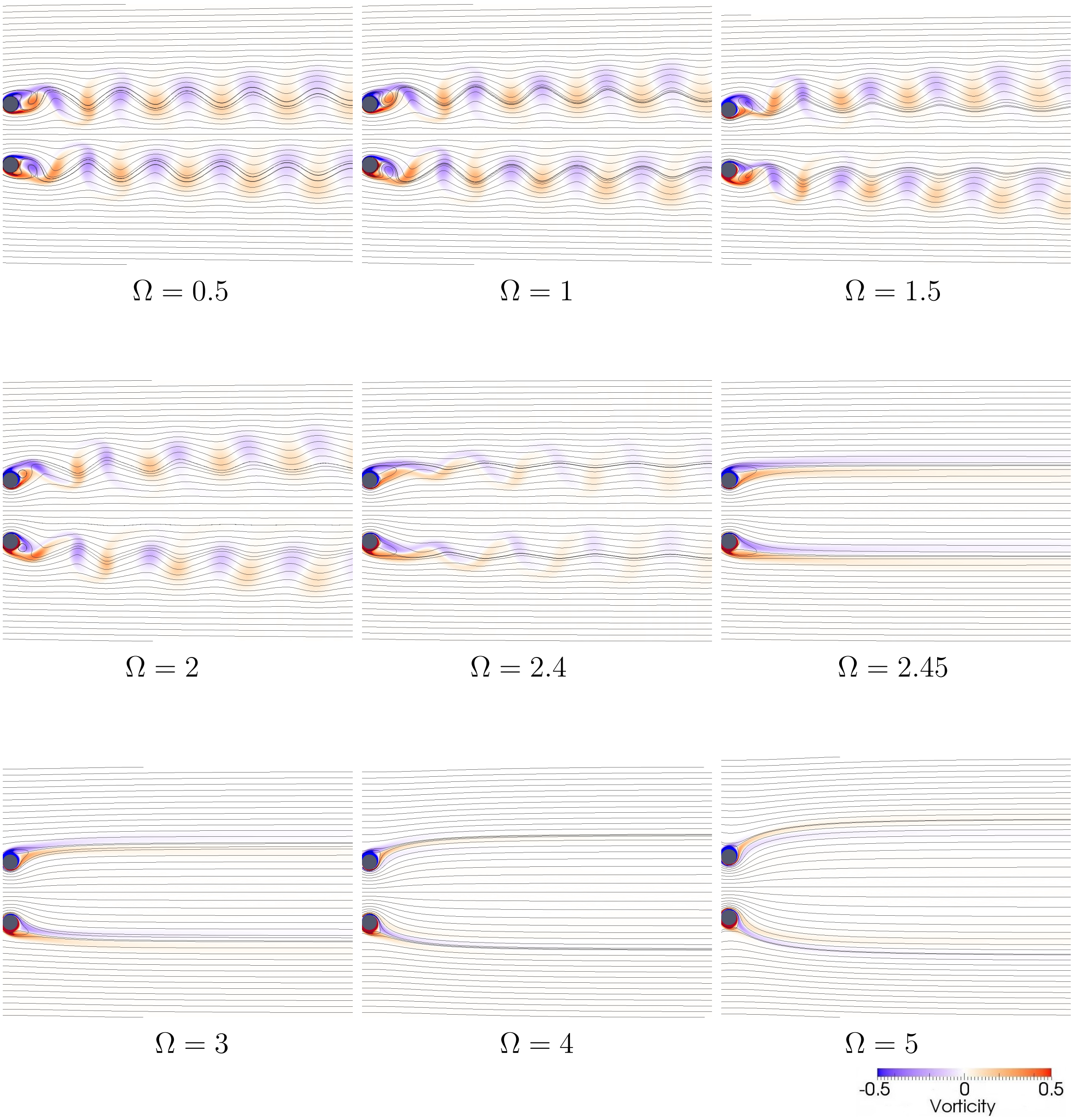

$\Omega = 0.5$ $\Omega = 1$ $\Omega = 1.5$

$\Omega = 2$ $\Omega = 2.4$ $\Omega = 2.45$

$\Omega = 3$ $\Omega = 4$ $\Omega = 5$

Figure 5.32: Instantaneous streamlines and vorticity for reverse doublet-like counter rotating cylinder (computational results): $Re = 150$, $g^* = 3$.

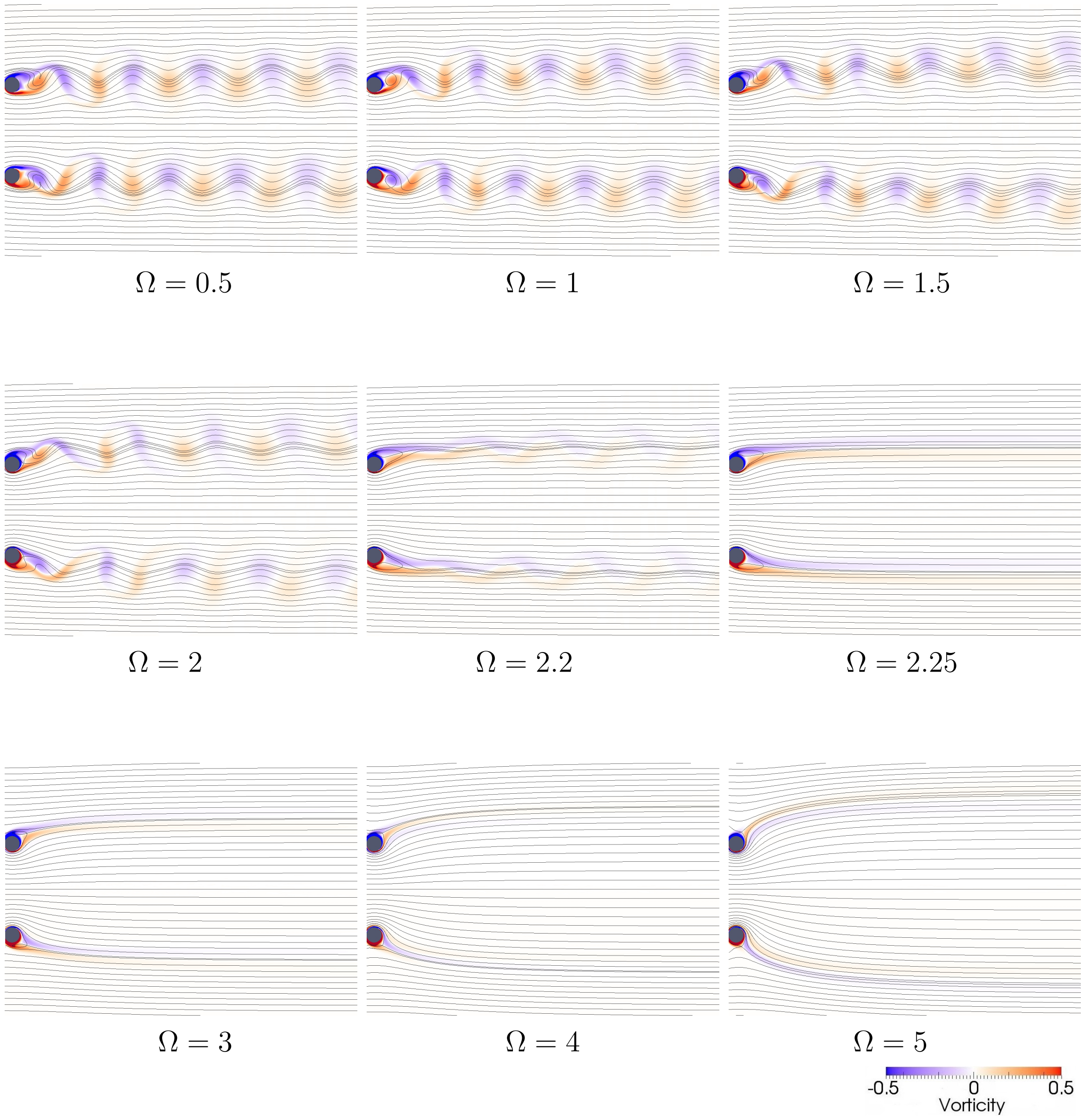

$\Omega = 0.5$ $\Omega = 1$ $\Omega = 1.5$

$\Omega = 2$ $\Omega = 2.2$ $\Omega = 2.25$

$\Omega = 3$ $\Omega = 4$ $\Omega = 5$

Figure 5.33: Instantaneous streamlines and vorticity for reverse doublet-like counter rotating cylinder (computational results): $Re = 150$, $g^* = 5$.

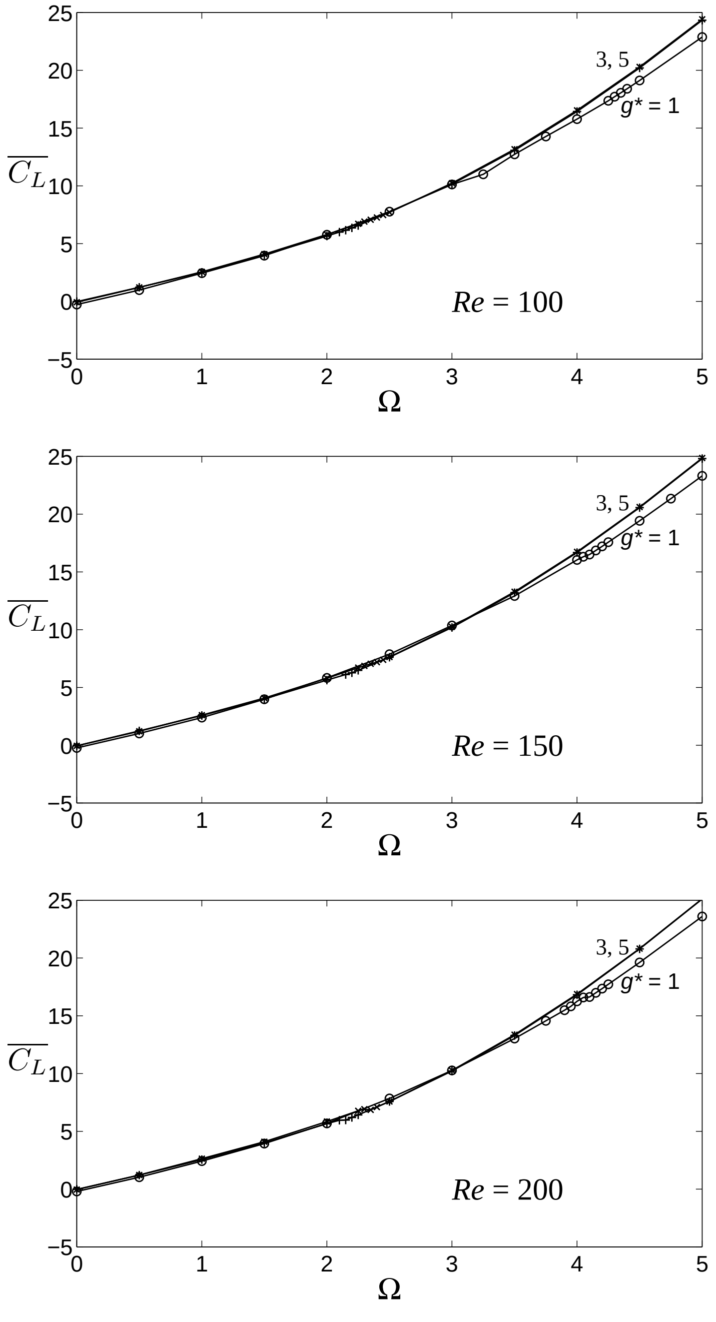

Figure 5.34: Flow past a reverse doublet-like counter-rotating cylinder: numerically determined time-averaged values of lift coefficient (lower cylinder).

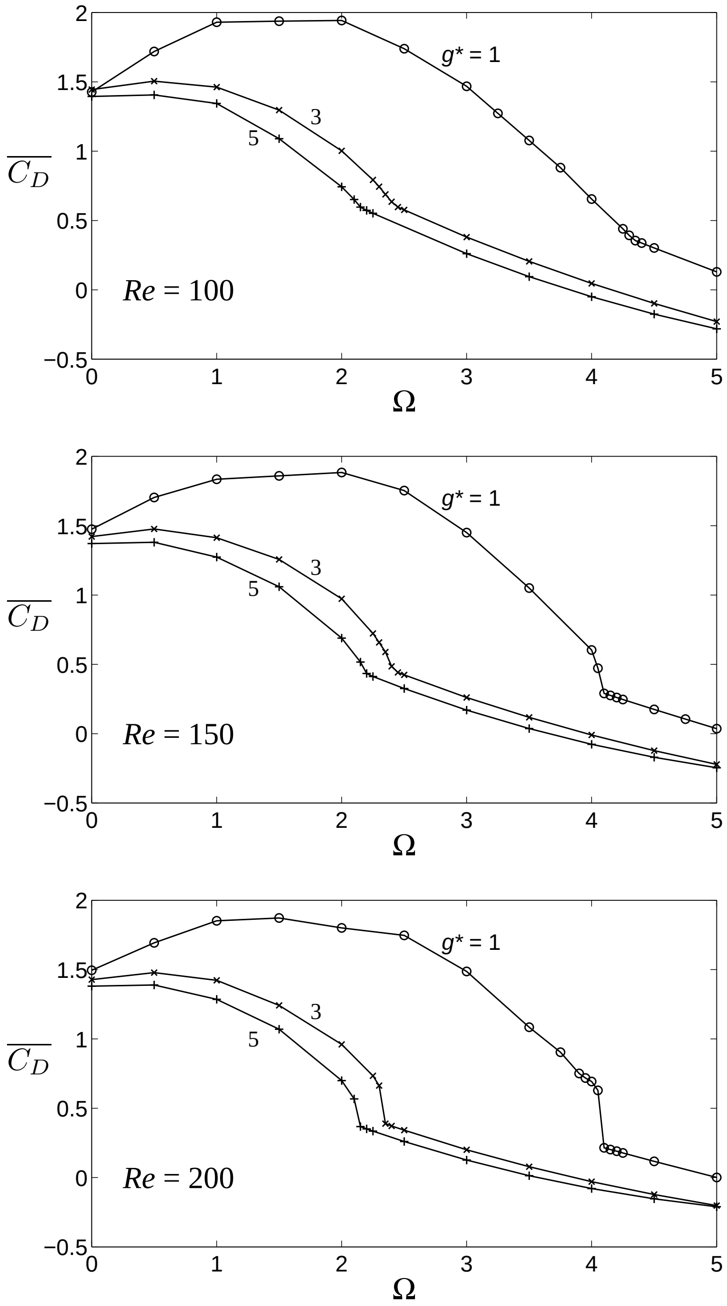

Figure 5.35: Flow past a reverse doublet-like counter-rotating cylinder: numerically determined time-averaged values of drag coefficient (lower cylinder).

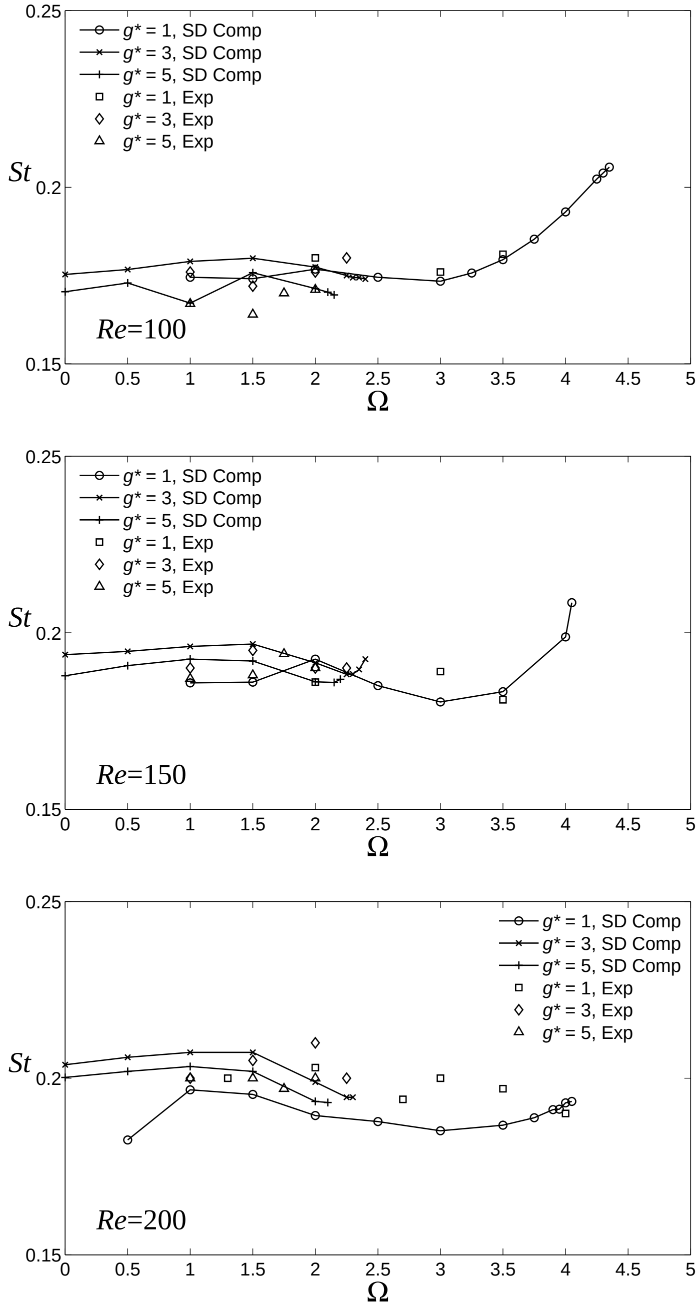

Figure 5.36: Flow past a reverse doublet-like counter-rotating cylinder: numerically determined Strouhal number (anti-phase shedding only).

agreement for all cases that were investigated, except for the reverse doublet configuration at $g^* = 1$ where the computational results are approximately 10 to 20 % larger than the experimental ones. Observations of the particle motion in the DPIV experiments suggest that at higher rotational speeds the flow exhibits a noticeable degree of three-dimensionality, particularly in the case of $g^* = 1$. Thus, it is possible that this discrepancy occurs because the computations used in this work were strictly two-dimensional. Nevertheless, the critical rotational speed monotonically decreased with increasing gap spacing, and the data suggest that Ω_{crit} depends more strongly on gap spacing than it does on Reynolds number.

For the doublet-like cylinder rotation (figure 5.39), $\Omega_{crit} < 1.9$ in all cases, and its value monotonically increases with increasing gap spacing and Reynolds number. The results presented by Yoon *et al.* [106] and the current investigation only have one point of overlap ($Re = 100$, $g^* = 3$), but in both studies the critical speed for vortex suppression was found to be 1.7. However, as seen in the figure 5.37, there is a small region of instability at speeds above Ω_{crit} for the larger gaps. This second instability mode occurs in the doublet-like configuration at $\Omega_{crit} \approx 3.25$ for $g^* = 3$ and $\Omega \approx 3.75$ for $g^* = 5$, but is suppressed for $g^* = 1$. As indicated earlier, this instability is related to the same phenomenon observed in the case of a single rotating cylinder, as investigated by Stojković *et al.* and Mittal and Kumar.

Rotation of the cylinder pair in the reverse doublet-like configuration reduces the interaction of the vortex streets resulting in higher critical rotation speeds (that is, $\Omega_{crit} > 2$). This is in contrast to the doublet-like configuration where increasing the gap spacing reduces the vortex suppression speeds. For $g^* = 1$, the critical speed is as high as $\Omega_{crit} = 4.4$, indicating that the proximity of a nearby cylinder promotes the instability of the wake. At the largest spacing, $g^* = 5$, Ω_{crit} collapses near 2.3 for all Reynolds numbers. Also, an increase in the gap spacing results in a monotonic decrease in the critical speed.

When the results for both rotational configurations are compared, it is observed that they appear to converge to a single value with increasing gap size. As noted earlier, this is not surprising, in that with increasing gap size the interaction between the two cylinder wakes diminishes, and in the limit it is expected that the two wakes to

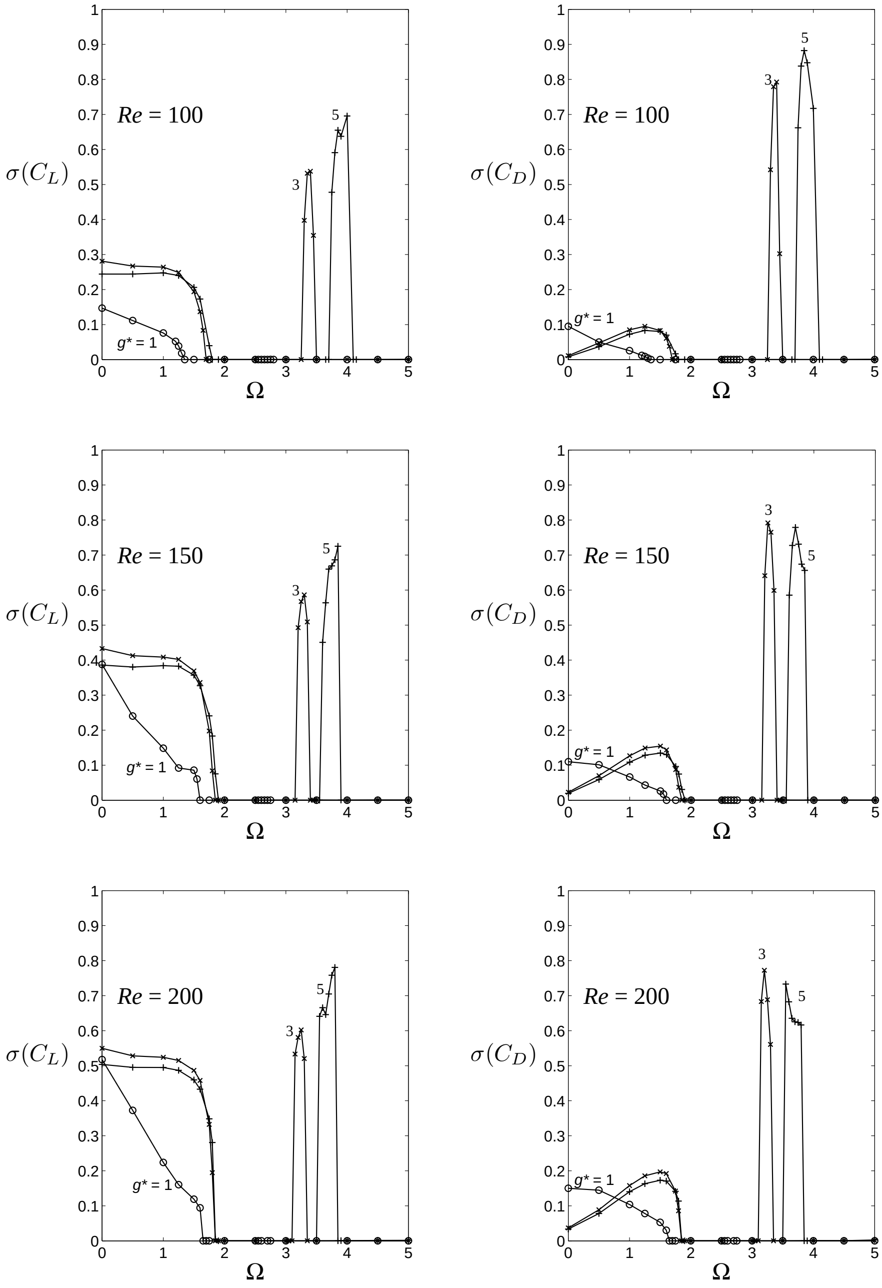

Figure 5.37: Flow past a doublet-like counter-rotating configuration: standard deviation of the coefficients of lift (left) and drag (right), obtained numerically.

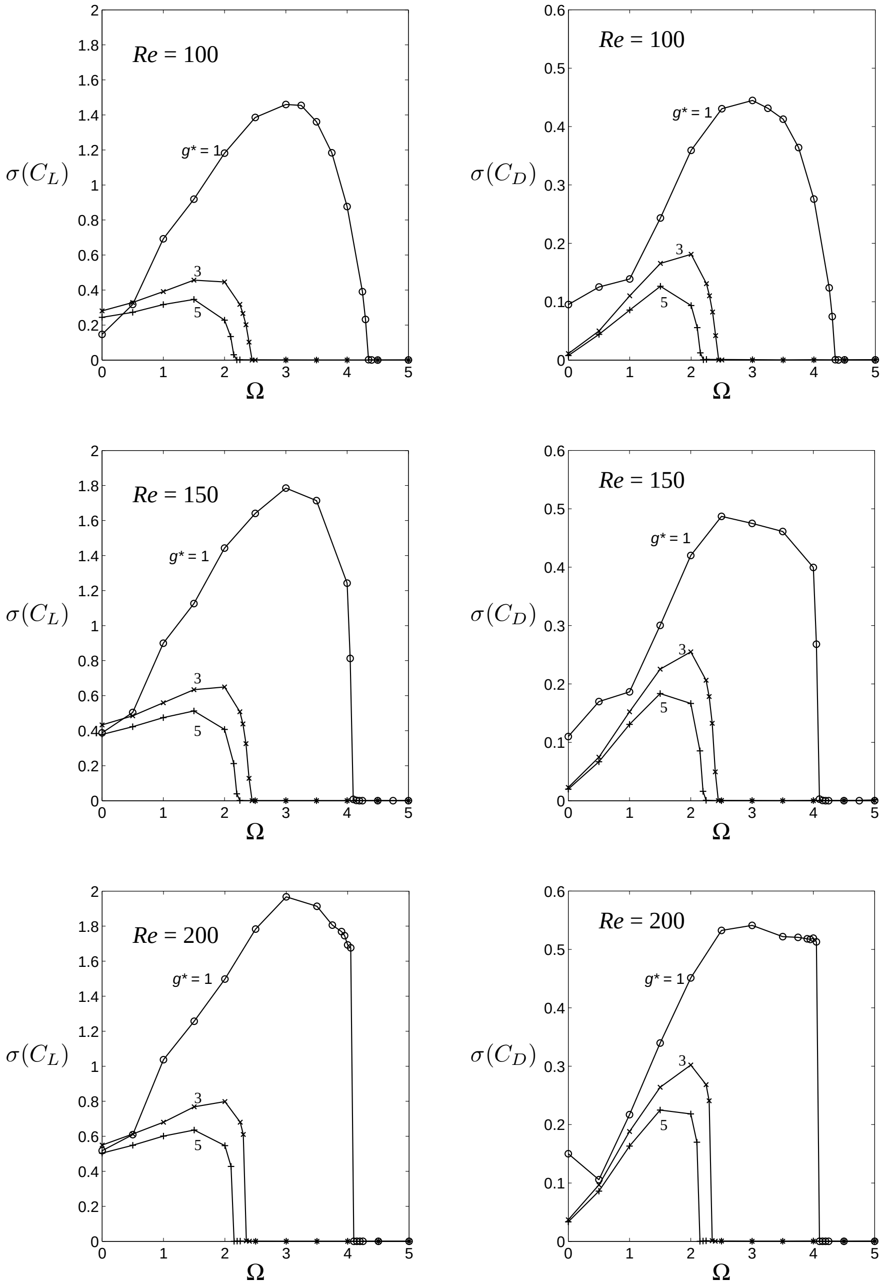

Figure 5.38: Flow past a reverse doublet-like counter-rotating configuration: the standard deviation of coefficients of lift (left) and drag (right).

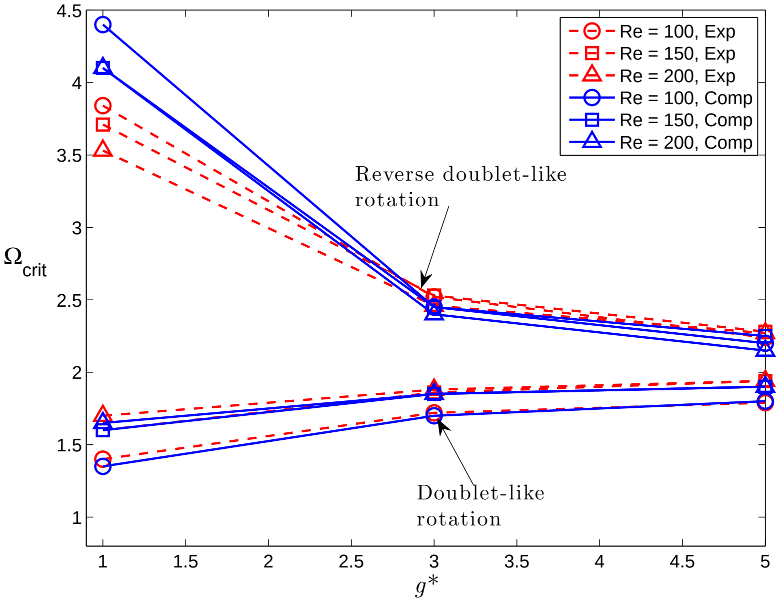

Figure 5.39: Critical rotation speed for vortex suppression.

become independent and to have Ω_{crit} approach the value to suppress vortex formation in the wake of a single rotating cylinder. Kang [101] found that for a single rotating cylinder at $Re = 100$, $\Omega_{crit} = 1.8$, and at $Re = 160$ it was 1.9, and Mittal and Kumar [80] reported the first critical suppression speed for a single cylinder to be 1.91 at $Re = 200$. These values are very similar to the convergent value suggested here, which gives $\Omega_{crit} \approx 1.9$ at $Re = 100$, and approximately 2 at $Re = 150$.

5.4.4 The second region of instability

In figure 5.37 there is an evidence for a small region of instability at speeds above Ω_{crit} for the doublet-like configuration that depends on the gap spacing. This region is essentially the secondary instability which also appears in the case of a single rotating cylinder as previously discussed in Section 5.2. In the current work, the computations and experiments indicate that when the gap is small (that is, $g^* = 1$) the interaction between the two vortex streets prevents the second instability from occurring. When

Doublet-like configuration

Re	$g^* = 1$	$g^* = 3$	$g^* = 5$
100	1.35 (1.4)	1.7 (1.72)	1.8 (1.79)
150	1.6 (1.6)	1.85 (1.86)	1.9 (1.94)
200	1.65 (1.7)	1.85 (1.88)	1.9 (1.94)

Reverse doublet-like configuration

Re	$g^* = 1$	$g^* = 3$	$g^* = 5$
100	4.4 (3.84)	2.45 (2.52)	2.2 (2.24)
150	4.1 (3.71)	2.45 (2.53)	2.25 (2.28)
200	4.1 (3.53)	2.4 (2.46)	2.15 (2.27)

Table 5.2: Critical rotational rate to suppress vortex formation, experimental values in parentheses.

the vortex shedding is suppressed at sufficiently high spin rate, there are two pairs of stationary stagnation points associated with the positive (red) and negative (blue) vortices from each cylinder, as shown on the left column of figures 5.20, 5.21 and 5.22. Each front stagnation point (that is, upstream of the cylinder centers) moves outward radially with increasing spin rate (that is, with increasing circulation) and its location follows the closed streamline around the cylinder body. In contrast, each rear stagnation point (that is, downstream of the cylinder centers) moves inward toward the front stagnation point as the spin rate increases. At some point, the two closed vortex systems merge into one, and the two stagnation points combine into a single point at a location near that of the rear stagnation point prior to merging. By increasing the spin rate further, each closed vortex system is stretched to resemble a tear drop shape, and the stagnation point progresses towards the horizontal center line. From observation, it is at this point that the second instability occurs prior to the appearance of the virtual elliptic body.

The relatively large gap sizes for which this instability occurs, that is $g^* = 3$ and 5, effectively cause the vortex street from each cylinder to appear similar to that produced by a single rotating cylinder. However, the interaction between the two vortex streets is apparently sufficient to lower the spin rate at which the instability appears when compared to the case of a single rotating cylinder. For the doublet-like rotation, it is observed that for $Re = 200$, $g^* = 5$, the second instability occurs at $3.55 \leqslant \Omega \leqslant 3.8$ over a Strouhal number range from 0.0143 to 0.0321. For $Re = 200$, $g^* = 3$, it occurs at $3.65 \leqslant \Omega \leqslant 3.85$ with $0.0155 \leqslant St \leqslant 0.0298$. As was shown in figure 5.26, there are some slight differences in the values of St and Ω corresponding to the second instability at different Reynolds numbers and gap spacings. For example, consider the vorticity and streamlines of the second instability shedding mode for $g^* = 3$ and $g^* = 5$ shown in figure 5.40. The red vortex was shed from the upper cylinder while the blue one was shed from the lower cylinder. The decreasing distance between successive vortex cores with increasing Strouhal number reflects the higher shedding frequency. Also note the excellent agreement between the computation and experiment shown in figure 5.41 for $Re = 100$, $g^* = 5$, and $\Omega = 4$.

In the reverse doublet-like case, the second instability does not occur in the speed range of the investigation because in the first steady flow region the positive and negative vortices in the vicinity of the cylinder bodies are less likely to affect one another. The front and rear stagnation points are produced away from the center line and in opposing pairs. Consequently it appears that this configuration helps delay the merging of the front and rear stagnation points. Figure 5.42 illustrates the progression from unsteady (left column) to steady flow (center and right columns) for $Re = 150$ for different gap sizes. It can be seen that at $\Omega = 5$ for $g^* = 3$ and 5 only a single stagnation point is formed for each cylinder.

5.4.5 Power consumption

The possible benefits of unsteady wake suppression bear a cost in terms of the power consumption required to overcome the translational aerodynamic drag as well as to maintain the rotational motion of the cylinder pair. This can be analyzed by calculating the time-averaged power coefficient using the equation 5.1. Figure 5.43 shows $\overline{CP}$ (of the upper cylinder) plotted against rotational speed for both the doublet-like and reverse doublet-like configurations in comparison to the single rotating cylinder

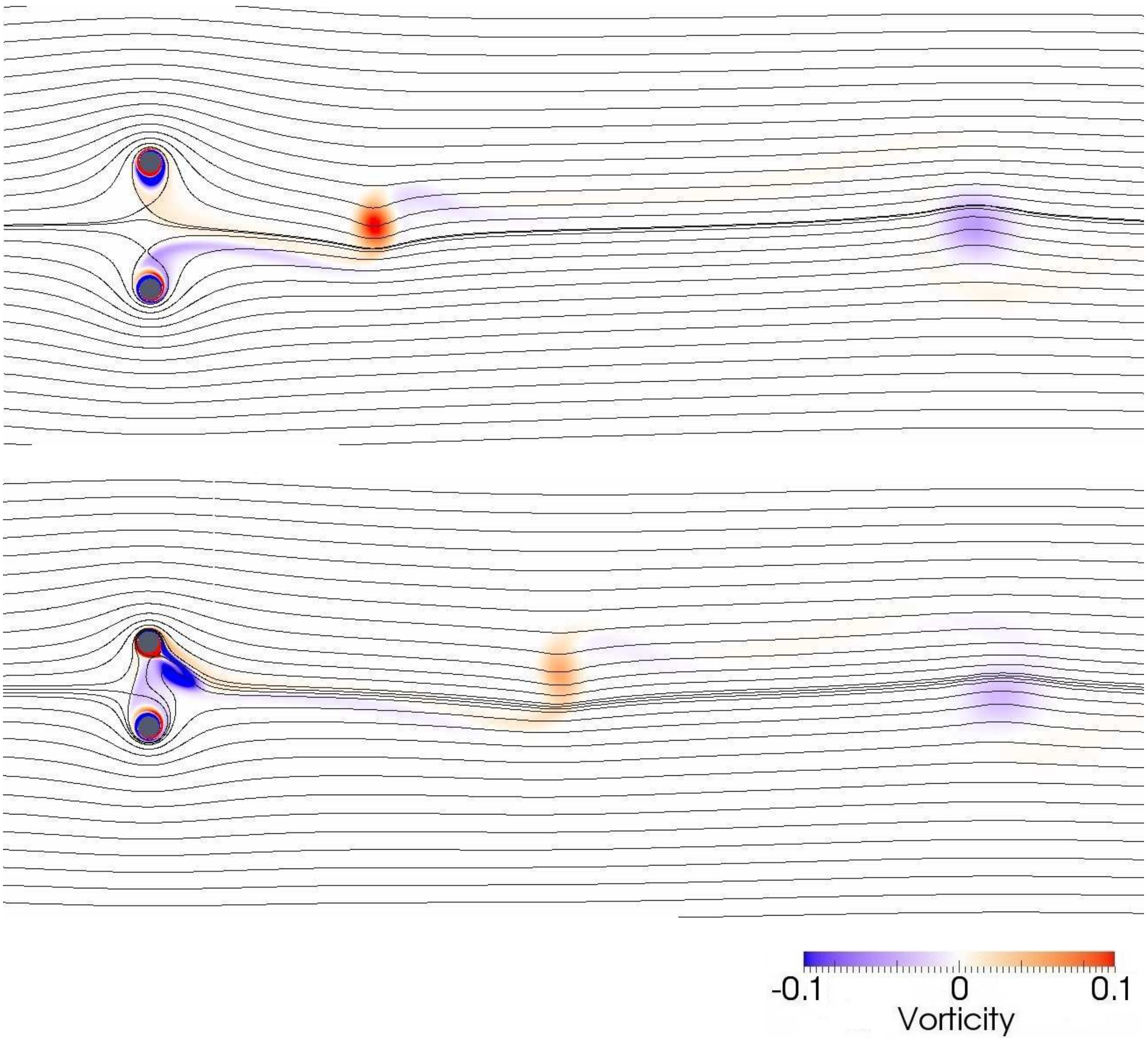

Figure 5.40: Instantaneous streamlines and vorticity for the second instability of the doublet-like counter-rotating configuration (computational results): a. $Re = 200$, $g^* = 5$, $\Omega = 3.75$ (top); b. $Re = 200$, $g^* = 3$, $\Omega = 3.25$ (bottom). Vorticity contour levels of the computational and experimental results are the same.

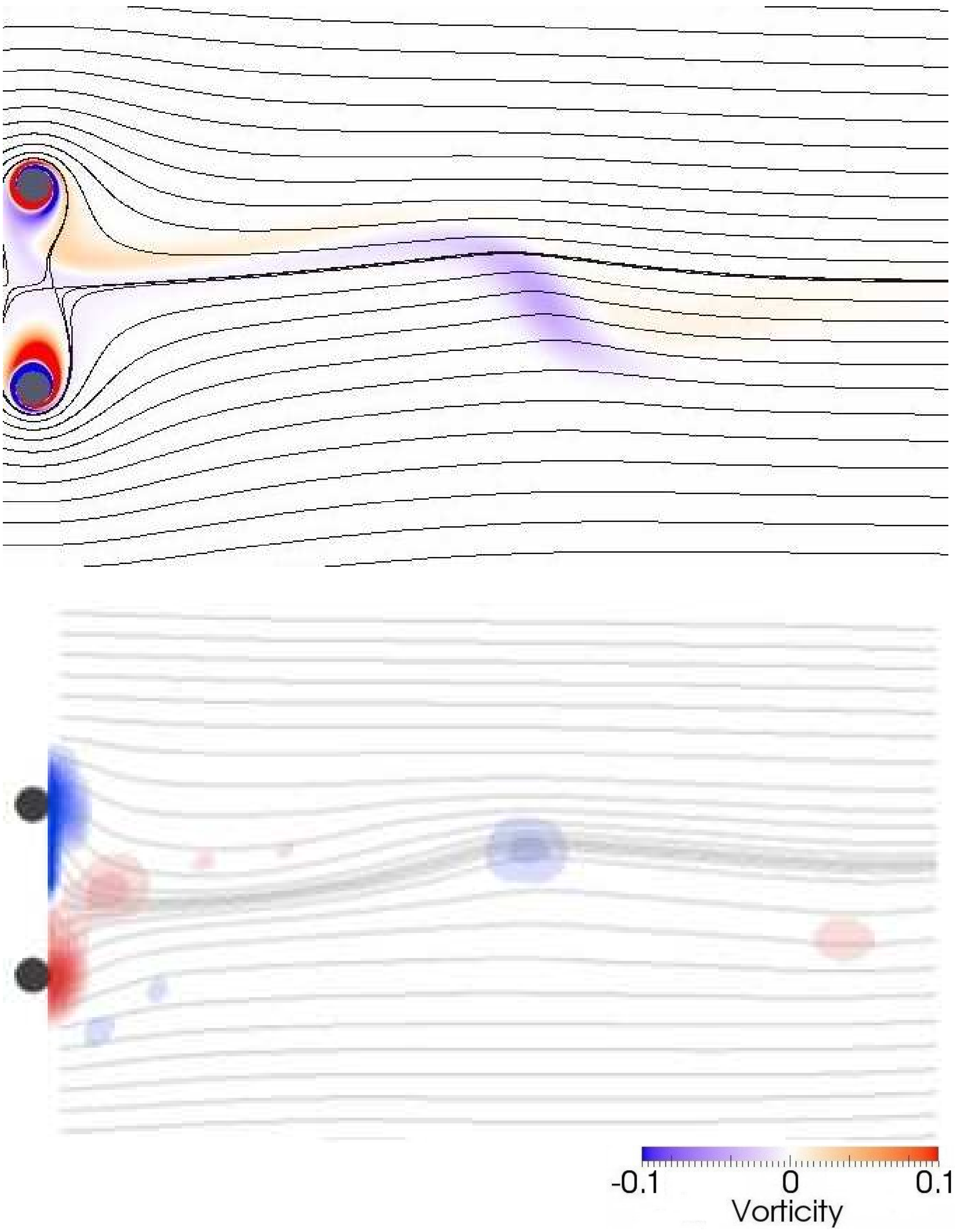

Figure 5.41: Instantaneous streamlines and vorticity for the second instability of the doublet-like counter-rotating configuration, $Re = 100$, $g^* = 5$, $\Omega = 4$: a. computational (top); b. experimental (bottom). Vorticity contour levels of the computational and experimental results are the same.

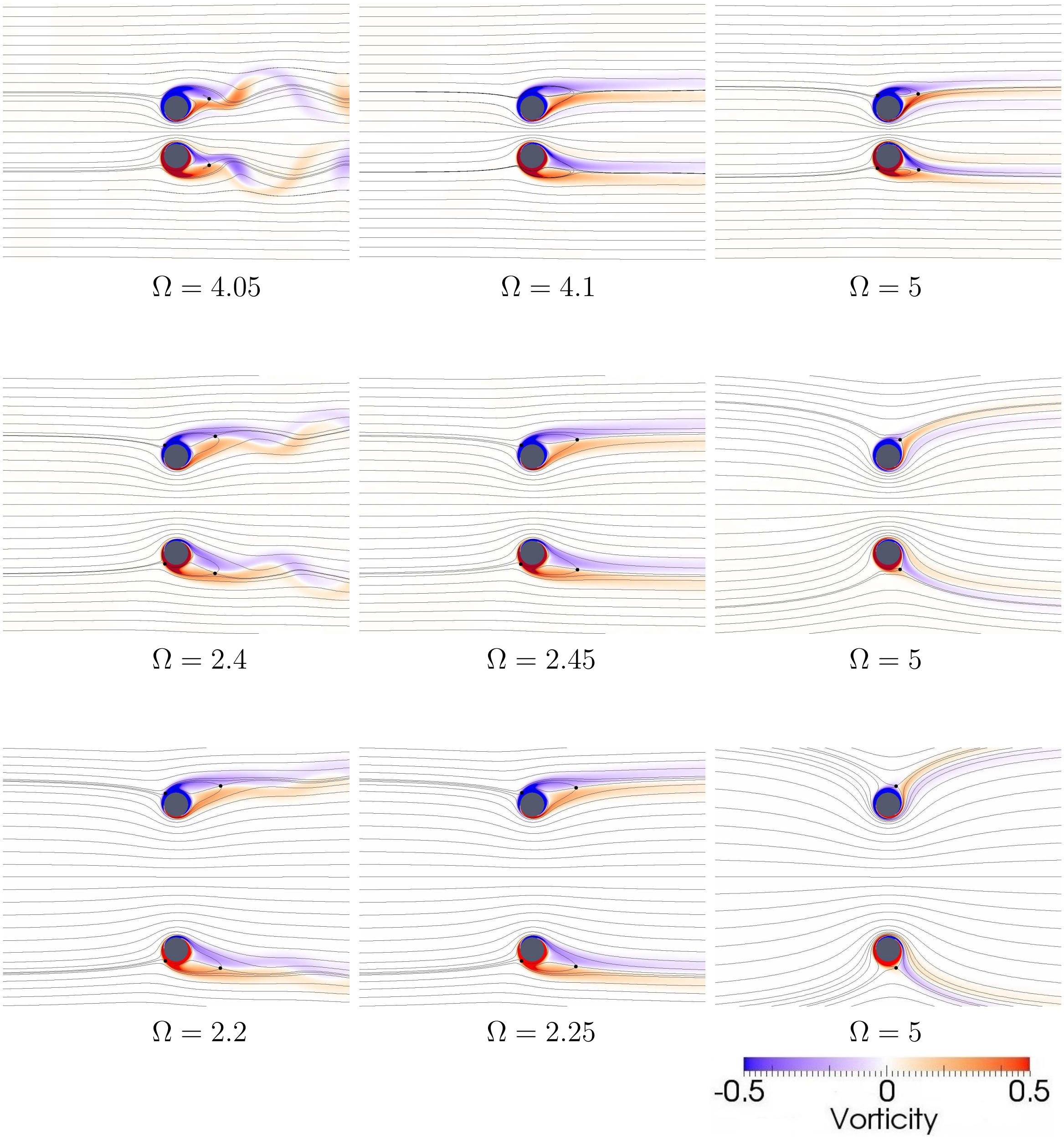

$\Omega = 4.05$ $\Omega = 4.1$ $\Omega = 5$

$\Omega = 2.4$ $\Omega = 2.45$ $\Omega = 5$

$\Omega = 2.2$ $\Omega = 2.25$ $\Omega = 5$

Figure 5.42: Flow past a reverse doublet-like counter-rotating configuration: instantaneous streamlines and vorticity at various rotational speeds (computational results). Stagnation points are represented by "●". First row: $Re = 150$, $g^* = 1$; second row: $Re = 150$, $g^* = 3$; third row: $Re = 150$, $g^* = 5$.

at $Re = 200$. The trends are similar for $Re = 100$ and 150. It is observed that in both rotational configurations, as the gap size increases, and not surprisingly the curves converge towards that of the single rotating cylinder. As the gap size decreases, it is advantageous, or more efficient, to rotate the cylinder pair in the doublet-like configuration due to a decrease in both the aerodynamic drag contribution, $(\overline{CP})_D$, and the required torque, $(\overline{CP})_M$, as shown in figure 5.44. Note that the aerodynamic drag contribution to $\overline{CP}$, shown in figure 5.44 (left), is essentially a replot of $\overline{C_D}$ for $Re = 200$ (figures 5.25 and 5.35).

An interesting phenomenon is observed in the doublet-like case where there appears to be a noticeable change in the slope of the power coefficient in the *transitional* range prior to the formation of the elliptical body. This is particularly so for $g^* = 1$, where a clear discontinuity in the spinning torque curve is observed (see figure 5.44), such that there is a sudden jump in $(\overline{CP})_M$ at $\Omega = 2.6$. In this rotational regime, the stagnation points transition from being vertically to horizontally aligned and the flow between the cylinder pair reverses direction, opposing the oncoming free-stream velocity. It may be that in this *transitional* regime, as the flow between the cylinder pair becomes stagnant before reversal, there is a significant reduction in the torque required to rotate the cylinders. Once the flow has reversed direction and the virtual elliptic body has formed, the cylinders must continually accelerate the fluid particles contained between the cylinder pair, thus returning the power coefficient to a monotonically increasing trend. This behavior occurs over a very short interval in Ω, and a further investigation of this flow mechanism is required to better understand the nature of this regime. It may also be possible that three-dimensionality plays an ever increasing role at lower gap spacings, potentially highlighted by the fact that such a large discontinuity in power coefficients is only seen for $g^* = 1$. For $g^* = 3$ and 5, the range of speeds where the slope changes also coincides with the occurrence of the second instability.

In the reverse-doublet configuration, no change in the slope of $(\overline{CP})_M$, figure 5.44, was observed at any gap spacing, since neither a closed body nor a secondary instability were present for the range rotational speeds examined here. Deviations in the slope of $\overline{CP}$ are the result of changes in the aerodynamic drag contribution,

$(\overline{CP})_D$, and a sharp transition occurs during the drag reduction phase just prior to the total suppression of unsteady wakes at $\Omega = 4.1$, 2.3 and 2.25 for $g^* = 1$, 3 and 5, respectively, see figures 5.43 and 5.44.

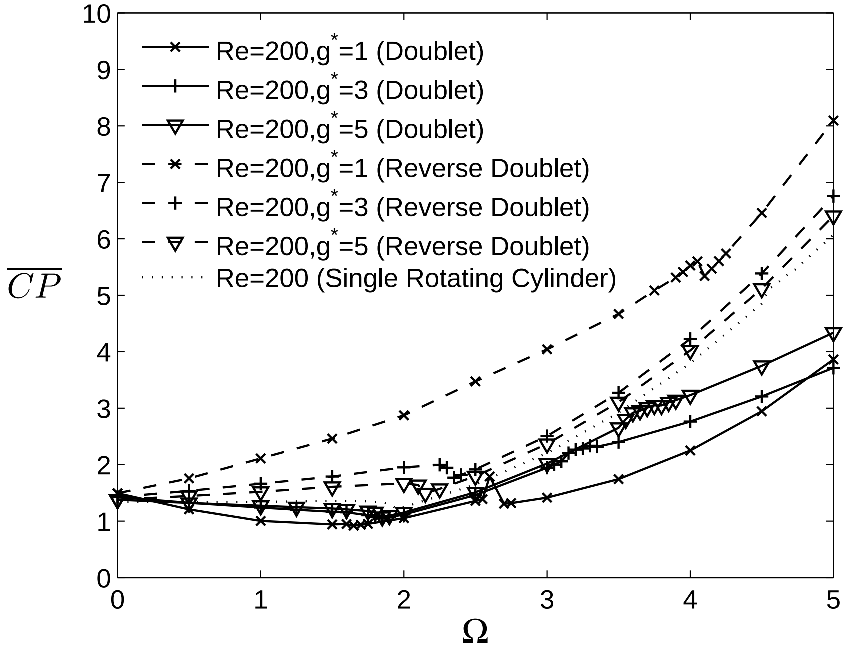

Figure 5.43: Flow past a counter-rotating cylinder: numerically determined time-averaged values of the power coefficient (upper cylinder, $Re = 200$).

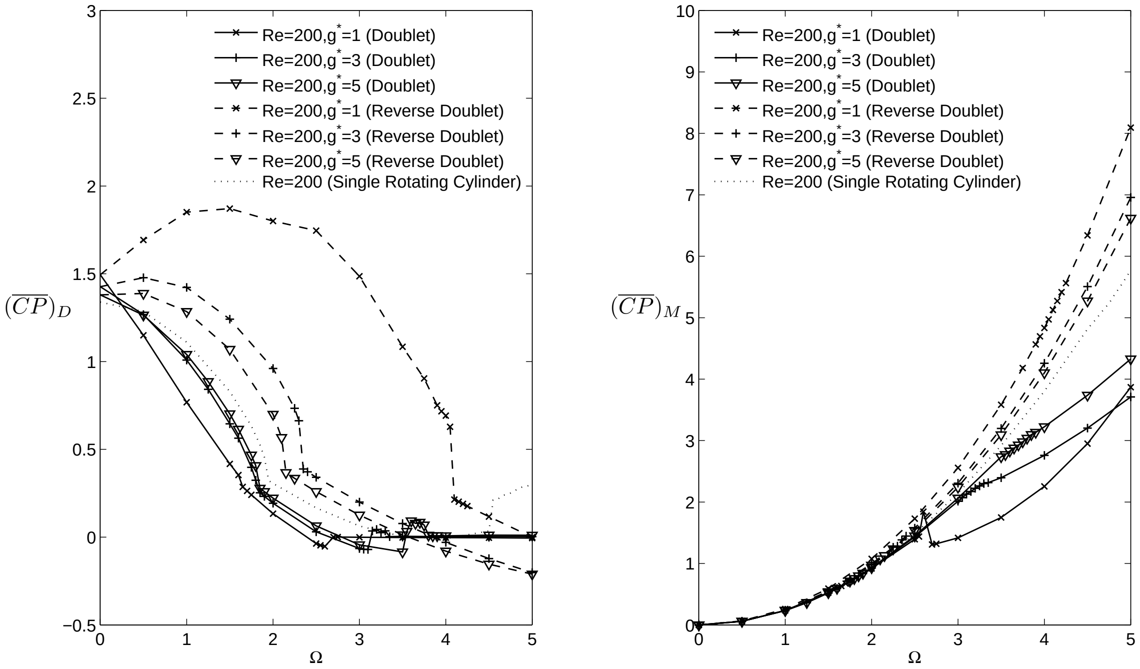

Figure 5.44: Flow past a counter-rotating cylinder: contributions of aerodynamic drag (left) and spinning torque (right) to the mean power coefficient (upper cylinder, $Re = 200$).

Chapter 6

Conclusions and future work

In the research described in this thesis, both passive and active vortex suppression techniques of laminar flow past bluff bodies have been investigated, primarily by way of numerical simulations. The passive technique involves the placement of a thin splitter plate downstream of a bluff body while the active technique focuses on counter-rotating a pair of cylinders. The numerical tools used for investigation include the commercially available incompressible flow solver based on the Semi-Implicit Method for Pressure-Linked Equation (SIMPLE) and the compressible solver based on high-ordered spectral difference (SD) method that has been developed at the Stanford Aerospace Computing Laboratory. Complimentary experiments have also been performed to correlate and verify some of the numerical findings. The splitter plate experiment was performed in a low speed wind tunnel using laser Doppler vibrometer to detect the oscillation due to vortex shedding. The counter-rotating cylinder experiment was performed in collaboration with Peter Dewey and Professor Alexander Smits of the Gas Dynamics Lab at Princeton University.

6.1 Splitter plate summary

Both the numerical simulations and wind tunnel experiments confirm that a thin splitter plate can be effectively used to control unsteady vortex shedding, vortex induced forces and thus vortex induced vibration when it is properly placed downstream of a bluff body. Focusing on flows at low Reynolds numbers, it is found that the effectiveness is relatively insensitive to variations of the splitter plate length in the range $0.25 \cdot d$ to $1.0 \cdot d$. However, there is a critical separation distance where a jump is observed in the fluctuating components of lift and drag. In an unbounded flow, a short and thin splitter plate can alter the shedding characteristics but does not completely eliminate the wake oscillation. However, the mean drag on the body is generally reduced. In a bounded flow, a splitter plate placed at a proper separation distance can completely eliminate the vortex instability and consequent force oscillations on a two-dimensional circular cylinder.

6.2 Counter-rotating circular cylinder pair summary

Digital particle image velocimetry and a high-order spectral difference computational method were employed to investigate the flow over a pair of counter-rotating cylinders. The experimental and computational results were generally in excellent agreement in resolving the wake structure and various stability regimes. For the doublet-like configuration at a slow rotational rate (i.e. unsteady regime), a synchronized in-phase vortex shedding mode that was unstable to small disturbances was present at $Re = 150$ and 200 for $g^* = 1$. Decreasing the Reynolds number to 100 for this case resulted in a wake structure similar to that of flow past a single bluff body. The existence of a virtual elliptic body, first predicted by Chan & Jameson (2010) to appear when the rotational speed is sufficiently large, was validated by the high-order SD computations, as well as by the experimental results. The size of the virtual elliptic body increases with increasing rotational speed. The values of the critical rotation rate Ω_{crit}, where the wake forms an elliptic body and the total drag reduces to zero, were found more precisely than in this previous work, and over a wider range of Reynolds number and gap sizes. In addition, for the first time, a secondary instability was observed for $g^* = 3$ and 5, at rotational speeds just prior to the formation of the virtual elliptic body.

For the reverse doublet-like rotational configuration, the in-phase shedding mode was present for $g^* = 1$ at all Reynolds numbers when $\Omega < 1$, and the anti-phase shedding mode was present when $1 < \Omega < \Omega_{crit}$. This is similar to that seen for a pair of non-rotating cylinders, but it was shown here for the first time that counter-rotation of the cylinder pair would lead to wake stabilization by transition to an anti-phase shedding mode for $1 < \Omega < \Omega_{crit}$.

For both rotational configurations, a stable anti-phase wake structure was observed for all Reynolds numbers at $g^* = 3$ and 5. For the doublet-like configuration, the value of Ω_{crit} monotonically increased with increasing gap spacing and Reynolds number, while for the reverse doublet-like configuration, it monotonically decreased with increasing gap spacing and Reynolds number. These opposing tendencies of the two rotational configurations with increasing gap spacing cause Ω_{crit} to converge towards the value needed to suppress vortex formation in the wake of a single rotating cylinder.

6.3 Recommendation for future work

In future work it is recommended that both passive and active vortex suppression techniques be investigated for flow past other bluff bodies other than the circular and square cylinders. It is also important to recognize that in reality, the flow past bluff bodies can be complex and three-dimensional at higher Reynolds numbers. Throughout this research, a sizable matrix of two-dimensional computations was performed in order to obtain the present results. It still would be a very expensive proposition to compute this matrix in three dimensions with the available resources. However as computer performance continues to improve and the computational cost continues its descending path, a similar matrix of three-dimensional calculations can be performed in the future.

Appendix A

Experimental methods

The contents of appendix A.2 were the work of Peter Dewey and Alexander Smits of Gas Dynamics Laboratory at Princeton University and were previously published by Chan *et al.* [70] [1].

A.1 Splitter plate experiment

An experiment to verify our numerical results of vortex induced vibration and its suppression using thin splitter plate has been carried out in a very low speed wind tunnel (figure A.1) with an achievable air speed range of 0.5 to 5.0 m/s. The wind tunnel is made of entirely out of Plexiglass – a clear acrylic material – which allows for the use of a laser Doppler vibrometer (LDV) to detect the test specimen motion. The wind tunnel length is approximately 3.5 feet long and is set up to operate in a suction mode where the driving fan is positioned at the diverging end of the tunnel as shown in figure A.1. The air speed is calculated from the dynamic pressure measurement using a simple total pressure tube made from bending the tip of a long hypodermic needle to be in-line with the flow stream as shown in figure A.2. The dynamic pressure is measured via Baratron capacitive micro-manometer made by MKS Technology. The manometer has a sensitivity of approximately 1 Pascal. The air speed is also

---

[1] Chan *et al.* , *J. Fluid Mech.* Copyright 2011. Reproduced with permission from Cambridge University Press. License Number 2671560868712.

measured by a hot-wire velocity probe for verification. The corresponding Reynolds number ranges from approximately 70 to 1,000 depending on the blockage factor and the diameter of the test cylinder.

The test section has a cross sectional area of 4.5 inches by 1.5 inches. A circular 416 stainless steel rod with a diameter of 1/16 inch is used as a test specimen. The 416 stainless steel is chosen because it has the magnetic property such that the cylinder can be levitated horizontally as shown in a couple of arrangements on figures A.3 and A.4. Note that the cylinder has pointed ends where one has a direct contact with one of the magnets and the other is floated but held horizontally by the fringe field of the other magnet. When the flow is introduced at the low Reynolds number range, the vortex shedding from the test cylinder induces a forcing function which causes a sinusoidal motion. The oscillatory motion is easily detectable near the floating end by processing the signal of an LDV beam via a dynamic signal analyzer. The cylinder does not move in a purely vertical motion. Rather it pivots around the pointed end that is physically connected to one of the magnets.

The unbounded flow condition can be set up as shown on figure A.3. Even though in theory the flow in a wind tunnel is bounded, the ratio of the test cylinder to the test section height, i.e. blockage factor, in this particular setup is much less than 0.1 and therefore can be considered unbounded. When the test cylinder is placed in a secondary enclosure, as shown on figure A.4, the setup is equivalent to the case of a bounded flow with stationary walls. In both cases, the test cylinder is placed in the developed flow region which is determined by theoretical calculation, and verified by using a total pressure tube and a Baratron pressure sensor at a few locations along the length of the test section. In order to determine the effectiveness of a splitter plate at variable separation distances, it is mounted on a movable, low profile stand, which can then be systematic placed directly downstream of the cylinder. It is important to note that the splitter plate needs to be made out of a non-magnetic material. A piece of plastic shim stock with a thickness of 0.15 mm is chosen for this experiment. The reason for such a choice is to prevent any interaction due to magnetic coupling force that can transmit back into the circular cylinder.

The frequency of the cylinder motion due to vortex shedding is identified by

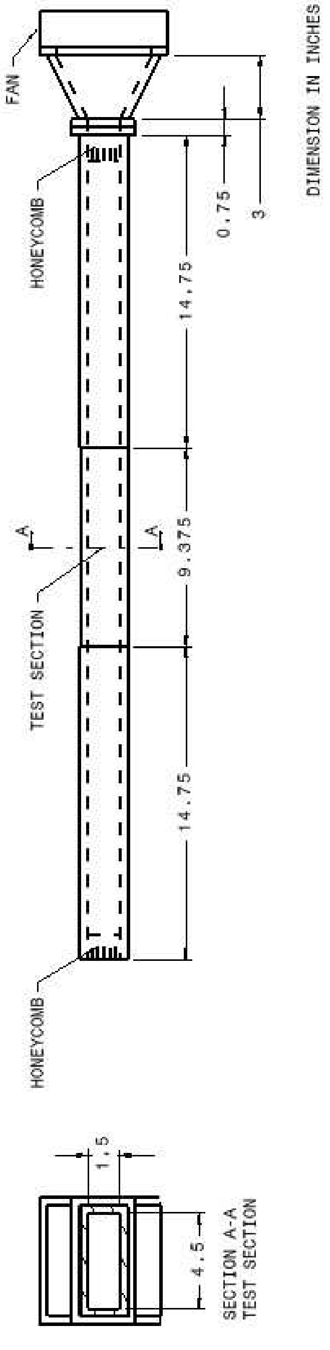

Figure A.1: Sketch of the low speed wind tunnel setup.

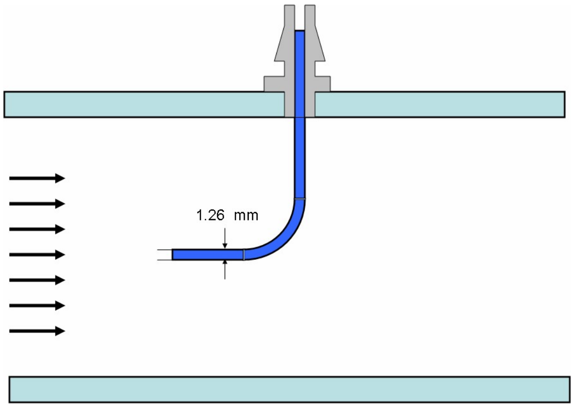

Figure A.2: Total pressure tube in the test section.

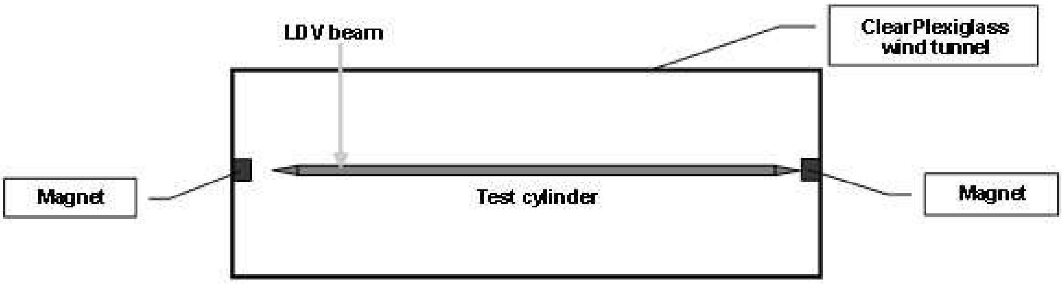

Figure A.3: Sketch of the test section in an unbounded flow arrangement.

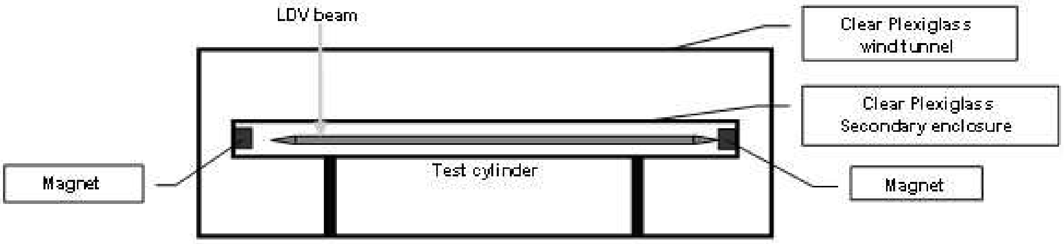

Figure A.4: Sketch of the test section in a bounded flow arrangement.

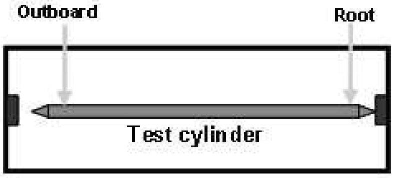

Figure A.5: LDV measurement points for identifying vibration mode due to vortex shedding.

processing the LDV signal via fast Fourier transform using a dynamic signal analyzer. Because of the presence of noise in the experimental system, the identification of this frequency requires careful examination of the data. In the two-dimensional shedding regime, this frequency will be distinct but depend solely on changes in the air speed. However, it is possible to falsely identify one of the harmonics of the fan modes, for example, to be the shedding frequency. One of the keys in isolating the vibration mode due to shedding is to normalize the signal measured at the outboard location of the cylinder, as shown in figure A.5, to the signal measured at the root section of the cylinder. Normalizing the two signals yields a distinctive mode of motion due to vortex shedding alone as shown in figure A.6. The frequency obtained from this vibration mode is used to calculate the Strouhal number. It will become clear later when a splitter plate is placed at a proper position that the vibration mode can be completely eliminated, which confirms the validity of this identification technique.

A.2 Counter-rotating circular cylinder pair experiment

The experimental portion of the counter-rotating cylinder pair research was performed in close collaboration with the Gas Dynamics Lab at Princeton University. The experimental investigation was entirely conducted by Peter Dewey and Professor Alexander Smits using digital particle image velocimetry (DPIV). The experimental method is briefly described here. To achieve counter rotation of a cylinder pair, a Pittman

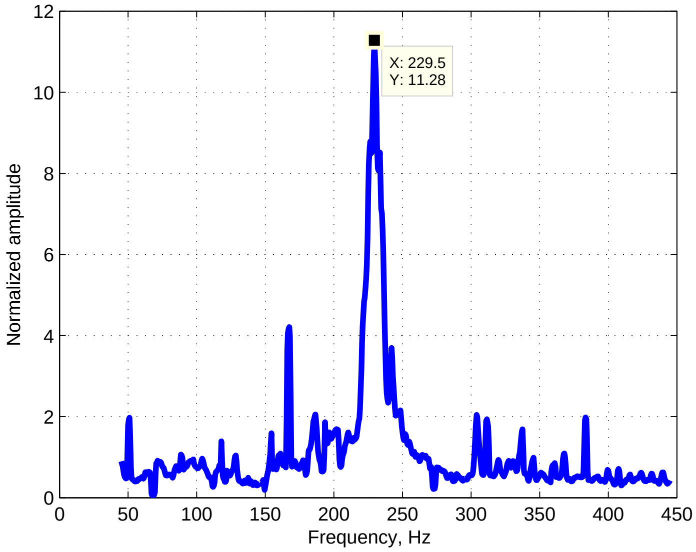

Figure A.6: Normalized power spectrum of outboard to root motion.

9236S009-R1 servo-motor attached to a timing belt with a 6:1 gear reduction ratio was used to rotate the cylinders. The rotation speed was determined by a data acquisition system that sampled the rotation speed at a frequency of 500 Hz from a digital optical encoder accompanying the motor. The apparatus was mounted in a closed loop, free surface water channel with a test section that is 0.46 m wide, 0.3 m deep, and 2.5 m long (see figure A.7). Surface waves were eliminated by mounting a clear acrylic plate to be in contact with the free surface, with the cylinder pair mounted vertically and protruding through a slot machined in the acrylic plate. The bottom of the cylinders were held in place by low-friction bearings, housed in a streamlined mounting block that extended 10 mm above the channel floor. The cylinders were 0.00635 m in diameter and 0.3 m long, producing an aspect-ratio of 47 to ensure two-dimensional flow past the cylinder pair. DPIV was conducted at the mid-span of the cylinder pair.

Neutrally buoyant silver-coated hollow ceramic spheres with a mean diameter of 93 μm were used as seeding particles (Potters Industries Inc. Conduct-O-Fil AGSL150

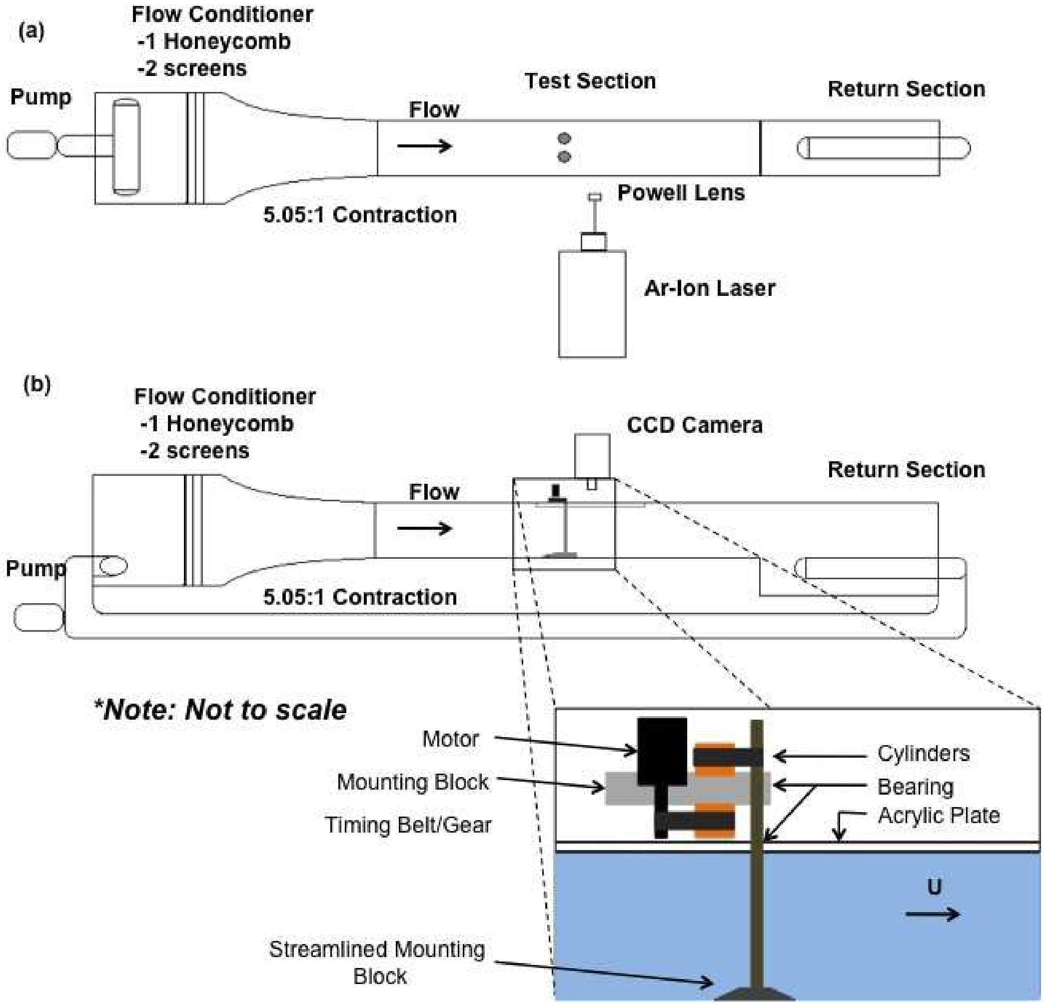

Figure A.7: Sketch of water channel and experimental apparatus. (a) Top view; (b) side view.

TRD). A Spectra Physics 2020 Argon-Ion laser coupled to a fiber optic delivery system and Powell lens (Oz Optics Ltd.) were used to produce a 1.5-mm-thick light sheet for the experiments. A Redlake MotionXtra HG-LE CCD camera with $1,128 \times 752$ pixel resolution was used to acquire the DPIV images. The camera frame rates ranged between 50 and 100 Hz, producing 30 to 60 discrete time intervals between subsequent vortices being shed, with a typical exposure time of 3 ms.

Two-dimensional discretely sampled velocity fields were computed by calculating local spatial cross-correlations using software developed by Jimenéz [107]. Three passes, with 64×64, 32×32, and subsequently 16×16 pixel windows with 50 % overlap were performed. To achieve sub-pixel accuracy, a 5×5 pixel Gaussian interpolation was utilized. In a typical DPIV pair, vector outliers were primarily constrained to the edges of the domain and regions of the domain with insufficient lighting (for instance, in the shadows created by the cylinders). Fewer than 1 % of vectors in the far-wake of the cylinders proved to be outliers, though resolving the near-wake of the cylinders was more challenging due to lighting issues. The analysis yielded, at most, 5 % error in velocity and 10 % error in vorticity. The vorticity was calculated at each point by computing the circulation about a closed contour formed by the eight neighboring points using a trapezoidal rule scheme [108]. There is an estimated error of 9 % in the determination of the critical rotation speed to suppress vortex formation, Ω_{crit}.

The DPIV system was validated by examining the flow past a stationary cylinder. A fast Fourier transform (FFT) was taken of the time-resolved velocity field in the cylinder wake to determine the vortex shedding frequency, and ultimately the Strouhal number, $St = fd/U$. The Strouhal number was found to be 0.163, 0.184 and 0.197 for Reynolds numbers of 100, 150 and 200, respectively, deviating less than 0.05 % from Williamson [8]. There is an estimated uncertainty of 5 % in the calculation of the Strouhal number. Note that the shedding frequency was captured equally well by taking the FFT of the vorticity field. The Strouhal number was found to be invariant for three different DPIV spatial resolutions (2.5, 5 and 8.5 vectors per cylinder diameter), and a spatial resolution of 5 vectors per cylinder diameter was selected for all results presented here.

A typical data set consisted of 1,200 image pairs that were phase averaged at the vortex shedding frequency to minimize noise. The phase-averaging was a two-step process: a first data set was used to find the shedding frequency from the cylinder pair, and then a second data set was acquired with the camera timing synchronized with the vortex shedding frequency. It should be noted that the time-resolved data was always used to determine quantities such as Ω_{crit} and Strouhal number, and the phase-averaged data was solely used for qualitative purposes in displaying vorticity contour plots. In the case where counter-rotation of the cylinder pair suppressed unsteadiness, all image pairs of the original data set were used in the averaging process. Due to optical constraints, only the wake region of the cylinder pair was investigated.

Appendix B

Additional numerical validation

The contents of this appendix were previously published by Chan *et al.* [70] [1].

B.1 Comparison of numerical results for flow past a stationary pair of circular cylinders

Here, the force coefficients for a stationary circular cylinder pair obtained using the fourth-order SD calculations are compared with the numerical results using the immersed boundary method by Kang [101]. Table B.1 lists the values of mean C_L and C_D as well as the standard deviation of C_L for the flip-flop shedding mode at $g^* = 1$, $Re = 100$ and for the anti-phase mode at $g^* = 3$, $Re = 100$. In general, the results are in reasonable agreement, further establishing the confidence in the SD approach used in this research.

---

[1] Chan *et al.* , *J. Fluid Mech.* Copyright 2011. Reproduced with permission from Cambridge University Press. License Number 2671560868712.

g^*	$\overline{C_D}$	$\overline{C_L}$	$\sigma(C_L)$	Source
1	1.427	0.259	0.147	Present (SD, Fourth order)
	1.44	0.28	0.17	Kang [101]
3	1.444	0.074	0.281	Present (SD, Fourth order)
	1.47	0.08	0.28	Kang [101]

Table B.1: Flow past a stationary circular cylinder pair at $Re = 100$: mean C_D, mean C_L and standard deviation of C_L.

B.2 Study of mesh density and SD order of accuracy

The numerical accuracy of different SD schemes has been documented by [57]. Here, an additional numerical accuracy test based on the mesh density and the SD order of accuracy is presented in table B.2 for the three gap sizes considered in this research. Listed are the mean and standard deviation values of force coefficients and the corresponding Strouhal numbers (for the anti-phase shedding pattern) of the top circular cylinder of the counter-rotating cylinder pair, for the stationary case and for the case with $\Omega = 3$. In this test case, two different sets of meshes – coarse and fine – were used. The fine mesh is essentially reconstructed from the coarse mesh by simply quadrupling the number of cells. The differences between the results obtained from the coarse mesh and those from the fine mesh are small when the fourth-order SD is used. However, the computational cost increases proportional to the number of degrees of freedom. Therefore, in order to perform a fairly large simulation matrix in a reasonable amount of time, the coarse meshes in conjunction with the fourth-order SD were used to obtain the final results presented in this research.

Configuration	Re	g^*	Ω	SD order	Number of cells	DOFs	$\overline{C_D}$	$\overline{C_L}$	$\sigma(C_D)$	$\sigma(C_L)$	St
1	150	1	0	2	5176 (Coarse)	20704	1.502	0.247	0.270	0.356	–
	150	1	0	2	20704 (Fine)	82816	1.504	0.232	0.369	0.395	–
	150	1	0	4	5176 (Coarse)	82816	1.474	0.227	0.110	0.388	–
	150	1	0	4	20704 (Fine)	331264	1.472	0.228	0.107	0.361	–
2	150	1	3	2	5176 (Coarse)	20704	0.082	6.045	0.000	0.000	–
	150	1	3	2	20704 (Fine)	82816	0.028	6.067	0.000	0.000	–
	150	1	3	4	5176 (Coarse)	82816	0.001	6.063	0.000	0.000	–
	150	1	3	4	20704 (Fine)	331264	0.002	6.077	0.000	0.000	–
3	150	3	0	2	7736 (Coarse)	30944	1.457	0.063	0.020	0.420	0.183
	150	3	0	2	30944 (Fine)	123776	1.444	0.061	0.022	0.431	0.190
	150	3	0	4	7736 (Coarse)	123776	1.421	0.057	0.023	0.429	0.193
	150	3	0	4	30944 (Fine)	495104	1.422	0.058	0.023	0.429	0.192
4	150	3	3	2	7736 (Coarse)	30944	0.060	9.250	0.000	0.000	–
	150	3	3	2	30944 (Fine)	123776	−0.013	9.373	0.000	0.000	–
	150	3	3	4	7736 (Coarse)	123776	−0.069	9.391	0.000	0.000	–
	150	3	3	4	30944 (Fine)	495104	−0.069	9.388	0.000	0.000	–
5	150	5	0	2	9088 (Coarse)	36352	1.420	0.032	0.017	0.382	0.180
	150	5	0	2	36352 (Fine)	145408	1.403	0.030	0.019	0.390	0.186
	150	5	0	4	9088 (Coarse)	145408	1.373	0.028	0.020	0.386	0.189
	150	5	0	4	36352 (Fine)	581632	1.373	0.028	0.020	0.386	0.188
6	150	5	3	2	9088 (Coarse)	36352	0.098	9.452	0.000	0.001	–
	150	5	3	2	36352 (Fine)	145408	0.029	9.549	0.000	0.000	–
	150	5	3	4	9088 (Coarse)	145408	−0.040	9.569	0.000	0.000	–
	150	5	3	4	36352 (Fine)	581632	−0.040	9.564	0.000	0.000	–

Table B.2: Numerical accuracy test based on SD order and mesh density: values of the force coefficients and Strouhal numbers of the top cylinder. The standard deviation of force coefficients are denoted by the symbol σ.

Bibliography

[1] L. Prandtl, O. G. Tietjens, and J. P. Den Hartog. *Applied hydro-and aeromechanics*. Dover New York, 1957.

[2] L. S. G. Kovásznay. Hot-wire investigation of the wake behind cylinders at low Reynolds numbers. *Proceedings of the Royal Society of London. Series A, Mathematical and Physical Sciences*, 198(1053):174–190, 1949.

[3] A. Roshko. On the drag and shedding frequency of two-dimensional bluff bodies. *NACA Technical Note 3169*, 1954.

[4] P. W. Bearman and M. M. Zdravkovich. Flow around a circular cylinder near a plane boundary. *Journal of Fluid Mechanics*, 89(01):33–47, 1978.

[5] Y. Lecointe and J. Piquet. On the use of several compact methods for the study of unsteady incompressible viscous flow round a circular cylinder. *Computers & Fluids*, 12(4):255–280, 1984.

[6] M. Braza, P. Chassaing, and H. H. Minh. Numerical study and physical analysis of the pressure and velocity fields in the near wake of a circular cylinder. *Journal of Fluid Mechanics*, 165:79–130, 1986.

[7] M. F. Unal and D. Rockwell. On vortex formation from a cylinder. Part 2. Control by splitter-plate interference. *Journal of Fluid Mechanics*, 190:513–529, 1988.

[8] C. H. K. Williamson. Oblique and parallel modes of vortex shedding in the wake of a circular cylinder at low Reynolds numbers. *Journal of Fluid Mechanics*, 206:579–627, 1989.

[9] R. D. Blevins. *Flow-induced vibration*. Van Nostrand Reinhold Company, 1990.

[10] C. H. K. Williamson and A. Roshko. Measurements of base pressure in the wake of a cylinder at low Reynolds numbers. *Zeitschrift für Flugwissenschaften und Weltraumforschung*, 14(1-2):38–46, 1990.

[11] A. Roshko. Perspectives on bluff body aerodynamics. *Journal of Wind Engineering and Industrial Aerodynamics*, 49(1-3):79–100, 1993.

[12] G. D. Miller and C. H. K. Williamson. Control of three-dimensional phase dynamics in a cylinder wake. *Experiments in Fluids*, 18(1):26–35, 1994.

[13] C. H. K. Williamson. Vortex dynamics in the cylinder wake. *Annual Review of Fluid Mechanics*, 28(1):477–539, 1996.

[14] C. H. K. Williamson and R. Govardhan. Vortex-induced vibrations. *Annual Review of Fluid Mechanics*, 36(1):413–455, 2004.

[15] E. Naudascher and D. Rockwell. *Flow-induced vibrations: an engineering guide*. Dover Publications, 2005.

[16] R. W. Davis and E. F. Moore. A numerical study of vortex shedding from rectangles. *J. Fluid Mech*, 116(3):475–506, 1982.

[17] R. W. Davis, E. F. Moore, and L. P. Purtell. A numerical-experimental study of confined flow around rectangular cylinders. *Physics of Fluids*, 27:46, 1984.

[18] A. Okajima. Strouhal numbers of rectangular cylinders. *J. Fluid Mech*, 123:379–398, 1982.

[19] A. Okajima. Numerical simulation of flow around rectangular cylinders. *Journal of Wind Engineering and Industrial Aerodynamics*, 33(1-2):171–180, 1990.

[20] A. Okajima, H. Ueno, and H. Sakai. Numerical simulation of laminar and turbulent flows around rectangular cylinders. *International journal for numerical methods in fluids*, 15(9):999–1012, 1992.

[21] K. M. Kelkar and S. V. Patankar. Numerical prediction of vortex shedding behind a square cylinder. *International journal for numerical methods in fluids*, 14(3):327–341, 1992.

[22] C. Norberg. Flow around rectangular cylinders: Pressure forces and wake frequencies. *Journal of Wind Engineering and Industrail Aerodynamics*, 49:187–196, 1993.

[23] A. Sohankar, L. Davidson, and C. Norberg. Numerical simulation of unsteady flow around a square two-dimensional cylinder. In *Twelfth Australasian Fluid Mechanics Conference*, pages 517–520, Sydney, Australia, December 1995.

[24] A. Sohankar, C. Norberg, and L. Davidson. Numerical simulation of unsteady low-Reynolds number flow around rectangular cylinders at incidence. *Journal of Wind Engineering and Industrail Aerodynamics*, 69:189–201, 1997.

[25] A. Sohankar, C. Norberg, and L. Davidson. Low-Reynolds-number flow around a square cylinder at incidence: Study of blockage, onset of vortex shedding and outlet boundary condition. *International Journal for Numerical Methods in Fluids*, 26(1):39–56, 1998.

[26] S. Sen, S. Mittal, and G. Biswas. Flow past a square cylinder at low Reynolds numbers. *International Journal for Numerical Methods in Fluids*, 67:1160–1174, 2011.

[27] 650 RAMAC announcement. `http://www-03.ibm.com/ibm/history/exhibits/650/650_pr2.html`. [Online accessed: October 15, 2012].

[28] Fluid dynamic bearing spindle motors: Their future in hard disk drives. `http://www.hgst.com/tech/techlib.nsf/techdocs/`

`089C4B963AEE9A6F86256D340%075052F/$file/FD_White_Paper_FINAL.pdf`, November 2007. [Online accessed: October 15, 2012].

[29] S. V. Patankar and D. B. Spalding. A calculation procedure for heat, mass and momentum transfer in three-dimensional parabolic flows. *International Journal of Heat and Mass Transfer*, 15(10):1787–1806, 1972.

[30] S. V. Patankar. A calculation procedure for two-dimensional elliptic situations. *Numerical Heat Transfer*, 4(4):409–425, 1981.

[31] J. P. Van Doormaal and G. D. Raithby. Enhancements of the SIMPLE method for predicting incompressible fluid flows. *Numerical Heat Transfer, Part A: Applications*, 7(2):147–163, 1984.

[32] S. V. Patankar. *Numerical heat transfer and fluid flow.* Hemisphere Publications, 1980.

[33] J. H. Ferziger and M. Perić. *Computational methods for fluid dynamics*. Springer Berlin, 2002.

[34] F. H. Harlow and J. E. Welch. Numerical calculation of time-dependent viscous incompressible flow of fluid with free surface. *Physics of Fluids*, 8(12):2182, 1965.

[35] C. M. Rhie and W. L. Chow. Numerical study of the turbulent flow past an airfoil with trailing edge separation. *AIAA Journal*, 21(11):1525–1532, 1983.

[36] R. I. Issa. Solution of the implicitly discretised fluid flow equations by operator-splitting. *Journal of Computational Physics*, 62(1):40–65, 1986.

[37] G. Iaccarino. Predictions of a turbulent separated flow using commercial cfd codes. *Journal of fluids engineering*, 123(4):819–828, 2001.

[38] B. Cockburn and C. W. Shu. TVB Runge-Kutta local projection discontinuous Galerkin finite element method for conservation laws. II: General framework. *Mathematics of Computation*, 52(186):411–435, 1989.

[39] B. Cockburn, S. Y. Lin, and C. W. Shu. TVB Runge-Kutta local projection discontinuous Galerkin finite element method for conservation laws. III: One-dimensional systems. *Journal of Computational Physics*, 84(1):90–113, 1989.

[40] B. Cockburn, S. Hou, and C. W. Shu. The Runge-Kutta local projection discontinuous Galerkin finite element method for conservation laws. IV: The multidimensional case. *Mathematics of Computation*, 54(190):545–581, 1990.

[41] B. Cockburn and C. W. Shu. The Runge-Kutta discontinuous Galerkin method for conservation laws. V: Multidimensional systems. *Journal of Computational Physics*, 141(2):199–224, 1998.

[42] J. S. Hesthaven and T. Warburton. *Nodal discontinuous Galerkin methods: algorithms, analysis, and applications.* Springer Verlag, 2007.

[43] D. A. Kopriva and J. H. Kolias. A conservative staggered-grid Chebyshev multidomain method for compressible flow. *Institute for Computer Applications in Science and Engineering*, 33:3, 1995.

[44] Y. Liu, M. Vinokur, and Z. J. Wang. Spectral difference method for unstructured grids. I: Basic formulation. *Journal of Computational Physics*, 216(2):780–801, 2006.

[45] Z. J. Wang, Y. Liu, G. May, and A. Jameson. Spectral difference method for unstructured grids. II: Extension to the Euler equations. *Journal of Scientific Computing*, 32(1):45–71, 2007.

[46] C. Liang, R. Kannan, and ZJ Wang. A p-multigrid spectral difference method with explicit and implicit smoothers on unstructured triangular grids. *Computers & Fluids*, 38(2):254–265, 2009.

[47] G. May and A. Jameson. A spectral difference method for the Euler and Navier-Stokes equations. *AIAA paper* 2006-304, 44th AIAA Aerospace Sciences Meeting and Exhibit, Reno, NV, January 2006.

[48] P. G. Huang, Z. J. Wang, and Y. Liu. An implicit space-time spectral difference method for discontinuity capturing using adaptive polynomials. *AIAA paper* 2005-5255, 17th AIAA Computational Fluid Dynamics Conference, Toronto, ON, June 2005.

[49] Y. Sun, Z. J. Wang, and Y. Liu. High-order multidomain spectral difference method for the Navier-Stokes equations on unstructured hexahedral grids. *Communication in Computational Physics*, 2:310–333, 2007.

[50] F. Bassi and S. Rebay. High-order accurate discontinuous finite element solution of the 2D Euler equations. *Journal of Computational Physics*, 138(2):251–285, 1997.

[51] Z. J. Wang. Spectral (finite) volume method for conservation laws on unstructured grids: Basic formulation. *Journal of Computational Physics*, 178(1):210–251, 2002.

[52] Z. J. Wang and Y. Liu. Extension of the spectral volume method to high-order boundary representation. *Journal of Computational Physics*, 211(1):154–178, 2006.

[53] C. Liang, S. Premasuthan, and A. Jameson. High-order accurate simulation of low-Mach laminar flow past two side-by-side cylinders using spectral difference method. *Computers & Structures*, 87(11-12):812–827, 2009.

[54] C. Liang, S. Premasuthan, A. Jameson, and Z. J. Wang. Large eddy simulation of compressible turbulent channel flow with spectral difference method. *AIAA paper* 2009-402, 47th AIAA Aerospace Sciences Meeting including The New Horizons Forum and Aerospace Exposition, Orlando, FL, January 2009.

[55] C. Liang, A. Jameson, and Z. J. Wang. Spectral difference method for compressible flow on unstructured grids with mixed elements. *Journal of Computational Physics*, 228(8):2847–2858, 2009.

[56] S. Premasuthan, C. Liang, A. Jameson, and Z. J. Wang. A p-multigrid spectral difference method for viscous compressible flow using 2D quadrilateral meshes. *AIAA paper* 2009-950, 47th AIAA Aerospace Sciences Meeting including The New Horizons Forum and Aerospace Exposition, Orlando, FL, January 2009.

[57] K. Ou, C. Liang, S. Premasuthan, and A. Jameson. High-order spectral difference simulation of laminar compressible flow over two counter-rotating cylinders. *AIAA paper* 2009-3956, 27th AIAA Applied Aerodynamics Conference, San Antonio, TX, June 2009.

[58] A. H. Mohammad, Z. J. Wang, and C. Liang. LES of turbulent flow past a cylinder using spectral difference method. *AIAA paper* 2008-7184, 26th AIAA Applied Aerodynamics Conference, Honolulu, HI, August 2008.

[59] H. T. Huynh. A flux reconstruction approach to high-order schemes including discontinuous Galerkin methods. *AIAA paper* 2007-4079, 18th AIAA Computational Fluid Dynamics Conference, Miami, FL, June 2007.

[60] A. Jameson. A proof of the stability of the spectral difference method for all orders of accuracy. *Journal of Scientific Computing*, pages 1–11, 2010.

[61] Y. Sun, Z. J. Wang, Y. Liu, and C. L. Chen. Efficient implicit LU-SGS algorithm for high-order spectral difference method on unstructured hexahedral grids. *AIAA paper* 2007-313, 45th AIAA Aerospace Sciences Meeting and Exhibit, Reno, NV, 2007.

[62] V. V. Rusanov. Calculation of interaction of non-steady shock waves with obstacles. *Journal of Computational and Mathematical Physics, USSR*, 1:261–279, 1961.

[63] P. L. Roe. Approximate Riemann solvers, parameter vectors, and difference schemes. *Journal of Computational Physics*, 43(2):357–372, 1981.

[64] A. Harten and J. M. Hyman. Self adjusting grid methods for one-dimensional hyperbolic conservation laws. *Journal of Computational Physics*, 50(2):235–269, 1983.

[65] A. Jameson, W. Schmidt, and E. Turkel. Numerical solutions of the Euler equations by finite volume methods using Runge-Kutta time-stepping schemes. *AIAA paper* 1981-1259, AIAA 14th Fluid and Plasma Dynamic Conference, Palo Alto, CA, June 1981.

[66] C. W. Shu. Total-variation-diminishing time discretizations. *SIAM Journal on Scientific and Statistical Computing*, 9(6):1073–1084, 1988.

[67] C.W. Shu and S. Osher. Efficient implementation of essentially non-oscillatory shock-capturing schemes. *Journal of Computational Physics*, 77(2):439–471, 1988.

[68] R. J. Spiteri and S. J. Ruuth. A new class of optimal high-order strong-stability-preserving time discretization methods. *SIAM Journal on Numerical Analysis*, 40(2):469–491, 2003.

[69] A. S. Chan and A. Jameson. Suppression of the unsteady vortex wakes of a circular cylinder pair by a doublet-like counter-rotation. *International Journal for Numerical Methods in Fluids*, 63(1):22–39, 2010.

[70] A. S. Chan, P. A. Dewey, A. Jameson, C. Liang, and A. J. Smits. Vortex suppression and drag reduction in the wake of counter-rotating cylinders. *Journal of Fluid Mechanics*, 679:343–382, 2011.

[71] A. Belov, L. Martinelli, and A. Jameson. A new implicit algorithm with multigrid for unsteady incompressible flow calculations. *AIAA paper* 1995-0049, 33rd Aerospace Sciences Meeting and Exhibit, Reno, NV, January 1995.

[72] A. Prothero and A. Robinson. On the stability and accuracy of one-step methods for solving stiff systems of ordinary differential equations. *Mathematics of Computation*, 28(125):145–162, 1974.

[73] M. Berzins and R. M. Furzeland. An adaptive theta method for the solution of stiff and nonstiff differential equations. *Applied numerical mathematics*, 9(1):1–19, 1992.

[74] R. D. Henderson. *Unstructured spectral element methods: Parallel algorithms and simulations*. PhD thesis, Princeton University, 1994.

[75] H. Ding, C. Shu, K. S. Yeo, and D. Xu. Numerical simulation of flows around two circular cylinders by mesh-free least square-based finite difference methods. *International Journal for Numerical Methods in Fluids*, 53(2):305–332, 2007.

[76] C. Liu, X. Zheng, and C. H. Sung. Preconditioned multigrid methods for unsteady incompressible flows. *Journal of Computational Physics*, 139(1):35–57, 1998.

[77] J. Park, K. Kwon, and H. Choi. Numerical solutions of flow past a circular cylinder at Reynolds numbers up to 160. *Journal of Mechanical Science and Technology*, 12(6):1200–1205, 1998.

[78] B. Sharman, F. S. Lien, L. Davidson, and C. Norberg. Numerical predictions of low Reynolds number flows over two tandem circular cylinders. *International Journal for Numerical Methods in Fluids*, 47(5):423–447, 2005.

[79] R. D. Henderson. Details of the drag curve near the onset of vortex shedding. *Physics of Fluids*, 7(9):2102–2104, 1995.

[80] S. Mittal and B. Kumar. Flow past a rotating cylinder. *Journal of Fluid Mechanics*, 476:303–334, 2003.

[81] C. Norberg. Fluctuating lift on a circular cylinder: review and new measurements. *Journal of Fluids and Structures*, 17(1):57–96, 2003.

[82] M. Sahin and R. G. Owens. A numerical investigation of wall effects up to high blockage ratios on two-dimensional flow past a confined circular cylinder. *Physics of Fluids*, 16:1305–1320, 2004.

[83] J. H. Chen, W. G. Pritchard, and S. J. Tavener. Bifurcation for flow past a cylinder between parallel planes. *Journal of Fluid Mechanics*, 284(5):23–41, 1995.

[84] C. P. Jackson. A finite-element study of the onset of vortex shedding in flow past variously shaped bodies. *Journal of Fluid Mechanics*, 182(1):23–45, 1987.

[85] Y. Ding and M. Kawahara. Three-dimensional linear stability analysis of incompressible viscous flows using the finite element method. *International journal for numerical methods in fluids*, 31(2):451–479, 1999.

[86] H. Suzuki, Y. Inoue, T. Nishimura, K. Fukutani, and K. Suzuki. Unsteady flow in a channel obstructed by a square rod (crisscross motion of vortex). *International Journal of Heat and Fluid Flow*, 14(1):2–9, 1993.

[87] C. J. Apelt, G. S. West, and A. A. Szewczyk. The effects of wake splitter plates on the flow past a circular cylinder in the range $10^4 < \mathrm{R} < 5 * 10^4$. *Journal of Fluid Mechanics*, 61:187–198, 1973.

[88] S. Mittal. Effect of a slip splitter plate on vortex shedding from a cylinder. *Physics of Fluids*, 15:817–820, 2003.

[89] L. Prandtl. Magnuseffekt und windkraftschiff. *Die Naturwissenschaften*, 13:93–108, 1925.

[90] H. M. Badr and S. C. R. Dennis. Time-dependent viscous flow past an impulsively started rotating and translating circular cylinder. *Journal of Fluid Mechanics*, 158(1985):447–488, 1985.

[91] M. Coutanceau and C. Menard. Influence of rotation on the near-wake development behind an impulsively started circular cylinder. *Journal of Fluid Mechanics*, 158(1):399–446, 1985.

[92] H. M. Badr, M. Coutanceau, S. C. R. Dennis, and C. Menard. Unsteady flow past a rotating circular cylinder at Reynolds numbers 10^3 and 10^4. *Journal of Fluid Mechanics*, 220(1):459–484, 1990.

[93] H. M. Badr, S. C. R. Dennis, and P. J. S. Young. Steady and unsteady flow past a rotating circular cylinder at low Reynolds numbers. *Computers & fluids*, 17(4):579–609, 1989.

[94] T. Tang and D. B. Ingham. On steady flow past a rotating circular cylinder at Reynolds numbers 60 and 100. *Computers & Fluids*, 19(2):217–230, 1991.

[95] S. Kang, H. Choi, and S. Lee. Laminar flow past a rotating circular cylinder. *Physics of Fluids*, 11:3312, 1999.

[96] D. Stojković, M. Breuer, and F. Durst. Effect of high rotation rates on the laminar flow around a circular cylinder. *Physics of Fluids*, 14:3160, 2002.

[97] D. Stojković, P. Schön, M. Breuer, and F. Durst. On the new vortex shedding mode past a rotating circular cylinder. *Physics of Fluids*, 15:1257, 2003.

[98] P. W. Bearman and A. J. Wadcock. The interaction between a pair of circular cylinders normal to a stream. *Journal of Fluid Mechanics*, 61(3):499–511, 1973.

[99] M. M. Zdravkovich. Review of flow interference between two circular cylinders in various arrangements. *Journal of Fluids Engineering*, 99:618, 1977.

[100] C. H. K. Williamson. Evolution of a single wake behind a pair of bluff bodies. *Journal of Fluid Mechanics*, 159:1–18, 1985.

[101] S. Kang. Characteristics of flow over two circular cylinders in a side-by-side arrangement at low Reynolds numbers. *Physics of Fluids*, 15(9):2486–2498, 2003.

[102] I. Peschard and P. Le Gal. Coupled wakes of cylinders. *Physical Review Letters*, 77(15):3122–3125, 1996.

[103] H. J. Kim. Investigation of the flow between a pair of circular cylinders in the flopping regime. *Journal of Fluid Mechanics*, 196:431–448, 1988.

[104] D. Sumner, S. S. T. Wong, S. J. Price, and M. P. Païdoussis. Fluid behaviour of side-by-side circular cylinders in steady cross-flow. *Journal of Fluids and Structures*, 13(3):309–338, 1999.

[105] A. E. Perry, M. S. Chong, and T. T. Lim. The vortex-shedding process behind two-dimensional bluff bodies. *Journal of Fluid Mechanics*, 116:77–90, 1982.

[106] H. S. Yoon, J. H. Kim, H. H. Chun, and H. J. Choi. Laminar flow past two rotating circular cylinders in a side-by-side arrangement. *Physics of Fluids*, 19:128103, 2007.

[107] J. M. Jimenéz. *Low Reynolds number studies in the wake of a submarine model using particle image velocimetry.* PhD thesis, Princeton University, 2002.

[108] M. Raffel, C. E. Willert, and J. Kompenhans. *Particle image velocimetry: a practical guide.* Springer Verlag, 1998.